Flight Dynamic Constraints in Conceptual Aircraft Multidisciplinary Analysis and Design Optimization

Craig C. Morris

Dissertation submitted to the Faculty of the
Virginia Polytechnic Institute and State University
in partial fulfillment of the requirements for the degree of

Doctor of Philosophy
in
Aerospace Engineering

Joseph A. Schetz, Chair
Cornel Sultan, Co-Chair
Rakesh K. Kapania
Edward Alyanak

December 4, 2013
Blacksburg, Virginia

Keywords: MDO, Dynamic Performance, Stability and Control, Linear Matrix Inequalities

Flight Dynamic Constraints in Conceptual Aircraft Multidisciplinary Analysis and Design Optimization

Craig C. Morris

ABSTRACT

This work details the development of a stability and control module for implementation into a Multidisciplinary Design Optimization (MDO) framework for the conceptual design of conventional and advanced aircraft. A novel approach, called the Variance Constrained Flying Qualities (VCFQ) approach, is developed to include closed-loop dynamic performance metrics in the design optimization process. The VCFQ approach overcomes the limitations of previous methods in the literature, which only functioned for fully decoupled systems with single inputs to the system. Translation of the modal parameter based flying qualities requirements into state variance upper bounds allows for multiple-input control laws which can guarantee upper bounds on closed-loop performance metrics of the aircraft states and actuators to be rapidly synthesized. A linear matrix inequality (LMI) problem formulation provides a general and scalable numerical technique for computing the feedback control laws using convex optimization tools. The VCFQ approach is exercised in a design optimization study of a relaxed static stability transonic transport aircraft, wherein the empennage assembly is optimized subject to both static constraints and closed-loop dynamic constraints. Under the relaxed static stability assumption, application of the VCFQ approach resulted in a 36% reduction in horizontal tail area and a 32% reduction in vertical tail area as compared to the baseline configuration, which netted a weight savings of approximately 5,200 lbs., a 12% reduction in cruise trimmed drag, and a static margin which was marginally stable or unstable throughout the flight envelope. State variance based dynamic performance constraints offer the ability to analyze large, highly coupled systems, and the linear matrix inequality problem formulation can be extended to include higher-order closed-loop design objectives within the MDO. Recommendations for further development and extensions of this approach are presented at the end.

This material is based on research sponsored by Air Force Research Laboratory under agreement number FA8650-09-2-3938. The U.S. Government is authorized to reproduce and distribute reprints for Governmental purposes notwithstanding any copyright notation thereon. The views and conclusions contained herein are those of the authors and should not be interpreted as necessarily representing the official policies or endorsements, either expressed or implied, of Air Force Research Laboratory or the U.S. Government.

Dedication

To my wife, for her patience and support while I completed my degree. And to my parents, for stimulating my childhood with erector sets and trips to space camp.

Acknowledgments

I am grateful for the support received from all members of my committee, both technical and otherwise. Sound advice was never far away with Dr. Schetz as an advisor, and his encouragement and counsel were incredibly influential to me during my time in graduate school. To Dr. Sultan, I am thankful for his always open door. There were weeks where my nose rarely left a book he had given me, and his chalkboard was frequently full of my scribbles as I tried to understand just a portion of his knowledge in dynamics and controls. I also extend my gratitude to Dr. Kapania, who provided me with one of the most inconspicuous but most invaluable assets a graduate student can have—secure funding for the duration of my studies. His tireless pursuit of research grants guaranteed my time in graduate school wasn't spent writing proposals every semester. Finally, I'd like to thank Dr. Alyanak, for being so down to Earth and the voice of reason when I was convinced academia was trying to swallow me up.

Other than my committee, I also owe many thanks to Dr. Darcy Allison—my officemate of 3+ years, and a great friend. He weathered the thick and thin with me, and we collaborated on almost everything we did while in graduate school. My experiences at Virginia Tech would not have been the same without him.

There is no such thing as a free lunch, and my time in graduate school is no different. I am grateful to the Multidisciplinary Sciences and Technology Center at the Air Force Research Laboratory in Dayton, OH, for their research grants and support provided to me through the AFRL-VT-WSU Collaborative Center for Multidisciplinary Sciences.

Contents

List of Symbols

$\bar{A}$	Model state matrix with desired eigenvectors and eigenvalues
$\mathcal{C}(M,N)$	Controllability matrix of the matrix pair (M,N)
C_D	Drag coefficient, nondimensional
C_{HT}	Horizontal tail volume coefficient
C_L	Lift coefficient, nondimensional
$C_{L_{\mathrm{HT}}}$	Horizontal tail lift coefficient
C_{L_R}	Lift coefficient at onset of takeoff rotation
$C_{L_{\max}}$	Maximum attainable lift coefficient
C_{VT}	Vertical tail volume coefficient
C_Y	Side force coefficient, nondimensional
C_ξ	Generalized aerodynamic force or moment coefficient
C_{ξ_x}	Derivative of aerodynamic coefficient C_ξ with respect to arbitrary variable x
C_l	Rolling moment coefficient, nondimensional
C_m	Pitching moment coefficient, nondimensional
C_{m_0}	Pitching moment coefficient at zero lift
$C_{m_{np}}$	Pitching moment about the neutral point
C_n	Yawing moment coefficient, nondimensional
$C_{n_{\beta_{\mathrm{dyn}}}}$	Dynamic C_{n_β} coefficient, a yaw departure predictor
D	Aerodynamic drag force

D_e	Drag of an inoperative engine
E	Column matrix of eigenvectors
$\bar{E}$	Column matrix of desired eigenvectors
F_B	Body-Fixed axes system
F_E	Earth-Fixed axes system
F_I	Inertial axes system
F_S	Stability axes system
H	Angular momentum
I	Inertia tensor
I_{xx}	Moment of Inertia about the x-axis
I_{xy}	Product of inertia, $x-y$ plane
I_{xz}	Product of inertia, $x-z$ plane
I_{yy}	Moment of Inertia about the y-axis
I_{yz}	Product of inertia, $y-z$ plane
I_{zz}	Moment of Inertia about the z-axis
K	Feedback gain matrix
L	Aerodynamic lift force
L	Body axes rolling moment
M	Body axes pitching moment
N	Body axes yawing moment
R_{RSS}	Range of the RSS configuration
R_{base}	Range of the baseline configuration
SM	Static margin
S_{HT}	Horizontal tail reference area
S_{VT}	Vertical tail reference area

$S_{r_{\mathrm{HT}}}$	Horizontal tail area ratio
S_{ref}	Wing reference area
T	Thrust
T_2	Time to double amplitude
T_B^I	Transformation matrix from the body to the inertial axes
T_B^W	Transformation matrix from the body to the wind axes
T_I^B	Transformation matrix from the inertial to the body axes
T_W^B	Transformation matrix from the wind to the body axes
T_{ccf}	Transformation to control canonical form
U_0	Wind axes x-component of the velocity vector, $U_0 = \|V_W\|$
U_{de}	Derived equivalent gust velocity
V_{HT}	Velocity at the horizontal tail
V_R	Rotation velocity at takeoff
V_{TO}	Takeoff velocity
V_W	Wind axes velocity vector
$V_{s_{\mathrm{TO}}}$	Stall velocity at takeoff
V_{stall}	Stall velocity
W	Weight of the aircraft at a given flight condition
W_{final}	Final vehicle gross weight, range calculation
X	Body axes x-component of resultant forces
X	State covariance matrix or controllability grammian
X_T	Propulsive force, x-axis component
$\hat{X}$	Control canonical form deterministic state covariance matrix
Y	Aerodynamic side force
Y	Body axes y-component of resultant forces

Y_T	Propulsive force, y-axis component
Z	Body axes z-component of resultant forces
Z_T	Propulsive force, z-axis component
$\Delta C_{D_{\text{trim}}}$	Increment in the drag coefficient due to trimmed elevator deflection
Γ_{ie}	Impulse-to-energy gain
$\mathbb{I}$	The identity matrix
Λ	Diagonal matrix of eigenvalues
$\bar{\Lambda}$	Diagonal matrix of desired eigenvalues
α	Angle of attack
$\alpha_{\text{HT}_{\text{eff}}}$	Effective angle of attack at the horizontal tail, includes downwash and tail incidence angle
$\hat{\dot{\alpha}}$	Nondimensional time derivative of the angle of attack
$\hat{\dot{\beta}}$	Nondimensional time derivative of the angle of sideslip
δ_a	Aileron deflection angle
δ_e	Elevator deflection angle
δ_r	Rudder deflection angle
η_{HT}	Horizontal tail dynamic pressure ratio
$\omega_{d_{\text{dr}}}$	Dutch-roll mode damped natural frequency
$\omega_{n_{\text{dr}}}$	Dutch-roll mode natural frequency
$\omega_{n_{\text{ph}}}$	Phugoid mode natural frequency
$\omega_{n_{\text{sp}}}$	Short-period mode natural frequency
ϕ	Bank angle
ϕ_W	Bank angle to wind axes
ψ	Azimuth angle
ψ_W	Azimuth angle to wind axes
ρ	Freestream density

σ	State variance vector
σ_i	State variance of the ith state
$\hat{\sigma}_i$	Control canonical form state variance of the ith state
τ_{r}	Roll mode time constant
τ_{s}	Spiral mode time constant
θ	Pitch angle
θ_W	Pitch angle to wind axes
θ_{mg}	Angle formed by the line through the main landing gear and the CG, relative to vertical
$\dot{\theta}_R$	Rotation rate at takeoff
ζ	Damping ratio, generally
ζ_{dr}	Dutch-roll mode damping ratio
ζ_{ph}	Phugoid mode damping ratio
ζ_{sp}	Short-period mode damping ratio
a_i	ith coefficient of the characteristic polynomial
b	Aircraft span
$\bar{c}$	Wing reference chord
$\bar{c}_{\mathrm{HT}}$	Horizontal tail reference chord
$\bar{c}_{\mathrm{VT}}$	Vertical tail reference chord
g	Gravitational acceleration constant
k_{dr}	Constant, degree of separation between minimum and maximum Dutch-roll natural frequencies
k_{ph}	Constant, degree of separation between short-period and phugoid natural frequencies
l_{HT}	Horizontal tail lever arm, distance from CG to tail aerodynamic center
l_{VT}	Vertical tail lever arm, distance from CG to tail aerodynamic center
l_h	x-axis distance from the neutral point to horizontal tail aerodynamic center

m	Mass
n	Load factor
np	Neutral point
p	Body axes roll angular rate
$\hat{p}$	Nondimensional body axes roll angular rate
q	Body axes pitch angular rate
$\bar{q}$	Dynamic pressure
$\bar{q}_{\mathrm{HT}}$	Dynamic pressure at the horizontal tail
$\hat{q}$	Nondimensional body axes pitch angular rate
r	Body axes yaw angular rate
$\hat{r}$	Nondimensional body axes yaw angular rate
$^t/_c$	Thickness-to-chord ratio
u	Body axes x-component of freestream velocity
$u_{\max}$	Maximum actuator deflection
$\dot{u}_{\max}$	Maximum actuator deflection rate
v	Body axes y-component of freestream velocity
w	Body axes z-component of freestream velocity
x_{HT}	x coordinate of the horizontal tail aerodynamic center
x_{cg}	x coordinate of the center of gravity
x_{mac}	x coordinate of the leading edge of the mean aerodynamic chord
x_{mg}	x coordinate of the main landing gear
x_{np}	x coordinate of the neutral point
$\bar{x}_{cg}$	nondimensional x coordinate of the center of gravity, percent mac
$\bar{x}_{np}$	nondimensional x coordinate of the neutral point, percent mac
y_e	Distance along y-axis from CG to engine centerline
z_T	z-axis distance between the thrust line of action and the center of gravity

Acronyms

mac Mean aerodynamic chord

CG Center of Gravity

CAP Control Anticipation Parameter

CCF Control Canonical Form

CCV Control Configure Vehicle

CFD Computational Fluid Dynamics

DLM Doublet Lattice Method

FAR Federal Aviation Regulation

FC Flight Condition

FLOPS Flight Optimization System

GUI Graphical User Interface

GW Gross Weight

LCDP Lateral Control Departure Parameter

LMI Linear Matrix Inequality

LOES Lower-order Equivalent System

LQR Linear Quadratic Regulator

LTI Linear Time Invariant

LTV Linear Time Varying

MDO Multidisciplinary Design Optimization

MIMO Multiple Input Multiple Output

MOOSCF Matlab Object Oriented Stability & Control Framework

NPSS Numerical Propulsion Simulation System

OML Outer mold line

RMS Root-mean-square

RSS Relaxed Static Stability

S&C Stability & Control

SAS Stability Augmentation System

SBW Strut Braced Wing

SFC Specific Fuel Consumption

SISO Single Input Single Output

SSD Spoiler-slot-deflector

TBW Truss-Braced Wing

TOGW Takeoff Gross Weight

VCFQ Variance Constrained Flying Qualities

VLM Vortex Lattice Method

VT Virginia Tech

VT-CST Virginia Tech Class Shape Transformation

List of Figures

List of Tables

Chapter 1

Introduction

Since before the Wright Flyer left the ground (Figure 1.1), aircraft designers have struggled with the necessary and challenging task of maintaining stability and control (S&C) of the vehicle. In 1809, Sir George Cayley became the first to recognize the force balance needed for flight in the first part of his three-part treatise on aerodynamics entitled, "On Aerial Navigation" [1]. Through observations of nature and his experiments with gliders, Cayley soon after discovered the need for wing dihedral and center of gravity positioning as crucial elements for stability in aircraft design [2, 3]. Even in the 21^{st} century, S&C continues to pose a challenge to aircraft designers. Often to the detriment of the final product, the traditional aircraft design process typically delays thorough study of aircraft S&C until after the conceptual design process [4, 5]. While integrated control design efforts have been made on specific configurations (so-called control-configured aircraft) [6, 7], there are many examples of modern aircraft which suffer from control design limitations that went unnoticed until late in the design process. This strategy of aircraft design is not only costly, as late redesigns are expensive, but also potentially performance limiting [8].

Several well-known aircraft have suffered from S&C related performance limitations not

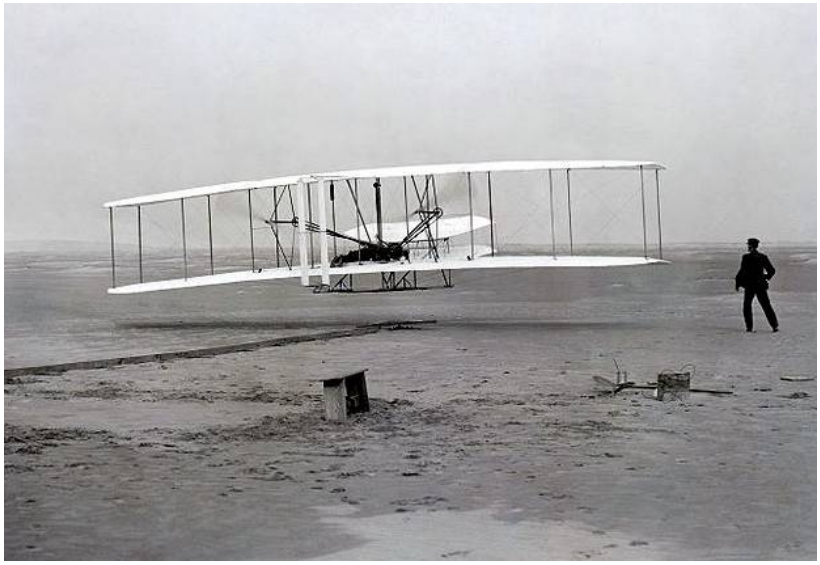

Figure 1.1: First flight of the Wright Flyer, an unstable, yet controllable aircraft that was notoriously difficult to fly

discovered during the early stages of design. As an example, the F-16 Falcon, seen in Figure 1.2a, was discovered to have a deep stall problem only after prototype aircraft were built and flight tested [9]. As the F-16 approaches angles of attack above 30°, the horizontal tail slips into the wake of the forebody and wing, drastically reducing its effectiveness. The tail is then unable to produce a sufficient nose down pitching moment, and the aircraft gets hung in a stall with an extreme angle of attack. No amount of control system design can increase the inherent effectiveness of a stalled surface, and S&C designers could not simply design a controller to fix the problem. As an alternative to a long and expensive alteration of the configuration, the designers of the F-16 were forced to implement an angle of attack limiter to prevent maneuvers from exceeding 28°, and training pilots on how to recover from the deep stall using a 'rocking' maneuver. Another interesting example of a control limited aircraft is the B-47 Stratojet, shown in Figure 1.2b, and its low altitude control reversal issues [10]. The Stratojet's long, flexible wings led conceptual designers to be concerned over the reversal of aileron control authority due to wing torsion and bending. Though the

problem was identified during the conceptual design phase, the limited computational tools of the time overpredicted the Stratojet's capabilities. The prototypes were manufactured with the fundamental design flaw. It was not until two years after the aircraft first flew that the analyses were of high enough fidelity to predict the phenomena observed during flight tests—providing a strong motivation for including higher fidelity physics earlier in the design process. The production B-47 aircraft were built as-is, since the cost of a redesign effort to eliminate the control reversal problems was greater than speed-limiting the aircraft at low altitudes.

(a) F-16 Fighting Falcon

(b) B-47 Stratojet

Figure 1.2: Examples of aircraft with inherent stability and control related design limitations

Not all discoveries of control limited aircraft were after the conceptual design phase. The B2 Stealth Bomber (Figure 1.6b), for example, underwent an aft planform redesign late in the conceptual design stage due to unforeseen aeroservoelastic coupling between the outboard elevon and the first wing bending mode [11]. Computational tools were able to identify the issue, and the cost of a structural redesign after prototype fabrication was

avoided. In fact, the aft planform modifications were combined with engine placement and exhaust modifications to extend the structural life of the surrounding surface. This success demonstrates the utility of higher fidelity conceptual design analyses and is another motivator for increasing the fidelity of conceptual design S&C tools.

The remainder of this chapter is intended to introduce and motivate the development of an S&C analysis package for use in conceptual design optimizations and trade studies. The chapter begins with a review of traditional conceptual design S&C analysis techniques, and then introduces Multidisciplinary Design Optimization (MDO) as a valuable tool for the 21^{st} century aircraft designer. The potential benefits of more thorough conceptual design S&C studies are then discussed, including an introduction of the dynamic performance constraints which are a major part of the technical contribution of this work. Finally, the research question and the scope of the work contained in this thesis are outlined.

1.1 Traditional Conceptual Design Stability & Control

Before exploring higher-fidelity analyses and their implementation into design optimization, it is important to discuss the traditional approach to conceptual design S&C analysis. The conceptual design phase is the earliest portion of a design's life cycle, and during this period the goal is to develop credible configurations which are capable of meeting all of the design requirements [5]. Designs during this phase only exist on paper, and they are produced with a minimum of manpower. Rarely is the focus on detailed analyses, but rather on broad design space searches and trade studies aimed at reducing the dimensions of the design space. Typically, S&C analyses in the conceptual design phase are based upon static analyses of the rigid aircraft, and the secondary lifting surfaces and control effectors are sized using these results [4, 5].

In most resources available on the conceptual design of aircraft, S&C analysis begins with the preliminary sizing of the horizontal and vertical tails [4, 5]. The most fundamental means of achieving a preliminary size is through tail volume coefficients—a nondimensionalization of the tail surface area (S_{HT}) and lever arm length (l_{HT}), scaled by a characteristic length and the wing reference area (S_{ref}). The term 'volume coefficient' stems from the units of the numerator. The horizontal tail volume coefficient is given by

$$C_{\mathrm{HT}} = \frac{l_{\mathrm{HT}} S_{\mathrm{HT}}}{\bar{c} S_{\mathrm{ref}}}, \tag{1.1}$$

where $\bar{c}$ is the wing reference chord. The vertical tail volume coefficient is similarly computed using the wing span, b, as

$$C_{\mathrm{VT}} = \frac{l_{\mathrm{VT}} S_{\mathrm{VT}}}{b S_{\mathrm{ref}}}. \tag{1.2}$$

Figures 1.3 and 1.4 illustrate the reference geometric parameters which appear in these relations. Equations (1.1) and (1.2) are made useful by the large amount of data available for the tail volume coefficients of existing configurations. The final tail sizes will depend upon the details of the configuration, such as the center of gravity (CG) location, and in turn the details of the configuration will depend upon the tail sizes, thus it is necessary to develop a preliminary estimate. To estimate the size of the vertical or horizontal tail, a conceptual designer simply looks up the volume coefficients for similar aircraft that have a demonstrated history of successful flights [4, 5]. From there, with the wing surface already designed, it is a simple exercise to compute the required tail volume (so-named for the units of the numerator in Eqs. (1.1) and (1.2)). The designer is then only required to verify the desired level of static stability and control authority of the aircraft, making further modifications as details of the design become available. This strategy has proven useful over the years as it leverages vast amounts of engineering design experience. Of course, the applicability of volume coefficients

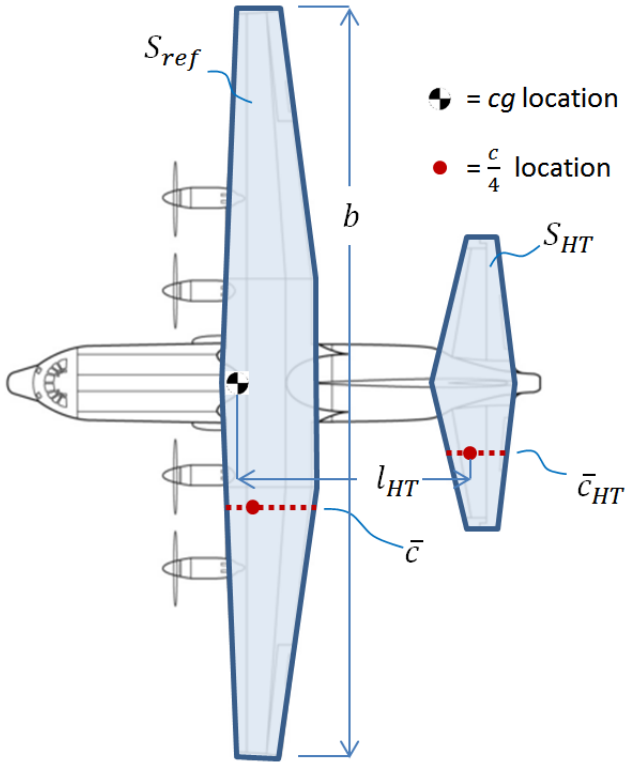

Figure 1.3: Illustration of reference dimensions related to the horizontal tail volume coefficient

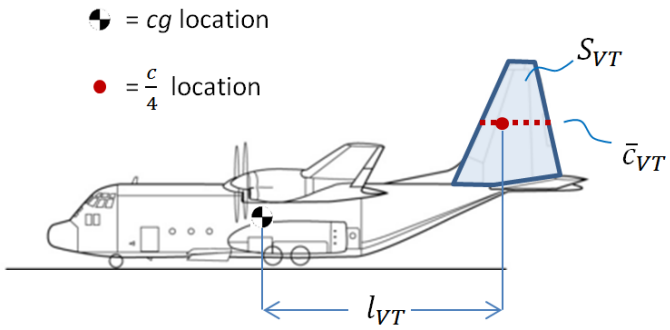

Figure 1.4: Illustration of reference dimensions related to the vertical tail volume coefficient

to complex or nontraditional configurations can be easily questioned. For unconventional configurations, there may be no precedent aircraft from which to reference. Or worse, for

tailless aircraft, the absence of a vertical or horizontal tail precludes the usefulness of tail volume coefficients altogether. Nonetheless, volume coefficients are important to identify as the most preliminary of the conceptual design S&C analyses.

Following the preliminary sizing of the tail surfaces, and after more details of the total aircraft design become available, the traditional conceptual design process moves on to static stability and static control sizing methods. Static sizing methods are those techniques by which the tails and control surfaces are sized using only static stability considerations. An aircraft is said to be statically stable if, upon being disturbed from an equilibrium, it tends toward the equilibrium from which it departed. This is in contrast to dynamic stability, which implies that the time evolution of the aircraft motions are such that, eventually, it will return to the equilibrium from which it was perturbed. It should be noted that static stability is a necessary, but not a sufficient condition for dynamic stability [12]—a fact that helps motivate the dynamic considerations developed later in this thesis. As noted by Nicolai [5], static sizing methods are used in conceptual design because dynamic considerations require information that is not typically available during the conceptual design phase.

Static S&C considerations stem from both engineering experience and federal regulations. Several documents govern the S&C characteristics of aircraft, including the Federal Aviation Regulations (FAR) Part 23 and 25, which are airworthiness standards for small and transport category aircraft, respectively [13, 14]. These documents are surprisingly relaxed in their requirements surrounding S&C, and they frequently use qualitative statements regarding the way the aircraft 'feels'. Both documents, however, dictate that the airplane must be longitudinally, directionally, and laterally statically stable. No explicit constraints on the dynamic performance are provided in either document, other than a general constraint of dynamic stability. More specific constraints on the aircraft dynamic behavior are provided by the MIL-STD-1797, "Flying Qualities of Piloted Aircraft," and civilian designers often

use this military standard for guidance [15].

At the most basic level, static stability is often expressed in terms of inequality constraints on certain aerodynamic stability derivatives. Stick-fixed longitudinal static stability, for example, can be reduced to the constraint

$$C_{m_\alpha} < 0, \tag{1.3}$$

where C_{m_α} is the pitching moment derivative with respect to angle of attack, α. Similarly, static directional stability is given by

$$C_{n_\beta} > 0, \tag{1.4}$$

and static lateral stability by

$$C_{l_\beta} < 0, \tag{1.5}$$

where C_{n_β} and C_{l_β} are the yawing and rolling moment derivatives with respect to sideslip angle, β, respectively. Much like with tail volume coefficients, the most rudimentary static sizing techniques involve empirical databases of these stability derivatives for existing aircraft. Designers simply solve a set of algebraic expressions derived from static equilibrium force and moment balances, sizing the surfaces to match the characteristics of existing aircraft. The details of particular static analyses are reserved for Chapter 3, where they are described in the context of the current S&C module development.

1.2 Multidisciplinary Design Optimization

In 1947, just 44 years after the Wright brothers first flight, the Bell X-1 rocket plane broke the sound barrier and began the era of high speed flight. Shortly thereafter, in 1953, North American Aviation's YF-100 became the first jet powered aircraft to repeat the feat in steady level flight [16]. Ever since, the promise of practical and affordable supersonic aircraft has driven government and industry alike to concentrate extensive research efforts in this area. From Richard Whitcomb's discovery of the area rule and the development of the F-102A Delta Dagger in 1954 [17], to Kelly Johnson's SR-71 Blackbird in 1964 [18] research and development efforts in military aviation were moving at a break-neck pace throughout the middle of the 20th century.

Commercial aviation did not sit idly by during this time, as tremendous advancements were made among transport aircraft, as well. Over the span of just 33 years, the single seat Wright Flyer had evolved into one of the most recognizable aircraft in aviation history—the DC-3. Regarded as the first profitable commercial transport [19], the DC-3 was so capable and affordable, it was adopted as a military aircraft for use in World War II under the moniker C-47. The jet age entered the commercial world just over a decade later, with the de Havilland DH 106 Comet as the world's first commercially produced jet-powered aircraft. Production of the Boeing 7xx series aircraft beginning in the 1950's, and the emergence of Airbus and the A300 in the early 1970's, has since paved the way towards the turbofan powered 'jumbo jets' of the modern age. Advancements in commercial technologies were certainly more subtle visually than military advancements, with the aircraft planforms largely remaining the same. Advances in engine technologies, fiber composites, avionics, and aerodynamic design, however, have made the transport aircraft designs of today technological leaps over those of the previous generation.

The pace of progress in aircraft design and aviation technologies is fascinating. But the 21^{st} century aircraft designer faces new challenges not faced in the past. Rapid technological developments, combined with shifting social and political climates, force designers to consider multidisciplinary aspects of their designs which may have been secondary in the past. Classical aircraft, like many of those previously mentioned, lack the blend of tangible and intangible performance standards demanded of next generation designs. It is no longer sufficient to just fly highest or fastest, or with the most range or endurance. Economics is the omnipresent design driver for commercial aircraft, but growing environmental concerns and airport noise restrictions have forced engine emissions and engine/airframe noise to be major considerations, as well. For a military aircraft, design objectives may include minimization of a sonic boom, reduction of airframe noise, or increased sensor coverage area. The recent ebb of defense funding has also reemphasized acquisition cost as a major driver for military aircraft [20].

Mixed objective design problems can be quite complex, and the aviation industry must adapt accordingly. In addition to modifying design practices to facilitate nontraditional design objectives, designers must also develop a diverse technological understanding in order to leverage interdisciplinary phenomena in their designs. Dramatic performance gains from individual disciplines grow less and less likely as much of the proverbial 'low hanging fruit' has been discovered. Instead, designers must exploit the mutually beneficial interaction of disciplines that have been traditionally separated in the aircraft conceptual design process. Many of these interdisciplinary phenomena are well known, but due to the difficulty of implementation, have yet to be employed outside of the laboratory or controlled experiment settings. These coupled disciplines are often labeled using terms like aeroelastics, the coupling of aerodynamics and structures, or aeroservoelastics, the coupling of aerodynamics, controls, and structures.

Part of the difficulty in exploiting interdisciplinary phenomena is that it must take place during the conceptual design phase. Decisions made during the conceptual design phase hold an irreversible impact on the final configuration [8], and to enjoy the full benefit of interdisciplinary design strategies, they must be implemented during this phase. The traditional aircraft design process typically involves a handful of high-level conceptual designers who develop a few baseline configurations created from their engineering experience. These baseline configurations undergo further analysis and design refinement to arrive at more polished configurations for final selection towards preliminary design. This selection process greatly simplifies the design space, but it is not without risk. The selection of baseline configurations is made very early in the design process when the least amount of information is known about a configuration, and yet these early decisions are the most influential on the final design [8]. By only studying a few configurations in further detail, the performance capabilities of the final design could potentially be very limited. As aircraft under development grow more complex the problem becomes worse, and the need to develop new conceptual design processes must follow suit. Fortunately, modern computers have provided engineers with a powerful tool to address the conceptual design of complex configurations, known as Multidisciplinary Design Optimization (MDO).

Multidisciplinary Design Optimization is the assembly and automation of a series of analyses in a deliberate manner to facilitate the cooperative optimization of a multidisciplinary objective function. More thoroughly, the American Institute of Aeronautics and Astronautics defines MDO as

> "*A methodology for the design of complex engineering systems and subsystems that coherently exploits the synergism of mutually interacting phenomena.*" [8]

One of the principal goals of MDO is the introduction of physics-based analyses earlier

into the design process. At the onset of any design project, engineers have a vast design space in which to operate, and with every decision made that space is narrowed. Early decisions in the conceptual design stage are the most influential (and costly) on the final product, and they are often made with back of the envelope calculations or semi-empirical tools derived from databases of existing aircraft. Providing conceptual designers with the capability to explore the broader design space with a physics-based analysis and optimization tool is of tremendous interest to the modern aerospace industry. The ability to leverage synergistic design phenomena that may have been overlooked by the traditional design process has great potential to transform the industry.

To construct an MDO, analysis tools are woven together with an optimizer to rapidly generate and analyze hundreds or thousands of feasible designs and focus the design space towards an optimum region. In the case of aircraft design, these analyses represent different disciplinary focuses such as airframe structures, vehicle performance, aerodynamics, propulsions, stability and control, and others. Design disciplines often have competing objectives, and the strategic implementation of these analyses inside a robust optimization process seeks to overcome this limitation. Larger payloads, increased range, decreased weight, lower emissions, and lower costs are just a few of the more noteworthy competing objectives. For example, while aerodynamic analyses may indicate that a highly swept, extremely thin wing offers the best performance for a given aircraft, the airframe structural analyses may push for a thick airfoil section with only modest sweep.

The effectiveness of an MDO framework is greatly influenced by its logic structure. Details of the assembly of a framework are well described by a process flow chart such as an N^2 diagram, an example of which is shown in Figure 1.5. The term N^2 arises from the $N \times N$ matrix created when the diagram is fully populated. These diagrams represent both the order of execution of the disciplinary analyses, as well as the information flow between

modules. The colored boxes along the diagonal in Figure 1.5 are the analyses in the order in which they are to be executed, from top left to bottom right. Information to the right of the diagonal is feedforward information provided by the analysis in that row, and it is passed down to the analysis in that column. Information to the left of the diagonal represents feedback information, and is passed up the column to the analysis above it. The nonexistence of prerequisite data prevents the simultaneous execution of all analyses at the same time, so the feedback and feedforward data transfer connections in the N^2 framework are a necessary result of the sequential nature of an aircraft analysis. Feedforward relationships are ideal in that downstream analyses receive the most up to date data available from precedent disciplines without any additional computational overhead. Feedback relationships, on the other hand, represent an undesirable inner-loop that requires iteration and convergence before further progress down the N^2 diagonal can be made. Minimization of the execution time of a single run through the entire N^2 diagram is very important, since hundreds or thousands of runs may be necessary in a design optimization. Therefore, framework designers must carefully arrange the order of execution of disciplinary analyses to reduce feedback relationships and minimize framework run times.

Under a collaborative effort involving Virginia Tech (VT), Wright State University, and the Air Force Research Laboratory Air Vehicles Directorate at Wright Patterson Air Force Base, an MDO framework has been constructed to facilitate conceptual design studies of advanced high-speed aircraft. The framework is called the VT High-Speed Aircraft MDO, and it builds upon earlier MDO work at Virginia Tech which focused on transport aircraft design [21, 22]. The VT High-Speed Aircraft MDO is composed of a series of disciplinary analyses that include both in-house developed and third-party codes. Each researcher involved in the framework's development is responsible for one or more disciplines and must establish the necessary input and output interfaces to the other disciplines. From the on-

Propulsion	Flow behind inlet shocks	Flow-through panels' data	Temp., Press., Alt., M, Dimen.	Engine weight	Engine weight	Engine data in flight envelope	Thrust available for vectoring		Exhaust speed and temp.		Thrust, Altitude, Mach #, BPR, etc.
Cowl and Inlet	**Geometry**	Configuration, Mach #, Alt.	Cowl, Aft deck	Configuration	Tank and engine	Wing area	Control effector data	Configuration	Noise shielding factor	Configuration, Fuel volume	Configuration
		Aerodynamics	Skin temp., Loading	Aerodynamic Loading		Aero. data in flight envelope	Stability derivatives				
			EEWS	EEWS weight	Structural weight - EEWS						
				Structures	Structural weight - other					Structural failure	
					Weights	Aircraft weight	Inertial properties				Take-off gross weight
						in flight envel.				Fuel volume, Req. maneuvers	Feasibility
						Mission Performance					
							Stability and Control			Added removed fuel volume	Feasibility
								RADAR Cross Section		RCS metric	
									Noise	Noise output	
										Constraints	Feasibility
Thrust, Altitude, Mach #, BPR, etc.	Configuration										**Optimization**

Figure 1.5: An example N^2 diagram indicating the structure of the current VT High-Speed Aircraft MDO framework.

set, the VT High-Speed Aircraft MDO framework was designed to support varying levels of fidelity among the disciplines by maintaining a structured input/output format between analyses. For example, regardless of the chosen fidelity level of the aerodynamics package used to fulfill the box on the N^2 diagram, the same set of data must be made available to the structures discipline. This not only facilitates the inevitable difference in development rates of disciplinary analyses, but also enables a 'dialable fidelity' approach to design optimization. Users of the VT High-Speed Aircraft MDO framework have the option to trade modeling fidelity for computational expense, allowing for both quick design space explorations or intensive configuration studies.

It is not the subject of this thesis to address the intricacies of the VT High-Speed Aircraft MDO framework assembly and execution. The full details of the N^2 diagram and its assembly can be found in the references by Allison, et al. [23, 24]. Also included in the references are framework validation studies and the results of an intensive design optimization study. Many of the analysis modules used in the VT High-Speed Aircraft MDO were developed in-house, including the geometry module [25], the engine exhaust wash surface module [26], and the S&C module which is the principle subject of this thesis. Third party software packages are also utilized in the framework. Some of the software used includes the Numerical Propulsion Simulation System (NPSS) within the propulsion module, the Flight Optimization System (FLOPS) within the mission performance and noise modules, NASTRAN within the structural module, and ZONAIR within the aerodynamic module. Details of the integration of the S&C module into the VT High-Speed Aircraft MDO framework, along with an overview of upstream analyses that directly interface with the S&C module, will be discussed in Chapter 5.

1.3 The Necessity of Dynamic Stability and Control Considerations in Conceptual Design

As already discussed, conceptual design level aircraft S&C analysis typically consists of little more than volume coefficients and static analyses [4, 5]. This approach has proven successful in the design of the conventional tube-and-wing transport aircraft with reasonably stiff structures and lightly coupled wing/tail/body aerodynamics, or military fighters with many precedent aircraft of similar configuration. It isn't until the preliminary design stage is reached that performance analyses involving aircraft dynamics and closed-loop system performance is accomplished. While static analyses are necessary to properly characterize the behavior of an aircraft, they are far from sufficient. Future generations of aircraft are likely to exploit relaxed static stability (RSS), or even instability, to reduce the trimmed drag of the aircraft[5], and closed-loop system analysis at the conceptual design stage will be demanded. Designers of RSS aircraft must consider dynamic behavior and flying qualities from the earliest stages of design. New control devices and unconventional configurations will complicate the S&C analysis even further. For these reasons and more, which are elaborated on in the following sections, the dynamics of next generation aircraft cannot be ignored during the conceptual design stage.

1.3.1 Nontraditional Means of Control

The S&C challenges facing next generation aircraft vary depending on the configuration under study, but certain commonalities afflict all aircraft. Potential performance gains from new, nontraditional control effectors will likely merit their use on both military and commercial configurations. Examples of nontraditional effectors include spoiler-slot-deflectors

(SSDs), clamshell elevons, thrust vectoring, all-moving wingtips, and many others (see Figure 1.6). For high-performance military aircraft, the benefits and increased performance

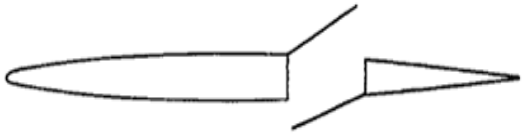

(a) Example airfoil cross section with spoiler slot deflector

(b) B2 Stealth Bomber with clamshell elevon deployed in foreground

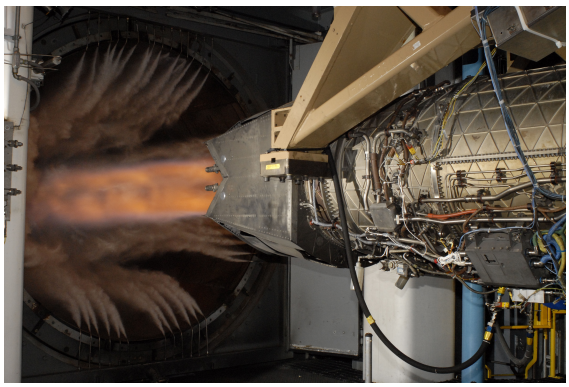

(c) Static test fire of the F119 engine, which is capable of thrust vectoring

Figure 1.6: Example nontraditional control effectors

potential of these devices is more clear. A commercial application, on the other hand, may be the active suppression of wing flutter on transonic aircraft with very thin wings—a design

strategy which reduces transonic drag and decreases the takeoff gross weight (TOGW).

Prediction of the behavior of nontraditional control effectors is complicated by their nonlinear aerodynamic behavior, as well as their aerodynamic influence about multiple axes [27, 28, 29]. The popular decoupling of longitudinal and lateral-directional equations of motion is made difficult by the coupled behavior of these control effectors. Configurations which make use of nontraditional control effectors will likely be unable to generate pure control moments (pure, in this context, referring to generation of a moment about one axis without significant adverse moment generation about another) [27]. It will be important, therefore, for the S&C module in an MDO framework to be capable of analyzing the coupled equations of motion.

1.3.2 Dynamic Constraints: Flying Qualities Requirements

It is not sufficient for designers to simply create an aircraft which is stable or controllable. Any aircraft which is to be piloted or occupied by humans must exhibit certain dynamic characteristics in order to 'feel good'. These dynamic constraints are known as the aircraft flying qualities, or handling qualities. Aircraft flying qualities are the subjective assessment of how easily the vehicle can perform a task. Cooper and Harper, best known for their pilot rating scale, define handling qualities as

> "*those qualities or characteristics of an aircraft that govern the ease and precision with which a pilot is able to perform the tasks required in support of an aircraft role.*" [30]

The subjective nature of flying qualities makes it difficult to define what qualifies as satisfactory, since two pilots in the same aircraft performing the same maneuver can perceive

very different workloads. For more than a century, many efforts have focused on quantifying pilot perception and developing physics-based criterion for 'satisfactory' flying qualities. An excellent review of these efforts is given by Mitchell, et al. [31].

Early flying qualities guidelines based on the work of Gilruth in 1943 were simple requirements on the number of cycles to damp and the stability of a perturbed control surface from trim [32]. For example, the lateral-directional requirement states that the control-free lateral oscillation should damp to one-half amplitude within two cycles and that the ailerons and rudder should return to their trimmed position when perturbed. While these requirements represented a significant leap forward in the definition of aircraft flying qualities, they suffer from many limitations. First, by only requiring constraints on the rate of damping, a pilot could theoretically be subjected to very large amplitude oscillations that decay quickly. Second, the trimmed perturbation requirements placed on the control effectors is practical for reversible controls, but lacks application for modern, hydraulically actuated, irreversible controls and fly-by-wire systems.

The limitations of Gilruth's work was quickly recognized, and many others continued to refine flying qualities definitions. In 1968, the foundation for modern flying qualities requirements was published by the Air Force as MIL-F-8785A, "Military Specification, Flying Qualities of Piloted Airplanes" [33]. This document described different levels of flying qualities according to aircraft type, maneuver type, and the modal response. For the first time, aircraft designers had a physics-based, mathematical description of how the aircraft dynamics should behave. The flying qualities of the aircraft could now be approximated before any fabrication or flight testing, allowing for flying qualities considerations in the preliminary design stage. Future revisions to the document [34, 35] added several new concepts to handle more complicated dynamics, control systems, and pilot-in-the-loop behavior. In 1990 the flying qualities requirements were revised into the MIL-STD-1797A [36], which

was later relaxed to flying qualities guidelines in the MIL-HDBK-1797 in 1997—allowing manufacturers to negotiate specific flying qualities criteria with their Department of Defense customers [37]. Finally, in 2006 the MIL-STD-1797B was introduced to supersede all previous documents, and it restated the contents as flying qualities requirements [15]. The modal-based foundation of the MIL-F-8785A still lies at the core of every revision of the MIL-STD-1797 guidelines. In fact the modal constraints used here in Chapter 4 are available in every edition. For this reason, and the fact that some revisions exist outside of the public domain, the flying qualities requirements will be uniformly referred to as the MIL-STD-1797.

Pilot flying qualities ratings of aircraft are influenced by many things, both measurable and immeasurable. Among the major contributors to the pilot's rating are the airframe dynamics, the stick forces and artificial feel system, the location of the gauges, the weather, and many other human factors which are difficult to quantify. At the conceptual design stage, the airframe dynamics are the most practical of the influences to account for, and the majority of the guidelines provided by the MIL-STD-1797 deal with constraints on airframe dynamics. Stability Augmentation Systems (SAS) are frequently used to modify the bare airframe dynamics in order to satisfy the flying qualities requirements. The capabilities of an SAS are not without limits, however, and it is still left to conceptual designers to produce configurations which exhibit satisfactory flying qualities. A dynamic performance analysis tool which was capable of developing a preliminary SAS design would allow designers to take flying qualities requirements into consideration during conceptual design. The development of such a tool is addressed in this work.

1.4 Problem Statement: Stability and Control in Multidisciplinary Design Optimization

Benefits from both Multidisciplinary Design Optimization and more thorough stability and control analyses are abundant in the literature [38, 39, 40, 41, 42]. However, in very few instances has the power of the two methods been combined. The fundamental question at hand is, 'How can a stability and control analysis, with both static and dynamic performance considerations, be implemented in the conceptual Multidisciplinary Design Optimization of an aircraft?'

The inclusion of dynamic performance metrics is key—not only because aircraft MDO efforts have already addressed the static stability problem [38, 43], but because the performance of next generation aircraft will likely have a more intimate marriage to dynamic S&C characteristics than existing aircraft. To fully exploit the interdisciplinary phenomena that will push aircraft performance beyond today's limits, the study of dynamic performance must begin at the conceptual design stage.

A properly formulated S&C analysis within the VT High-Speed Aircraft MDO framework must be general in nature, and fully-automated, since the utility of an MDO would be nullified by requiring a man-in-the-loop. In addition, the analysis must be able to handle unstable or marginally stable configurations, which requires the analysis to include a preliminary feedback control system design. The S&C module on the N^2 diagram would serve as a constraint within the design optimization, one whose purpose is to assess whether or not a given aircraft configuration is capable of overcoming the static and dynamic challenges previously addressed. The optimizer can make use of this feasibility information to minimize the size and installation penalty of control surfaces subject to constraints on the static and dynamic capabilities of the aircraft.

1.5 Purpose and Scope of This Study

The purpose of this study is the development and construction of an S&C module for use within an VT High-Speed Aircraft MDO framework. The analysis includes both static and dynamic performance metrics, and is conducted at a fidelity level sufficient for conceptual design. The scope of this study does not include direct investigations into higher-order design objectives such as aeroelastic tailoring, span-load shaping, active flutter suppression, or gust load alleviation. However, the development of the S&C analysis will lay the groundwork for exploiting these synergistic aircraft phenomena within an MDO framework. It will be critical to leverage these synergistic phenomena in the design of next generation aircraft in order to further reduce the weight and drag, and increase efficiencies.

In Chapter 2, a review of relevant efforts to include Stability & Control in MDO and/or at automating the S&C analysis process is conducted, and the benefits and shortcomings of the methods are identified. Following that, Chapter 3 provides the technical background of the development of the new S&C module and the Variance Constrained Flying Qualities approach—a novel approach to flight dynamics assessment in MDO. The details of the Variance Constrained Flying Qualities approach are given in Chapter 4. Chapter 5 focuses on the computational implementation of the code, detailing its data relationships within the N^2 diagram. Immediately following, in Chapter 6, is a demonstration of the S&C module through a design study conducted on a traditional commercial transport aircraft. The empennage assembly of the aircraft is redesigned to relax the inherent stability of the configuration, decrease the trimmed drag, and decrease the TOGW while still maintaining satisfactory static and dynamic performance. Chapter 7 reviews the impact of the developed capability, as well as offers guidance for future studies using the developed method and code.

Chapter 2

Stability and Control in MDO

In this chapter, some of the most relevant previous studies on conceptual design stability and control in Multidisciplinary Design Optimization are reviewed. Each study is grouped into one of three categories. The first category, the Integrated Control Design studies, seek to simultaneously design the control system and some portion of the aircraft configuration. Occasionally labeled as Control Configured Vehicle (CCV) studies, these studies were among the earliest attempts to leverage the benefits of an active control system during the conceptual design phase. Many of these efforts predated large-scale computing, and as such, CCV studies do not typically appear under the moniker Multidisciplinary Design Optimization. CCV studies usually rely upon very simple models in all disciplines except controls, utilizing analytic models or only very simple computations in the other disciplines.

The second category is those studies which directly include S&C within an MDO framework. The distinction between the CCV and the MDO studies is equal parts semantics, chronology, and fidelity level. CCV studies include multiple disciplines, but they are predominately 'controls-centric', while MDO studies traditionally attempt to model all disciplines at similar levels of fidelity. Chronology is also a factor in the sense that MDO is an

acronym which has grown in popularity in recent years, and similar studies conducted just a few years earlier are likely to identify with the first category. In most cases, the particular classification of the research is identified by the author, and this categorization is honored.

The third category is different in that it includes existing conceptual aircraft design software available in academia or industry. Some of these products are not available to the public or exist under proprietary/controlled-release governance—nevertheless, several of these software tools are in wide use today and merit at least some further discussion.

2.1 Integrated Control Design

This section is comprised of studies which either identify themselves as CCV studies, or which are easily identified as a controls-centric integrated design effort. Documents reviewed range in publication date from 1972 to more recent years—an indicator of how long conceptual design S&C has been a topic of concerted interest.

A 1972 report by Edmund Rynaski and Norman Weingarten, of the Cornell Aeronautical Laboratory, entitled, "Flight Control Principles for Control Configured Vehicles," is one of the earliest published attempts to utilize a flight control system during a conceptual design optimization to fulfill certain S&C requirements [44]. Their stated objective was to investigate the 'compatibility' of three competing S&C objectives in an attempt to minimize the drag of an RSS version of a T-33 aircraft. The S&C objectives were maneuver load control, relaxed static stability, and flying qualities requirements. This study is surprisingly reminiscent of the objectives of the research contained in this thesis. Design optimization was accomplished through a reduction of the tail surface area and the tail length, and stability augmentation systems were designed using optimal control theory to minimize an objective function composed of the aircraft drag, the wing root bending moment, the control energy,

and the error between dynamical response of the RSS design and an idealized model. This latter objective is used as a flying qualities metric, whereby the aircraft being synthesized is compared to a reference configuration which exhibits satisfactory flying qualities. The authors applied their CCV strategy to the decoupled equations of motion and utilized simple algebraic relations and empirical data to model the structural and aerodynamic disciplines. They then examined the influence of each S&C objective on the final achievable design. Results of the study indicated that the T-33 with an SAS would be capable of flying with a 15% reduction in static margin and a structural weight savings of approximately 500 pounds—a 5% savings from the actual T-33 empty weight. It is interesting to note that the authors identified the acceptance of fly-by-wire flight control systems, a standard technology on almost every aircraft produced today, as a necessary preliminary to exploiting the benefits of S&C. Furthermore, they conclude that application of CCV concepts on existing configurations will yield limited results, and instead they should be applied during the earliest stages of design.

Another CCV study, which was conducted at Virginia Tech by Anderson and Mason [7], began to blur the lines between CCV and MDO by identifying itself as both. The study remains in the present integrated control design section, however, since the modeling of disciplines other than S&C and aerodynamics remained rudimentary. The authors developed a risk-based metric of the control system's complexity, and the design optimization objective was to minimize a scalar combination of the drag coefficient and the risk metric of the form

$$J = C_D + \mu R, \tag{2.1}$$

where C_D is the drag coefficient, R is the scalar risk metric, and μ is a user-controlled weighting coefficient. The risk metric was assigned using fuzzy logic and a set of assumed control system architectures. Configurations were assigned a control architecture, and therefore a

risk metric, based upon computed aerodynamic parameters. While successful in demonstrating the reduction in trimmed drag due to a relaxation of stability, no actual control laws were designed in the process. Rather, the method serves as a *heuristic* for predicting regions of the design space which may pose significant S&C challenges. The *a priori* control architecture assumptions, as well as the somewhat ambiguous scalar value of risk and its associated weighting coefficient, make implementation of this method into a full MDO problematic.

In addition to the self-identified CCV studies previously discussed, there are several studies targeted more towards the development of an automated S&C analysis that also have great relevance. Broadly, these studies focus on the technical development of routines through which a control system can be designed, and a dynamic objective can be simultaneously satisfied. Among the earliest of these efforts is that by Morris and Kroo [41] on the introduction of dynamic performance constraints into an aircraft design optimization. Their work makes use of a quadratic dynamic cost function, J_d, of the form

$$J_d = \int_0^\infty \left(\epsilon^T Q \epsilon + u^T R u\right) dt, \tag{2.2}$$

where Q and R are user-selected weighting matrices and ϵ and u represent the state error and the control input, respectively. The dynamic performance cost function is minimized using methods from optimal control theory to drive the closed-loop response of the aircraft being synthesized towards that of a 'model' aircraft—that is, an aircraft whose dynamic response is considered ideal. A similar approach was discussed previously in the work of Rynaski and Weingarten [44]. Morris and Kroo also include a nondynamic performance cost function, J_{nd}, to handle mission performance parameters such as the aircraft weight, drag, or fuel burn, and a constraint cost function, J_{pen}, used to penalize any additional explicit or

implicit constraints. The result is the total scalar cost function of the form

$$J = K_d J_d + J_{\text{nd}} + J_{\text{pen}}, \tag{2.3}$$

where K_d is a user-selected weighting factor to scale the relative importance of the dynamic and nondynamic constraints. This method was demonstrated to be effective in leveraging the benefits of simultaneous control and aircraft design, particularly when it comes to weight reduction or the suppression of flutter. A sizable limitation of the method, however, is the need to identify a reference model which achieves the desired dynamic characteristics. Additionally, the scalar result of the total cost function is not directly indicative of dynamic performance. Once the design optimization is complete, a post simulation of the results is required to identify configurations with acceptable MIL-STD-1797 flying qualities. Integration into a full scale MDO was not a stated objective of their work, but the manual post-processing and necessary prerequisite reference aircraft make modification towards automation for MDO difficult.

Of all of the works reviewed, one of the most influential on this thesis was that by Kaminer, Howard, and Buttrill [45]. These authors took a different approach to the inclusion of dynamic performance than any previous effort in the literature. Their approach is to establish feasibility criteria for the existence of a feedback control law which satisfies a set of dynamic constraints—which, in this case, are the flying qualities requirements. Kaminer et al. developed a set of linear matrix inequality (LMI) constraints on the closed-loop pole locations and the control effector dynamics of the aircraft under design. Linear matrix inequalities are convex constraints for which solutions are easily found using modern numerical methods [46, 47]. An overview of LMI's is given here in Chapter 3, or the interested reader can find more thorough details in Refs. [48] and [46]. The feasibility problem perspective is useful in that conceptual designers are unlikely to be interested in finding the best con-

trol law, but rather are satisfied with the knowledge that a sufficient control law exists. It is this same perspective which is retained by the methods developed in this thesis. While many of the techniques and strategies were borrowed for further development in this work, a direct implementation of the results of this earlier study was not used. One significant limitation of that method is the necessity of decoupled equations of motion, and the inability to separately enforce constraints on the different classical aircraft modes. For example, pole placement constraints placed upon the heavily damped and undesirable short-period mode are uniformly enforced upon the less critical phugoid mode. This 'total pole placement' limitation overburdens the control system, and causes many configurations which would be otherwise satisfactory to be disregarded. The problem grows rapidly worse with the inclusion of additional states, such as actuator dynamics or the lateral-directional modes of motion.

2.2 Dynamic Stability and Control in MDO

Though MDO is frequently championed as a means to address the shortcomings of the typical design process, rarely does an aircraft MDO effort include an S&C analysis. Of those that do address S&C, they typically consist of static sizing scenarios like minimum static margin, takeoff nose-up moment generation, engine-out trim, and cross-wind landing constraints. Dynamic analysis is particularly challenging at the conceptual design stage due to the significant knowledge of aerodynamic and inertial properties that is required. MDO helps alleviate some of these difficulties since much of the required data is generated by analyses upstream in the N^2 diagram. However, MDO also introduces new challenges associated with automation and computational cost. Any analysis integrated into an MDO framework must have a low computational cost and perform autonomously without human interaction or post-processing requirements. For this reason, most precedent full MDO efforts

do not include dynamic performance.

Before this research began, Virginia Tech conducted a supersonic aircraft MDO effort studying the High Speed Civil Transport (HSCT). This tailed transport aircraft was to be designed for a Mach 2.4 cruise with the capability to ferry 251 passengers up to 5500 nautical miles [43]. HSCT studies focused on the development of aerodynamic models [49], response surface generation and optimization [40], and aircraft performance with trim and control considerations [43]. Of particular interest is the work by MacMillan [43] in which several static sizing methods were employed. The vertical tail was sized using both engine-out and crosswind landing scenarios, while the horizontal tail was sized according to field performance constraints. While the study successfully demonstrated the impact of static trim and stability constraints in MDO, it failed to address the dynamics of the aircraft. Static stability is not sufficient to describe the response of the aircraft to gusts or disturbances, and a statically stable airplane may still exhibit an undesirable dynamic response.

Another relevant MDO effort that took place at Virginia Tech is the Strut Braced Wing (SBW) transonic transport aircraft. The aircraft was designed to perform a distinctly different mission than the HSCT study; the cruise Mach number was 0.85 with a range of 7380 nautical miles and a passenger capacity of 305 in mixed-class seating [39]. Conceptually, the aircraft seeks to capitalize on the load alleviation provided by a strut to increase the wing aspect ratio, decrease the wing thickness, and decrease drag, thereby reducing the aircraft takeoff gross weight or fuel burn. In order to further reduce the wing thickness, tip mounted engines were examined as a means of inertial relief. As with any aircraft with wing mounted engines, the ability to trim the aircraft should one engine fail is a critical lateral-directional tail sizing scenario. The VT SBW group examined the impact of static stability constraints on the lateral-directional behavior of the aircraft with wingtip mounted engines and one engine out. Saturation constraints were enforced to ensure that the ailerons and the rudder

maintained a sufficient maneuver margin while still successfully trimming the aircraft. The static results proved to be quite influential on the design optimization and helped to integrate physically realistic S&C constraints into the VT SBW MDO. No longitudinal static stability analysis was conducted in this study, and as with the HSCT, no dynamic metrics or flying qualities assessment was performed.

Aside from Virginia Tech, a great deal of work in MDO has also come from the University of Toronto in recent years. In particular, one study by Perez, Liu, and Behdinan [50], focuses on the implementation of a flight dynamics and control discipline within their MDO framework. The goals of this study share great commonality with those of this thesis in that they seek to leverage the benefits of stability augmentation and feedback control from within a conceptual design MDO. They also use an N^2 diagram approach to the disciplinary structure, and the dynamic performance assessments deal largely with aircraft flying qualities. A thorough suite of static constraints also accompany their dynamic constraints. However, the authors do make certain assumptions regarding the presence of traditional response modes and the means of control system design which separate them from the methods of Chapter 3 and 4 here. For one, the SAS design is assumed to be decoupled between the longitudinal and the lateral-directional states. This assumption is particularly problematic if the configuration exhibits coupled dynamics or utilizes nontraditional control effectors with multi-axis aerodynamic influences. Also, the control system design is conducted as a local optimization within a collaborative optimization setup. Collaborative optimization is a bilevel optimization strategy by which each discipline is decoupled from the rest, enabling many local optimization processes which are then subject to global constraint parameters [51]. While the local optimization of the control system is not problematic, the absence of a particular control design scheme is undesirable. The authors used minimum control energy as their local optimization objective function, but the presence of the global 'coupling' constraints

prevents the implementation of linear quadratic or other optimal control strategies.

Outside of the academic environment, additional full-aircraft MDO efforts are underway. Researchers at NASA Langley are actively developing MDO software for the design of supersonic aircraft [38]. The study focuses on the development of tools and methods for the assembly and utilization of a multidisciplinary analysis and optimization framework to address the technical challenges associated with the design of supersonic aircraft. A special emphasis has been placed on environmental considerations including sonic boom and noise constraints. The approach is similar to that adopted in the development of the collaborative MDO framework discussed in Chapter 1, in that a multi-fidelity N^2 diagram approach to framework development is implemented within Phoenix Integration's ModelCenter^{TM} software [23]. Stability and control analyses are implemented into the NASA framework using the Matlab Stability and Control Toolbox (MaSCoT), an in-house developed code which can perform trim and static stability analyses [42]. Enhancements to MaSCoT were later made to allow for dynamic stability analyses, but private communication with the authors suggested that the integration of MaSCoT into the MDO was unsatisfactory and was later removed [52]. The authors cited cumbersome implementation and usage as well as a lack of validation as the primary causes for removal from their tool suite. As of the date of correspondence, no replacement dynamic S&C analysis had been developed.

2.3 Aircraft Conceptual Design Software

In the aircraft conceptual design community, there are a number of privately developed and maintained suites of software at each of the major aerospace companies. The details of these programs are often considered trade secrets, and few publications or technical details ever emerge about the software itself. As such, the following review of conceptual design software

is based on those programs which are either documented in the public domain, or through the government communication channels available to this research project.

The first codes discussed are lower-fidelity, rapid implementation MDO codes in popular use today. These two codes are likely the most popular conceptual design software suites available: the Flight Optimization System (FLOPS) [53], produced by Arnie McCullers at NASA Langley Research Center, and AirCraft Synthesis (ACS-ACSYNT) [54], produced by AVID LLC. These codes are semi-empirical in nature, relying heavily upon databases of existing aircraft characteristics. The user-supplied geometry is decomposed into high-level aircraft design parameters such as sweep, taper ratio, aspect ratio, etc., which are inputs to semi-empirical response surface models of many of the major technical disciplines. Both programs offer a wide range of disciplinary analyses including mission performance, aircraft weight, propulsion, aerodynamics, and more. The ACS-ACSYNT program also contains a GUI for the generation of parameterized aircraft geometries, whereas FLOPS utilizes a text file based input. Results from these programs are surprisingly detailed, and include predictions of individual component weights, integrated mission profile analysis detailing the thrust states and fuel levels, and even technical details of the landing gear. Despite all of this, neither of these semi-empirical MDO codes includes any kind of S&C analysis. Admittedly, gathering and reducing S&C data into a useful database would be a difficult task due to the many different control effectors and effector arrangements present on existing aircraft.

Another approach to conceptual design software comes from academia, and the researchers at the University of Texas at Arlington. The Aeromech sofware, developed by Chudoba and others [55], is *"a vehicle configuration independent aircraft conceptual design stability and control tool, developed to help the conceptual designer to address stability and control for conventional to unconventional design proposals."*[56] AeroMech is primarily an

aerodynamics and S&C tool, and does not include any other aircraft disciplines in the analysis. Models are constructed by the user, which include the geometric and mass properties of the aircraft. Aerodynamic databases are then generated using a variety of aerodynamics tools with varying levels of fidelity. Linearized models of the aircraft equations of motion are then built using this data, and the user is supplied with several control system design capabilities. Control laws are based on linear-quadratic optimal control methods with output feedback, allowing the user to modify the aircraft dynamics and investigate the closed-loop flying qualities. While the program offers designers a powerful resource for conceptual design by consolidating and simplifying tools, it relies on a user-in-the-loop for the control system design, which makes it impractical for MDO implementation. In the most recent publication found on Aeromech, mention was made of its inclusion into a larger conceptual design software suite [56], but searches in the literature for the design suite did not produce any results.

Advancements in aircraft conceptual design S&C software are not constrained to the borders of the United States. A union of European aerospace organizations working under a project called SimSAC, is collaboratively developing the CEASIOM software package [57]. SimSAC stands for 'Simulating Aircraft Stability and Control Characteristics,' and is focused on S&C tools for aircraft conceptual design studies. As a component of the SimSAC project, the 'Computerized Environment for Aircraft Synthesis and Integrated Optimization Methods,' or CEASIOM, seeks to establish a multidisciplinary analysis tool with multiple levels of fidelity and an emphasis on early adoption of S&C tools. Implemented in Matlab and well-documented, the CEASIOM package is available for download and use on any computer with a Matlab license. While CEASIOM is not an optimization tool, it is a multidisciplinary analysis tool that contains a fully-developed S&C module called the 'Simulation and Dynamic Stability Analyzer,' or SDSA. The module features a well-polished graphical

user interface (GUI) that automatically inherits aerodynamic data from the aerodynamics module, and presents the user with the ability to analyze flying qualities, compute performance metrics, and simulate the six-degree-of-freedom nonlinear response of the aircraft. Flight control system design is also possible by making use of the built in Linear Quadratic Regulator (LQR) features. Despite the advanced development of the SDSA module and the CEASIOM software package, it was still found to be unsuitable for MDO implementation. The graphical user interface does not facilitate automated design optimization, and the post-processing required for flying qualities and S&C assessment is unsuitable for MDO.

Another overseas software product with a focus on aircraft conceptual design comes from PACE in Berlin, Germany. Their software, Pacelab APD, is a modeling suite which 'supports the modeling, analysis, and optimization of new and derivative aircraft in the conceptual and preliminary design phases [58].' The program itself relies on databases and a baseline suite of early conceptual design tools to provide a 'rapid prototyping' software environment. Pacelab APD contains a S&C analysis module based on the semi-empirical techniques of Torenbeek [59] which is capable of estimating static stability and controllability, as well as predicting the center of gravity location. Baseline analysis modules can be supplemented, or replaced, by user defined analysis tools, making Pacelab APD an extensible architecture. However, there are no inherent tools for dynamic stability or the prediction of flying qualities within Pacelab APD, and the heavy reliance on GUI's limits its applicability for large scale MDO.

2.4 Literature Review Conclusions

Countless other efforts to include S&C in some level of design exist in the literature. All of these approaches, including those just discussed, possess some limitation which prevents their use in the MDO framework. Chapters 3, 4, and 5 detail the theoretical background, development, and implementation of a new S&C tool which seeks to overcome these limitations. The S&C tool was developed to be as general as possible in that as few assumptions as tractable were made in its development. Where the use of an assumption could not be avoided, it is clearly noted to avoid misguided use of the tool.

Chapter 3

Stability and Control Module Development

This chapter details the technical preliminaries to the development of the new S&C module and the Variance Constrained Flying Qualities (VCFQ) approach. It begins with a brief derivation of the equations of motion and their linearization, and all of the assumptions used are meticulously detailed. The derivations are intended to be complete, but the reader is expected to have some previous exposure to rigid-body dynamics and kinematics. Following the derivation of the equations of motion, a discussion of static stability and the associated design constraints is given in Section 3.3. Section 3.4 then offers a technical background on several subjects that are preliminary to the development of the dynamic S&C analysis, including details of the flying qualities requirements and an introduction to linear matrix inequalities. The final section offers discussion of the limitations of the flying qualities requirements as given, and includes a motivational example for an alternative metric.

3.1 Equations of Motion

Foundational to any analysis of an aircraft is the construction of a model. In this case, the model referred to is the set of ordinary differential equations, derived from first principles, which govern the rigid body motion of the aircraft. The derivation of the rigid body equations of motion can be found in almost any text on aircraft dynamics, including those by Pamadi [60], Etkin [61], and Duke, et. al, [62] from which the following derivations are developed. Occasionally, assumptions are required during the derivation to make solutions more tractable or to eliminate unnecessary terms. These simplifications are justified by either physics or experience, and the consequences of each is addressed in turn. At the end of the section, Table 3.1 restates all of the assumptions made as well as a reference to the first equation to leverage them.

To begin, we must state our first assumption: the dynamics of the aircraft are sufficiently well described by the rigid-body equations of motion. This statement inherently assumes that the dynamic aeroelastic response of the aircraft does not significantly influence the rigid-body motions. Since the goal of this study is to assess the airframe static and dynamic stability, and not to perform flutter or other dynamic aeroelastic analyses, this assumption was adopted. It should be noted, however, that this assumption does not preclude the use of aerodynamic stability derivatives which account for the static aeroelastic deformation of the structure—a topic which will be discussed further in Chapter 5. The second assumption is based on the formative work of George Hartley Bryan [63], a professor and the author of *Stability in Aviation*. Credited with being the first to derive the six-degree-of-freedom rigid-body equations of motion of an aircraft, Bryan made the assumption that the aerodynamic forces and moments depend only on the instantaneous values of the motion variables. This quasi-static assumption is widely used in almost every text on aircraft dynamics, and provided the motions of interest remain small, has been demonstrated to be a valid assumption [64].

3.1.1 Coordinate Systems

Before the equations of motion can be derived from first principles, a few comments on the coordinate systems commonly used in flight dynamics are necessary. There are infinitely many coordinate systems that could be used, and only several of the ones most important to flight dynamics will be discussed here. Often, one coordinate system will offer a mathematical advantage over another, which can then be exploited to simplify the resulting equations of motion. Coordinate systems are labeled using the notation F_*, where the subscript $*$ is an appropriate identifier. The individual axes of the system, F_*, are similarly labeled as x_*, y_*, and z_*.

Inertial Axes, $\mathbf{F_I}$

The most important of the axis systems to be defined is the inertial axes, F_I. An inertial frame is a set of three mutually orthogonal unit vectors with their origin at a point which remains fixed with respect to inertial space. The importance of the inertial frame stems from the fact that Newton's laws of motion are valid only in an inertial frame. In general, there is no truly inertial frame, since any reference point known to man is technically moving. The flight dynamics expert is left to choose a reference point which is 'inertial enough'—that is, the error associated with the choice of inertial frames is inconsequential. Obviously, the reference frames to describe the motions of a kite, a satellite, and an interplanetary spacecraft would be different. It is common in flight dynamics to assume the inertial frame to be a nonrotating set of axes fixed at the center of the Earth with z_I pointing north as shown in Figure 3.1.

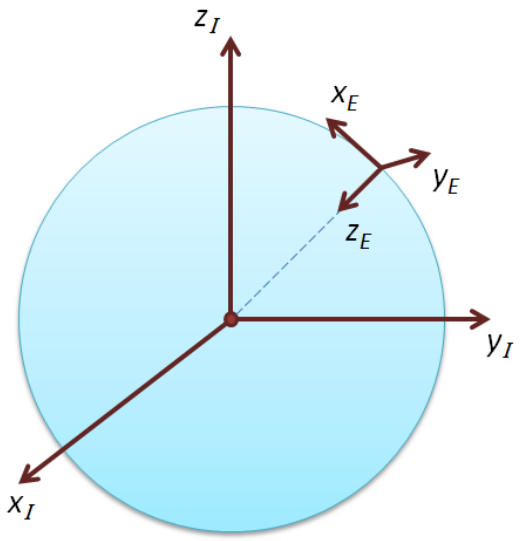

Figure 3.1: Inertial (F_I) and Earth-Fixed (F_E) Coordinate Systems

Earth-Fixed Axes, $\mathbf{F_E}$

Another very important axis system is the Earth-fixed axis system, which is also shown in Figure 3.1. The Earth-fixed frame, F_E, has its origin on the Earth's surface, with z_E pointed towards the Earth's center, x_E pointed towards the local north, and y_E defined by the right hand rule. This system is widely used in flight dynamics when the rotation of the Earth can be neglected and any frame fixed to the Earth is 'inertial enough'. The implication of ignoring the Earth's rotation is the removal of the Coriolis and centripetal acceleration terms (essentially a 'flat-Earth') that arise in the equations of motion. These terms are demonstrably very small for aircraft moving at subsonic and supersonic speed, but may be important for hypersonic flight or long distance navigation problems where the geographic location of the vehicle is important [60]. Etkin found the influence of the Earth's rotation to have less than a 1% effect on the force equations of motion, and even smaller on the moments, for flight Mach numbers of approximately 3.0 and less [61]. It is standard practice for the origin of F_E to be chosen such that its directly beneath the aircraft at time $t = 0$.

Body-Fixed Axes, $\mathbf{F_B}$

If a set of axes is fixed to the aircraft such that it moves with it, then the axes are called body-fixed axes, F_B. The origin of F_B is frequently chosen to be the center of gravity of the vehicle, as is the case in this study. The x_B axis is typically chosen to lie along the longitudinal centerline and is positive in the direction of motion, and the y_B axis is perpendicular to the plane of symmetry ($x_B - z_B$ plane) and points towards the right wing. The right-hand rule defines the downward pointing z_B axis (see Figure 3.2). Body-fixed axes are particularly useful in flight dynamics, because the moments and products of inertia are constant in this system (with the exception, of course, of mass flux due to fuel burn, payload drop, etc.). Also shown in Figure 3.2 are several terms affiliated with the body-fixed axes that are worth defining at this time. Indicated on the axes are the body axis roll, pitch, and yaw moments, L, M, and N, the roll, pitch and yaw angular rates, p, q, and r, the resultant aerodynamic forces, X, Y, and Z, and the components of freestream velocity, u, v, and w.

Stability Axes, $\mathbf{F_S}$

The final coordinate system to be addressed here is the stability axis system, F_S. A special case of the body-fixed axes, the stability axes share a similar orientation as the x_B, y_B, and z_B axes. The difference between the systems is that x_S is rotated through the angle of attack, α, such that it points into the relative wind when there is no sideslip, $\beta = 0$. In the presence of sideslip, x_S lies along the projection of the relative wind vector upon the $x_B - z_B$ plane (the plane of symmetry). As before, the y_S axis is perpendicular to the plane of symmetry and points to the right wing, and the z_S axis is determined by the right hand rule. Figure 3.3 illustrates the relationship between the body and stability axes. This system

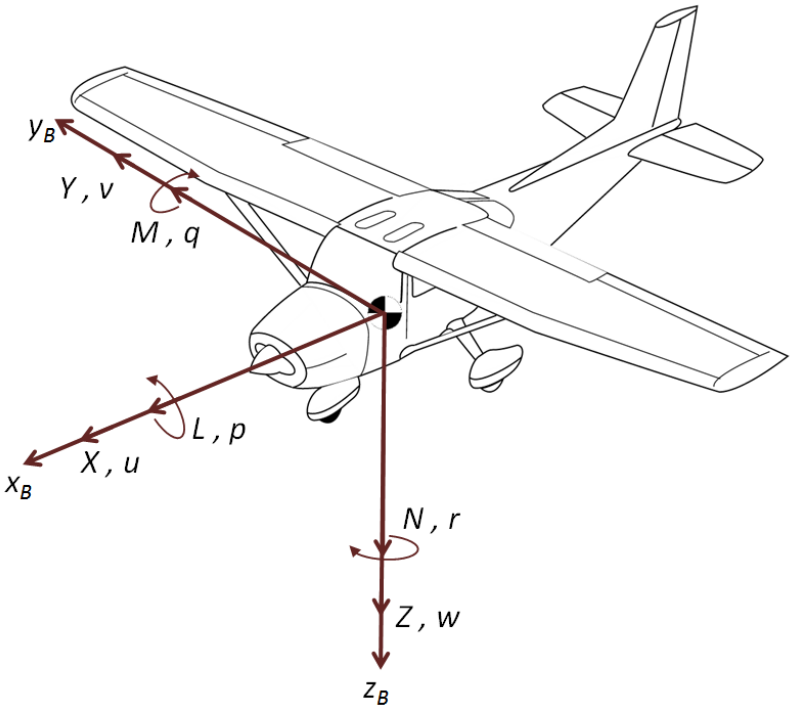

Variable	Description
L, M, N	rolling, pitching, and yawing moment
p, q, r	rolling, pitching, and yawing angular rate
X, Y, Z	components of resultant aerodynamic force
u, v, w	components of freestream velocity

Figure 3.2: Body-Fixed (F_B) Coordinate System and associated flight dynamics variables

is commonly used in small perturbation analysis, and it is desirable for the fact that the lift vector is directly opposite of z_S, and, if $\beta = 0$, the drag vector is directly opposite of x_S.

Transformation of Axes

Transformation between the various axes can be accomplished using a variety of methods including Euler angles, direction cosines, Euler axes, and quaternions. Euler angles are the most common, despite their limitations of singularities at extreme angles (extreme for an aircraft). A solid background in the kinematics of aircraft and their most common coordinate

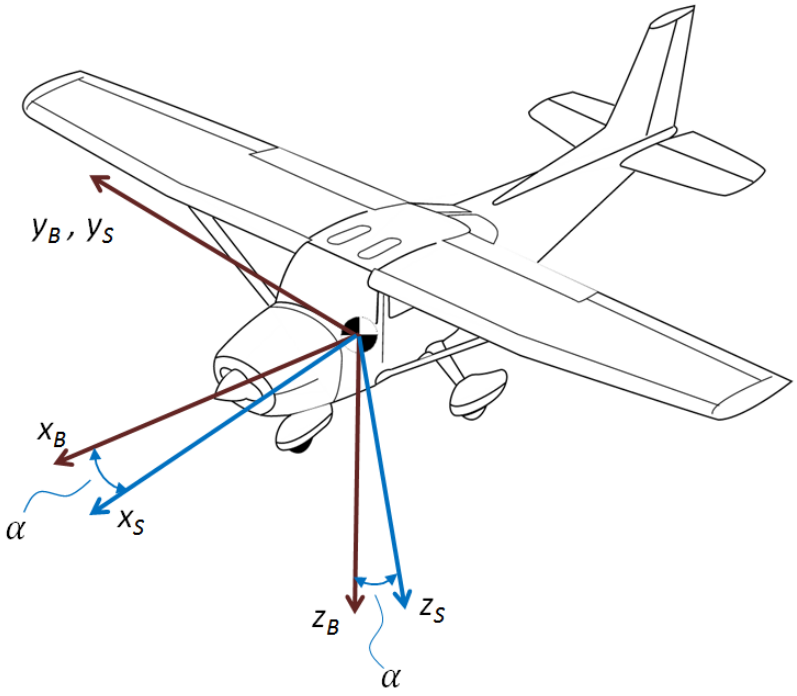

Figure 3.3: Body-Fixed Axes (F_B) rotated through the angle of attack, α, to the Stability Axes (F_S)

systems can be found in any text on flight dynamics [60, 61]. It is common when describing the dynamics of an aircraft to utilize a 3-2-1 rotation through the three angles ψ, θ, and ϕ, to describe the relationship between the body frame and the inertial frame. Here, the 3-2-1 notation specifies the sequence and the axis about which each rotation is to be taken. The angle ψ is often called the azimuth angle, θ the pitch angle, and ϕ the bank angle. Together, these angles and the rotation sequence provide the necessary information to develop the transformation from the inertial frame (F_I) to the body frame (F_B) as

$$T_I^B = \begin{bmatrix} \cos\theta\cos\psi & \cos\theta\sin\psi & -\sin\theta \\ \sin\theta\sin\phi\cos\psi - \sin\psi\cos\phi & \sin\psi\sin\theta\sin\phi + \cos\psi\cos\phi & \sin\phi\cos\theta \\ \sin\theta\cos\phi\cos\psi + \sin\psi\sin\phi & \sin\psi\sin\theta\cos\phi - \cos\psi\sin\phi & \cos\phi\cos\theta \end{bmatrix}. \quad (3.1)$$

It is a trivial extension to find the transformation from the body to the inertial system, since the inverse transformation is simply the transpose such that $T_B^I = (T_I^B)'$. Equation (3.1) and its constituent rotations are foundational to the remainder of the derivation of the equations of motion. They will be used to transform vectors and their time derivatives from the inertial frame, where Newton's laws are valid, to the body frame, where the aircraft aerodynamic and mass property data are readily calculated.

A similar transformation can be used to transform the body axes such that the x_B axis aligns with the freestream velocity to arrive at the so-called wind axes, F_W. This is just another special case of a body-fixed system, and as such is not discussed earlier. The wind axes transformation facilitates the computation of the body axes velocity components u, v, and w. A 3-2-1 rotation is used, again, with the rotation angles of $\psi_W = -\beta$, $\theta_W = \alpha$, and any ϕ_W based on the aircraft bank angle. This gives the transformation from the wind axes to the body axes system as

$$T_W^B = \begin{bmatrix} \cos\alpha\cos\beta & -\cos\alpha\sin\beta & -\sin\alpha \\ \sin\alpha\sin\phi\cos\beta + \sin\beta\cos\phi & -\sin\beta\sin\alpha\sin\phi + \cos\beta\cos\phi & \sin\phi\cos\alpha \\ \sin\alpha\cos\phi\cos\beta - \sin\beta\sin\phi & -\sin\beta\sin\alpha\cos\phi - \cos\beta\sin\phi & \cos\phi\cos\alpha \end{bmatrix}. \quad (3.2)$$

As before, the inverse transformation is given by the transpose such that $T_B^W = (T_W^B)'$. Given that the definition of the velocity vector in the wind axes is

$$V_W = \begin{bmatrix} U_0 \\ 0 \\ 0 \end{bmatrix}, \quad (3.3)$$

the body axis velocities are easily obtained through the relationship

$$V_B = \begin{bmatrix} u \\ v \\ w \end{bmatrix} = T_W^B V_W$$
$$= U_0 \begin{bmatrix} \cos\alpha\cos\beta \\ \sin\alpha\sin\phi\cos\beta + \sin\beta\cos\phi \\ \sin\alpha\cos\phi\cos\beta - \sin\beta\sin\phi \end{bmatrix}. \tag{3.4}$$

From Eq. (3.4), and provided that the bank angle is small, the traditional definitions for angle of attack α, and sideslip angle β, can be given as

$$\alpha = \tan^{-1}\left(\frac{w}{u}\right), \tag{3.5}$$
$$\beta = \sin^{-1}\left(\frac{v}{U_0}\right). \tag{3.6}$$

3.1.2 Kinematic Relations

Using the component rotations that make up the transformation matrix given in Eq. (3.1), the body axis angular rates, p, q, and r, can be related to the Euler angle rates, $\dot{\phi}$, $\dot{\theta}$, and $\dot{\psi}$. The derivation of the relationship is straightforward, and the details can be found in the literature. It is important to restate that these results are for a nonrotating Earth.

Conversion from the Euler angle rates to the body axis angular rates is given by

$$\begin{bmatrix} p \\ q \\ r \end{bmatrix} = \begin{bmatrix} 1 & 0 & -\sin\theta \\ 0 & \cos\phi & \sin\phi\cos\theta \\ 0 & -\sin\phi & \cos\phi\cos\theta \end{bmatrix} \begin{bmatrix} \dot{\phi} \\ \dot{\theta} \\ \dot{\psi} \end{bmatrix}. \tag{3.7}$$

The inverse relationship is achieved through a formal inversion of Eq. (3.7). Since the Euler angles are not mutually orthogonal, the convenient relationship of the transpose equaling the inverse no longer holds. Carrying out the inversion gives the final kinematic relationship

$$\begin{bmatrix} \dot{\phi} \\ \dot{\theta} \\ \dot{\psi} \end{bmatrix} = \begin{bmatrix} 1 & \tan\theta\sin\phi & \cos\phi\tan\theta \\ 0 & \cos\phi & -\sin\phi \\ 0 & \sec\theta\sin\phi & \sec\theta\cos\phi \end{bmatrix} \begin{bmatrix} p \\ q \\ r \end{bmatrix} \tag{3.8}$$

Equations (3.7) and (3.8) will be utilized later in the formulation of the complete set of equations of motion. As they stand, they represent a set of highly nonlinear, coupled, ordinary differential equations. To be of use in the linear analysis that follows, they will be linearized about an equilibrium state (trim state).

3.1.3 Newton's Laws

Derivation of the equations of motion of an aircraft is the subject of entire textbooks [65], but here we seek to provide sufficient background for the familiar reader. We begin with the force and moment equations given by Newton's laws as

$$F = m\left(\frac{dV}{dt}\right)_I \tag{3.9}$$

$$\mathcal{M} = \left(\frac{dH}{dt}\right)_I \tag{3.10}$$

where m is the mass, V is the velocity vector, H is the angular momentum vector, and the subscript I refers to the applicability of these equations in the inertial frame, F_I. Equation (3.10) can be further expanded by utilizing the relationship $H = I\omega$ such that

$$\mathcal{M} = \left(\frac{d(I\omega)}{dt}\right)_I \tag{3.11}$$

where ω is the angular velocity vector and I is the inertia tensor. Note that I is a symmetric matrix with the special structure

$$I = \begin{bmatrix} I_{xx} & -I_{xy} & -I_{xz} \\ -I_{xy} & I_{yy} & -I_{yz} \\ -I_{xz} & -I_{yz} & I_{zz} \end{bmatrix}. \tag{3.12}$$

As before, I_{xx}, I_{yy}, and I_{zz} are the moments of inertia about the x, y, and z axes, respectively, and I_{xy}, I_{xz}, and I_{yz} are the products of inertia in the $x-y$, $x-z$, and $y-z$ planes, respectively. The right side of Eq. (3.11) involves computations in the inertial frame. Measuring the time derivative of the inertia tensor in the inertial frame is difficult, however, since this term varies with the spatial orientation of the aircraft and requires recalculation at each instant in time. Fortunately, I is constant in the body axes since the axes move with the vehicle (and the vehicle has been assumed to be rigid), and the moving axis theorem provides a means to change the reference frame. The moving axis theorem states that the time rate of change of an arbitrary vector, v, can be resolved in the inertial frame when given in a body frame according to

$$\left(\frac{dv}{dt}\right)_I = \left(\frac{dv}{dt}\right)_B + \omega_{I,B}^B \times (v)_B. \tag{3.13}$$

The subscript notation of $\omega_{I,B}^B$ refers to the angular velocity of the F_B frame with respect to the F_I frame, and the superscript refers to the vector being resolved in the F_B frame.

Note that $(v)_B$ is the vector v resolved in the body frame. In the future, the parentheses surrounding vectors or matrices declared in one frame or the other will be dropped when the intended meaning is obvious.

Using the moving axis theorem, as well as the rigid-body assumption, Eq. (3.10) can be rewritten as

$$\begin{aligned}\mathcal{M} &= \left(\frac{dH}{dt}\right)_I \\ &= \left(\frac{dH}{dt}\right)_B + \omega_{I,B}^B \times (H)_B \\ &= I_B\dot{\omega}_B + \tilde{\omega}_B I_B \omega_B, \end{aligned} \tag{3.14}$$

where the tilde is indicative of the skew symmetric matrix of the vector ω_B such that

$$\tilde{\omega}_B = \begin{bmatrix} 0 & -r & q \\ r & 0 & -p \\ -q & p & 0 \end{bmatrix}. \tag{3.15}$$

Under the rigid-body assumption, Eq. (3.14) can be expanded to the set of scalar, nonlinear equations

$$\begin{aligned} L &= I_{xx}\dot{p} - I_{yz}\left(q^2 - r^2\right) - I_{zx}\left(\dot{r} + pq\right) - I_{xy}\left(\dot{q} - rp\right) - \left(I_{yy} - I_{zz}\right)qr \\ M &= I_{yy}\dot{q} - I_{zx}\left(r^2 - p^2\right) - I_{xy}\left(\dot{p} + qr\right) - I_{yz}\left(\dot{r} - pq\right) - \left(I_{zz} - I_{xx}\right)rp \\ N &= I_{zz}\dot{r} - I_{xy}\left(p^2 - q^2\right) - I_{yz}\left(\dot{q} + rp\right) - I_{zx}\left(\dot{p} - qr\right) - \left(I_{xx} - I_{yy}\right)pq. \end{aligned} \tag{3.16}$$

Finally, it is usual for aircraft to possess a plane of symmetry defined by the x and z axes. When this is the case, the inertia products I_{xy} and I_{yz} become zero, and the moment equations simplify to

$$\begin{aligned} L &= I_{xx}\dot{p} - I_{zx}\left(\dot{r} + pq\right) - \left(I_{yy} - I_{zz}\right)qr \\ M &= I_{yy}\dot{q} - I_{zx}\left(r^2 - p^2\right) - \left(I_{zz} - I_{xx}\right)rp \\ N &= I_{zz}\dot{r} - I_{zx}\left(\dot{p} - qr\right) - \left(I_{xx} - I_{yy}\right)pq. \end{aligned} \tag{3.17}$$

Equation (3.17) is boxed because these equations represent three of the fundamental equations of motion governing the rigid body dynamics. In addition to the moment equations, the force equations are similarly derived. Once again, utilizing the moving axis theorem, and exploiting the nonrotating Earth and rigid-body assumptions, and with the origin of the body frame collocated with the center of gravity, Eq. (3.9) can be written

$$\begin{aligned} F &= m\left(\frac{dV}{dt}\right)_I \\ &= m\left(\left(\frac{dV}{dt}\right)_B + \omega_{I,B}^B \times V_B\right), \end{aligned} \tag{3.18}$$

which is then easily expanded to the scalar equations

$$\begin{aligned} X &= m\left(\dot{u} + qw - rv\right) \\ Y &= m\left(\dot{v} + ru - pw\right) \\ Z &= m\left(\dot{w} + pv - qu\right). \end{aligned} \tag{3.19}$$

Completing the Equations of Motion

Equations (3.17) and (3.19) are the three moment and three force equations that constitute half of the twelve equations needed to fully describe the motion of a six degree of freedom rigid body. Three of the remaining equations were already discussed in Section 3.1.2 in matrix form (Eq. 3.8), but can be decomposed into the three scalar equations

$$\begin{aligned}
\dot{\phi} &= p + q\tan\theta\sin\phi + r\tan\theta\cos\phi \\
\dot{\theta} &= q\cos\phi - r\sin\phi \\
\dot{\psi} &= q\sec\theta\sin\phi + r\sec\theta\cos\phi.
\end{aligned} \tag{3.20}$$

These are the kinematic relations that define the relationship between the body angular rates, and the Euler angle rates that describe the orientation of the body with respect to the inertial frame.

The final three equations are the navigation equations. These equations describe the inertial position of the vehicle in three dimensions, and can be easily derived using the transformations between inertial and body axis vectors, T_I^B, as

$$\begin{aligned}
V_B &= T_I^B V_I \\
&= T_I^B \left(\frac{dR}{dt}\right)_I
\end{aligned} \tag{3.21}$$

where $R = [x \quad y \quad z]^T$. Inverting this relationship, the navigation equations in matrix form are

$$\left(\frac{dR}{dt}\right)_I = T_B^I V_B, \tag{3.22}$$

where T_B^I is the inverse transformation of Eq. (3.1), and is simply found using the transpose as $T_B^I = (T_I^B)'$. The scalar expansion of this relationship is then

$$\begin{aligned}
\dot{x} &= u(\cos\theta\cos\psi) + v(\sin\theta\sin\phi\cos\psi - \sin\psi\cos\phi) + w(\sin\theta\cos\phi\cos\psi + \sin\psi\sin\phi) \\
\dot{y} &= u(\cos\theta\sin\psi) + v(\sin\psi\sin\theta\sin\phi + \cos\psi\cos\phi) + w(\sin\psi\sin\theta\cos\phi - \cos\psi\sin\phi) \\
\dot{z} &= -u(\sin\theta) + v(\sin\phi\cos\theta) + w(\cos\phi\cos\theta).
\end{aligned} \tag{3.23}$$

The twelve scalar equations in Eqs. (3.17), (3.19), (3.20), and (3.23) represent the twelve,

nonlinear, coupled, ordinary differential equations of motion which govern the motion of a rigid body under the assumptions accumulated in Table 3.1. Numerical integration and simulation of these equations would provide the complete, nonlinear response of the aircraft provided the applied forces (X, Y, and Z) and the applied moments (L, M, and N) could be described as functions of the twelve states, their derivatives, and time. While theoretically this is possible using aerodynamic analysis software and performing an in-the-loop analysis to compute the aerodynamic forces and moments at each instant in time, the practicality of doing so in conceptual design MDO is poor. However, aerodynamicists and control system designers alike make excellent use of linearized and/or simplified models throughout the design process. The subject of the next section will be the linearization of the equations of motion about a reference flight condition, and the aerodynamic modeling of the applied forces and moments.

Table 3.1: Major Assumptions used in Equations of Motion Derivation

Assumption	**Equation Utilized**
• Dynamic aeroelastic influence on the aircraft rigid body motions is negligible	(3.17), (3.19)
• The effect of Earth's rotation on the aircraft dynamics is negligible	(3.7),(3.8)
• The aircraft is symmetrical about the $x-z$ plane	(3.17)
• The origin of the body frame, F_B, is at the aircraft center of gravity	(3.19)

3.2 Linearization of the Equations of Motion

The intent of the previous section was to remain as general as practical in the derivation of the equations of motion. In order to be of utility in the MDO framework, however, those equations must be linearized about a trimmed condition to obtain a linear time invariant (LTI), state-space model of the equations of motion. Linearized models are valid only in the neighborhood of the equilibrium solution about which they are taken, and they are invaluable tools in any designer's toolbox at any point in the design stage. Typically, not enough data is available to construct or use nonlinear aerodynamic models during the conceptual design stage, particularly in MDO, and simulation of the equations of motion is undesirable for design optimization studies. Thus, it is common for a conceptual designer to make many individual linearized models that piece-wise approximate the dynamics of an aircraft across its flight envelope. With the exception of large perturbation maneuvers that may be required of fighter or attack aircraft, small perturbation, linearized models are sufficient to ascertain a significant amount of knowledge about the configuration. In conceptual design optimization, linearized models of the equations of motion are universally used [38, 41, 42, 45]. Even the MIL-STD's which govern the flying qualities requirements, and are of significant relevance to this research, are based upon linearized models [15].

We seek to develop a set of linear differential equations in the standard state space form

$$\dot{x}(t) = Ax(t) + Bu(t), \tag{3.24}$$

where $A \in \mathbb{R}^{n\times n}$ and $B \in \mathbb{R}^{n\times m}$ are constant matrices. Often, Eq. (3.24) is accompanied by the standard output equation of the form

$$y(t) = Hx(t) + Fu(t), \tag{3.25}$$

where $H \in \mathbb{R}^{n\times n}$ and $F \in \mathbb{R}^{n\times m}$ are constant matrices. The methods to be developed in the coming sections will utilize the assumption of perfectly measurable states, known as full-state feedback, which is the special case of $H = \mathbb{I}$ and $F = 0$, where $\mathbb{I}$ is the identity matrix. It is, in fact, never the case in the real world that all of the states are perfectly measurable. Typically, sensors can only measure a subset or a combination of the states, and they have significant noise associated with the measurements. Furthermore, it is never the case that all of the sensors are placed at the instantaneous center of gravity for all time. The complications of sensor placement and sensor dynamics are beyond the scope of a full airframe conceptual design MDO. All of the state feedback control system design methods developed in next sections have 'output' based counterparts, meaning they would operate on $y(t)$ rather than $x(t)$, and it is a recommendation in the future work at the end of this thesis to investigate the impact of sensors and sensor dynamics through this avenue. It is with this justification that the standard output equation is reduced to $y(t) = x(t)$, thus the terms outputs and states are used synonymously.

Many approaches to the linearization of equations of motion have been taken in the literature, but none are more general than that by Duke et al. [62] This model avoids the tedious algebraic manipulation of the scalar equations and instead focuses on a matrix approach to linearization. The results obtained are identical, but the matrix approach facilitates computer calculations and generality of the approach. It is this approach that is presented herein. To begin, collect the equations of motion into the general, nonlinear vector function

$$T\dot{x}(t) = \mathbf{f}\left[\dot{x}(t), x(t), u(t)\right], \tag{3.26}$$

where T is a constant matrix in $\mathbb{R}^{n\times n}$. The presence of T arises from the desire to include state rates, $\dot{x}(t)$, in the applied force and moment terms, and will be made more clear later. For now, it suffices to identify its presence as a means of making the solution more

general [62]. Given an input, $u_0(t) \in \mathbb{R}^{n\times m}$, and a known solution of the state differential equations of motion, $x_0(t) \in \mathbb{R}^n$, Eq. (3.26) can be linearized about a trajectory such that

$$T\dot{x}_0(t) = \mathbf{f}\left[\dot{x}_0(t), x_0(t), u_0(t)\right]. \tag{3.27}$$

The assumption of linearization must now be made: approximation to the solution of the exact differential equations of motion can be made using a linear model provided the deviations from the equilibrium solution are small. Thus one can write

$$\begin{aligned} u(t) &= u_0(t) + \Delta u(t) \\ x(t) &= x_0(t) + \Delta x(t) \\ \dot{x}(t) &= \dot{x}_0(t) + \Delta\dot{x}(t) \end{aligned} \tag{3.28}$$

where the terms prefixed by Δ represent small deviations in their respective vectors.

Borrowing the notation of Duke et al. [62], a small perturbation about the equilibrium solution of Eq. (3.27) can then be expanded in a Taylor's series as

$$T\left[\dot{x}_0(t) + \Delta\dot{x}(t)\right] = \mathbf{f}\left[\dot{x}_0(t), x_0(t), u_0(t)\right] + \frac{\partial \mathbf{f}}{\partial x}\Delta x + \frac{\partial \mathbf{f}}{\partial \dot{x}}\Delta\dot{x} + \frac{\partial \mathbf{f}}{\partial u}\Delta u + h(t), \tag{3.29}$$

where $h(t)$ is the sum of the higher-order terms that are ignored under the small perturbation assumption. The other terms in Eq. (3.29) are

$$\begin{aligned} \frac{\partial \mathbf{f}}{\partial x} &= \left.\frac{\partial \mathbf{f}}{\partial x}\right|_{(x_0,\dot{x}_0,u_0)} \\ \frac{\partial \mathbf{f}}{\partial \dot{x}} &= \left.\frac{\partial \mathbf{f}}{\partial \dot{x}}\right|_{(x_0,\dot{x}_0,u_0)} \\ \frac{\partial \mathbf{f}}{\partial u} &= \left.\frac{\partial \mathbf{f}}{\partial u}\right|_{(x_0,\dot{x}_0,u_0)} \end{aligned} \tag{3.30}$$

where the (i,j)th elements are defined as

$$\begin{aligned}\left(\frac{\partial \mathbf{f}}{\partial x}\right)_{i,j} &= \frac{\partial \mathbf{f}_i}{\partial x_j} \\ \left(\frac{\partial \mathbf{f}}{\partial \dot{x}}\right)_{i,j} &= \frac{\partial \mathbf{f}_i}{\partial \dot{x}_j} \\ \left(\frac{\partial \mathbf{f}}{\partial u}\right)_{i,j} &= \frac{\partial \mathbf{f}_i}{\partial u_j}.\end{aligned} \tag{3.31}$$

Each partial derivative in Eq. (3.31) is evaluated at the equilibrium condition, and each term represents the derivative of the ith equation within Eq. (3.26) to the jth variable in the vectors x, $\dot{x}$, and u. Finally, the nonlinear equilibrium solution in Eq. (3.27) can be subtracted from the Taylor's series expansion of Eq. (3.29) to arrive at

$$\left[T - \frac{\partial \mathbf{f}}{\partial \dot{x}}\right] \Delta\dot{x}(t) = \frac{\partial \mathbf{f}}{\partial x}\Delta x(t) + \frac{\partial \mathbf{f}}{\partial u}\Delta u(t). \tag{3.32}$$

Note that the higher-order terms, $h(t)$, have been neglected. By inverting the first matrix term on the left, one can arrive at the standard state space form

$$\Delta\dot{x}(t) = \left[T - \frac{\partial \mathbf{f}}{\partial \dot{x}}\right]^{-1} \frac{\partial \mathbf{f}}{\partial x}\Delta x(t) + \left[T - \frac{\partial \mathbf{f}}{\partial \dot{x}}\right]^{-1} \frac{\partial \mathbf{f}}{\partial u}\Delta u(t). \tag{3.33}$$

The Δ prefixes can now be dropped with the recognition that the linearized equations represent a small perturbation from the equilibrium solution of the nonlinear equations. Also, gather terms into the familiar A and B matrices of Eq. (3.24) as

$$\begin{aligned}\dot{x}(t) &= Ax(t) + Bu(t) \\ A &= \left[T - \frac{\partial \mathbf{f}}{\partial \dot{x}}\right]^{-1} \frac{\partial \mathbf{f}}{\partial x} \\ B &= \left[T - \frac{\partial \mathbf{f}}{\partial \dot{x}}\right]^{-1} \frac{\partial \mathbf{f}}{\partial u}.\end{aligned} \tag{3.34}$$

3.2.1 Selection of the States

Equation (3.34) is the backbone of the linearization process. From the twelve equations of motion, analytic partial derivatives with respect to each variable can be computed about the equilibrium, and an LTI system can be constructed to model the behavior under the small-perturbation assumption. The selection of the state variables to be used is not unique, and as a means of convenience it is common to choose a set of states about a mixed system of axes. In particular, the body axis velocities u, v, and w, are commonly replaced with their wind axis counterparts such that the final state vector is

$$x = [p \quad q \quad r \quad V \quad \alpha \quad \beta \quad \phi \quad \theta \quad \psi \quad h \quad x \quad y]^T, \tag{3.35}$$

where h, the altitude, is the negative of the downward pointing variable z. These are the states used in the remainder of this thesis, and the complete set of nonlinear, scalar equations of motion in this form is included in Appendix A.

Conversion of the force equations of motion from body to wind axes introduces the more easily recognized aerodynamic forces of L, D, and Y—the lift, drag, and side forces. These forces are ubiquitous in the aerodynamic community, and their appearance in the Eqs. (A.20)-(A.22) facilitates compatibility of the aerodynamic analysis with the construction of the dynamic model. Also, to separate the effects of aerodynamic and propulsive effects, the body axis thrust forces X_T, Y_T, and Z_T are introduced in these equations. Once the equations of motion are linearized about an equilibrium, these thrust forces will only arise as sensitivities, so their absolute magnitude is not of great consequence. A full derivation of the conversion of the force equations of motion from body to wind axes can be found in Duke, et al. [62]

3.2.2 Aerodynamic Modeling

In general, the aerodynamic forces are nonlinear functions of the states and their time histories. Under Bryan's assumption of quasi-static aerodynamics, however, one can develop an approximate linear model of the aerodynamic force and moment terms which arise in the equations of motion. As before, this linearized model is subject to the small-perturbation assumption as well as the assumption that the influence of aeroelasticity on the aerodynamics is sufficiently captured by a static aeroelastic analysis. All of the assumptions made in the modeling of aerodynamic forces and moments are tabulated in Table 3.2 at the end of this section.

While the resultant aerodynamic forces and moments are technically functions of the state vector, x, its time derivatives, and the control surface deflections, a finite set of the most influential parameters must be selected for practical implementation. This choice may ultimately be flight condition dependent, but remaining consistent with the work of Etkin [61] and Duke et al.[62], it is assumed that the forces and moments, $\mathcal{F}$, are functions of the form

$$\mathcal{F} = \Phi\left(\alpha, \beta, V, h, x, y, p, q, r, \phi, \theta, \psi, \dot{\alpha}, \dot{\beta}, \delta_1, \ldots, \delta_n\right), \tag{3.36}$$

where Φ is an arbitrary function, and δ_i are the n control surface deflections. Note that the only time derivatives of states selected for modeling are $\dot{\alpha}$ and $\dot{\beta}$. The resultant forces and

moments of $\mathcal{F}$ can be written in their nondimensional form as

$$C_D = \frac{D}{\bar{q}S_{\text{ref}}} \tag{3.37}$$

$$C_Y = \frac{Y}{\bar{q}S_{\text{ref}}} \tag{3.38}$$

$$C_L = \frac{L}{\bar{q}S_{\text{ref}}} \tag{3.39}$$

$$C_l = \frac{L}{\bar{q}S_{\text{ref}}b} \tag{3.40}$$

$$C_m = \frac{M}{\bar{q}S_{\text{ref}}\bar{c}} \tag{3.41}$$

$$C_n = \frac{N}{\bar{q}S_{\text{ref}}b}, \tag{3.42}$$

where b is the total span and $\bar{c}$ is the mean aerodynamic chord (mac). The dynamic pressure, $\bar{q}$, is given by

$$\bar{q} = \frac{1}{2}\rho V^2, \tag{3.43}$$

where ρ is the freestream air density. The overloaded use of the character L to represent both the lift force and the rolling moment is a common idiosyncrasy within the aerodynamics community. In most cases, the intended use of the character is clear—if any confusion exists at any point, clarification will be made.

The nondimensionalization of the forces and moments is useful, since most aerodynamic analyses produce results in this form. By linearizing each coefficient, C_ξ, where ξ is representative of one of the six force and moment coefficients, the linear approximation to each

coefficient can be written as

$$\begin{aligned} C_\xi =& C_{\xi_0} + C_{\xi_\alpha}\alpha + C_{\xi_\beta}\beta + C_{\xi_V}V + C_{\xi_h}h + C_{\xi_x}x + C_{\xi_y}y + C_{\xi_{\hat{p}}}\hat{p} \\ &+ C_{\xi_{\hat{q}}}\hat{q} + C_{\xi_{\hat{r}}}\hat{r} + C_{\xi_\phi}\phi + C_{\xi_\theta}\theta + C_{\xi_\psi}\psi + C_{\xi_{\dot{\hat{\alpha}}}}\dot{\hat{\alpha}} + C_{\xi_{\dot{\hat{\beta}}}}\dot{\hat{\beta}} + \sum_{i=1}^{n} C_{\xi_{\delta_i}}\delta_i. \end{aligned} \tag{3.44}$$

In Eq. (3.44), C_{ξ_0} is the equilibrium value of C_ξ, and the double subscripted notation C_{ξ_x} is defined as

$$C_{\xi_x} = \frac{\partial C_\xi}{\partial x}, \tag{3.45}$$

where x can be any of the states, state rates, or control inputs declared in Eq. (3.36). Also of note in Eq. (3.44) is the 'hat' character above the angular rate terms. While most of the aerodynamic coefficients, C_{ξ_x}, are nondimensional, several of them, including the angular rates, require additional constants to be nondimensionalized. The nondimensional angular rates are defined as

$$\hat{p} = \frac{bp}{2V_0} \tag{3.46}$$

$$\hat{q} = \frac{\bar{c}q}{2V_0} \tag{3.47}$$

$$\hat{r} = \frac{br}{2V_0} \tag{3.48}$$

$$\dot{\hat{\alpha}} = \frac{\bar{c}\dot{\alpha}}{2V_0} \tag{3.49}$$

$$\dot{\hat{\beta}} = \frac{b\dot{\beta}}{2V_0}, \tag{3.50}$$

but it is conventional to drop the hat symbol when defining their respective aerodynamic

coefficients as

$$C_{\xi_p} = \frac{\partial C_\xi}{\partial \hat{p}} = \frac{\partial C_\xi}{\partial (bp/2V_0)} \tag{3.51}$$

$$C_{\xi_q} = \frac{\partial C_\xi}{\partial \hat{q}} = \frac{\partial C_\xi}{\partial (\bar{c}q/2V_0)} \tag{3.52}$$

$$C_{\xi_r} = \frac{\partial C_\xi}{\partial \hat{r}} = \frac{\partial C_\xi}{\partial (br/2V_0)} \tag{3.53}$$

$$C_{\xi_{\dot{\alpha}}} = \frac{\partial C_\xi}{\partial \hat{\dot{\alpha}}} = \frac{\partial C_\xi}{\partial (\bar{c}\dot{\alpha}/2V_0)} \tag{3.54}$$

$$C_{\xi_{\dot{\beta}}} = \frac{\partial C_\xi}{\partial \hat{\dot{\beta}}} = \frac{\partial C_\xi}{\partial (b\dot{\beta}/2V_0)}. \tag{3.55}$$

There are two other stability derivatives which are commonly reported in dimensional terms, and those are the velocity and altitude derivatives of

$$C_{\xi_V} = \frac{\partial C_\xi}{\partial V} \tag{3.56}$$

$$C_{\xi_h} = \frac{\partial C_\xi}{\partial h}. \tag{3.57}$$

The navigational states of x and y would also have dimensional derivatives, but under the flat, nonrotating Earth assumption these derivatives are always zero in the equations of motion. All assumptions utilized in this section are summarized in Table 3.2.

3.2.3 Linearization of the Scalar Equations

With the aerodynamics linearized, it is now possible to linearize the equations of motion. In Appendix A, the nonlinear, scalar equations of motion are written in the form

$$\dot{x}_k(t) = \mathbf{f}\left[\dot{x}(t), x(t), u(t)\right], \tag{3.58}$$

Table 3.2: Aerodynamic Modeling Assumptions

Assumption	**Equation Utilized**
• Perturbations from the equilibrium state are small	(3.44)
• Aerodynamic forces and moments are quasi-static, depending only on the instantaneous aircraft states and time derivatives	(3.36),(3.44)
• Aeroelastic influence on the aerodynamics is sufficiently captured by a static aeroelastic analysis	(3.36),(3.44)
• Linearized aerodynamic coefficients are sufficiently approximated by the Taylor series expansion involving the variables in Eq. (3.36)	(3.44)

where k is indicative of the kth state variable. In this form, partial derivatives of each equation with respect to each state variable can be taken in order to populate the $n \times n$ matrices

$$\frac{\partial \mathbf{f}}{\partial x} = \begin{bmatrix} \frac{\partial \dot{p}}{\partial p} & \frac{\partial \dot{p}}{\partial q} & \cdots & \frac{\partial \dot{p}}{\partial y} \\ \frac{\partial \dot{q}}{\partial p} & \frac{\partial \dot{q}}{\partial q} & \cdots & \frac{\partial \dot{q}}{\partial y} \\ \vdots & \vdots & & \vdots \\ \frac{\partial \dot{y}}{\partial p} & \frac{\partial \dot{y}}{\partial q} & \cdots & \frac{\partial \dot{y}}{\partial y} \end{bmatrix}, \tag{3.59}$$

and

$$\frac{\partial \mathbf{f}}{\partial \dot{x}} = \begin{bmatrix} \frac{\partial \dot{p}}{\partial \dot{p}} & \frac{\partial \dot{p}}{\partial \dot{q}} & \cdots & \frac{\partial \dot{p}}{\partial \dot{y}} \\ \frac{\partial \dot{q}}{\partial \dot{p}} & \frac{\partial \dot{q}}{\partial \dot{q}} & \cdots & \frac{\partial \dot{q}}{\partial \dot{y}} \\ \vdots & \vdots & & \vdots \\ \frac{\partial \dot{y}}{\partial \dot{p}} & \frac{\partial \dot{y}}{\partial \dot{q}} & \cdots & \frac{\partial \dot{y}}{\partial \dot{y}} \end{bmatrix}, \tag{3.60}$$

and the $n \times m$ matrix

$$\frac{\partial \mathbf{f}}{\partial u} = \begin{bmatrix} \frac{\partial \dot{p}}{\partial u_1} & \frac{\partial \dot{p}}{\partial u_2} & \cdots & \frac{\partial \dot{p}}{\partial u_m} \\ \frac{\partial \dot{q}}{\partial u_1} & \frac{\partial \dot{q}}{\partial u_2} & \cdots & \frac{\partial \dot{q}}{\partial u_m} \\ \vdots & \vdots & & \vdots \\ \frac{\partial \dot{y}}{\partial u_1} & \frac{\partial \dot{y}}{\partial u_2} & \cdots & \frac{\partial \dot{y}}{\partial u_m} \end{bmatrix}. \tag{3.61}$$

Duke et al. [62] offer an extensive derivation of each partial derivative required in Eq. (3.59), (3.60), and (3.61). These generalized derivatives are lengthy and not reproduced herein—the interested reader is referred to Ref. [62]. It is worth noting that the $\frac{\partial \mathbf{f}}{\partial \dot{x}}$ matrix is sparse, since the only state rates which were selected for modeling were $\dot{\alpha}$ and $\dot{\beta}$, a fact that makes its numerical inversion less computationally costly.

It is convenient at this time to address the utility of the constant square matrix, T, which appears in Eq. (3.26). The matrix was retained from the derivation by Duke et al., only in an effort to present the most general solutions possible. This matrix is used in the reference to scale the equations of motion into a decoupled body axis system where many terms in the rotation rate expressions drop out. A reduction in complexity is gained on the front end, with the downside being the need to rescale the solutions back to the desired body axes. For simplicity, no scaling of the body axes rates is utilized in this derivation, and the T matrix can be supplanted with the identity matrix such that Eq. (3.34) becomes

$$\begin{aligned} \dot{x}(t) &= Ax(t) + Bu(t) \\ A &= \left[\mathbb{I} - \frac{\partial \mathbf{f}}{\partial \dot{x}}\right]^{-1} \frac{\partial \mathbf{f}}{\partial x} \\ B &= \left[\mathbb{I} - \frac{\partial \mathbf{f}}{\partial \dot{x}}\right]^{-1} \frac{\partial \mathbf{f}}{\partial u}. \end{aligned} \tag{3.62}$$

Before building the matrices of Eq. (3.62), some additional considerations of the partial derivatives are necessary. These assumptions are congruent with those used by Etkin [61] and

Duke et al. [62], and the notation used is borrowed from the latter. First, partial derivatives of states with respect to themselves are unity, such that

$$\frac{\partial p}{\partial p} = \frac{\partial q}{\partial q} = \frac{\partial r}{\partial r} = \frac{\partial V}{\partial V} = \frac{\partial \alpha}{\partial \alpha} = \frac{\partial \beta}{\partial \beta} = \frac{\partial \phi}{\partial \phi} = \frac{\partial \theta}{\partial \theta} = \frac{\partial \psi}{\partial \psi} = \frac{\partial h}{\partial h} = \frac{\partial x}{\partial x} = \frac{\partial y}{\partial y} = 1, \tag{3.63}$$

while all other derivatives of states with respect to states are zero. Additionally, the derivatives of states with respect to time derivatives of states are also zero. Derivatives associated with the thrust generated forces and moments also carry some assumptions. The thrust forces, $\mathcal{F}_T = [X_T \quad Y_T \quad Z_T]^T$, are assumed to only vary with respect to the wind axis variables V, α, and β, and the control inputs, δ_i, while all other sensitivities are zero,

$$\frac{\partial \mathcal{F}_T}{\partial p} = \frac{\partial \mathcal{F}_T}{\partial q} = \frac{\partial \mathcal{F}_T}{\partial r} = \frac{\partial \mathcal{F}_T}{\partial \phi} = \frac{\partial \mathcal{F}_T}{\partial \theta} = \frac{\partial \mathcal{F}_T}{\partial \psi} = \frac{\partial \mathcal{F}_T}{\partial h} = \frac{\partial \mathcal{F}_T}{\partial x} = \frac{\partial \mathcal{F}_T}{\partial y} = 0. \tag{3.64}$$

Similarly, the thrust generated moments, $\mathcal{M}_T = [L_T \quad M_T \quad N_T]^T$, are assumed to vary with respect to the body axis angular rates, p, q, and r, and the wind axis variables V, α, and β, while all other sensitivities are zero,

$$\frac{\partial \mathcal{M}_T}{\partial \phi} = \frac{\partial \mathcal{M}_T}{\partial \theta} = \frac{\partial \mathcal{M}_T}{\partial \psi} = \frac{\partial \mathcal{M}_T}{\partial h} = \frac{\partial \mathcal{M}_T}{\partial x} = \frac{\partial \mathcal{M}_T}{\partial y} = \frac{\partial \mathcal{M}_T}{\partial \delta_i} = 0. \tag{3.65}$$

The final linearization assumption implemented by Duke et al. [62], is that all atmospheric properties including temperature, density, viscosity, and ambient pressure are only sensitive to altitude, and all other sensitivities are zero. These terms are retained for generality, but in the coming sections, altitude variations about an equilibrium solution are assumed to be small, and these terms will vanish.

All of the assumptions implemented in the linearization of the equations of motion are tabulated in Table 3.3. These assumptions, along with those made in the previous sections,

facilitate the construction of the matrices of Eqs. (3.59),(3.60) and (3.61). The details of the derivation of each specific term in these matrices can be found in Ref. [62].

Table 3.3: Linearization Assumptions

Assumption	**Equation Utilized**
• Derivatives of states with respect to themselves are unity, all other state to state derivatives are zero	(3.63)
• Thrust force only vary with respect to the wind axes variables V, α, and β, and the control inputs, δ_i	(3.64)
• Thrust moments only vary with respect to the body axes angular rates, p, q, and r, and the wind axes variables V, α, and β	(3.65)

3.2.4 Decoupled Equations of Motion

In many applications, including the MIL-STD-1797, a complete decoupling of the longitudinal and lateral-directional states is assumed. The longitudinal states are

$$x_{\text{long}} = [q \quad V \quad \alpha \quad \theta \quad h \quad x]^T , \tag{3.66}$$

and the lateral-directional states are

$$x_{\text{lat-dir}} = [p \quad r \quad \beta \quad \phi \quad \psi \quad y]^T . \tag{3.67}$$

Under only modest assumptions, uncoupled longitudinal motions can exist. Chief among these assumptions is a plane of symmetry in the flight condition such that all the states in

$x_{\text{lat-dir}}$ are zero. The other crucial assumption is the absence of rotor gyroscopic effects, which is implicit in the single rigid-body assumption already discussed. Rotor gyroscopic effects would serve to couple the longitudinal motions with lateral-directional forces. Assumptions required for the existence of the decoupled longitudinal motions are contained in Table 3.4.

Table 3.4: Assumptions for Decoupled Longitudinal Motion

Assumption	**Equation Utilized**
• The flat, nonrotating Earth approximation	(3.7),(3.8)
• A plane of symmetry exists in the motion of the vehicle	(3.68)
• Rotor gyroscopic effects are negligible	(3.68)

Under these assumptions, a symmetric flight condition can be completely described by two force equations, one moment equation, one kinematic relation, and two navigation equations. Returning to the nonlinear equations of motion of Eqs. (3.17), (3.19), (3.20), and (3.23), the longitudinal equations of motion can be derived as

$$\begin{aligned} X &= m\left(\dot{u} + qw\right) \\ Z &= m\left(\dot{w} - qu\right) \\ M &= I_{yy}\dot{q} \\ \dot{\theta} &= q \\ \dot{x} &= u\cos\theta + w\sin\theta \\ \dot{z} &= -u\sin\theta + w\cos\theta. \end{aligned} \tag{3.68}$$

Note that, while still nonlinear, only longitudinal variables are present in Eq. (3.68).

Unlike the lateral-directional equations of motion, no assumption of linearity is required for uncoupled longitudinal motion. The longitudinal equations of motion could then be linearized just as in Sections 3.2 and 3.2.2, where the assumption of symmetric flight would similarly influence the aerodynamic linearization.

As mentioned, the lateral-directional equations of motion require the additional assumptions listed in Table 3.5. Assumptions needed beyond those of the longitudinal equations of motion are the linearization of the equations and the absence of aerodynamic cross-coupling terms. The linearization is easily demonstrated by the pitching moment equation in Eq. (3.17). This equation was identified as a longitudinal equation of motion, but under the assumption that the $x_{\text{lat-dir}}$ states are nonzero and the x_{long} are zero (except for velocity and pitch angle, where $V = V_0$ and $\theta = \theta_0$), the equation reduces to

$$M = -I_{zx}\left(r^2 - p^2\right) - \left(I_{zz} - I_{xx}\right) rp. \tag{3.69}$$

After linearization and its implicit small-perturbation assumption, the higher-order terms (r^2, p^2, and rp) will be neglected. The end result is what is expected for the lateral-directional equations in that $M = 0$.

Aerodynamic cross-coupling terms are also neglected, the necessity of which is easily illustrated by the altitude variable z (or h in the wind axes). All aerodynamic and stability derivatives are functions of z due to the change in atmospheric parameters with altitude. Since z is a member of x_{long}, these sensitivities must be ignored in order to avoid coupling terms in the applied forces and moments. Control derivatives which constitute the matrix $\partial \mathbf{f}/\partial u$ are also subject to the cross-coupling term assumption. This is in direct contradiction to the identified behavior of nontraditional control effectors, which generate strong cross-axis forces and moments upon deployment. Nonetheless, the decoupling approximation is quite

Table 3.5: Assumptions for Decoupled Lateral-Directional Motion

Assumption	Equation Utilized
• The flat, nonrotating Earth approximation	(3.7),(3.8)
• The linearization of the equations of motion	(3.70)
• Rotor gyroscopic effects are negligible	(3.70)
• Aerodynamic cross-coupling terms are negligible	(3.70)

common and an essential part to the MIL-STD-1797, and thus to the VCFQ approach introduced here. With all of the assumptions applied, the decoupled, linearized, lateral-directional equations of motion are

$$\begin{aligned} Y &= m\left(\dot{v} + rV_0\right) \\ L &= I_{xx}\dot{p} - I_{zx}\dot{r} \\ N &= I_{zz}\dot{r} - I_{zx}\dot{p} \\ \dot{\phi} &= p + r\tan\theta_0 \\ \dot{\psi} &= r\sec\theta_0 \\ \dot{y} &= V_0\cos\theta_0\psi + v. \end{aligned} \tag{3.70}$$

3.3 Static Stability and Control

There are two fundamental types of static analyses used in conceptual aircraft design: static stability analyses, and static control analyses. The former category focuses on achieving

desirable levels of static margin or constraints on the aerodynamic coefficients C_{m_α}, C_{n_β}, and C_{l_β} as discussed in Chapter 1. Constraints on static stability are typically governed by policy and not physics. These are the types of constraints one seeks to relax through the integrated design of the control system. The static control analyses, however, are constructed from physics-based static equilibrium analyses. Even the best stability augmentation system would be incapable of trimming or maneuvering an aircraft if the available control effectors couldn't generate sufficient forces and moments. It is these types of constraints which need further discussion.

Before beginning a discussion of static S&C constraints and sizing techniques, it is important to define a few preliminary terms. First, the neutral point (*np*), is defined as the center of gravity location about which the pitching moment coefficient, C_m, is invariant with angle of attack, $C_{m_\alpha} = 0$. Its location along the x-axis, x_{np}, is typically reported nondimensionally according to

$$\bar{x}_{np} = \frac{x_{np} - x_{mac}}{\bar{c}}, \tag{3.71}$$

where x_{mac} is the x coordinate of the leading edge of the *mac*, and $\bar{c}$ is the *mac* length. This nomenclature is adopted throughout, with the over-bar indicating the dimension in percent *mac*.

Another particularly important value is the Static Margin (SM), defined as

$$SM = \frac{x_{np} - x_{cg}}{\bar{c}} = \bar{x}_{np} - \bar{x}_{cg}. \tag{3.72}$$

The static margin is a nondimensional measure of the distance between the neutral point and the *CG* as measured along the longitudinal axis. It is indicative of the vehicle longitudinal static stability, with positive values of SM indicating static stability, and negative values static instability. The term Relaxed Static Stability, introduced in Chapter 1, refers to an

aircraft which has a smaller than normal or a negative value of the SM. The SM also has implications on the maneuverability of the aircraft. An aircraft with a large, positive SM is likely to feel sluggish to a pilot, while a small SM can lead to extreme maneuverability. When the aircraft is statically unstable ($SM < 0$), the pilot must maintain acute control of the vehicle at all times, since the natural tendency of the aircraft would be to diverge out of control. Stability augmentation is one means of addressing the flight dynamic deficiencies of an unstable aircraft by using the control system to artificially stabilize the vehicle. It is no great challenge to compute the SM of a vehicle, since it is the result of a simple static moment balance which gives

$$SM = -\frac{C_{m\alpha_{cg}}}{C_{L_\alpha}}. \tag{3.73}$$

where $C_{m\alpha_{cg}}$ is the pitching moment derivative with respect to alpha, taken at the CG, and C_{L_α} is the lift curve slope.

Static analyses commonly used in aircraft design are typically derived from simplifications of the equations of motion in Eq. (3.17) and (3.19). For example, using the linearized aerodynamic model of Section 3.2.2, the control deflection needed to trim an aircraft in symmetric flight with a load factor $n = 1$, where load factor is the ratio of the lift to the vehicle weight, is given by

$$\begin{aligned} 0 &= M \\ 0 &= C_{m_0} + C_{m_\alpha}\alpha + \sum_{i=1}^{n} C_{m_{\delta_i}}\delta_i, \end{aligned} \tag{3.74}$$

where C_{m_0} is the zero-lift pitching moment coefficient. Under the assumption of only one control effector, the elevator, the required elevator deflection to trim can be computed as

$$\delta_e = \frac{-C_{m_0} + (SM)C_L}{C_{m_{\delta_e}}}, \tag{3.75}$$

where δ_e is the elevator deflection.

While algebraically quite simple, static results such as Eq. (3.75) carry a hidden degree of complexity: every parameter within the equation is a nonlinear function of the flight condition. In particular, SM is very sensitive to Mach number effects and the rearward shift of the neutral point at transonic and supersonic speeds. Additionally, the perturbation of a control surface will necessarily change the required lift to trim a given load factor such that

$$n = \frac{\text{Lift}}{\text{Weight}} = \frac{q\left(C_L S_{\text{ref}} + \eta_{\text{HT}} C_{L_{\text{HT}}} S_{\text{HT}}\right)}{W} = \text{constant}, \tag{3.76}$$

where $C_{L_{\text{HT}}}$ is the lift from the horizontal tail, W is the aircraft weight, and η_{HT} is the ratio of the dynamic pressure at the horizontal tail ($\bar{q}_{\text{HT}}$) to that of the freestream defined by

$$\eta_{\text{HT}} = \frac{\bar{q}_{\text{HT}}}{\bar{q}}. \tag{3.77}$$

If the tail produces more (or less) lift due to the deflection of the elevator, the load carried by the wing must compensate to maintain a constant load factor. Thus, the static solution is, in fact, iterative, and must be conducted at each flight condition of interest.

There are even greater challenges to static stability analyses which are almost universally ignored in the literature studied in Chapter 2. In the same sense that the balance of lift between the wing and tail was iterative, the effects of static aeroelasticity are also iterative. Deflection of a control surface drives a change in the load distribution, which disturbs the statically deflected shape of the aircraft and, in turn, the effectiveness of the control surface. Fortunately, the complication of trimming an aircraft subject to static aeroelastic deflections is often handled by software which is capable of resolving those deflections. If multiple control surfaces are present, especially if any exhibit cross-axis behavior, then static analyses must be further supplemented with constraint functions in order to have the same number of

equations as independent variables.

In light of these limitations, many of the trim analyses built into the new S&C module are handled by the aeroelastic solver, and will be detailed in Chapter 5. However, some of the basic static analyses are insightful into the types of constraints that drive the static sizing of control surfaces, and they are briefly discussed further.

3.3.1 Longitudinal Static Sizing

Nicolai [5] suggests that there are four longitudinal conditions which will drive the static sizing requirements of the tail: trim drag, high load factor maneuvers, takeoff rotation, and high angle of attack trim at low dynamic pressures.

Trim Drag

Trim drag is the drag-due-to-lift associated with the generation of moments required to trim the aircraft. It is the drag that is in excess of the total drag of the configuration at the same flight condition with no control surfaces articulated. Reference [5] provides an approximate expression for the trimmed drag during flight with a unit load factor as

$$D_{\text{trim}} = \eta_{\text{HT}} \bar{q} S_{\text{HT}} K_{\text{HT}} C_{L_{\text{HT}}}^2, \tag{3.78}$$

where K_{HT} is a constant. Trim drag reduction can be achieved through a reduction in static stability, increasing the tail volume coefficient, or increasing the tail aspect ratio—though each of these alterations will have other design and performance consequences. No explicit static constraints on trim drag are used in the present S&C module, but the degraded performance caused by excessive trim drag would be captured by mission performance analyses

within the MDO framework.

High Load Factor Maneuver

Depending on the aircraft configuration, the ability to trim a high load factor pull-up or pushover is critical. The additional control surface deflection required to trim at load factors other than $n = 1$ is given by [5] as

$$\Delta\delta_e = -\frac{\left[-SM + (\rho S_{\text{ref}}\bar{c}/4m)C_{m_q}\right](n-1)C_{L_{n=1}}}{C_{m_\delta}}, \tag{3.79}$$

where $C_{L_{n=1}}$ is the lift coefficient for $n = 1$ flight, and C_{m_q} is the pitch damping derivative

$$C_{m_q} = \frac{\partial C_m}{\partial(q\bar{c}/2V)}. \tag{3.80}$$

Thus, the total deflection is the sum of Eqs. (3.75) and (3.79). At each desired load factor, the capability to trim with a sufficient control margin remaining should be confirmed. As before, the presence of multiple longitudinal control effectors and static aeroelastic effects results in solutions which are far more complicated than the simple algebraic approximation of Eq. (3.79).

Takeoff Rotation

The low dynamic pressures at takeoff velocities reduce the effectiveness of control effectors. A common critical static sizing case is the aircraft takeoff rotation—the ability of the aircraft to generate a sufficient nose-up moment to rotate about the main landing gear. Figure 3.4 illustrates the major forces which are relevant to performing a takeoff rotation analysis. An approximate expression relating the takeoff rotation rate, $\dot{\theta}_R$, and the tail lift coefficient can

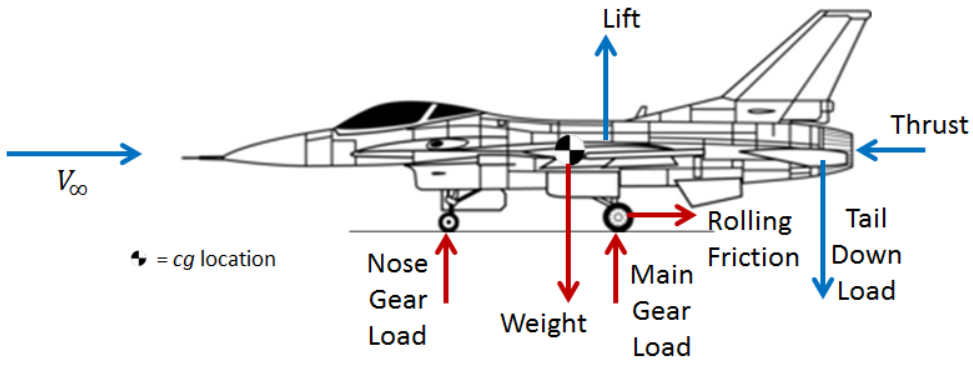

Figure 3.4: Illustration of the major forces involved during the takeoff rotation

.

be found in [59] as

$$\frac{S_{\text{HT}}}{S_{\text{ref}}} = \frac{\bar{c}}{l_h}\frac{C_{L_{\max}}}{\eta_h \eta_q C_{L_{\text{HT}}}}\left\{\frac{C_{m_{np}}}{C_{L_{\max}}} - \left(\frac{V_{s_{\text{TO}}}}{V_R}\right)^2 \times \frac{x_{mg} - z_T\frac{T}{W} - x_{cg}}{\bar{c}}\right\} + \frac{C_{L_R}}{C_{L_{\text{HT}}}}\left(\bar{x}_{mg} - \bar{x}_{np}\right), \quad (3.81)$$

where

$$\eta_h = \frac{x_{\text{HT}} - x_{mg}}{l_h}\left(\frac{V_{\text{HT}}}{V_R}\right)^2$$
$$\eta_q = 1 + \frac{C_{L_{\alpha_{\text{HT}}}}}{C_{L_{\text{HT}}}}\frac{\dot{\theta}_R\left(x_{\text{HT}} - x_{mg}\right)}{V_R},$$

$C_{L_{\max}}$ is the maximum attainable lift coefficient, $C_{m_{np}}$ is the pitching moment taken about the neutral point, $V_{s_{\text{TO}}}$ is the stall speed during takeoff, V_R is the rotation velocity, C_{L_R} is the lift coefficient at rotation, T is the thrust, V_{HT} is the velocity at the horizontal tail, and all of the remaining geometric parameters are defined in Figure 3.5.

Equation (3.81) does not explicitly contain a control surface deflection term, however, the tail lift coefficient, $C_{L_{\text{HT}}}$ can be expanded to included the zero angle of attack tail lift

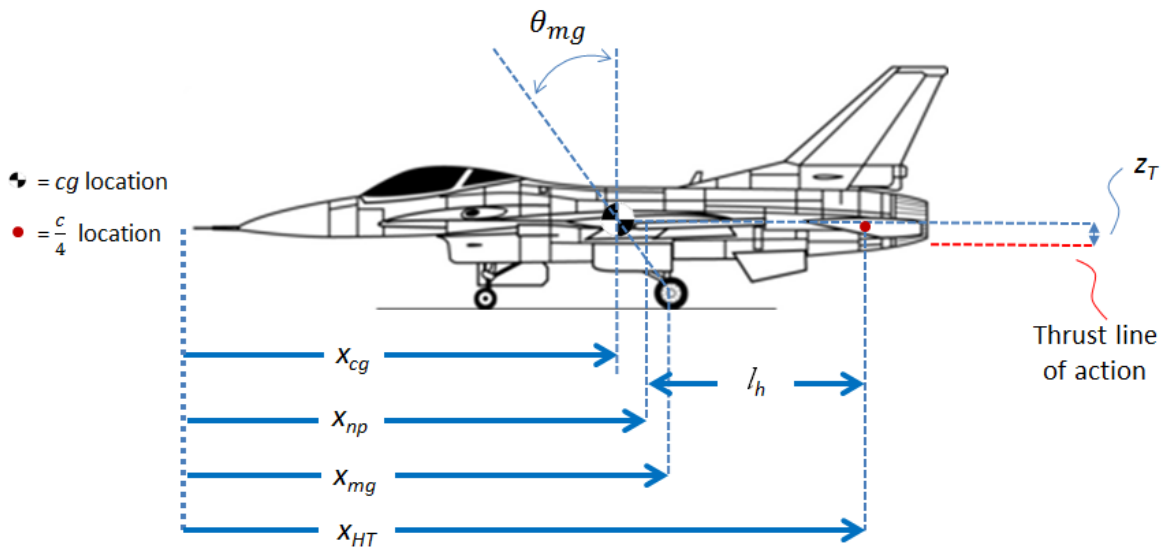

Figure 3.5: Illustration of the dimensions pertinent to the takeoff rotation calculations

.

plus the elevator contribution as

$$C_{L_{\mathrm{HT}}} = (C_{L_{\mathrm{HT}}})_{\alpha=0} + C_{L_{\mathrm{HT}_{\delta_e}}} \delta_e. \tag{3.82}$$

Low-Speed, High Angle of Attack Trim

At low speeds, aircraft often utilize high lift devices and high angles of attack to achieve sufficient lift—particularly during the landing approach. The dynamic pressures during this time are at a minimum, and yet the pitching moments from high lift devices are often quite high. In order to be able to trim an aircraft in this condition, the control effectors must be sufficiently sized. As noted in Ref. [5], it is common for this critical flight condition to establish the forwardmost *CG* limit for the aircraft. From reference [59], the equation

relating the elevator deflection to trim is given by

$$\frac{S_{\mathrm{HT}}}{S_{\mathrm{ref}}} = \frac{\bar{c}}{l_h} \frac{C_{L_{\max}}}{\eta_h C_{L_{\mathrm{HT}}}} \left(\frac{C_{m_{np}}}{C_{L_{\max}}} + \bar{x}_{cg} - \bar{x}_{np} \right), \tag{3.83}$$

where

$$\eta_h = \frac{(x_{\mathrm{HT}} - x_{cg}) \cos \alpha}{l_h} \left(\frac{V_{\mathrm{HT}}}{V} \right)^2. \tag{3.84}$$

Just as before, the control surface deflection is implicitly embedded in $C_{L_{\mathrm{HT}}}$ as

$$C_{L_{\mathrm{HT}}} = C_{L_{\mathrm{HT}_\alpha}} \alpha_{\mathrm{HT}_{\mathrm{eff}}} + C_{L_{\mathrm{HT}_{\delta_e}}} \delta_e, \tag{3.85}$$

where $\alpha_{\mathrm{HT}_{\mathrm{eff}}}$ refers to the effective angle of attack at the horizontal tail (includes the effects of downwash and tail incidence angle).

3.3.2 Lateral-Directional Static Sizing

As with the longitudinal analyses, several lateral-directional scenarios are easily identified to be critical. Reference [5] identifies these as crosswind landing, asymmetric power, spin susceptibility, and roll-rate requirements. Each of these is briefly visited in the following sections.

Crosswind Takeoff and Landing

According to the FARs [13, 14], an aircraft must be capable of tracking a straight path during normal takeoff and landing while subjected to crosswind velocities of 20 knots or 20% of the takeoff velocity, V_{TO}, whichever is greater (up to a maximum of 25 knots). This could mean the rudder must hold a sideslip angle of up to $\beta = 11.5^\circ$ during approach. Sufficient

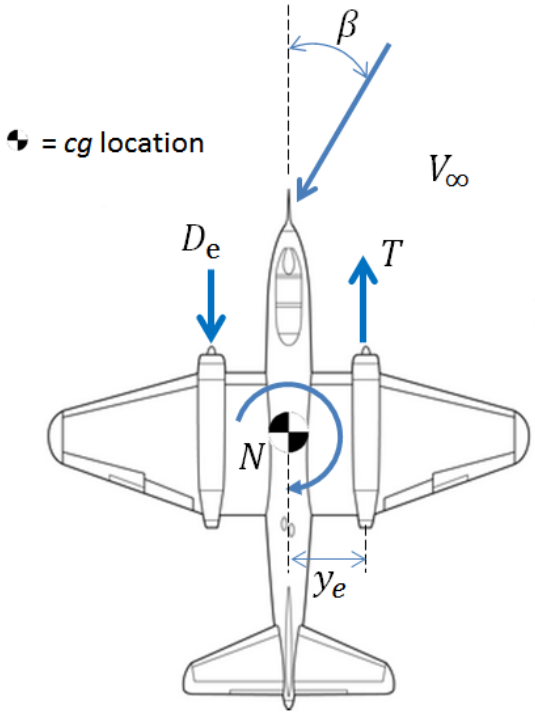

Figure 3.6: Illustration of port-side engine out scenario on the twin engine B-57

surplus control authority must be maintained even while in a crosswind, and MIL-STD-1797 requires that 25% of the available effector travel remain available for maneuver [15]. The moment balance which describes the required rudder deflection to balance the moments is given by

$$C_n = 0 = C_{n_\beta}\beta + C_{n_{\delta_r}}\delta_r, \tag{3.86}$$

where δ_r is the rudder deflection, and the sideslip angle, β, can be seen in Figure 3.6. Just as with the longitudinal trim cases, the presence of multiple control effectors or static aeroelasticity results in a more complicated set of equations.

Asymmetric Power Condition

When one or more engines fail on an aircraft, the vertical tail and rudder must be capable of maintaining control of the aircraft. In fact, the FARs [13, 14] require that at $1.3V_{\text{stall}}$ with one engine inoperative (in a twin engine aircraft) the aircraft be capable of trimming to zero sideslip, $\beta = 0$, with the flaps deployed, at the maximum landing weight, and with the most unfavorable CG. For aircraft with more than two engines, the same constraints apply under the condition of multiple engine failures occuring on the same side of the aircraft. Figure 3.6 illustrates the port-side engine out scenario on the twin engine B-57 aircraft. The resulting moment balance which describes the required rudder deflection is

$$C_n = 0 = -\frac{(T + D_e)y_e}{\bar{q}S_{\text{ref}}b} + C_{n_{\delta_r}}\delta_r, \tag{3.87}$$

where D_e is the drag of the inoperative engine, and y_e is the distance along the y-axis from the CG to the engine. Again, the presence of multiple effectors and structural flexibility can complicate the solution of this equation.

Spin Susceptibility

For highly maneuverable configurations such as fighter or attack aircraft, the potential for the configuration to develop a spin while turning requires special attention. Two scalar parameters based upon static coefficients attempt to predict this dynamic phenomenon. The first parameter, the Lateral Control Departure Parameter (LCDP) attempts to predict spin which occurs due to adverse yaw and roll reversal at high angles of attack. Details and further discussion of the LCDP parameter can be found in Refs. [60] and [61], or in the

MIL-STD-1797 [15]. The LCDP is computed as

$$\text{LCDP} = C_{n_\beta} - C_{l_\beta} \frac{C_{n_{\delta_a}}}{C_{l_{\delta_a}}}, \tag{3.88}$$

where δ_a is the aileron deflection. An aircraft which has an LCDP > 0 will exhibit predictable roll characteristics to the pilot, and is therefore unlikely to develop a spin. If LCDP < 0, then aileron inputs are reversed and the potential to achieve an undesirable spin is increased.

The second parameter is $C_{n_{\beta_{\text{dyn}}}}$, a scalar predictor of yaw departure at high angle of attack. The expression is derived from the open-loop lateral directional equations of motion and is given in [60] as

$$C_{n_{\beta_{\text{dyn}}}} = C_{n_\beta} \cos\alpha - \frac{I_{zz}}{I_{xx}} C_{l_\beta} \sin\alpha. \tag{3.89}$$

At low angles of attack, Eq. (3.89) is equivalent to the static stability derivative, C_{n_β}. If the value of $C_{n_{\beta_{\text{dyn}}}}$ is positive, then the aircraft is unlikely to experience yaw departure at high angles of attack. The inertia ratio I_{zz}/I_{xx} is often quite large for slender aircraft such as fighters or supersonic configurations. In fact, in Ref. [66] the authors stated that for supersonic configurations like the Concorde, this ratio could be from 2-7 times larger than for conventional transport aircraft. Thus, $C_{n_{\beta_{\text{dyn}}}}$ is a particularly important parameter for high-performance aircraft.

Both the LCDP and $C_{n_{\beta_{\text{dyn}}}}$ are scalar *indicators* of a dynamic characteristic. Their use is based equally on physics and correlation with data, and they are not guarantees of behavior. Nonetheless, when performing conceptual design studies of high-performance aircraft, both parameters are easily computed evidence of the expected performance of the vehicle.

Roll Rate Requirements

The previous lateral-directional critical static scenarios all dealt with the vertical tail and the yaw control device. This last category is different in that it deals primarily with the roll control devices, typically ailerons, and is governed by requirements found in Ref. [15]. Using the result from Ref. [5], the roll rate can be estimated as

$$P = -\frac{2V}{b}\frac{C_{l_{\delta_a}}}{C_{l_p}}\delta_a. \tag{3.90}$$

Roll rate requirements found in the MIL-STD-1797 are given as an angular displacement requirement over a given time—effectively a time average of the angular velocity. Constraints are sorted by flight velocity, flight category, and aircraft classification. Flight categories and aircraft classifications are discussed further in Section 3.4.2. Once the average angular rate is found, it is trivial to compute the required aileron deflection using Eq. (3.90). The simplicity of this relationship is dependent upon the single input and rigid airframe assumptions highlighted in the other static scenarios.

3.4 Dynamic Stability and Control

Dynamic S&C is the study of the time history of the response of the aircraft and its characteristic stability. Stability of a dynamic system is the subject of textbooks, and many different definitions of stability exist. Aleksandr Lyapunov's work *"The General Problem of the Stability of Motion"*, written in Russian in 1892 [67], provides the foundation of the most common definition of stability. Lyapunov was the first to recognize that the stability of a nonlinear system could be predicted near an equilibrium by assessing the stability of the

linearized system about the same point. An equilibrium point, x_e, of a system of the form

$$\dot{x}(t) = \mathbf{f}[x(t)], \quad x(0) = x_0 \quad x \in \mathbb{R}^n, \tag{3.91}$$

is said to be locally stable in the sense of Lyapunov at $t = t_0$ if for any $\epsilon > 0$ there exists a $\delta(t_0, \epsilon) > 0$ such that

$$\|x_0 - x_e\| < \delta \Longrightarrow \|x(t) - x_e\| < \epsilon, \quad \forall t \geq t_0. \tag{3.92}$$

In other words, the system is locally Lyapunov stable about the equilibrium x_e if it starts within a small ball of radius δ about x_e and remains within a ball of radius ϵ about x_e for all time [61]. Note that the system does not have to return to the equilibrium to be stable in the sense of Lyapunov, but must only remain "close enough". The notion of asymptotic stability expands upon Lyapunov stability in that it adds the requirement of local attraction. If a system is stable in the sense of Lyapunov about an equilibrium x_e, it is said to be asymptotically stable if there exists a $\delta > 0$ such that if

$$\|x_0 - x_e\| < \delta \Longrightarrow \lim_{t \to \infty} x(t) = 0. \tag{3.93}$$

Thus, asymptotic stability requires that the trajectory $x(t)$ eventually return to the equilibrium, x_e. An even more restrictive definition is that of exponential stability, which demands the convergence to equilibrium occur at least as fast as a known rate. For LTI systems, asymptotic and exponential stability are synonymous.

In addition to introducing the fundamental definitions of stability, Lyapunov also developed sufficient conditions for the stability of a dynamical system about its origin. Application of his work extends beyond LTI systems and sees regular use in linear time-varying [68] and

nonlinear systems theory [69], as well. According to Lyapunov's theory, an LTI system is asymptotically stable if a function $V(x)$, called the Lyapunov function, can be found such that

$$V(x) \geq 0 \quad \forall x \in \mathbb{R}^n, \quad V(x) = 0 \quad \text{iff } x = 0, \tag{3.94}$$

$$\dot{V}(x) = \frac{dV}{dt} = \frac{\partial V}{\partial x}\frac{dx}{dt} < 0. \tag{3.95}$$

With some further specifications, this method is also applicable to nonlinear systems [69]. No general procedure exists for finding Lyapunov functions for nonlinear systems, however, and the search can prove to be an arduous and fruitless task. Fortunately, for LTI systems of the form $\dot{x} = Ax$, there is a procedure which reduces to solving a linear algebraic equation. Candidate Lyapunov functions for these systems are of the form

$$V(x) = x^T P x, \quad P = P^T > 0, \tag{3.96}$$

where the inequality refers to the positive definiteness of P. The matrix P is said to be positive definite if it satisfies the relation

$$u^T P u > 0, \quad \forall u \neq 0, u \in \mathbb{R}^n. \tag{3.97}$$

Equivalently, a positive definite matrix also has strictly positive eigenvalues. Negative definiteness is similarly defined as having strictly negative eigenvalues, and the inequality sign reversed in Eq. (3.97). Using these definitions, Eq. (3.95) then leads to

$$\dot{V}(x) = x^T(A^T P + PA)x < 0, \tag{3.98}$$

which can be reduced to the Lyapunov inequality

$$A^T P + PA < 0, \quad P > 0. \tag{3.99}$$

Thus, a sufficient condition for the asymptotic stability of an LTI system $\dot{x} = Ax$, is given by the existence of a positive definite matrix P, such that Eq. (3.99) holds. The Lyapunov inequality can be equivalently written as an equality condition

$$A^T P + PA = -Q, \quad Q = Q^T > 0, \tag{3.100}$$

where Q is any positive definite matrix [68]. The Lyapunov inequality of Eq. (3.99) is a critical element in the development of the Variance Constrained Flying Qualities approach, and will be revisited in Chapter 4. As it turns out, a great deal of information can be extracted from this most fundamental formulation.

The more well known definition of asymptotic stability is also worth noting since it possesses its own merits. A linear system of the form $\dot{x} = Ax$ is asymptotically stable if and only if all of the eigenvalues of A have negative real parts, i.e.

$$\mathrm{Re}\left[\lambda_i(A)\right] < 0, \tag{3.101}$$

where λ_i is the ith eigenvalue of A. Note that the eigenvalue decomposition of A leads to a necessary and sufficient condition for stability. Modal decomposition of a linear system also offers an engineer some intuition into the response of the system, which is easily obfuscated by the matrices of the Lyapunov stability interpretation. Where the eigenvalue approach to stability analysis proves more limited is in its extensions to nonlinear systems [69].

With the understanding of dynamic stability developed, the control aspect still deserves

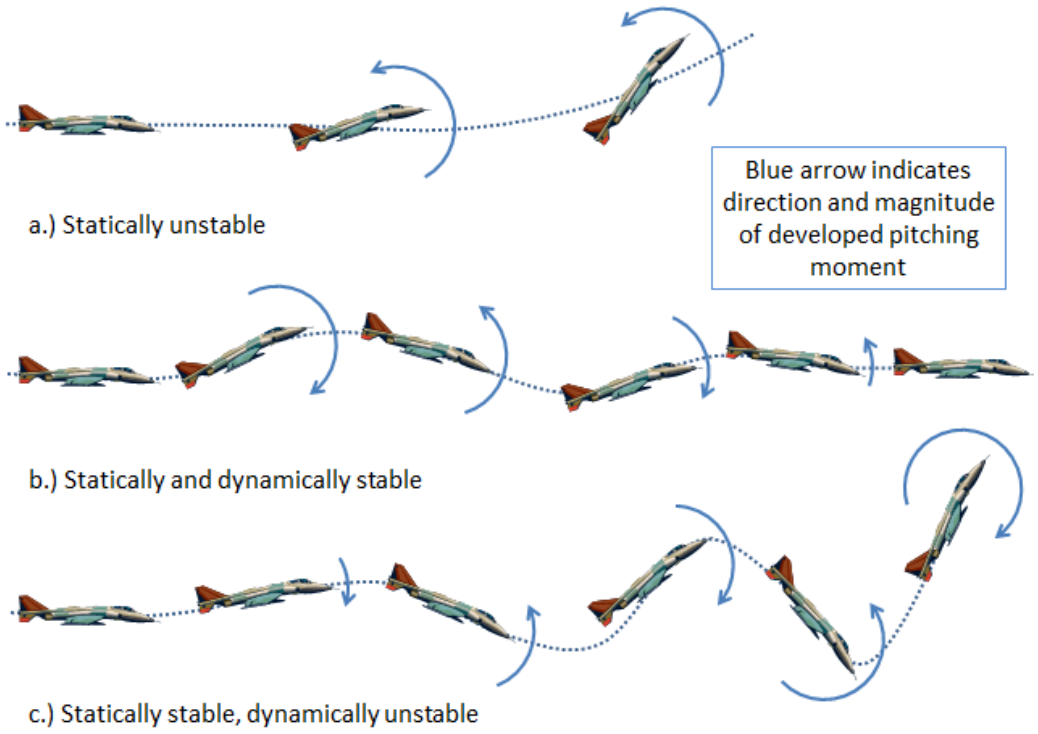

Figure 3.7: Dynamic response of aircraft with different stability characteristics to a nose-up disturbance

discussion. The static stability of a configuration is a necessary but not a sufficient indicator of the stability of the time history of the aircraft response. This is illustrated in Figure 3.7, where a statically unstable aircraft is compared to two statically stable configurations for which one is dynamically stable and the other dynamically unstable. All three configurations are disturbed by a nose-up disturbance. The statically stable configurations always develop pitching moments which are counter to the direction of motion, while the statically unstable configuration develops a pitching moment in the direction of the disturbance, which leads to divergence. In addition to generating restoring moments in the correct direction, the dynamically stable configuration also tends to damp the motions, while the dynamically unstable configuration tends to oscillate into a divergence. Thus, it is possible for a statically stable configuration to possess unsatisfactory dynamic behavior. A simple dynamic stability

analysis within an S&C module could declare the bare airframe behavior as dynamically stable or unstable, but doing so would ignore the potential performance advantages of stability augmentation and active control. A well-designed control system can overcome both static and dynamic instabilities, augmenting the bare airframe dynamics to be more desirable. The automated design of an SAS is a major part of the Variance Constrained Flying Qualities approach developed here in Chapter 4. In most cases in aircraft design, it is insufficient to simply design for dynamic stability, but rather some more restrictive dynamic objective is required. For piloted aircraft, these constraints deal with flying qualities and pilot comfort, whereas on an unmanned aircraft, dynamic constraints may deal with sensor oscillations or payload accelerations.

Before moving on to the primary technical contribution of this thesis, the Variance Constrained Flying Qualities approach, it is important to introduce some technical preliminaries which are vital to the development. Sufficient detail is provided for the reader to become familiar with the subjects, and references to more thorough resources are given throughout.

3.4.1 Linear Matrix Inequalities (LMI)

While not strictly related to dynamics and S&C, linear matrix inequalities (LMI) are a mathematical construct with tremendous utility in systems and control theory. An LMI is a convex constraint which is very general in structure. Many common inequality constraints can be written as LMI's [48], including linear inequalities, convex quadratic inequalities, matrix norm inequalities, the Riccati inequality, and the Lyapnuov inequality of Eq. (3.99). An LMI has the form

$$F(x) \triangleq F_0 + \sum_{i=1}^{m} x_i F_i > 0, \tag{3.102}$$

where $x \in \mathbb{R}^m$ is a vector of decision variables and the symmetric matrices $F_i = F_i^T \in \mathbb{R}^{n \times n}$, $i = 0, \ldots, m$, are known. The inequality symbol, when used in the matrix sense, refers to the positive definiteness of $F(x)$ as discussed in the previous section. The matrix inequality, $F(x)$, is an affine constraint on the vector, x.

The utility of LMI's is due to a number of beneficial properties. First, an LMI in $\mathbb{R}^{n \times n}$ can be equivalently written as n polynomial inequalities by using the mathematical fact that a real symmetric matrix is positive definite if and only if all of its principal minors are positive. This result is explored further in Refs. [48], [46], and [47], and can be helpful in developing an understanding of the relationship between well understood scalar inequalities and their matrix counterparts.

A second beneficial LMI characteristic, and possibly the most important, is their convexity. A set, C, is convex if

$$\lambda x + (1 - \lambda) y \in C, \quad \forall \quad x, y \in C \text{ and } \lambda \in (0, 1). \tag{3.103}$$

An LMI of the form of Eq. (3.102) is demonstrably convex by defining two vectors x and y such that $F(x) > 0$ and $F(y) > 0$, and $\lambda \in (0, 1)$. Using Eq. (3.103) in Eq. (3.102) then gives

$$\begin{aligned} F(\lambda x + (1 - \lambda) y) &= F_0 + \sum_{i=1}^{m} (\lambda x_i + (1 - \lambda) y_i) F_i \\ &= \lambda F_0 + (1 - \lambda) F_0 + \lambda \sum_{i=1}^{m} x_i F_i + (1 - \lambda) \sum_{i=1}^{m} y_i F_i \\ &= \lambda F(x) + (1 - \lambda) F(y) \\ &> 0. \end{aligned} \tag{3.104}$$

Thus, the constraint $F(x) > 0$ is a convex constraint and the set $\{x|F(x) > 0\}$ is convex. The importance of convexity can not be overstated, since convex problems are easily solved using numerical means such as ellipsoidal peeling or interior-point methods [46].

A third property of LMI's which can be of great utility is that a system of LMI's is not unique. As demonstrated in Ref. [48], if an arbitrary matrix function $A(x)$ is positive definite, then $A(x)$ when subject to a congruence transformation is also positive definite. This is best illustrated by example:

$$\begin{aligned} A > 0 &\iff x^T A x > 0, \quad \forall x \neq 0 \\ &\iff (Mz)^T A (Mz) > 0, \quad \forall z \neq 0, \quad M \text{ nonsingular} \\ &\iff M^T A M > 0. \end{aligned} \tag{3.105}$$

Thus, under a nonsingular transformation, M, the matrix A remains positive definite. This property is useful in that often times the introduction of a transformation will facilitate a restructuring of the problem, leading to a simplification or a convex formulation.

The final beneficial property of LMI's is their ability to be trivially combined. Multiple LMI's of the form

$$F_1(x) > 0, F_2(x) > 0, \ldots, F_k(x) > 0$$

can be rewritten as the equivalent single LMI as

$$F(x) = F_0 + \sum_{i=1}^{m} x_i F_i = \text{diag}\left[F_1(x), F_2(x), \ldots, F_k(x)\right] > 0, \tag{3.106}$$

where

$$F_i = \text{diag}\left[F_{1_i}, F_{2_i}, \ldots, F_{k_i}\right], \forall i = 0, \ldots, m. \tag{3.107}$$

The result of Eq. (3.106) is that $F(x)$ is equivalently written as a block-diagonal matrix

where each block is composed of the individual LMI constraints. Thus, no particular effort is required to assemble a large set of LMI's, since the individual LMI's need only be appended together along the diagonal to create a larger LMI.

Before concluding this brief introduction to LMI's, one noteworthy property is discussed. A wide class of systems of interest in dynamics and control appear in the form of convex nonlinear inequalities as:

$$R(x) > 0, \quad Q(x) - S(x)R(x)^{-1}S(x)^T > 0, \tag{3.108}$$

where $Q(x) = Q(x)^T$, $R(x) = R(x)^T$, and $S(x)$ all depend affinely on x. This system can be rewritten using the Schur complement lemma as the equivalent LMI's

$$\begin{bmatrix} Q(x) & S(x) \\ S(x)^T & R(x) \end{bmatrix} > 0, \tag{3.109}$$

a proof of which can be found in Ref. [48] or many other mathematical references. The Schur complement facilitates the development of LMI's for many popular problems in controls, including maximum singular value constraints, ellipsoidal inequalities, and the Algebraic Riccati inequality, to name only a few.

3.4.2 Flying Qualities Requirements

There are many guidelines and equations offered in the MIL-STD-1797 [15] to perform a detailed analysis of the flying qualities of an aircraft late in the design stage. Models are provided for maneuvers, field performance, pilot-in-the-loop behavior, and even ground performance. Of primary interest to conceptual aircraft designers are the flying qualities guidelines pertaining to the major flight categories and tasks that dominate the intended use of the

aircraft. Examples include the behavior during cruise, climb, pull-up, or landing maneuvers when subjected to gusts or other disturbances. Typical guidelines include constraints on the minimum or maximum damping ratio, natural frequency, or time constant. In some cases, as in the short-period mode requirements, the limits on modal parameters are obfuscated through the use of a flight condition dependent term like the Control Anticipation Parameter (CAP). When provided with flight condition information, these guidelines are easily reduced to modal constraints on the closed-loop system. An example of a typical closed-loop pole location boundary from the MIL-STD-1797 is shown in Figure 3.8.

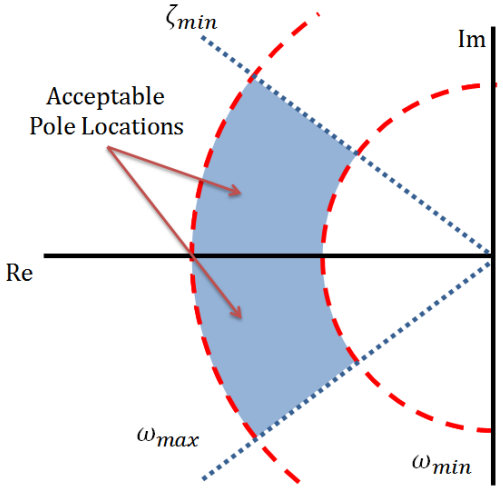

Figure 3.8: Example pole location boundaries as interpreted from the MIL-STD-1797B

Specific requirements within the MIL-STD-1797 are given according to the Level of flying qualities, the aircraft classification, and the flight category. Flying qualities are based upon pilot opinion assessed using the Cooper-Harper scale [30], and are classified as being Level I, II, or III as defined in Table 3.6. Somewhat colloquially, a flying qualities Level IV exists in some references, but in general it refers to a scenario in which the aircraft can not be flown at all, and thus the formal definition of such a level is excluded from the MIL-STD-1797.

Table 3.6: Summary of flying qualities levels defined in the MIL-STD-1797

Level I	Flying qualities are clearly adequate for the mission flight phase.
Level II	Flying qualities are adequate to accomplish the mission flight phase when some increase in pilot workload or degradation in mission effectiveness exists or both.
Level III	Flying qualities are such that the mission can be controlled safely, but pilot workload is excessive or mission effectiveness is inadequate or both.

The aircraft themselves are classified according to their size and primary mission. This classification is designed to address the fact that fighters, transports, and general aviation aircraft are not all expected to share similar dynamic characteristics. The details of the aircraft classifications are provided in Table 3.7.

Finally, the last categorization is that of the flight conditions. Flight Categories A, B, and C, serve to classify different segments of flight according to their relative intensity and pilot workload. A pilot attempting to perform an aerial refueling maneuver or land on a carrier deck at night is subjected to a drastically different workload than the sports commentator loitering in his single engine general aviation aircraft above a game. Categorization of the flight conditions is intended to address these differences, and in most cases, the constraints placed on the aircraft dynamics are more restrictive for the higher workload maneuvers. Descriptions of each of the flight categories is summarized in Table 3.8, with the full details available in Ref. [15].

The advent of high-order feedback control laws has driven the more recent military flying qualities requirements to include the Lower-order Equivalent System (LOES) concept. As the order of feedback control systems grew in recent years, the application of flying qualities requirements first conceived for aircraft without control systems became problematic. Conceptually, the idea behind the LOES is that a high-order system of ordinary differential

Table 3.7: Summary of aircraft classifications defined in the MIL-STD-1797

Class I	Small, light air vehicles such as • light utility • primary trainer • light observation
Class II	Medium weight, low-to-medium maneuverability air vehicles such as • heavy utility/search and rescue • light or medium transport/cargo/tanker • early warning/electronic countermeasures/airborne command, control, or communications relay • antisubmarine • assault transport • reconnaissance • tactical bomber • heavy attack • trainer for Class II
Class III	Large, heavy, low-to-medium maneuverability air vehicles such as • heavy transport/cargo/tanker • heavy bomber • patrol/early warning/electronic countermeasures/airborne command, control, or communications relay • trainer for Class III
Class IV	High-maneuverability air vehicles such as • fighter/interceptor • attack • tactical reconnaissance • observation • trainer for Class IV
Class V	Rotorcraft
Class VI	V/STOL air vehicles

Table 3.8: Summary of flight categorization defined in the MIL-STD-1797

Category A	Nonterminal flight phases that require rapid maneuvering, precision tracking, or precise flight-path control. Included in this category are air-to-air combat, ground attack, weapons delivery/launch, aerial recovery, reconnaissance, in-flight refueling, terrain following, antisubmarine search, close formation flying, low-altitude parachute extraction, and precision hover.
Category B	Nonterminal flight phases that are normally accomplished using gradual maneuvers and without precision tracking, although accurate flight-path control may be required. Included in this category are climb, cruise, loiter, in-flight refueling, descent, emergency descent, emergency deceleration, aerial delivery, hover, station keeping, hover translation, accelerating transition, and decelerating transition.
Category C	Terminal flight phases that are normally accomplished using gradual maneuvers and usually require accurate flight-path control. Included in this category are takeoff, catapult takeoff, power approach, waveoff/go-around, landing, carrier approach, bolter, ground handling, carrier landing, short takeoff, vertical takeoff, short landing, and vertical landing.

equations can be approximately modeled by using a smaller system of ordinary differential equations. In order to model the full-order dynamics of an aircraft and its control system, a narrow frequency range is selected and a second-order system is fitted, by numerical means, to match the frequency response. This lower-order system is then used in the evaluation of flying qualities. The details of the calculation of an LOES can be found in Ref. [15]. The topic is somewhat controversial [31], but the LOES concept is not needed in the development of the VCFQ approach anyway. While VCFQ could facilitate the design of high-order controllers, the metric is developed assuming static state feedback, and thus does not introduce additional controller dynamics.

It was stated earlier that the MIL-STD-1797 contains many different flying qualities criteria. Among them are the traditional modal constraints, the Neal-Smith criterion, the Bandwidth criterion, the Ride Quality Index, and others. Most of these methods are transfer function based and would be challenging to implement in an automated sense for multiple

input systems. It has been the pattern during conceptual design studies which observe flying qualities requirements [41, 45], and in texts on flight dynamics which contain flying qualities analysis case studies [60], to only observe the traditional modal constraints during conceptual design.

Longitudinal Modes of Motion

Conventional aircraft exhibit two distinct modes of motion which can be observed through a modal decomposition of the longitudinal equations of motion: the phugoid mode and the short-period mode. Phugoid motion is very lightly damped and is driven by the energy exchange between gravitational potential and kinetic energy. The time constant of phugoid motion is very large—so large, in fact, that it is common for pilots to naturally suppress phugoid oscillations. For this reason, phugoid dynamics are only lightly constrained by the MIL-STD-1797 according to Table 3.9. These constraints are only on the damping ratio

Table 3.9: MIL-STD-1797 phugoid damping requirements

Level	Damping Requirement
I	$\zeta > 0.04$
II	$\zeta > 0.0$
III	$T_2 \geq 55\,\text{sec}$

(ζ) for this motion, and do not vary with aircraft classification or flight category. Level III phugoid motions are allowed to be unstable, but only slightly so such that the pilot can easily maintain control of the vehicle. The Level III constraint is given as a time to double, T_2, which is the time it takes for a disturbance to grow in amplitude by a factor of two.

Short-period motions are heavily damped and occur at a much higher frequency than the phugoid. These motions typically last only a few seconds, and involve rapid oscillations in the angle of attack, pitch angle, and pitch rate while the forward speed is largely constant.

Short-period motions can be uncomfortable to a pilot, and are traditionally the source of unsatisfactory longitudinal flying qualities. As such, more constraints exist for short-period oscillations than the phugoid. Tables 3.10 and 3.11 detail the constraints placed by Ref. [15] on the damping ratio and the Control Anticipation Parameter (CAP), respectively. The CAP is the ratio of the initial pitching acceleration to the steady-state normal acceleration, or load factor, given by

$$\text{CAP} = \frac{\ddot{\theta}_0}{n}. \tag{3.110}$$

Within the linear range of angle of attack, and with negligible control system dynamics, the CAP is often written as

$$\text{CAP} = \frac{\omega_{n_{\text{sp}}}^2}{(n/\alpha)}, \tag{3.111}$$

where $\omega_{n_{\text{sp}}}$ is the short-period natural frequency. Knowledge of the flight condition's load factor and trimmed angle of attack then allow for the easy computation of the limits placed upon $\omega_{n_{\text{sp}}}$.

Table 3.10: MIL-STD-1797 short-period damping requirements

	Cat A and C $\zeta_{\text{sp,min}}$	Cat A and C $\zeta_{\text{sp,max}}$	Cat B $\zeta_{\text{sp,min}}$	Cat B $\zeta_{\text{sp,max}}$
Level I	0.35	1.30	0.30	2.0
Level II	0.25	2.0	0.20	2.0
Level III	0.15	—	0.15	—

Table 3.11: MIL-STD-1797 limits on the Control Anticipation Parameter (CAP)

	Cat A min	Cat A max	Cat B min	Cat B max	Cat C min	Cat C max
Level I	0.28	3.6	0.085	3.6	0.16	3.6
Level II	0.16	10.0	0.038	10.0	0.096	10.0
Level III	0.16	—	0.038	—	0.096	—

Lateral-Directional Modes of Motion

Lateral-directional motions are characterized by three modes: the roll mode, the dutch-roll mode, and the spiral mode. Two of these modes are non-oscillatory, corresponding to real roots in the eigenvalue decomposition of the lateral-directional equations of motion. These modes are the roll and spiral modes. The roll mode, occasionally called the roll-subsidence mode, is a heavily damped motion about the body x-axis. The dihedral effect produces damping moments about the roll axis, but no natural restoring moments are generated—thus an aircraft disturbed in roll will maintain the achieved roll angle, though it will dissipate the roll rate. This lack of a restoring force prevents the motion from being oscillatory, and instead the classical first-order system behavior is observed. Constraints on the behavior of the roll mode are, therefore, given as maximum allowable time constants in Ref. [15], and are reproduced in Table 3.12

Table 3.12: MIL-STD-1797 maximum allowable roll mode time constants

Class	Category	Level I	Level II	Level III
I,IV	A	1.0	1.4	10.0
II,III	A	1.4	3.0	10.0
I,II,III,IV	B	1.4	3.0	10.0
I,IV	C	1.0	1.4	10.0
II,III	C	1.4	3.0	10.0

The first-order spiral mode of an aircraft is actually allowed to be open-loop unstable. Spiral mode divergence occurs when a lateral gust puts an aircraft into a sideslipping motion with nonzero roll angle. A directionally stable aircraft will yaw into the sideslip, steepening the angle and increasing the roll rate in the same direction. This spiraling motion is much like a spin, but with the fundamental difference that the wings and control surfaces are not stalled like they are in a spin. Constraints on the spiral mode are dictated as minimum time to double, where the times were determined to be large enough such that a pilot could easily

manage the disturbance [15]. These constraints are reproduced in Table 3.13.

Table 3.13: MIL-STD-1797 minimum time to double spiral mode constraint

Category	Level I	Level II	Level III
A,C	12.0	8.0	4.0
B	20.0	8.0	4.00

As a quick aside, it is possible for the roll and spiral modes to coalesce into a combined roll-spiral oscillatory mode. While this case is generally considered undesirable, and forbidden for Flight Category A, it is allowable under certain conditions. A thorough discussion and explanation of the constraints on the coupled modes is found in Ref. [15].

The last of the lateral-directional modes, and possibly the most important, is the Dutch-roll mode. Oscillatory motions which follow the heavily damped roll subsidence mode are are a combination of sideslip and yawing motions and are said to have the appearance of a Dutch figure skater as they sway from side to side to generate forward locomotion. The Dutch-roll mode is comprised largely of perturbations in sideslip angle and yaw rates, though a certain degree of coupling with the roll angle and roll rates exists. As with the short-period mode of the longitudinal dynamics, the Dutch-roll mode is likely to be the most critical lateral-directional mode in terms of pilot opinion and flying qualities ratings. In addition to the constraints on Dutch-roll natural frequency, $\omega_{n_{\mathrm{dr}}}$, and damping ratio, ζ_{dr}, there is also a constraint on their product, $\omega_{n_{\mathrm{dr}}}\zeta_{\mathrm{dr}}$. A summary of the constraints provided in Ref. [15] are given in Table 3.14.

Table 3.14: MIL-STD-1797 Dutch-roll mode constraints

Level	Category	Class	Min ζ_{dr}	Min $\omega_{n_{\text{dr}}}\zeta_{\text{dr}}$ (rad/s)	Min $\omega_{n_{\text{dr}}}$ (rad/s)
I	A	I,IV	0.19	0.35	1.0
I	A	II,III	0.19	0.35	0.4
I	B	I,II,III,IV	0.08	0.15	0.4
I	C	I,II-C†, IV	0.08	0.15	1.0
I	C	II-L†,III	0.08	0.10	0.4
II	A,B,C	I,II,III,IV	0.02	0.05	0.4
III	A,B,C	I,II,III,IV	0.0	—	0.4

†The -C and -L suffix denote carrier and land-based aircraft

3.5 Limitations of the Modal Constraints

The fact that the flying qualities guidelines are given as constraints on modal parameters is less than ideal for the development of an S&C module for an MDO framework. First, the consistency of the modal parameter constraints is easily questioned, since the MIL-STD-1797 makes no attempt to constrain the eigenvectors—a fundamental element in the modal decomposition. Unconventional configurations are unlikely to possess the same characteristic modes of motion as those described by the MIL-STD-1797, which will likely lead to false predictions of the sufficiency of the dynamic response. Second, most modern control techniques do not lend themselves to pole placement-type problems, adding complexity to the control design task. This section serves to illuminate these deficiencies and establish the motive for an alternative means of predicting flying qualities during the conceptual design phase. A simple example will be used to illustrate the shortcomings of eigenvalue constraints on clearly defining the response of the aircraft. This is followed by a discussion of the limitations of modern control methods as they apply to pole placement.

General Aviation Motivational Example

Consider a model of the linearized longitudinal equations of motion for a NAVION general aviation aircraft like that shown in Figure 3.9. This model first appeared in Ref. [70], and was reproduced in Ref. [60] as an example configuration. The flight Mach number is low subsonic at sea level, and the remainder of the details of the mass and aerodynamic properties can be found in Ref. [60] or [70].

Figure 3.9: North American L-17A NAVION

The state space model of the form $\dot{x} = Ax$ is defined by

$$\mathbf{x} = \begin{bmatrix} u \\ \Delta\alpha \\ q \\ \Delta\theta \end{bmatrix}, \quad \mathbf{A} = \begin{bmatrix} -0.0453 & 0.0363 & 0 & -0.1859 \\ -0.3717 & -2.0354 & 0.9723 & 0 \\ 0.3398 & -7.0301 & -2.9767 & 0 \\ 0 & 0 & 1 & 0 \end{bmatrix}, \tag{3.112}$$

where the states are nondimensional velocity $u = \Delta u/V$, the perturbation in angle of attack $\Delta\alpha$, the pitch rate q, and the perturbation in pitch angle $\Delta\theta$. An eigenvalue decomposition of A yields the open-loop eigenvalues as $\lambda_{1,2} = -2.5118 \pm 2.5706i$ and $\lambda_{3,4} = -0.0169 \pm 0.2174i$.

The pole-zero plot of the system is given in Figure 3.10, where the MIL-STD-1797 minimum short-period natural frequency and damping ratio boundaries are also shown (the maximum natural frequency boundary lies well outside of the range of the axes).

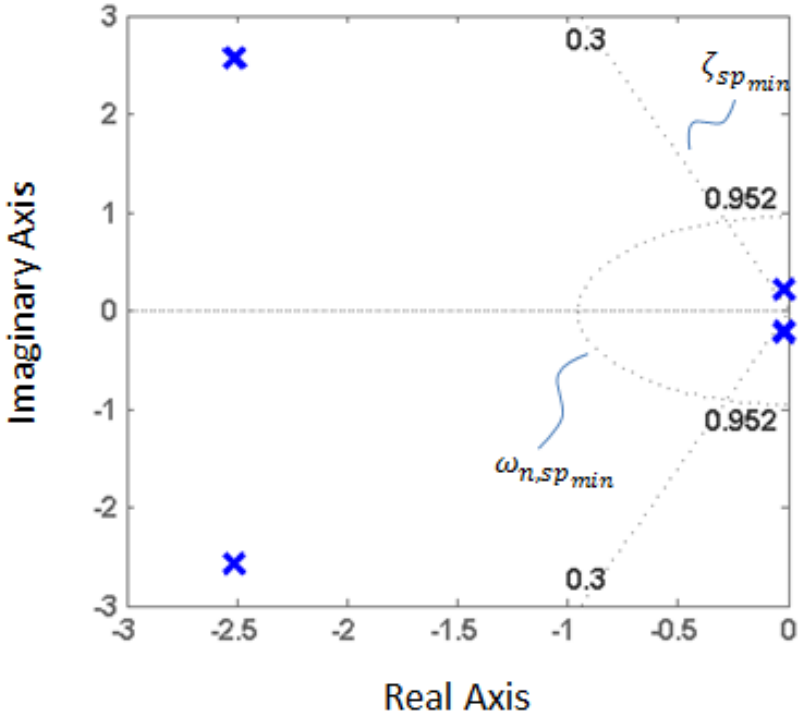

Figure 3.10: Open-loop eigenvalues of the system described by Eq. (3.112) plotted on the complex plane. Dotted lines represent the MIL-STD-1797 flying qualities boundaries as labeled

Clearly, the open-loop characteristics of the NAVION general aviation aircraft are satisfactory according to the flying qualities modal boundaries. This should not be surprising, since aircraft of this type rarely have augmented dynamics and are designed with the greatest simplicity in mind. The time history of the state response to a 10° impulsive disturbance in angle of attack can be seen in Figure 3.11. Examination of the state behavior shows a great deal of response in the state variables $\Delta\alpha$ and q near time $t = 0$. This behavior, which is not well resolved on the timescale of Figure 3.11, is indicative of the characteristic short-period

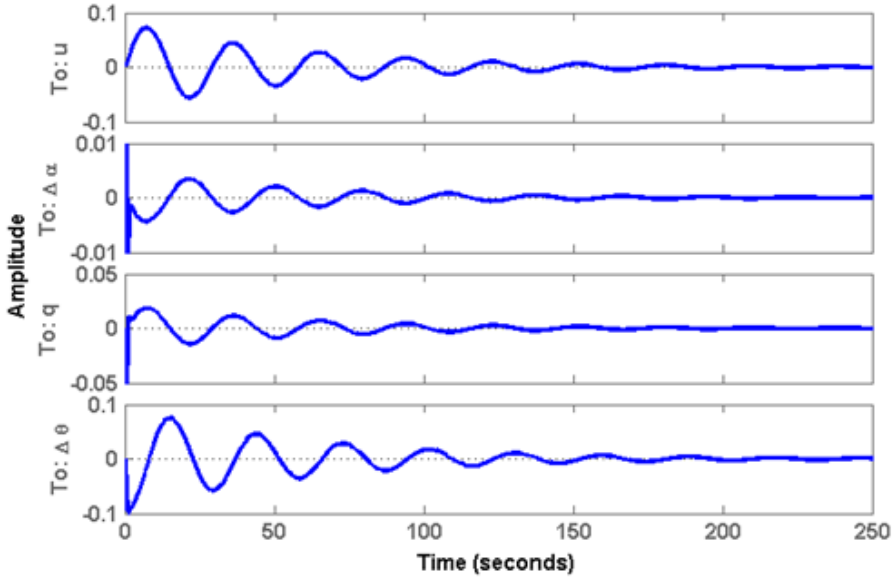

Figure 3.11: Time history of the state response of the system described by Eq. (3.112) when subjected to a 10° impulsive disturbance in angle of attack.

response in these variables. The time scales of the state response in u and $\Delta\theta$ is much longer, which is characteristic of the phugoid motions. The plotted motions have been identified by pilots as satisfactory—that is, they fulfill the modal constraints of the flying qualities requirements.

Now consider a perturbation to the state space system which describes the NAVION's dynamic response as given by

$$\mathbf{x} = \begin{bmatrix} u \\ \Delta\alpha \\ q \\ \Delta\theta \end{bmatrix}, \quad \mathbf{A} = \begin{bmatrix} -0.0453 & 0.0363 & \mathbf{0.1} & -0.1859 \\ -0.3717 & -2.0354 & 0.9723 & 0 \\ \mathbf{0.5097} & -7.0301 & -2.9767 & 0 \\ 0 & 0 & 1 & 0 \end{bmatrix} \tag{3.113}$$

This new altered system, which differs by only two terms in the matrix A (shown in red), is not necessarily justified by aerodynamic reasoning—that is, no particular design changes

were considered here that would elicit the alterations to the aerodynamic coefficients as presented. Rather, they were selected arbitrarily to develop a qualitative demonstration of the importance of eigenvectors in the modal decomposition. Reexamining the eigenvalue decomposition yields $\lambda_{1,2} = -2.5259 \pm 2.5735i$ and $\lambda_{3,4} = -0.0028 \pm 0.2284i$, and the eigenvalues are plotted as before in Figure 3.12.

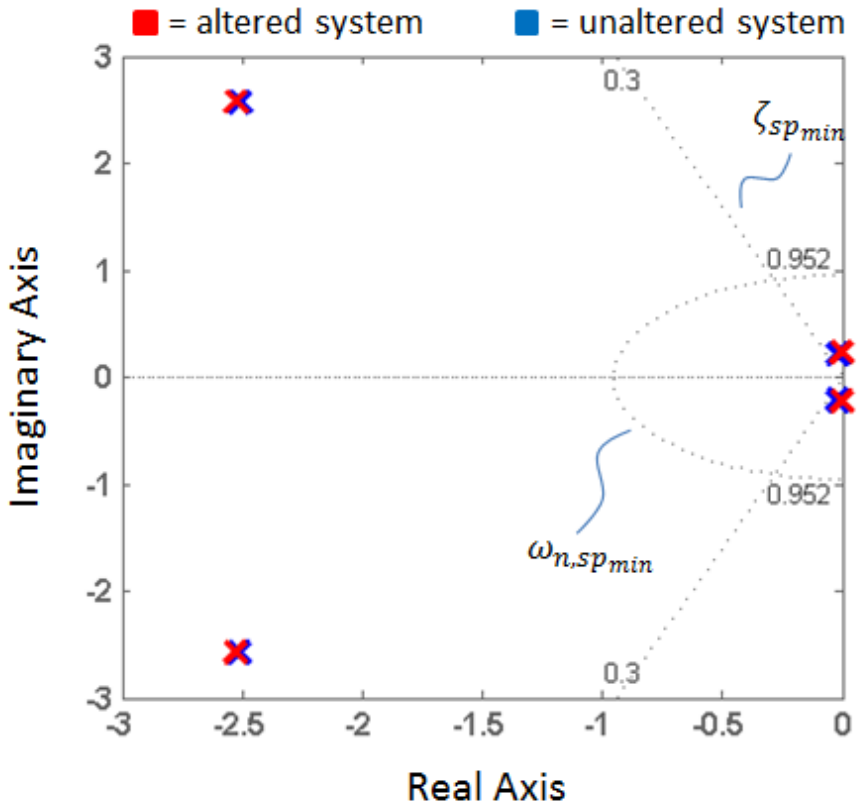

Figure 3.12: Open-loop eigenvalues of the unaltered and altered systems described by Eqs. (3.112) **and** (3.113)**, plotted on the complex plane. Dotted lines represent the MIL-STD-1797 flying qualities boundaries as labeled**

Note that the eigenvalues of the altered system (shown in red) have only been marginally perturbed, and the flying qualities requirements are still easily satisfied by the open-loop characteristics. What is not indicated by Figure 3.12 is the perturbation of the eigenvectors and the additional blending of modes caused by the alterations made in Eq. (3.113). Evi-

dence of this alteration does arise in the impulse response simulation, shown in Figure 3.13. Examination of the state response of the altered system as compared to the unaltered system

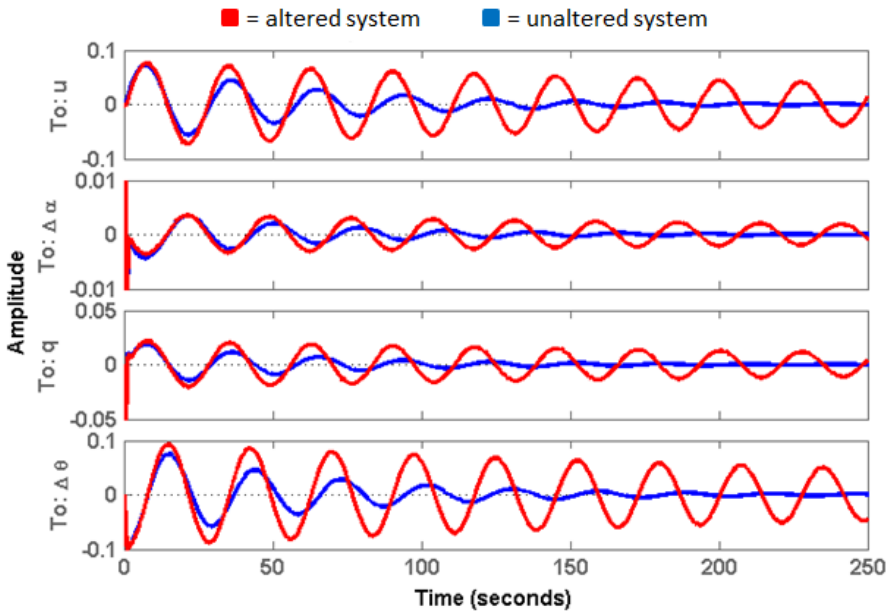

Figure 3.13: Time history of the state response of the unaltered and altered systems described by Eqs. (3.112) **and** (3.113) **when subjected to a** 10° **initial condition perturbation in angle of attack.**

reveals a marked difference in their behavior. While the results should only be interpreted as a qualitative example, Figure 3.13 reveals that tiny perturbations in the eigenvalue decomposition of an LTI system can result in drastic changes in the state behavior. The alterations made to the components of the A matrix were not large relative to the magnitude of neighboring terms—certainly it must be assumed that errors of similar relative magnitude are produced by aerodynamic analyses, particularly when conducted at a low level of fidelity. An expert on flying qualities may argue that the large changes only occurred in the phugoid mode, which is not of great concern during flying qualities evaluation. While this observation is justified in that the short-period mode remained largely unchanged and pilots can typically damp phugoid oscillations themselves, the example serves to demonstrate the limi-

tations of flying qualities requirements which do not observe the influence of the eigenvectors on the response. Without the existence of traditional modes of motion, the flying qualities requirements as currently defined leave a definitive avenue for large errors in projected pilot opinions.

Pole Placement and Modern Control

As aircraft complexity has increased, so has the methodologies for control law design. Classical control methods make use of transfer functions and root-locus formulations of the control design problem, and they operate very well when the system possesses only a single input. Control design techniques like pole placement, which is a control design strategy that seeks to place the closed-loop eigenvalues in predetermined locations, are easily carried out using classical control strategies. Unfortunately, classical methods do not directly apply to time-varying or nonlinear systems, and they do not handle Multiple Input Multiple Output (MIMO) systems well, either [71]. When handled using classical control methods, MIMO systems result in an unwieldy matrix of Single Input Single Output (SISO) transfer functions.

Modern computing has reduced the need for the Laplace transform and the associated frequency domain techniques of classical control. This is not a short-sighted statement to make claim that classical methods should be discarded, but rather a recognition that before the arrival of transistors and integrated circuits, the matrix computations required of state-space methods were impractical. Modern control theory consists predominately of techniques which operate in the time-domain and use the state-space representation of the system. The benefit of modern control theory lies in the ability to design high performance controllers for large systems with many inputs and significant cross-coupling behavior among the states. Pole placement is an easily achieved design strategy in the state space, and even the MIMO

case can be handled. There is an added difficulty when implementing a pole placement strategy with MIMO systems, however, since the approach produces an underdetermined set of equations, forcing the control designer to establish additional constraint or objective functions to provide unique solutions [72]. This may seem like a mild shortcoming, but the system performance and control energy required may depend completely on the designer's choice of objective function. For example, a poor choice of objective function could lead to the saturation of one system input, while another remains unused. This ambiguity is easily overcome during an *ad hoc* control system design where the result can be manually tuned, but design automation demands the satisfaction of performance constraints without human interaction.

Pole placement strategies are of interest to the conceptual aircraft designer due to their utility in fulfilling the modal constraints of the flying qualities requirements. The presence of multiple, coupled control effectors, would likely drive them towards state space approaches and modern control techniques, but would still leave the untended problem of uniqueness of solutions. Successful efforts have been made on several fronts to combat this dilemma by blending pole placement objectives with more conventional modern control strategies. Major efforts have focused on the modification of the linear quadratic regulator (LQR) design problem and LMI formulations of a constrained H_∞ control design problem. Algorithms have been developed which modify the LQR problem such that it can place the closed-loop poles in a vertical strip [73], in a hyperbola [74], in a disk [75], and with a prescribed damping and degree of stability [76]. Similarly, Chilali and Gahinet[77] developed a flexible approach to placing the closed-loop poles in convex regions of the complex plane using LMI's and H_∞ control. This latter approach is quite powerful due to its utilization of an LMI problem formulation. In fact, previous efforts have shown the utility of this approach for conceptual design feasibility studies with flying qualities considerations [45, 78].

The limitations of the regional LQR and H_∞ approaches are realized as the order of the system grows. Flying qualities constraints are defined using the classical decoupled airplane modes, typically involving only a few aircraft states and a single input. For example, the longitudinal dynamics are assumed to be decoupled from the lateral-directional dynamics and are typically composed of the states velocity (V), angle of attack (α), pitch rate (q), and pitch angle (θ) (other state formulations exist) [60]. The conventional longitudinal response of an aircraft is then further decomposed into a short-period mode involving α and q, and a phugoid mode involving V and θ. Each of these modes has separate constraints placed on the eigenvalue locations for satisfaction of the flying qualities requirements given in MIL-STD-1797. Utilizing either of the regional pole placement methods, that is the LQR or the H_∞, will uniformly enforce the pole placement constraint upon all of the poles, failing to address the differences between the short-period and phugoid mode requirements. This limitation, earlier referred to as the total pole placement limitation, is the fundamental reason that regional eigenvalue placement strategies cannot work for coupled systems.

The total pole placement problem is exacerbated for high performance aircraft that operate under neutral, or even negative, static stability since the short-period and phugoid modes grow more difficult to distinguish from one another [60]. Other complications include the recoupling of the equations of motion and the inclusion of aerodynamic cross-coupling due to the presence of nontraditional control effectors.

One final comment on the effectiveness of modal parameters and pole placement for achieving satisfactory flying qualities is worth making. Designing for modal performance does not provide the designer with any information regarding actuator behavior unless simulation is done. Dynamic behavior is, after all, a result of a disturbance which occurs in the time domain. As with many other design disciplines, a dynamic S&C analysis would require the selection of critical gust and disturbance cases for simulation, and actuator performance

and constraints would be assessed as a post-processing technique. Thus, a dynamic S&C analysis of this type would require a great deal of simulation and iteration before a feasibility assessment could be made. A superior strategy would be to include these dynamic scenarios as additional constraints to be considered during the control design process—an approach which would not require post-processing and control system redesigns.

3.5.1 A New Strategy

The new Variance Constrained Flying Qualities approach developed in the next chapter circumvents the challenges of pole placement by recasting the modal constraints as state variance constraints. By implementing state-by-state variance constraints, the recoupling of the equations of motion and the aerodynamic cross-coupling interactions can be achieved without the total pole placement limitation. Additionally, the Variance Constrained Flying Qualities approach is flight condition dependent, which allows for actuator performance constraints to influence the design of the controller and eliminate the need for post-processing and simulation.

Chapter 4

The Variance Constrained Flying Qualities Approach

The need for a new conceptual design dynamic S&C tool has been emphasized repeatedly in the preceding chapters. This chapter details the development of a new approach to performing closed-loop dynamic performance assessments in conceptual aircraft MDO. This method, called the Variance Constrained Flying Qualities (VCFQ) approach, is a novel means of assessing the dynamic performance of conceptual design configurations by using a state variance-based, flight condition dependent approximation to the military specification flying qualities requirements.

This chapter begins with a discussion of controllability and the controllability grammian, which are preliminaries to the definition of the deterministic state covariance matrix in Section 4.2. A comment on the relationship between the stochastic and deterministic interpretations of the state covariance matrix are also included in this section. In Section 4.3, the relationship between the control canonical form (CCF) state variances and the modal parameter based flying qualities guidelines is presented. Then, the flight condition dependent

transformation back to the physical states and their implementation into a state feedback control design strategy is detailed in Sections 4.4.2 and 4.5. Computational implementation of the VCFQ approach and the associated analyses is the subject of Chapter 5.

4.1 Controllability and the Controllability Grammian

For much of this chapter, we will work with linear systems of the form

$$\dot{x}(t) = A(t)x(t) + B(t)u(t), \tag{4.1}$$

or more specifically, its time invariant version

$$\dot{x}(t) = Ax(t) + Bu(t), \tag{4.2}$$

where $x \in \mathbb{R}^n$, $A \in \mathbb{R}^{n\times n}$, $B \in \mathbb{R}^{n\times m}$, and $u \in \mathbb{R}^m$. These systems will be referred to as the standard linear time varying (LTV) and the standard linear time invariant (LTI) systems, respectively. Solutions to these systems are usually discussed in introductory courses on linear systems, but a review can be found in almost any text on dynamics [60, 61, 68, 71]. Much of the nomenclature of this chapter is borrowed from Ref. [71], though this is by no means a unique source for the mathematical results contained herein. The solution to the standard LTI system is given by

$$x(t) = e^{A(t-t_0)}x(t_0) + \int_{t_0}^{t} e^{A(t-\sigma)}Bu(\sigma)d\sigma, \tag{4.3}$$

where t_0 is the initial time (typically taken as zero), e^{At} is the matrix exponential, and σ is an arbitrary variable of integration. There are several ways to compute the matrix

exponential e^{At}, including the inverse Laplace transform $\mathcal{L}^{-1}$, spectral decomposition of A, and the summation of inverse Laplace functions. These function can be computed as

$$e^{At} = \mathcal{L}^{-1}[s\mathbb{I} - A]^{-1} \tag{4.4}$$

$$e^{At} = Ee^{\Lambda t}E^{-1} \tag{4.5}$$

$$e^{At} = \sum_{i=0}^{n-1} A^i \alpha_i(t), \tag{4.6}$$

where E is a column matrix of eigenvectors of A, and Λ is a diagonal matrix of the eigenvalues of A such that the spectral decomposition of A is given by $A = E\Lambda E^{-1}$. The functions $\alpha_i(t)$ are given by the inverse Laplace transforms of

$$\begin{aligned}
\alpha_{n-1}(s) &= |s\mathbb{I} - A|^{-1} \\
\alpha_{n-2}(s) &= |s\mathbb{I} - A|^{-1}(s + a_{n-1}) \\
\alpha_{n-3}(s) &= |s\mathbb{I} - A|^{-1}(s^2 + a_{n-1}s + a_{n-2}) \\
&\vdots \\
\alpha_0(s) &= |s\mathbb{I} - A|^{-1}(s^{n-1} + a_{n-1}s^{n-2} + \cdots a_2 s + a_1)
\end{aligned} \tag{4.7}$$

where $|s\mathbb{I} - A|$ is the characteristic polynomial given by

$$|s\mathbb{I} - A| = s^n + a_{n-1}s^{n-1} + a_{n-2}s^{n-2} + \cdots a_1 s + a_0. \tag{4.8}$$

The controllability of a linear system is defined in Ref. [71] as follows:

Definition 4.1. A linear system of the form of Eq. (4.1) or (4.2) is said to be completely state controllable at time $t = t_0$ if there exists a time $t_f > t_0$ and a control $u(t)$, $t \in [t_0, t_f]$

such that the state is transferred from an arbitrary initial state $x(t_0) = x_0$ to an arbitrarily specified $x(t_f) = x_f$ in a finite time $t_f < \infty$.

Thus, controllability is the system's ability to 'move' itself from one arbitrary state to another in a finite amount of time. Controllability is a very general concept that applies to linear and nonlinear systems, but when a linear system is a local approximation of a nonlinear system, like in aircraft dynamics studies, it poses additional challenges. If the system leaves the region of linearity, or if the control effectors saturate (introducing a nonlinearity in the input channel), then the linear system no longer adequately describes the behavior of the nonlinear system. For the development of the S&C module for the VT High-Speed Aircraft MDO framework, controllability of a linearized model about an equilibrium is highly desirable, but the effects of control effector saturation make it an insufficient measure of feasibility for design optimization. A 'weakly' controllable system may be able to move to an arbitrary state in finite time, but it may not be able to do so under the dynamic constraints of the flying qualities requirements.

Nevertheless, for the time invariant system, controllability implies there exists an input $u(\sigma)$, $\sigma \in [t_0, t_f]$ such that

$$\int_{t_0}^{t_f} e^{A(t-\sigma)} B u(\sigma) d\sigma = \tilde{x}, \tag{4.9}$$

for some $t_f < \infty$ and for any value of $\tilde{x} \triangleq x_f - e^{A(t-t_0)} x(t_0)$. Since by definition, the choice of $\tilde{x}$ is arbitrary, the term $e^{A(t-\sigma)}B$ must be a basis of $\mathbb{R}^n$, and thus have linearly independent columns, on the interval $\sigma \in [t_0, t_f]$. Therefore, $e^{A(t-\sigma)}B$ must also satisfy the relation

$$\begin{aligned} X(t_f) &= \int_{t_0}^{t_f} e^{A(t_f-\sigma)} B B^T e^{A^T(t_f-\sigma)} d\sigma > 0 \\ &= \int_0^{t_f-t_0} e^{A\tau} B B^T e^{A^T\tau} d\tau > 0. \end{aligned} \tag{4.10}$$

The time derivative of Eq. (4.10) then yields

$$\begin{aligned} \dot{X}(t) &= X(t)A^T + AX(t) + BB^T \\ X(t_0) &= 0 \\ X(t_f) &> 0, \end{aligned} \tag{4.11}$$

which is quite similar to the Lyapnuov equality of Eq. (3.100). Since $e^{A\tau}BB^Te^{A^T\tau} \geq 0$, then $X(t_f)$ is necessarily positive semi-definite with $X(t_2) \geq X(t_1)$ for any $t_2 \geq t_1$. Futhermore, the existence of any $X(t_f) > 0$ implies that $X(\tilde{t}) > 0$ for every $\tilde{t} \geq t_f$, including the limiting case of $t_f = \infty$. Similarly, if $X(\infty)$ is not positive definite, then $X(\tilde{t})$ is also not positive definite for any $t_f < \infty$. These conclusions lead to the powerful result that an LTI system is completely state controllable if, and only if, there exists some $t_f < \infty$ such that

$$X(t_f) = \int_0^{t_f} e^{A\tau}BB^Te^{A^T\tau}d\tau > 0, \tag{4.12}$$

or equivalently from Eq. (4.11)

$$X(t_f) > 0, \quad \dot{X}(t_f) = X(t_f)A^T + AX(t_f) + BB^T. \tag{4.13}$$

By taking $t_f = \infty$, and defining $X(\infty) = X$, Eq. (4.12) can be written as the more convenient integral

$$X = \int_0^{\infty} e^{A\tau}BB^Te^{A^T\tau}d\tau, \tag{4.14}$$

which is known as the controllability grammian, and Eq. (4.13) becomes

$$X > 0, \quad 0 = XA^T + AX + BB^T. \tag{4.15}$$

Equation (4.15) provides a necessary and sufficient condition for the state controllability of the matrix pair (A, B). As it turns out, the controllability grammian bears a close relationship to the state covariance matrix discussed in the next section. The popular rank test for controllability also stems from the controllability grammian. Decomposing the matrix X using Eq. (4.6) leads to

$$X = [B \quad AB \dots A^{n-1}B]\Omega[B \quad AB \dots A^{n-1}B]^T, \tag{4.16}$$

where

$$\Omega = \int_0^\infty \begin{bmatrix} \alpha_0(t)\mathbb{I} \\ \alpha_1(t)\mathbb{I} \\ \vdots \\ \alpha_{n-1}(t)\mathbb{I} \end{bmatrix} [\alpha_0(t)\mathbb{I} \quad \alpha_1(t)\mathbb{I} \dots \alpha_{n-1}(t)\mathbb{I}]dt. \tag{4.17}$$

The matrix Ω is positive definite for any matrix A [71], and thus the rank test

$$\text{rank}[B \quad AB \cdots A^{n-1}B] = n \tag{4.18}$$

is sufficient to demonstrate that $X > 0$, and therefore, that the matrix pair (A, B) is controllable. The matrix $[B \quad AB \dots A^{n-1}B]$ is commonly called the controllability matrix, and the nomenclature

$$\mathcal{C}(M, N) = [M \quad MN \dots M^{n-1}N] \tag{4.19}$$

will be used to refer to the controllability matrix of the pair (M, N), where $M \in \mathbb{R}^{n\times n}$ and $N \in \mathbb{R}^{n\times m}$ are arbitrary matrices.

One final controllability result must be discussed, and that is its relationship to stability. During the discussion of Lyapnuov stability in Chapter 3, a candidate Lyapunov function

was posited in Eq. (3.96) as

$$V(x) = x^T P x, \quad P = P^T > 0. \tag{4.20}$$

If the candidate function was instead chosen to be

$$V(x) = x^T X^{-1} x, \quad X^{-1} > 0, \tag{4.21}$$

where X is the controllability grammian of Eq. (4.14), the resulting Lyapunov equality is

$$0 = XA^T + AX + BB^T. \tag{4.22}$$

Thus, the existence of a matrix $X > 0$ which satisfies the Lyapunov equality of Eq. (4.22) guarantees that the system $\dot{x} = Ax$ is asymptotically stable and that the pair (A, B) is controllable. A related statement can be made regarding the stability of the system from the associated Lyapunov inequalities:

$$\text{if } \exists X > 0, \quad \text{such that} \quad XA^T + AX < 0, \tag{4.23}$$

then the system $\dot{x} = Ax$ is asymptotically stable. Clearly, the controllability grammian has an intimate connection to many other aspects of the system dynamics, including the stability of the system, and as will be shown next, the state covariance matrix.

4.2 The Deterministic State Covariance

For generality, a slight variation of the standard LTI state space system is introduced in this section such that

$$\dot{x} = Ax + Bu + Dw, \tag{4.24}$$

where $x(t) \in \mathbb{R}^n$, $u(t) \in \mathbb{R}^m$, $w(t) \in \mathbb{R}^{n_w}$, and $D \in \mathbb{R}^{n \times n_w}$. The vector w is typically referred to as the exogenous input or the disturbance channel. Define $x(i,t) \in \mathbb{R}^n$ as the state response at time t due to the ith excitation event. There are three types of permissible excitation events to be defined, the first of which is an impulsive exogenous input such that

$$w_i(t) = \mathrm{w}_i\delta(t), \quad w_j(t) = 0, \quad i \neq j, \quad i = 1 \ldots n_w, \quad u(t) = 0, \quad x(0) = 0. \tag{4.25}$$

The second permissible excitation event is the impulsive actuator input event given by

$$u_i(t) = \mathrm{u}_i\delta(t), \quad u_j(t) = 0, \quad i \neq j, \quad i = 1 \ldots m, \quad w(t) = 0, \quad x(0) = 0. \tag{4.26}$$

The third permissible excitation event is the initial condition response given by

$$x_i(0) = x_{i_0}, \quad x_j(0) = 0, \quad i \neq j, \quad i = 1 \ldots n, \quad u(t) = 0, \quad w(t) = 0. \tag{4.27}$$

Note that this last excitation event is a special case of the first, achieved by selecting $w = \mathbb{I}_n$ and D to be a the diagonal matrix composed of the elements of an initial condition $x(0)$, such that $D = \mathrm{diag}[x_1(0), x_2(0), \ldots, x_n(0)]$. The ith impulsive excitation event would then be equivalent to the initial condition response from the ith term of the initial condition vector $x(0)$.

The deterministic state covariance matrix for an LTI system is defined as

$$X \triangleq \sum_{i=1}^{r} \int_0^\infty x(i,t)x(i,t)^T dt, \tag{4.28}$$

where r is the number of excitation events, and $x(i,t)$ corresponds to the response to the ith permissible excitation event. The deterministic state covariance matrix is also a solution to the Lyapnuov equality

$$0 = XA^T + AX + D\mathcal{W}D^T, \quad \text{where} \quad \mathcal{W} = \text{diag}[\text{w}_1^2 \ldots \text{w}_{n_w}^2] > 0, \tag{4.29}$$

the proof of which can be found in Ref. [68]. If the excitation events occur through the input u rather than w, the Lyapunov equality becomes

$$0 = XA^T + AX + B\mathcal{U}B^T, \quad \text{where} \quad \mathcal{U} = \text{diag}[\text{u}_1^2 \ldots \text{u}_m^2] > 0, \tag{4.30}$$

and likewise, for the initial condition excitation events

$$0 = XA^T + AX + X_0, \quad \text{where} \quad X_0 = \text{diag}[x_1(0)^2 \ldots x_n(0)^2] > 0. \tag{4.31}$$

The preceding Lyapunov equalities lead to an important observation regarding the controllability grammian of Eq. (4.14). For the special case of unit impulse disturbances, that is $\mathcal{W} = \mathbb{I}$ and $\mathcal{U} = \mathbb{I}$, solutions of Eqs. (4.29) and (4.30) are exactly the controllability grammian for the matrix pairs (A, D) and (A, B), respectively. In Section 4.1, the controllability grammian was explored along with the implications of its existence and positive definiteness. The inheritance of these properties by the deterministic state covariance matrix is an important part of its great utility.

The existence of a matrix $X > 0$ which is a solution to Eqs. (4.29), (4.30), or (4.31)

guarantees that:

i. The system $\dot{x} = Ax$ is asymptotically stable.
ii. All of the eigenvalues of A lie in the open left half plane.
iii. X is the deterministic state covariance.
iv. Matrix pairs (A, D) or (A, B) are controllable in Eq. (4.29) or (4.30), respectively.

In addition to being an indicator of stability and controllability, the deterministic state covariance matrix also contains significant information regarding system performance. The diagonal elements of X represent the state variances, σ_i, of each of the n states such that

$$\sigma_i^{1/2} = [X_{ii}]^{1/2} = \|x_i\|_{\mathcal{L}_2} = \left[\sum_{i=1}^{n} \int_0^\infty x_i^2(i,t)dt\right]^{1/2}, \tag{4.32}$$

where $i = 1 \ldots n$. The state variances are equivalent to the $\mathcal{L}_2$-norm of the state response to the specified excitation event [71]. Note the similarity of Eq. (4.32) with the more familiar definition of the root-mean-square (RMS) response of a state, given by

$$\|x_i\|_{\text{RMS}} = \left[\frac{1}{T}\int_0^T x_i^2(t)dt\right]^{1/2}. \tag{4.33}$$

Clearly, the deterministic state covariance matrix has strong implications on system stability and performance. Skelton et al. [71], develop many relationships between the deterministic state covariance matrix and popular metrics for performance including $\mathcal{L}_2$, H_2, and H_∞ norms of the system response. They also discuss and develop measures for system robustness to account for modeling and parameter uncertainties. These results are not used directly in the development of the present S&C module and are not repeated here. It is noted, however, that these relationships suggest that many powerful opportunities remain for

exploiting the second-order information available within the deterministic state covariance matrix—a topic which will be addressed in the final chapter of this thesis.

A Note on the Stochastic State Covariance

To most individuals with previous exposure to covariance analysis, the absence of an expectation operator $\mathcal{E}[\cdot]$ in the definition of the deterministic state covariance matrix in Eq. (4.28) is probably surprising. A more familiar definition for the state covariance might be

$$X_s(t) \triangleq \mathcal{E}\left[x(t)x(t)^T\right]. \tag{4.34}$$

Under a stochastic interpretation, the excitation events would no longer be impulse functions, but instead would become white noise processes. A thorough comparison of the stochastic and the deterministic interpretations of the state covariance matrix is given in Ref. [71]. In particular, the authors define the conditions under which the two are equal, $X = X_s$, as well as an analysis of their differences. While the deterministic case is demonstrated to be a 'friendlier' interpretation mathematically, what is likely to be the most important result is the proof that the deterministic problem is conservative with respect to the stochastic problem:

$$X(\infty) \geq X_s(\infty). \tag{4.35}$$

In the coming sections on covariance controllers, the term 'deterministic' is dropped due to the applicability of the mathematics to both deterministic and stochastic interpretations of the excitations. The interested reader is referred to Refs. [71] and [68] for further analysis of the two approaches.

4.3 State Variances and the Characteristic Polynomial

Covariance controllers are controllers which seek to assign a given state covariance matrix to a system. The first publications on the matter appeared around 1987 by Skelton and others [79, 80], and continue to see development in the literature for both discrete and continuous time sytems [81, 82]. The intent of covariance controllers is to address the fundamental flaw of eigenvalue-based (pole placement) and optimal control methods, which are typically only capable of making performance guarantees on the state vector as a whole. This point was demonstrated in the example problem in Chapter 3. Using those methods, very little information can be ascertained about the transient behavior of individual states. As pointed out by Skelton [68], this could result in one state with such large transients that the linear system is no longer valid. The fundamental idea of covariance controllers is to ensure each individual state exhibits good behavior.

Of the more important results in the covariance control literature is the relationship between state variances and the characteristic polynomial coefficients when there is a single input to the system and it is in Control Canonical Form (CCF) [71, 81]. This unique relationship between the n values of the CCF state variances, $\hat{\sigma}_i$, and the n values of the characteristic polynomial coefficients, a_i, is fundamental to the development of the Variance Constrained Flying Qualities approach herein.

To demonstrate this important result, we return to the generic LTI system with the modification that $w \in \mathbb{R}^1$ is now the single input such that

$$\dot{x} = Ax + Dw, \tag{4.36}$$

where $x \in \mathbb{R}^n$, $A \in \mathbb{R}^{n \times n}$, and $D \in \mathbb{R}^{n \times 1}$. This LTI system must then be converted to

control canonical form using the coordinate transformation

$$T_{\text{ccf}} = \begin{bmatrix} D & AD & A^2D & \cdots & A^{n-1}D \end{bmatrix} \begin{bmatrix} a_2 & a_3 & \cdots & a_n & 1 \\ a_3 & a_4 & \cdots & 1 & 0 \\ \vdots & \vdots & \ddots & \vdots & \vdots \\ a_n & 1 & \cdots & 0 & 0 \\ 1 & 0 & \cdots & 0 & 0 \end{bmatrix}, \tag{4.37}$$

where the $a_1 \ldots a_n$ terms are the characteristic polynomial coefficients of A according to

$$\lambda^n + a_n\lambda^n - 1 + \cdots + a_2\lambda + a_1 = 0. \tag{4.38}$$

Note that the first bracketed term on the right hand side of Eq. (4.37) is the controllability matrix $\mathcal{C}(A, D)$. Any single input LTI system of the form of Eq. (4.36) can be placed in Control Canonical Form provided that the matrix pair (A, D) is controllable [72]. Application of Eq. (4.37) to the original system results in

$$\dot{\hat{x}} = \hat{A}\hat{x} + \hat{D}w \tag{4.39}$$

where

$$\hat{x} = T_{\text{ccf}}^{-1}x \tag{4.40}$$

$$\hat{A} = T_{\text{ccf}}^{-1}AT_{\text{ccf}} = \begin{bmatrix} \mathbf{0} & & \mathbb{I}_n \\ & -a^T & \end{bmatrix} \tag{4.41}$$

$$\hat{D} = T_{\text{ccf}}^{-1}D = \begin{bmatrix} \mathbf{0} \\ 1 \end{bmatrix} \tag{4.42}$$

$$a^T = \begin{bmatrix} a_1 & a_2 & \cdots & a_n \end{bmatrix} \tag{4.43}$$

and the boldface **0** is representative of a matrix (or vector) of zeros of appropriate size. The utility of the CCF system is the direct presence of the characteristic polynomial coefficients, a_i, in the system matrix $\hat{A}$. Recall that the characteristic polynomial of a matrix is invariant under a congruence transformation [68].

Application of the control canonical form transformation T_{ccf}, to the Lyapunov equality of Eq. (4.29) yields

$$0 = \hat{X}\hat{A}^T + \hat{A}\hat{X} + \hat{D}\hat{D}^T, \tag{4.44}$$

where $\hat{X}$ is the CCF deterministic state covariance matrix. Also define

$$\hat{\sigma}_i \triangleq \hat{X}_{ii} \tag{4.45}$$

as the CCF state variances. A relationship between X and $\hat{X}$ is easily seen by returning to the definition of the deterministic state covariance as

$$\begin{aligned} X &\triangleq \sum_{i=1}^{r} \int_0^\infty x(i,t)x^T(i,t)dt \\ &= \sum_{i=1}^{r} \int_0^\infty T_{\text{ccf}}\hat{x}(i,t)\left(T_{\text{ccf}}\hat{x}(i,t)\right)^T dt \\ &= \sum_{i=1}^{r} \int_0^\infty T_{\text{ccf}}\hat{x}(i,t)\hat{x}^T(i,t)T_{\text{ccf}}^T dt \\ &= T_{\text{ccf}}\left(\sum_{i=1}^{r} \int_0^\infty \hat{x}(i,t)\hat{x}^T(i,t)dt\right)T_{\text{ccf}}^T \\ &= T_{\text{ccf}}\hat{X}T_{\text{ccf}}^T. \end{aligned} \tag{4.46}$$

This last relationship will prove useful in the next section.

As shown in Refs. [71] and [81], all solutions $\hat{X} > 0$ to the CCF Lyapunov equality in

Eq. (4.44) have a special 'Signature Hankel' structure of the form

$$\hat{X} = \begin{bmatrix} \hat{\sigma}_1 & 0 & -\hat{\sigma}_2 & 0 & \hat{\sigma}_3 & 0 & -\hat{\sigma}_4 & & \\ 0 & \hat{\sigma}_2 & 0 & -\hat{\sigma}_3 & 0 & \hat{\sigma}_4 & 0 & & \\ -\hat{\sigma}_2 & 0 & \hat{\sigma}_3 & 0 & -\hat{\sigma}_4 & 0 & \hat{\sigma}_5 & & \\ 0 & -\hat{\sigma}_3 & 0 & \hat{\sigma}_4 & 0 & -\hat{\sigma}_5 & 0 & & \\ \hat{\sigma}_3 & 0 & -\hat{\sigma}_4 & 0 & \hat{\sigma}_5 & 0 & -\hat{\sigma}_6 & & \\ 0 & \hat{\sigma}_4 & 0 & -\hat{\sigma}_5 & 0 & \hat{\sigma}_6 & 0 & & \\ -\hat{\sigma}_4 & 0 & \hat{\sigma}_5 & 0 & -\hat{\sigma}_6 & 0 & \hat{\sigma}_7 & & \\ & & & & & & & \ddots & \\ & & & & & & & & \hat{\sigma}_n \end{bmatrix}. \tag{4.47}$$

Selecting the candidate Lyapunov function as $V(\hat{x}(t)) = \hat{x}\hat{X}^{-1}\hat{x}$, the special structure of $\hat{X}$ can then be exploited to arrive at the relationship between the $\hat{\sigma}_i$ CCF state variances and the a_i characteristic polynomial coefficients. The results of this selection are reproduced herein, and the proof can be found in Ref. [71].

First, the odd and even coefficients of the characteristic polynomial are collected in the vectors

$$a_o \triangleq \begin{bmatrix} a_1 \\ a_3 \\ a_5 \\ \vdots \end{bmatrix}, \quad a_e \triangleq \begin{bmatrix} a_2 \\ a_4 \\ a_6 \\ \vdots \end{bmatrix}, \tag{4.48}$$

such that $a_o \in \mathbb{R}^{n_o}$ and $a_e \in \mathbb{R}^{n_e}$. If n is even, then $n_o = n_e = n/2$. If n is odd, then $n_o = n_e + 1$ and $n_e = (n-1)/2$. Next, $\hat{X}$ is decomposed into two Hankel matrices composed

of the $\hat{\sigma}_i$ as

$$\hat{X}_o = \begin{bmatrix} \hat{\sigma}_1 & -\hat{\sigma}_2 & \hat{\sigma}_3 & -\hat{\sigma}_4 & & \\ -\hat{\sigma}_2 & \hat{\sigma}_3 & -\hat{\sigma}_4 & \hat{\sigma}_5 & & \\ \hat{\sigma}_3 & -\hat{\sigma}_4 & \hat{\sigma}_5 & -\hat{\sigma}_6 & & \\ -\hat{\sigma}_4 & \hat{\sigma}_5 & -\hat{\sigma}_6 & \hat{\sigma}_7 & & \\ & & & & \ddots & \\ & & & & & \hat{\sigma}_n \end{bmatrix} \tag{4.49}$$

$$\hat{X}_e = \begin{bmatrix} \hat{\sigma}_2 & -\hat{\sigma}_3 & \hat{\sigma}_4 & -\hat{\sigma}_5 & & \\ -\hat{\sigma}_3 & \hat{\sigma}_4 & -\hat{\sigma}_5 & \hat{\sigma}_6 & & \\ \hat{\sigma}_4 & -\hat{\sigma}_5 & \hat{\sigma}_6 & -\hat{\sigma}_7 & & \\ -\hat{\sigma}_5 & \hat{\sigma}_6 & -\hat{\sigma}_7 & \hat{\sigma}_8 & & \\ & & & & \ddots & \\ & & & & & \hat{\sigma}_n \end{bmatrix} \tag{4.50}$$

where $\hat{X}_o \in \mathbb{R}^{n_o \times n_o}$ and $\hat{X}_e \in \mathbb{R}^{n_e \times n_e}$. For a positive definite matrix, $\hat{X}$, which is a solution to the Lyapunov equality in Eq. (4.44), and is structured as in Eq. (4.47), the coefficients of the characteristic polynomial are given by:

for $n =$ even

$$a_o = \hat{X}_o^{-1}\hat{X}_e\mathbf{1}, \qquad a_e = \frac{1}{2}\hat{X}_e^{-1}\mathbf{1}, \qquad \mathbf{1} \triangleq \begin{bmatrix} \mathbf{0} \\ 1 \end{bmatrix}, \tag{4.51}$$

or for $n =$ odd

$$a_o = \frac{1}{2}\hat{X}_o^{-1}\mathbf{1}, \qquad a_e = \hat{X}_e^{-1}\begin{bmatrix} \mathbf{0} & \mathbb{I}_{n_e} \end{bmatrix}\hat{X}_o\mathbf{1}, \tag{4.52}$$

where $\mathbb{I}_{n_e} \in \mathbb{R}^{n_e \times n_e}$ is the identity matrix, and $\mathbf{0}$ is a matrix of zeros of appropriate dimension.

Equations (4.51) and (4.52) provide the unique mathematical relationship between the n

values of $\hat{\sigma}_i$ and the n values of a_i for a single input system in the control canonical form. The relationship can be symbolically expanded for a given value of n, and indeed, this is done by Skelton, et al. [71], for $n \leq 6$. This powerful result effectively maps the CCF state variances to the characteristic polynomial—establishing a mathematical link between individual state performance and the modal parameters. Of even greater interest to the VCFQ approach is the inverse mapping from a given set of modal parameters (and therefore characteristic polynomial coefficients) to the CCF state variances. This inverse mapping is achieved in Ref. [71] by collecting the results of Eqs (4.51) and (4.52) into matrices as

$$\begin{bmatrix} X_e a_e - [\mathbf{0} \quad \mathbb{I}_{n_e}] X_o \mathbf{1} \\ X_o a_o \end{bmatrix} = \begin{bmatrix} \mathbf{0} \\ \frac{1}{2}\mathbf{1} \end{bmatrix} \tag{4.53}$$

and

$$\begin{bmatrix} X_o a_o - X_e \mathbf{1} \\ X_e a_e \end{bmatrix} = \begin{bmatrix} \mathbf{0} \\ \frac{1}{2}\mathbf{1} \end{bmatrix}, \tag{4.54}$$

respectively. The components X_o and X_e are both functions of the $\hat{\sigma}_i$, $i = 1 \ldots n$, CCF state variances, and thus the above matrix relations can be rewritten in terms of the vector

$$\hat{\sigma}^T = \begin{bmatrix} \hat{\sigma}_1 & \hat{\sigma}_2 & \hat{\sigma}_3 & \cdots & \hat{\sigma}_n \end{bmatrix}. \tag{4.55}$$

Rearranging the elements of Eqs. (4.53) and (4.54) and collecting terms results in the expressions

$$\Lambda_o \hat{\sigma} = \begin{bmatrix} \mathbf{0} \\ \frac{1}{2}\mathbf{1} \end{bmatrix} \tag{4.56}$$

and

$$\Lambda_e \hat{\sigma} = \begin{bmatrix} \mathbf{0} \\ \frac{1}{2}\mathbf{1} \end{bmatrix}, \tag{4.57}$$

where $\Lambda_o \in \mathbb{R}^{n \times n}$ and $\Lambda_e \in \mathbb{R}^{n \times n}$ have a special structure. Both Λ_o and Λ_e are composed of

'signature Toeplitz' matrices according to

$$\Lambda_o \triangleq \begin{bmatrix} \Lambda_{eo} \\ \Lambda_{oo} \end{bmatrix}, \quad \Lambda_e \triangleq \begin{bmatrix} \Lambda_{oe} \\ \Lambda_{ee} \end{bmatrix} \tag{4.58}$$

where

$$\Lambda_{eo} \in \mathbb{R}^{\frac{n-1}{2} \times n}, \Lambda_{oo} \in \mathbb{R}^{\frac{n+1}{2} \times n},$$

$$\Lambda_{eo} = \begin{bmatrix} 0 & \cdot & \cdot & \cdot & & \cdot & \cdot & & 0 & \cdots & 0 \\ \vdots & \ddots & \ddots & \ddots & & & \ddots & \ddots & & & \vdots \\ \vdots & & \ddots & \tilde{a}_2 & \tilde{a}_4 & \tilde{a}_6 & \cdots & \tilde{a}_{n-1} & \tilde{\mathbf{1}} & & \vdots \\ \vdots & & & \ddots & \ddots & \ddots & \ddots & & \ddots & \ddots & 0 \\ \vdots & & \cdots & & 0 & \cdot & \cdot & \cdot & & \cdot & \cdot \end{bmatrix}, \tag{4.59}$$

$$\Lambda_{oo} = \begin{bmatrix} \cdot & \cdot & \cdot & & \cdot & & 0 & \cdots & & 0 \\ 0 & \ddots & \ddots & \ddots & & \ddots & & \ddots & & \vdots \\ \vdots & \ddots & \tilde{a}_1 & \tilde{a}_3 & \tilde{a}_5 & \cdots & \tilde{a}_n & & \ddots & \vdots \\ \vdots & & \ddots & \ddots & \ddots & \ddots & & \ddots & & 0 \\ 0 & & \cdots & 0 & \cdot & \cdot & \cdot & & & \cdot \end{bmatrix} \tag{4.60}$$

and

$$\Lambda_{oe} \in \mathbb{R}^{\frac{n}{2} \times n}, \Lambda_{ee} \in \mathbb{R}^{\frac{n}{2} \times n},$$

$$\Lambda_{oe} = \begin{bmatrix} \cdot & \cdot & \cdot & \cdot & & \cdot & \cdot & & 0 & \cdots & 0 \\ 0 & \ddots & \ddots & \ddots & & & \ddots & \ddots & & \ddots & \vdots \\ \vdots & \ddots & \tilde{a}_1 & \tilde{a}_3 & \tilde{a}_5 & \cdots & & \tilde{a}_{n-1} & \tilde{\mathbf{1}} & & \vdots \\ \vdots & & \ddots & \ddots & \ddots & \ddots & & & \ddots & \ddots & 0 \\ 0 & & \cdots & 0 & \cdot & \cdot & \cdot & & & \cdot & \cdot \end{bmatrix}, \tag{4.61}$$

$$\Lambda_{oo} = \begin{bmatrix} 0 & \cdot & \cdot & \cdot & & \cdot & & 0 & \cdots & 0 \\ \vdots & \ddots & \ddots & \ddots & \ddots & & \ddots & & \ddots & \vdots \\ \vdots & & \tilde{a}_2 & \tilde{a}_4 & \tilde{a}_6 & \cdots & \tilde{a}_n & & \vdots & \\ \vdots & & & \ddots & \ddots & \ddots & \ddots & & \ddots & 0 \\ 0 & & \cdots & & 0 & \cdot & \cdot & \cdot & & \cdot \end{bmatrix} \tag{4.62}$$

where the diagonal dotted lines denote elements of a vector arranged diagonally, and the vectors $\tilde{a}_i$ are given by

$$\tilde{a}_i \triangleq \bar{\mathbf{1}} a_i, \quad i = \begin{cases} 1, 5, 9, 13, 17, \cdots \\ 2, 6, 10, 14, 18, \cdots \end{cases} \quad i \leq n \tag{4.63}$$

$$\tilde{a}_j \triangleq -\mathbf{1} a_j, \quad j = \begin{cases} 3, 7, 11, 15, \cdots \\ 4, 8, 12, 16, \cdots \end{cases} \quad j \leq n \tag{4.64}$$

$$\tag{4.65}$$

where

$$\bar{\mathbf{1}}^T \triangleq \begin{bmatrix} 1 & -1 & 1 & -1 & 1 & -1 & \cdots \end{bmatrix} \tag{4.66}$$

$$\tilde{\mathbf{1}} \triangleq (-1)^{n_e} \bar{\mathbf{1}}. \tag{4.67}$$

Finally, we arrive at the mapping from characteristic polynomial coefficients to the CCF

state variances:

for $n = \text{odd}$

$$\hat{\sigma} = \frac{1}{2}\Lambda_o^{-1}\mathbf{1}, \qquad \Lambda_o \triangleq \begin{bmatrix} \Lambda_{eo} \\ \Lambda_{oo} \end{bmatrix}, \tag{4.68}$$

for $n = \text{even}$

$$\hat{\sigma} = \frac{1}{2}\Lambda_e^{-1}\mathbf{1}, \qquad \Lambda_e \triangleq \begin{bmatrix} \Lambda_{oe} \\ \Lambda_{ee} \end{bmatrix}. \tag{4.69}$$

The importance of these relationships cannot be overstated. Equations (4.68) and (4.69) describe the unique relationship between the n coefficients of the characteristic polynomial and the n CCF state variances. This explicit connection between the characteristic polynomial, which is directly related to the modal parameters, and the CCF state variances holds the key to developing an approximation to the modal parameter based flying qualities requirements of the MIL-STD-1797. As before, for a given value of n, the values of $\hat{\sigma}_i$ can be written directly in terms of the a_i coefficients, the results of which can be found in [71] for $n \leq 6$. These results are repeated in Table 4.1 for $n \leq 4$ (the largest system utilized in this study).

Table 4.1: Algebraic relationship between a_i and $\hat{\sigma}_i$

	$n = 2$	$n = 3$	$n = 4$
$\hat{\sigma}_1$	$\frac{1}{2a_1a_2}$	$\frac{a_3}{2\Omega_3 a_1}$	$\frac{a_3a_4-a_2}{2\Omega_4 a_1}$
$\hat{\sigma}_2$	$\frac{1}{2a_2}$	$\frac{1}{2\Omega_3}$	$\frac{a_4}{2\Omega_4}$
$\hat{\sigma}_3$		$\frac{a_2}{2\Omega_3}$	$\frac{a_2}{2\Omega_4}$
$\hat{\sigma}_4$			$\frac{a_2a_3-a_1a_4}{2\Omega_4}$

$\Omega_3 = a_2a_3 - a_1$

$\Omega_4 = a_2(a_3a_4 - a_2) - a_1a_4^2$

4.4 Flying Qualities to State Variance Bounds

Much has been said about the merits of covariance based control methods and the additional performance information ascertainable from second-order information. However, there has never been, to this author's knowledge, any exploration of the use of state variances as a flying qualities metric. It is easy to qualitatively argue that state variances may offer a physically more realistic metric of what the pilots feel than does modal information—after all, pilots don't feel eigenvalues and damping ratios, but they do feel states and state rates. The best strategy for investigating state variances as a viable metric for flying qualities assessment would be to revisit the original data sources (Cooper-Harper ratings from pilots amassed over many flights and many years) and search for correlations between pilot ratings and the state covariance matrix. That task would be monumental, requiring both a concerted effort to gather the data and to correlate it. Results of such an effort would be of great utility, however, in that it would immediately facilitate state-specific constraints and multiple input control strategies in the conceptual design process.

An alternative strategy for predicting satisfactory state variances would be to leverage the existing modal parameter based flying qualities requirements. A very large number of man-hours were surely invested in the development of these constraints, and yet they still only represent an approximation to what a pilot believes to be satisfactory flying qualities. The only true metric of flying qualities is to place a pilot in the operational aircraft. Fortunately, early conceptual design studies do not require a high level of certainty in flying qualities predictions. It is in this spirit that the Variance Constrained Flying Qualities approach is introduced here as an approximation of the modal parameter based flying qualities constraints of the MIL-STD-1797. The VCFQ approach is intended to fulfill the needs of early conceptual designers and the current trends of MIMO systems and modern control design. The approach will also simultaneously facilitate the inclusion of dynamic performance

constraints in the S&C module for the VT High-Speed Aircraft MDO framework.

4.4.1 Variance Constrained Flying Qualities

The main thesis and major assumptions of the VCFQ method are now introduced: Given a linear aircraft model, the associated set of modal constraints on the flying qualities which bound a region of the complex plane, and a disturbance vector D, the results of Section 4.3 can be used to map this region to the equivalent CCF state variances $\hat{\sigma}_i$, $i = 1 \ldots n$. Knowledge of the desired eigenvector structure of the configuration will then allow for the CCF state variances to be mapped into the physical state variances, σ_i, $i = 1 \ldots n$. An aircraft which exhibits state variances which are bounded above by $\sigma_{i_{\max}}$, where $\sigma_{i_{\max}}$ is the maximum state variance of each state within the region, will, *as a reasonable approximation suitable for conceptual design feasibility studies*, exhibit satisfactory flying qualities.

There are two important points worth noting at this time regarding the approximation of the modal constraints. First, the satisfaction of the flying qualities guidelines is approximate in the sense that there may be combinations of state variances, (σ_1, σ_2, $\ldots$ σ_n), that satisfy constraints on the individual terms,

$$\sigma_i < \sigma_{i_{\max}}, \quad i = 1 \ldots n, \tag{4.70}$$

and yet do not correspond to a pole location within the acceptable domain. Physically, this is a result of the fact that the variances of each state may peak at different eigenvalue locations within the complex plane. This may be perceived as a shortcoming, but since the modal guidelines are themselves an approximation to the state behavior which pilots felt were 'satisfactory', it is not believed to render this method invalid for the purposes of conceptual design feasibility studies.

The second approximation worth noting is attributed to the inherently coupled, nonlinear relationship between the CCF state variances and the eigenvalue locations. While it is algebraically trivial to compute the CCF state variances from a given characteristic polynomial, it is less straight forward to analytically resolve eigenvalue boundaries. To illustrate this dilemma, consider the case of $n = 2$ with the characteristic polynomial

$$\begin{aligned} s^2 + a_2 s + a_1 = 0 \quad &\Longleftrightarrow \quad s^2 + 2\zeta\omega_n s + \omega_n^2 = 0 \\ \Longrightarrow \quad \begin{bmatrix} a_1 \\ a_2 \end{bmatrix} &= \begin{bmatrix} \omega_n^2 \\ 2\zeta\omega_n \end{bmatrix}. \end{aligned} \tag{4.71}$$

where ζ and ω_n are the damping ratio and natural frequency, respectively. It is apparent that while a_1 is strictly a function of ω_n, a_2 depends on both ζ and ω_n. Thus, for a constant damping ratio, the value of a_2 is implicitly a nonlinear function of a_1 as

$$a_2 = 2\zeta\sqrt{a_1}. \tag{4.72}$$

This complication stems from the fact that the characteristic polynomial is related to the eigenvalues of a matrix in a complex, nonlinear manner. Unfortunately, this complication is transferred to the CCF state variances. From Table 4.1 with $n = 2$, the analytic relationship between $\hat{\sigma}$ and a is

$$\hat{\sigma} = \begin{bmatrix} \frac{1}{2a_1a_2} \\ \frac{1}{2a_2} \end{bmatrix}. \tag{4.73}$$

Substituting in the ζ and ω_n relationships of Eq. (4.71) gives

$$\hat{\sigma} = \begin{bmatrix} \frac{1}{2(\omega_n^2)(2\zeta\omega_n)} \\ \frac{1}{2(2\zeta\omega_n)} \end{bmatrix} = \begin{bmatrix} \frac{1}{4\zeta\omega_n^3} \\ \frac{1}{4\zeta\omega_n} \end{bmatrix}. \tag{4.74}$$

Again, for a fixed value of ζ, $\hat{\sigma}_1$ and $\hat{\sigma}_2$ are inherently coupled by the natural frequency.

As the problem dimension grows, the connection between the characteristic polynomial and the eigenvalues grows more complex, thus the interdependence of the CCF state variances also grows more complex. The real and imaginary components of an eigenvalue compose an orthonormal basis for the complex space $\mathbb{C}^2$. Translation of eigenvalues into CCF state variances through the characteristic polynomial and Eq. (4.69) results in an effective coordinate system which is no longer orthogonal (the term coordinate system is used loosely, referring to the fact than an ordered pair $(\hat{\sigma}_1, \hat{\sigma}_2)$ uniquely defines the real and imaginary components of the eigenvalues). This is an unavoidable consequence of spectral decomposition and provides additional motive to directly investigate pilot Cooper-Harper ratings for state covariance correlations from the onset.

The complications just discussed do not present a problem in the direct computation of the maximum CCF state variances, since a given set of eigenvalue locations uniquely determines $\hat{\sigma}_1 \ldots \hat{\sigma}_n$. They do become influential, however, when inequality constraints are introduced. A bound on an eigenvalue location, such as $\gamma_1 < \mathrm{Re}[\lambda] < \gamma_2$, where γ_1 and γ_2 are arbitrary scalars, cannot be directly communicated into an equivalent set of *uncoupled* inequality constraints on the CCF state variances (and therefore the physical state variances). The coupling of the inequality constraints poses a challenge for the formulation of linear inequalities and prevents the LMI formulation of Section 4.5 from being strictly equivalent to the constraints on the modal parameters. Nevertheless, it is still tractable to compute maximum state variances within a modal region and enforce these upper bounds as in Eq. (4.70).

4.4.2 Computing the State Variances of the Physical States

Until now, reference has been continually made to computations involving the state variances of the CCF system. Section 4.3 showed, for a given single input system, how to compute the CCF transformation and the CCF state variances. However, it is the physical state variances within the acceptable flying qualities modal region which are actually of interest. This section details two critical concepts in the VCFQ approach: the selection of the disturbance vector D, and the construction of the transformation from the CCF system to the physical system using knowledge of the desired eigenvectors.

The Disturbance, D

It has been stated before that the VCFQ approach is an initial condition dependent recasting of the modal parameter based flying qualities requirements. In fact, it is the selection of the disturbance vector D, which appears in the T_{ccf} transformation, that captures this initial condition dependence. Recall from Eqs. (4.29) and (4.31) that when there are multiple inputs to the system, choosing $D = \text{diag}[x_1(0), x_2(0), \ldots, x_n(0)]$ with unit impulsive inputs in $w(t)$ resulted in a deterministic state covariance matrix that was equivalent to that obtained from the initial condition response with $X_0 = \text{diag}[x_1(0)^2, x_2(0)^2, \ldots, x_n(0)^2]$. This is a result of the well-known equivalence between the initial condition and the unit impulse response of an LTI system. Of course, the use of the Control Canonical Form and the results of Section 4.3 require that the system have only a single input, and thus $D \in \mathbb{R}^{n\times 1}$. Fortunately, the definition of the deterministic state covariance matrix in Eq. (4.28) includes a summation over each of the r disturbances applied one at a time. Thus, the deterministic state covariance matrix due to the initial condition response is equivalently achieved by a summation of the

$i = 1 \ldots n$ initial condition terms applied one at a time such that

$$D_i = \begin{bmatrix} 0 \\ \vdots \\ 0 \\ x_i(0) \\ 0 \\ \vdots \\ 0 \end{bmatrix}, \tag{4.75}$$

where $x_i(0)$ is the ith term of the initial condition $x(0)$ and appears in the ith component of D_i, while all other entries are zero. So, using Eq. (4.46), the physical state variances can be computed using the summation

$$X = \sum_{i=1}^{r} T_{\text{ccf}}(A, D_i)\hat{X}T_{\text{ccf}}(A, D_i)^T, \tag{4.76}$$

where $\hat{X}$ is the CCF deterministic state covariance matrix, and $T_{\text{ccf}}(A, D_i)$ is the CCF tranformation matrix computed for the matrix pair (A, D_i) using Eq. (4.37). The resultant deterministic state covariance computed using Eq. (4.76) is a solution to the Lyapnuov equality

$$0 = AX + XA^T + X_0. \tag{4.77}$$

It is possible to solve Eq. (4.77) directly using numerical solvers built into Matlab (or similar software), but there are benefits to using the summation formulation of Eq. (4.76). The advantage lies in the fact that the computation of the CCF deterministic state covariance matrix, $\hat{X}$, is invariant with respect to the disturbance D_i. Therefore, CCF state variances can be computed as a function of the characteristic polynomial coefficients and stored in a database. In this manner, the search for the maximum state variance in the domain can be

accelerated by using the precomputed CCF state variance results and then computing the physical state variances via Eq. (4.76). Additionally, it is common for initial conditions to be applied to only one or two states, which makes the cost of summing results from each D_i inconsequential.

Unlike the CCF covariance matrix which has the 'signature Hankel' structure, the deterministic state covariance matrix X will, in general, have no particular special structure. State variances are easily extracted from X, since according to the definition of σ in Eq. (4.32), individual state variances are simply the diagonal elements of the deterministic state covariance matrix as

$$\sigma_i = X_{ii}, \quad i = 1 \dots n. \tag{4.78}$$

State variances obtained from X have the additional interpretation of being the impulse-to-energy gain, Γ_{ie}, between the input and the ith state variable [71]. The impulse-to-energy gain between a vector-valued impulse $z(t) = z_0\delta(t)$, where $\|z_0\|$ is the magnitude of the impulse, and a vector-valued output y is given by

$$\Gamma_{ie} \triangleq \sup_{\substack{z(t)=z_0\delta(t) \\ \|z_0\|\leq 1,\ z_0\neq 0}} \|y\|_{\mathcal{L}_2}. \tag{4.79}$$

A final comment on the controllability of the matrix pair (A, X_0) is necessary. Solutions to the Lyapunov equality in Eq. (4.77) only correspond to the state variances of the response of the LTI system if the pair is controllable, and thus the selection of $x(0)$ must consider this requirement.

Transformation to the Physical States

Given a controllable, single input LTI system, it is not difficult to compute the corresponding CCF transformation T_{ccf}. This transformation can then be used in Eq. (4.76) to relate the CCF covariance matrix to the deterministic state covariance matrix due to the initial condition response. However, when sampling the acceptable flying qualities modal domain in search of the maximum state variances, this transformation requires reconsideration at each unique set of eigenvalue locations. Recall that the transformation T_{ccf} is a function of both A and D_i, and that application of the transformation to the LTI system results in $\hat{A}$ and $\hat{D}_i$, where the last row of $\hat{A}$ is the characteristic polynomial. As the eigenvalues are perturbed to sample a new location in the acceptable flying qualities domain, a new characteristic polynomial will necessarily result. The perturbed characteristic polynomial corresponds to a new CCF state matrix, $\hat{\bar{A}}$, which still possesses the classical CCF structure. Its relationship to the physical states, however, has been fundamentally altered from that of $\hat{A}$. Therefore, a new transformation matrix $T_{\text{ccf}}(\bar{A}, D_i)$ is required to compute the physical state variances.

Unfortunately, a transformation cannot be developed using only knowledge of $\hat{\bar{A}}$ and D_i, and additional modal information is required. This can be seen by returning to the definition of the deterministic state covariance matrix and utilizing the modal decomposition $A = E\Lambda E^{-1}$, such that

$$\begin{aligned} X &= \sum_{i=1}^{r} \int_0^t x(i,t)x(i,t)^T dt \\ &= \sum_{i=1}^{r} \int_0^t (e^{At}x_0(i,t))(e^{At}x_0(i,t))^T dt \\ &= \sum_{i=1}^{r} \int_0^t (Ee^{\Lambda t}E^{-1}x_0(i,t))(Ee^{\Lambda t}E^{-1}x_0(i,t))^T dt, \end{aligned} \tag{4.80}$$

where E is the column matrix of eigenvectors and Λ is the diagonal matrix of eigenvalues

of A. Clearly, Eq. (4.80) shows the influence of the eigenvectors on the computation of the deterministic state covariance matrix. When searching the acceptable flying qualities domain for the maximum state variances, the eigenvalues can be chosen according to the MIL-STD-1797, but further consideration must also be given to the eigenvectors.

No guidance on the eigenvectors is given in any of the documents governing flying qualities, civilian or military. The next best resource for a desirable eigenvector structure would be from an existing configuration for which only small changes were desired. For example, in Chapter 6 during the empennage design of a transport aircraft, a baseline configuration is known *a priori* for which the open-loop characteristics are known to satisfy the MIL-STD-1797 flying qualities requirements. Knowledge of these eigenvectors is an ideal resource, since pilots have already identified their structure (in tandem with the open-loop eigenvalues) as acceptable. The selection of the baselines eigenvector structure also has an intuitive physical interpretation—if the variance of a state was identified as acceptable with a full-sized tail, it stands to reason that a reduction in tail area alone should not modify the opinion of the pilot to the same state variances. A similar process was used in Ref. [83], where the longitudinal flying qualities of an X-29 were considered in the control system design by using the eigenstructure of an ideal reference model.

To this point, the only design studies conducted using the current VCFQ approach have relied upon a reference eigenvector structure. However, there are several results in the literature which seek to address the shortcomings of the MIL-STD-1797 and attempt to prescribe an eigenvector structure for satisfactory flying qualities. Efforts have focused on both longitudinal [83, 84] and lateral-directional [85, 86] flying qualities, and even particular airframe applications such as tailless aircraft [87] or rotorcraft handling qualities [86]. The work of Srinathkumar [86] is likely to be the single most complete resource on the subject, and in addition to providing guidance on choosing the desired eigenstructure for a vehicle, he

also provides metrics and techniques for designing robustness to modeling uncertainties into the selection of the eigenvectors. It remains a topic of future research to fully investigate and automate the selection of the desired eigenvector structure for aircraft without any relevant reference configurations.

Once a desired eigenvector matrix, $\bar{E}$, has been determined, either from a reference model or the resources just discussed, it is a simple matter to compute the state variances within the acceptable flying qualities domain. From a set of eigenvalue locations in the domain, the characteristic polynomial and the CCF deterministic state covariance matrix can be computed. In addition, the matrix $\bar{A}$, which possesses the desired eigenvector structure and eigenvalues, can be computed as

$$\bar{A} = \bar{E}\bar{\Lambda}\bar{E}^{-1}, \tag{4.81}$$

where $\bar{\Lambda}$ is the diagonal matrix of eigenvalues corresponding to the set of eigenvalues being sampled. Constructing the CCF transformation $T_{\text{ccf}}(\bar{A}, D_i)$, and using Eq. (4.76), the deterministic state covariance matrix can be computed.

It is important to recognize that the deterministic state covariance matrix computed using $\bar{A}$ is that which would be achieved by the aircraft if it could undergo a change in its eigenvalues without any perturbation in the eigenvectors. While there is an embedded implication of eigenvector assignability in this computation (the ability of a control system to assign both eigenvalues and eigenvectors [86]), the goal of the VCFQ approach is not to assign an eigenstructure to a system. Rather, the VCFQ approach seeks to make use of existing modal requirements to compute the state variances which pilots identified as acceptable. Since the MIL-STD-1797 lacks any requirements on the eigenvectors, approximations based on proven baseline configurations or from eigenstructure assignment efforts in the literature offer the only means of characterizing the satisfactory performance of individual states. This can be contrasted with the typical eigenvalue placement strategies of most control

system design efforts reviewed in Chapter 2, which do not consider the eigenvectors in any capacity. The embedded eigenvector information in the VCFQ approach is an advantage over eigenvalue-only metrics, since the time-domain response depends on eigenvalues and eigenvectors.

4.4.3 Searching for the Maximum State Variances

Computing the maximum state variance within a region of the complex plane is best accomplished numerically, though for very low-order systems, it could potentially be computed analytically. For the rigid-body motions of an aircraft, there are at most twelve states of interest. Under the associated assumptions, however, these motions are typically decoupled into the longitudinal and lateral-directional states as in Section 3.2. For flying qualities evaluation, the navigational states are also dropped from consideration, since under the flat, nonrotating Earth assumption none of the aerodynamic or body axis parameters depend on these states [60, 61]. This includes the altitude state, which typically manifests itself in the aerodynamic and propulsive parameters as a change in atmospheric properties and propulsive efficiency. Thus, the assumption is made that for flying qualities assessment, the altitude is sufficiently constant to make these terms negligible. It should be noted that these assumptions are only needed for the computation of the maximum state variances, and their use here does not preclude the inclusion of these states in the equations of motion for dynamic analysis discussed later in Section 4.5. Accordingly, the longitudinal and lateral-directional state vectors become

$$x_{\text{long}} = \begin{bmatrix} V & \alpha & \hat{q} & \theta \end{bmatrix}^T \tag{4.82}$$

$$x_{\text{latdir}} = \begin{bmatrix} \beta & \hat{r} & \hat{p} & \phi \end{bmatrix}^T. \tag{4.83}$$

The flying qualities requirements of the MIL-STD-1797 deal only with the decoupled equations of motion. Therefore, the worst-case scenario is that the maximum state variances must be computed for the case of $n = 4$. For the longitudinal equations of motion, both the short-period and the phugoid modes are oscillatory, and for Level I flying qualities the short-period mode is heavily constrained, while the phugoid mode is only required to be lightly damped. For the lateral-directional equations of motion, the Dutch-roll mode is oscillatory while the spiral and roll modes are overdamped and non-oscillatory. Level I flying qualities require that the Dutch-roll mode meet requirements on both the damping and the natural frequency, while the roll and spiral modes must meet a minimum time constant, and a maximum time-to-double constraint, respectively. This knowledge of the types of modal constraints required by the MIL-STD-1797 facilitates certain assumptions in the numerical search for $\sigma_{1_{\max}}, \ldots, \sigma_{n_{\max}}$.

In the next section, a simplified version of the flying qualities domain search is detailed. This example problem makes use of a second-order case, like that of Section 4.4.1, for ease of explanation. Following the two-state example problem, the process for computing state variances under the longitudinal flying qualities requirements and the lateral-directional flying qualities requirements is explored.

Second-Order CCF State Variance Computation

Consider the domain shown in Figure 4.1, which is a typical eigenvalue boundary for a second-order, oscillatory system found in the flying qualities requirements. For completeness, the characteristic polynomial of a second-order system and its decomposition into the damping

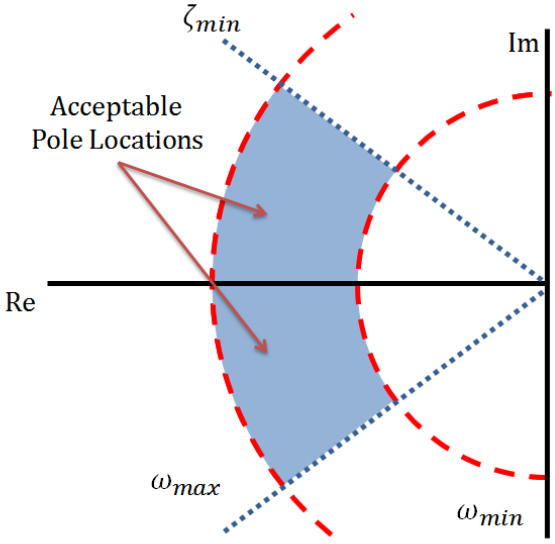

Figure 4.1: Example modal domain from the MIL-STD-1797 flying qualities requirements

ratio and natural frequency are restated as

$$s^2 + a_2 s + a_1 = 0 \iff s^2 + 2\zeta\omega_n s + \omega_n^2 = 0$$
$$\implies \begin{bmatrix} a_1 \\ a_2 \end{bmatrix} = \begin{bmatrix} \omega_n^2 \\ 2\zeta\omega_n \end{bmatrix}. \tag{4.84}$$

From the figure, constraints on the characteristic polynomial coefficients can be written as

$$(\omega_n^2)_{\min} \leq a_1 \leq (\omega_n^2)_{\max}$$
$$2(\zeta\omega_n)_{\min} \leq a_2 \leq 2(\zeta\omega_n)_{\max}. \tag{4.85}$$

For the simple case of a second-order system, these inequalities can be rewritten using Eq. (4.73) to directly compute the minimum and maximum CCF state variance in the domain

as

$$\left(\frac{1}{2a_1a_2}\right)_{\min} \leq \hat{\sigma}_1 \leq \left(\frac{1}{2a_1a_2}\right)_{\max}$$
$$\left(\frac{1}{2a_2}\right)_{\min} \leq \hat{\sigma}_2 \leq \left(\frac{1}{2a_2}\right)_{\max}. \tag{4.86}$$

Given a desired eigenvector structure $\bar{E}$, and an initial condition $x(0)$, Eqs. (4.81) and (4.76) could then be used to convert these to analytic bounds on the physical state variances. In general, it is far simpler to find the maximum state variances numerically. When the system order is greater then $n = 2$, or when the domains of interest grow more complex, it will be impractical to find analytic maximums of the CCF state variances and the associated transformation to the physical states. To demonstrate the numerical search procedure in its simplest form, it is presented first using the two-state system.

The process begins by developing a mesh of eigenvalue locations which fall into the acceptable domain. In this case, since the poles were assumed to be oscillatory and therefore complex conjugates, it was only necessary to mesh the second quadrant of the complex plane as in Figure 4.2. At each location in the domain, the corresponding characteristic polynomial was computed, the vector of coefficients extracted, and the corresponding CCF state variances computed using Eq. (4.73). The result is two contour plots, one each for $\hat{\sigma}_1$ and $\hat{\sigma}_2$, which present contours of their magnitudes versus the location of the associated eigenvalues in the complex plane. This can be seen in Figure 4.3. Not surprisingly, the CCF state variances peak at pole locations with a minimum damping ratio and a minimum natural frequency—modal parameters that indicate a slow response with significant oscillation. Contours of the physical state variances would depend upon the desired eigenvector structure and the prescribed initial condition.

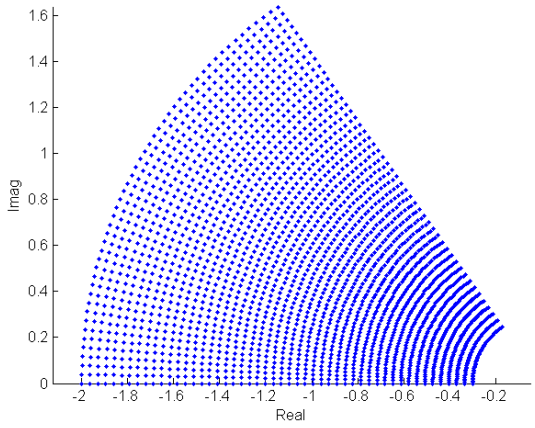

Figure 4.2: Meshed upper quadrant of left-half plane

Longitudinal CCF State Variance Computation

When working with a fourth-order system, the numerical search scheme grows more complicated, but not overly so. The characteristic polynomial is now of the form

$$(s^2 + 2\zeta_{\text{sp}}\omega_{n_{\text{sp}}} + \omega_{n_{\text{sp}}}^2)(s^2 + 2\zeta_{\text{ph}}\omega_{n_{\text{ph}}} + \omega_{n_{\text{ph}}}^2) = 0, \tag{4.87}$$

which is exactly the product of two second-order systems. Constraints on the flying qualities are placed on these individual second-order systems, and the numerical approach to finding the maximum state variances is essentially a double iteration—hold the eigenvalues fixed for one mode, and iterate the other, storing the maximum state variances at each iteration. Next, alter the eigenvalues of the first mode, iterate the other again, and store the largest state variances. This method is rather "brute force" and without a great deal of elegance, but the algebraic equations solved are trivial for a computer, taking only a few seconds to compute several hundred or thousand iterations. In practice, it has been found that roughly 5,000 computations provide a sufficient balance between resolution and computation time.

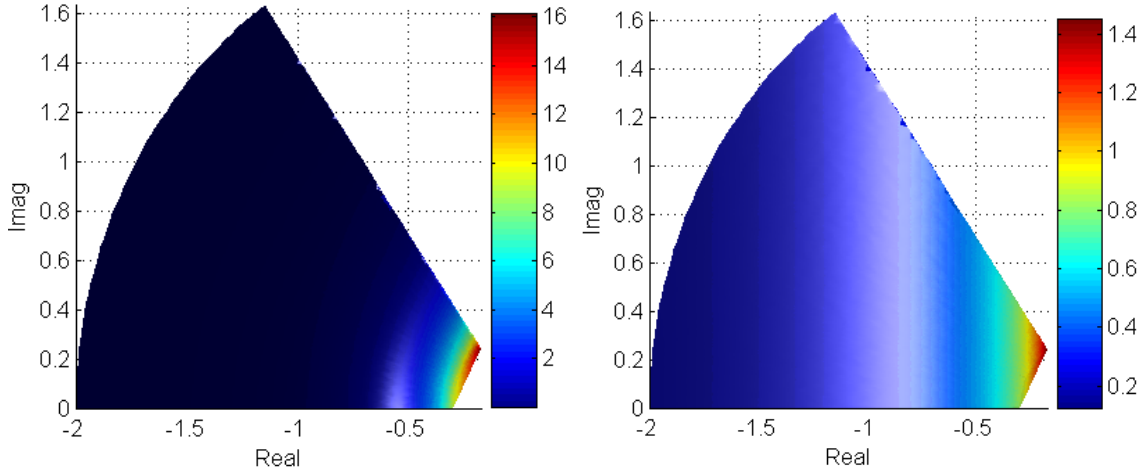

(a) Contour plot of $\hat{\sigma}_1$ (b) Contour plot of $\hat{\sigma}_2$

Figure 4.3: Contour plots of the CCF state variances for an example two-state system

Essentially, the search is conducted over a domain described by the four inequality constraints

$$\begin{aligned} c_1 \leq & a_{1_{\text{sp}}} \leq c_2 \\ c_3 \leq & a_{2_{\text{sp}}} \leq c_4 \\ c_5 \leq & a_{1_{\text{ph}}} \leq c_6 \\ c_7 \leq & a_{2_{\text{ph}}} \leq c_8, \end{aligned} \tag{4.88}$$

where $c_1 \ldots c_8$ are constants defined by the damping ratio and natural frequency requirements of the MIL-STD-1797.

The flying qualities requirements have relatively strict constraints on the short-period mode, requiring it to satisfy both a damping ratio constraint (Table 3.10) and a CAP constraint (Table 3.11). The CAP constraint is effectively a flight condition dependent constraint on the natural frequency, and is easily computed about a trim condition using Eq. (3.111). Thus, meshing the short-period eigenvalue domain is identical to the process demonstrated

in the two-state example problem as:

$$\begin{aligned} \omega^2_{n_{\text{sp,min}}} \leq & a_{1_{\text{sp}}} \leq \omega^2_{n_{\text{sp,max}}} \\ (2\zeta_{\text{sp}}\omega_{n_{\text{sp}}})_{\min} \leq & a_{2_{\text{sp}}} \leq (2\zeta_{\text{sp}}\omega_{n_{\text{sp}}})_{\max} \end{aligned} \tag{4.89}$$

Establishing a domain for the mesh of the phugoid mode takes an extra degree of consideration. While the flying qualities requirements only enforce a very relaxed damping ratio constraint (Table 3.9), there are still potential pitfalls associated with the phugoid natural frequency. As described in Chapter 3, state variances only exist for systems which are asymptotically stable, and therefore, have all of their eigenvalues in the open left half plane. The flying qualities requirements demand a stable phugoid mode (at least for Level I and II classifications), but only enforce a damping ratio constraint, allowing the phugoid eigenvalues to approach arbitrarily close to the origin. This effectively allows the aircraft to develop a pseudo-neutrally stable phugoid mode. The consequence of a neutrally stable mode is the asymptotic growth of the predicted state variances. Recall the definition of the deterministic state covariance matrix as

$$X \triangleq \sum_{i=1}^{r} \int_0^\infty x(i,t)x(i,t)^T dt. \tag{4.90}$$

If the eigenvalues of an LTI system lie on the $j\omega$-axis, the integral in the deterministic state covariance matrix evaluates to infinity since $x(i,\infty) \neq 0$. This is clearly undesirable, and is easily prevented by enforcing a lower bound on the phugoid natural frequency.

It is necessary to initiate some engineering judgment when establishing the minimum phugoid natural frequency bound. Within the MIL-STD-1797, the section on the development of the lower-order equivalent system for the phugoid mode cites 0.01 rad/s as the lower limit of the matching frequencies [15], a number which was adopted here for use in Chapter 6.

Similarly, when discretizing the domain, an upper bound on the natural frequency must also be established. Engineering judgment is utilized again, and the upper bound on the phugoid natural frequency is determined as a fraction of the short-period minimum natural frequency according to

$$\omega_{n_{\text{ph,max}}} \leq k_{ph}\omega_{n_{\text{sp,min}}}, \tag{4.91}$$

where k_{ph} is a user-established constant to determine the required degree of separation of the natural frequencies. This is a very practical constraint, since it is generally considered undesirable (though sometimes unavoidable) for the short-period and phugoid modes to coalesce [60]. Experience with this parameter has found the search for the maximum state variances to be largely insensitive to the user choice, provided $k_d \lesssim 0.9$. The reason for this can likely be attributed to the fact that state variance will naturally be larger if the system is slow in its recovery to equilibrium—a scenario which occurs when the phugoid eigenvalues are closer to the imaginary axis.

Lateral-Directional CCF State Variance Computation

The lateral-directional process is much like the longitudinal process in that a multi-tiered iteration is carried out over the coefficients of

$$(s^2 + 2\zeta_{\text{dr}}\omega_{n_{\text{dr}}} + \omega_{n_{\text{dr}}}^2)\left(s + \frac{1}{\tau_{\text{r}}}\right)\left(s + \frac{1}{\tau_{\text{s}}}\right) = 0, \tag{4.92}$$

where τ_{r} and τ_{s} are the roll and spiral mode time constants, respectively. In contrast to the longitudinal modes, however, the lateral-directional modes are composed of one second-order system and two first-order systems.

The second-order system, the Dutch-roll mode, has natural frequency, damping ratio, and damped natural frequency constraints (Table 3.14), where the damped natural frequency

is given by

$$\omega_{d_{\mathrm{dr}}} = \omega_{n_{\mathrm{dr}}} \zeta_{\mathrm{dr}}. \tag{4.93}$$

Much like the short period constraints, these can be written as inequality constraints of the characteristic polynomial coefficients. Engineering judgment is again required to identify a natural frequency upper bound since none is given by the MIL-STD-1797. A scaling coefficient is used to express the maximum Dutch-roll natural frequency in terms of the minimum Dutch-roll natural frequency as

$$\omega_{n_{\mathrm{dr,max}}} \geq k_{dr} \omega_{n_{\mathrm{dr,min}}}, \tag{4.94}$$

where k_{dr} is a user-selected constant. As with the phugoid results, the maximum state variances occur when the Dutch-roll response is slowest, thus the results have been found to be relatively insensitive to the choice of k_{dr} provided that $k_{dr} \gtrsim 1.1$. The result is the boundaries

$$\begin{aligned} \omega^2_{n_{\mathrm{dr,min}}} \leq & a_{1_{\mathrm{dr}}} \leq \omega^2_{n_{\mathrm{dr,max}}} \\ 2\omega_{d_{\mathrm{dr,min}}} \leq & a_{2_{\mathrm{dr}}} \leq 2\omega_{d_{\mathrm{dr,max}}}. \end{aligned} \tag{4.95}$$

Dealing with the first-order constraints poses a peculiar challenge. The spiral mode, for one, is not required to be stable to satisfy Level I flying qualities requirements—an artifact of the pilot's natural tendency to stabilize this slowly divergent mode. This is a particularly difficult challenge for the VCFQ approach, since the existence of the deterministic state covariance matrix demands the system be stable. Currently, the VCFQ approach does not have a means to handle allowable instabilities in a particular mode, and this remains a

topic of future research. In the interim, the spiral mode is required to be stable, but only marginally so. This is not a severe limitation, however, since an autopilot system on a manned or unmanned aircraft would require all modes to be closed-loop stable. A maximum allowable time constant for the spiral mode, $\tau_{s_{max}}$, must be defined by the user in order to maintain a feasible numerical solution:

$$\tau_s < \tau_{s_{max}} \tag{4.96}$$

The second of the first-order modes, the roll mode, is constrained by a maximum allowable time constant by the flying qualities requirements (Table 3.12). This leads to a constraint similar to that for the spiral mode as

$$\tau_r < \tau_{r_{max}}. \tag{4.97}$$

By iterating over the two real eigenvalues of the first-order modes, and the complex conjugate eigenvalues of the oscillatory Dutch-roll mode, a multi-tiered numerical search over the lateral-directional domain can be accomplished just like was done for the longitudinal modes.

4.4.4 Selecting the Initial Conditions

An interesting observation regarding the spectral decomposition of a linear system is that the modal parameters are not functions of any initial condition. This then raises the question of why the VCFQ approach requires the selection of an initial condition. The reason is that the state variances of an unperturbed system are zero (see the definition of the deterministic state covariance matrix in Eq. (4.32)), which is a trivial solution that doesn't provide any

information regarding system performance or stability. As it turns out, if the modal parameters are the only constraint of interest in the design of the control system, the selection of the initial condition $x(0)$ is somewhat arbitrary (provided (A, X_0) is controllable).

This previous statement is best illustrated by observing that for a given system matrix A, the eigenvalues $\lambda_1 \ldots \lambda_n$ are independent of any initial condition $x(0)$. Qualitatively speaking, a disturbance D applied to the system, which is small as measured by $\|D\|_{\mathcal{L}_2}$, leads to a solution of the Lyapunov equality that gives a small state variance vector, as measured by $\|\sigma\|_{\mathcal{L}_2}$, where

$$\sigma = \begin{bmatrix} \sigma_1 & \sigma_2 & \ldots & \sigma_n \end{bmatrix}^T. \tag{4.98}$$

A larger disturbance, naturally, leads to a larger state variance vector, yet the eigenvalues of A remain unchanged. Thus, the choice of the initial conditions does not alter the modal properties of the system, but it does facilitate the computation of state variances—which have already been shown to have great utility in measuring performance and predicting flying qualities. Additionally, careful selection of initial conditions facilitates the inclusion of constraints on the actuator dynamics during the design of the control system.

Still, the issue of choosing particular initial conditions remains. The Federal Aviation Regulations (FAR) prescribe gust load cases which all aircraft must demonstrably be capable of withstanding [13, 14]. Gust scenarios range in complexity from discrete to continuous gusts, with both static aeroelastic and dynamic aeroelastic considerations [88]. Traditionally, these gust cases are used to size the structural components of the aircraft, thus they represent suitable 'edges' of the flight envelope to bound the dynamic performance for controls considerations as well. Of course, these cases could be augmented with additional initial conditions as the control designer sees fit.

Following the work of Kaminer, et al., [45] the gust cases are modeled here using discrete

static gusts and the derived equivalent gust velocity, U_{de}. The derived equivalent gust velocity is a fictitious velocity that is derived from acceleration measurements recorded in operational flight and computed by solving

$$\Delta n = K_g \frac{U_{de} V C_{L_\alpha}}{498 \frac{W}{S_{\text{ref}}}}, \tag{4.99}$$

where K_g is a coefficient which approximates the aerodynamic lag in lift generation and is given by

$$K_g = \frac{0.88 \mu_g}{5.3 + \mu_g}, \tag{4.100}$$

where μ_g is a mass parameter given by

$$\mu_g = \frac{2W}{\rho g S_{\text{ref}} \bar{c} C_{L_\alpha}}. \tag{4.101}$$

Basically, U_{de} is a velocity which would give an equivalent peak acceleration of the aircraft subject to an assumed one-minus-cosine gust shape applied during symmetrical, level flight [88]. The FAR's prescribed values of U_{de} as functions of altitude and airspeed, the results of which were collected in [88] and reproduced in Table 4.2. Derived equivalent gusts still exist in Part 23 of the FARs [13], which is applicable to 'normal, utility, acrobatic, and commuter category airplanes'. However, they have been replaced in the FAR Part 25 for 'Transport Category Airplanes' by more advanced dynamic gust models, which seek to capture the inertial effects of airplane loading and unloading on the structure [14]. But, the derived equivalent gust is still useful in generating initial conditions for the VCFQ approach for several reasons. First, the inertial effects which are captured by more advanced dynamic models are discarded by the rigid-body assumptions of Chapter 3. Second, similar discrete gust techniques exist in the most recent MIL-STD-1797 [15]. Third, we only seek a starting point for developing critical initial conditions, and the designers judgment can overrule the

inclusion or exclusion of particular gust cases.

Table 4.2: FAR Derived Equivalent Gust Velocities, U_{de}

For Altitudes $\leq$ 20,000 ft.	
at V_B (design rough-air speed)	$U_{de} = 66$ fps
at V_C (design cruise speed)	$U_{de} = 50$ fps
at V_D (design dive speed)	$U_{de} = 25$ fps
For Altitudes $>$ 20,000 ft, but $<$ 50,000 ft	
U_{de} decreases linearly from 20,000 ft. value to 50,000 ft. value	
For Altitude = 50,000 ft	
at V_B	$U_{de} = 38$ fps
at V_C	$U_{de} = 25$ fps
at V_D	$U_{de} = 12.5$ fps

In generating the initial conditions for the VCFQ approach, the designer selects cases based upon the U_{de} velocity applied at different angles. For example, three gust cases might be that the aircraft must be able to withstand a rough air speed disturbance head on, vertically, and as a crosswind. These are easily translated into perturbations in the longitudinal or lateral-directional states by using the definitions of α and β from Eqs. (3.5) and (3.6), respectively.

4.5 State Variance Constrained Control

Following the methods of the previous sections, a designer has now translated the flying qualities requirements given in modal parameters to a state variance upper bound for a selected initial condition. It is the purpose of the VCFQ approach to use this information to construct an LMI feasibility problem and automate the search for a satisfactory static state feedback controller. There is a significant amount of literature on variance constrained

control [68, 71, 80, 89], and the brief overview that follows is not intended to serve as a fully inclusive introduction. This section relies upon the state feedback covariance bounded control work by Skelton et. al, [71] and extends the utility of these methods by leveraging LMI techniques developed by Boyd et al. [46].

To begin, consider the continuous-time Lyapunov inequality introduced in Section 4.2 given by

$$AQ + QA^T + DD^T < 0, \tag{4.102}$$

where the use of $Q \in \mathbb{R}^{n\times n}$ is to distinguish it from the deterministic state covariance matrix X that was computed from the flying qualities requirements in the preceding section. It is a known result in covariance control theory that any matrix $Q > 0$ which satisfies Eq. (4.102) is an upper bound on the state covariance provided that the system is excited by white noise, $w \in \mathbb{R}^{n_w}$, with covariance $\mathbb{I}$ [71]. By selecting DD^T to be $X_0 = \text{diag}[x_1(0)^2 \dots x_n(0)^2]$, the diagonal initial condition matrix of Eq. (4.31), a solution $Q > 0$ to

$$AQ + QA^T + X_0 < 0, \tag{4.103}$$

is a guaranteed upper bound on the state covariance due to the initial condition response. Recall from Section 4.2 that the existence of a $Q > 0$ which satisfies the Lyapunov inequality is also sufficient to demonstrate stability of the system. The open-loop Lyapunov inequality can be extended to the closed-loop static state feedback case, $u = Kx$, as

$$(A + BK)Q + Q(A + BK)^T + X_0 < 0, \tag{4.104}$$

where $K \in \mathbb{R}^{m\times n}$ is the matrix of feedback control gains. Finding matrix solutions, K and $Q > 0$, is sufficient to demonstrate stability of the closed-loop system. Modern convex optimization tools have little difficulty finding feasible solutions for well-posed LMI problems,

but Eq. (4.104) is not linear in both Q and K. Using a technique from Boyd et al.,[46] a new matrix variable $Y = KQ \in \mathbb{R}^{m\times n}$ can be introduced, and the substitution $K = YQ^{-1}$ can be made to arrive at

$$QA^T + AQ + Y^T B^T + BY + X_0 < 0. \tag{4.105}$$

Equation (4.105) is linear in both Q and Y, and the feedback gain matrix K can be obtained through a trivial post-processing step using $K = YQ^{-1}$.

Since the objective is not just to find any stabilizing controller, but rather to find any stabilizing controller subject to state variance bounds, additional inequality constraints are required. Bounding the diagonal elements of Q as

$$Q_{kk} < \sigma_{k_{\max}}, \tag{4.106}$$

will further constrain the matrix solutions Q and K such that the state variances are less than $\sigma_{1_{\max}} \ldots \sigma_{n_{\max}}$ for the chosen initial condition response. Here, $\sigma_{k_{\max}}$ are the maximum allowable state variances derived from the flying qualities requirements in the preceding sections. At the conceptual design stage, the existence of a K and $Q > 0$ which satisfy Eqs. (4.105) and (4.106) is sufficient to answer the question, 'Does a static state feedback control law exist such that the design being synthesized will be capable of (*approximately*) satisfying the Level I flying qualities guidelines?'

4.5.1 Constraints on the Control Input

A solution to the LMI's presented in Section 4.5 lacks any constraints on the feedback gain matrix, K, or the input, u. Without these constraints, there is the potential for unrealisti-

cally high gains which can lead to actuator saturation and/or violation of the linear model. Fortunately, an LMI formulation of an invariant ellipsoid approach was developed by Boyd et al. [46], to place bounds on the input amplitude of the closed-loop response of an LTI system. This work was later utilized by Kaminer, et al. [45], where they demonstrated the application as bounds on aircraft effectors and developed a capability to bound the actuation rate. These methods were all accomplished using an LMI problem formulation, and are therefore easy to implement alongside the covariance upper bound controller.

4.5.2 Single Input Systems

To develop the ellipsoidal interpretation first note that if Eq. (4.105) is satisfied, then the quadratic Lyapunov function $V(\xi) = \xi^T Q^{-1} \xi$ proves stability of the closed-loop system. Given the matrix $Q > 0$, let ε denote the ellipsoid centered at the origin

$$\varepsilon = \left\{ \xi \in \mathbb{R}^n | \xi^T Q^{-1} \xi \leq 1 \right\}. \tag{4.107}$$

This ellipsoid is defined as invariant if for every trajectory $x(t)$, that $x(t_0) \in \varepsilon$ implies $x(t) \in \varepsilon$ for all $t \geq t_0$. In other words, the state vector x is bounded for all time by the ellipsoid ε. The ellipsoid can also be used to bound the control inputs using the relationship $u(t) = Kx(t) = YQ^{-1}x(t)$. Then, for $x(t) \in \varepsilon$, the input can be bounded by

$$\begin{aligned} \max_{t \geq 0} \|u(t)\| &= \max_{t \geq 0} \|YQ^{-1}x(t)\| \\ &\leq max_{x \in \varepsilon} \|YQ^{-1}x(t)\| \\ &\leq \lambda_{\max} \left(Q^{-1/2} Y^T Y Q^{-1/2} \right). \end{aligned} \tag{4.108}$$

This equation is in a useful form, as now it matches the Generalized Eigenvalue Problem (Boyd et al.[46], Sect 2.2.3):

$$\begin{aligned} \text{minimize} \quad & \lambda_{\max}(A(x), B(x)) \\ \text{subject to} \quad & B(x) > 0, \quad C(x) > 0, \end{aligned}$$

where $\lambda_{\max}(M, N)$ denotes the largest generalized eigenvalue of the pencil $\lambda N - M$, with $N > 0$. Identically, this evaluates to the largest eigenvalue of the matrix $N^{-1/2} M N^{-1/2}$. In the nomenclature used in Eq. (4.108), this gives

$$\lambda_{\max} Q - Y^T Y \geq 0, \tag{4.109}$$

where the non-strict inequality sign refers to the positive (or negative) semi-definiteness of the matrix. It is desired that $\|u(t)\| < u_{\max}^2 = \lambda_{\max}$, where $u_{\max}$ is a prescribed actuator deflection upper bound, thus

$$\begin{aligned} u_{\max}^2 Q - Y^T Y &\geq 0 \\ Q - Y^T \left(\frac{1}{u_{\max}^2} \right) Y &\geq 0. \end{aligned}$$

Making use of the Schur complement, with $Q > 0$, this can be rewritten as the LMI

$$\begin{bmatrix} Q & Y^T \\ Y & u_{\max}^2 \mathbb{I} \end{bmatrix} \geq 0. \tag{4.110}$$

In addition, a constraint is made such that $x(0) \in \varepsilon$, or equivalently, $x(0)^T Q^{-1} x(0) \leq 1$ [46]. by the LMI

$$\begin{bmatrix} 1 & x(0)^T \\ x(0) & Q \end{bmatrix} \geq 0. \tag{4.111}$$

Equations (4.105), (4.106), (4.110), and (4.111) define the necessary LMI statements to find a feasible feedback control law, $K = YQ^{-1}$, subject to an initial condition, $x(0)$, such that the closed-loop system is stable and with an upper bound on the input amplitude and state variances.

4.5.3 Multiple Input Systems

On modern aircraft, as with many other systems, the number of inputs is often greater than one. Therefore, a means to apply maximum amplitude constraints on multiple input systems is desirable. In a similar manner as the single input case, Boyd et al. [46], explain how one would implement a multiple input setup through which a bound on the maximum amplitude of all actuators could be enforced:

$$\|u(t)\|_{\max} \triangleq \max_i |u_i(t)|$$

where $u \in \mathbb{R}^m$. The approach begins by a scaling of the actuator amplitudes such that all actuators have equivalent bounds on the feasible domain. The remainder of the derivation

follows as before

$$\begin{aligned}\max_{t\geq 0} \|u(t)\|_{\max} &= \max_{t\geq 0} \|YQ^{-1}x(t)\|_{\max} \\ &\leq \max_{x\in\varepsilon} \|YQ^{-1}x\|_{\max} \\ &\leq \max_{i} \left(YQ^{-1}Y^T\right)_{ii}. \end{aligned} \tag{4.112}$$

Thus, the constraint $\|u(t)\|_{\max} \leq u_{\max}$ for $t \geq 0$ can be written as an LMI by introducing a new matrix variable $R \in \mathbb{R}^{m\times m}$ such that

$$\begin{bmatrix} R & Y \\ Y^T & Q \end{bmatrix} \geq 0, \quad R_{ii} \leq u_{\max}^2, \quad Q > 0, \tag{4.113}$$

with the additional constraint that the LMI's in Eq. (4.105), (4.106) and (4.111) must also be satisfied, simultaneously.

4.5.4 Actuator Rate Constraints

An additional constraint which has broad-reaching implications is the application of actuator rate constraints. This constraint is important because it demonstrates the means by which additional states can be added to the system, facilitating the development of higher-order constraints on aeroelastic performance [41] or even unsteady aerodynamic terms [64]. The first step is developing a model for the added state, in this case a typical actuator rate response is modeled well by a first-order system

$$U(s) = \frac{a}{s+a}, \tag{4.114}$$

where $a \in \mathbb{R}^1$ is the actuator bandwidth, and $U(s)$ is the transfer function from the commanded to the actual actuator deflection. A single actuator, for example, leads to the new system

$$\mathcal{G}_l = \begin{cases} \dot{x} = Ax + Bu \\ u = K \begin{bmatrix} x^T & x_a \end{bmatrix}^T \\ \dot{x}_a = -ax_a + au \end{cases} \Leftrightarrow \begin{cases} \dot{x} = Ax + Bu \\ u = K \begin{bmatrix} x^T & x_a \end{bmatrix}^T \\ \dot{x}_a = -ax_a + aK \begin{bmatrix} x^T & x_a \end{bmatrix}^T \end{cases} \Leftrightarrow \begin{cases} \dot{\nu} = (F + GK)\nu \\ u = K\nu \\ \dot{x}_a = a(K - [\mathbf{0} \quad 1])\nu \end{cases} \tag{4.115}$$

where $\nu = \begin{bmatrix} x \\ x_a \end{bmatrix}$ and the new system matrices are

$$F = \begin{bmatrix} A & B \\ \mathbf{0} & -a \end{bmatrix} \in \mathbb{R}^{(n+1)\times(n+1)}, \quad G = \begin{bmatrix} \mathbf{0} \\ a \end{bmatrix} \in \mathbb{R}^{(n+1)\times 1}. \tag{4.116}$$

The new input to the system, G, has only one nonzero element corresponding to the actuator input command—an important distinction which deserves restating. In Eq. (4.116), the input to the system is the actuator commanded deflection $u = x_{a_{\text{cmd}}}$, and the state x_a is the actual deflected state of the actuator. Using the methods of Section 4.5.2, an input command upper bound can now be placed on $x_{a_{\text{cmd}}}$ to guarantee the actuator never reaches its deflection limits.

An output bounding method, developed in Ref. [46], gives the capability to bound the Euclidean norm of a subset of the outputs, $\|z(t)\|$, using the invariant ellipsoid approach. Typically for state feedback, the system output is assumed equal to the state vector as

$$z(t) = C_z x(t) = \mathbb{I}x(t) = x(t). \tag{4.117}$$

To bound a particular output, however, we introduce $C_z \neq \mathbb{I}$ to extract specific states of

interest. When the initial condition is known, suppose

$$\varepsilon = \left\{ \xi \in \mathbb{R}^{n+1} | \xi^T P \xi \leq 1 \right\} \tag{4.118}$$

is an invariant ellipsoid containing $x(0)$, where $P > 0 \in \mathbb{R}^{n+1}$. The selected outputs are then bounded above according to

$$z(t)^T z(t) \leq \max_{\xi \in \varepsilon} \xi^T C_z^T C_z \xi \tag{4.119}$$

for all $t \geq 0$. Using the matrix pencil approach of Section 4.5.2, this can be written as

$$\begin{bmatrix} P & C_z^T \\ C_z & z_{\max}^2 \mathbb{I} \end{bmatrix} \geq 0, \tag{4.120}$$

where $z_{\max} = z(t)^T z(t)$. When it is desired to constrain the behavior of the single actuator state, x_a, the choice of $C_z = [\mathbf{0} \quad 1]$ results in $z = x_a$ and $z_{\max} = \max_{t \geq 0} x_a$.

Returning to the system $\mathcal{G}_l$ of Eq. (4.115), note that by selecting

$$C_z = a[K - [\mathbf{0} \quad 1]], \tag{4.121}$$

the observed state is the actuator rate $\dot{x}_a$. So, the LMI constraint

$$\begin{bmatrix} P & a[K - [\mathbf{0} \quad 1]]^T \\ a[K - [\mathbf{0} \quad 1]] & \dot{u}_{\max}^2 \end{bmatrix} \geq 0, \tag{4.122}$$

bounds the actuator rate to be less than $\dot{u}_{\max}$, a prescribed upper bound on the actuator deflection rate. To be compatible with the LMIs of the previous sections, the choice of $P = Q^{-1}$ must be made. As before, this LMI is not linear in matrix variables Q and K, but

by pre- and post-multiplying by the congruence transformation

$$T = \begin{bmatrix} Q & \mathbf{0} \\ \mathbf{0} & \mathbb{I} \end{bmatrix}, \tag{4.123}$$

and using the relation $K = YQ^{-1}$, one can obtain the relation

$$\begin{bmatrix} Q & a[Y - [\mathbf{0} \quad 1]Q]^T \\ a[Y - [\mathbf{0} \quad 1]Q] & \dot{u}_{\max}^2 \end{bmatrix} \geq 0. \tag{4.124}$$

This LMI is linear in both Q and Y, and bounds the actuation rate to be less than $\dot{u}_{\max}$.

An important observation regarding the augmentation of the rigid-body states with the actuator state is that the order of the controller necessarily increases to $K \in \mathbb{R}^{n+1}$. This naturally assumes that the state of the actuator is available for feedback, which is not an unrealistic assumption. If a state is appended to this system which is not observable, and it is desired to exclude the added state from the state feedback solution, an output feedback solution must be adopted wherein the feedback controller depends on the output y, where

$$y(t) = Cx(t), \tag{4.125}$$

and C is chosen to exclude the unobservable states. The feedback control solution is then given by $u(t) = KCx(t)$, where the dimension of the gain matrix K depends on the number of states observable through C. In most cases, the extension to output feedback is trivial, and further detail can be found in Ref. [46].

A final comment on the actuator saturation constraint is its extension to the multiple input case. When more than one actuator is present, Eq. (4.124) can simply be included m times where in each occurrence, C_z is chosen to singly identify a single actuator's rate response.

4.5.5 System Response Lower Bound

One limitation of the current VCFQ approach described in the previous sections, is the inability to enforce lower bounds on the state variances. The concept itself is counterintuitive, since the objective of a variance constrained control system is to suppress the state variance of the system subject to a disturbance. As shown in Section 4.3, however, an arbitrarily small state variance is not likely to correspond to a desirable pole placement solution, since modes that are very fast are also considered undesirable. Thus, it can be necessary for the LMI feasibility statement to capture this lower bound constraint on the state variances. The difficulty of this task arises from the fact that the assignment of a state variance lower bound is not a convex problem, and is therefore not amenable to LMI formulation. Fortunately, a partial implementation of the LMI pole placement strategies developed by Chilali and Gahinet [77] can be used. In their work, the definition of stability is effectively altered to only include systems with eigenvalues in a convex region of the complex plane. A maximum

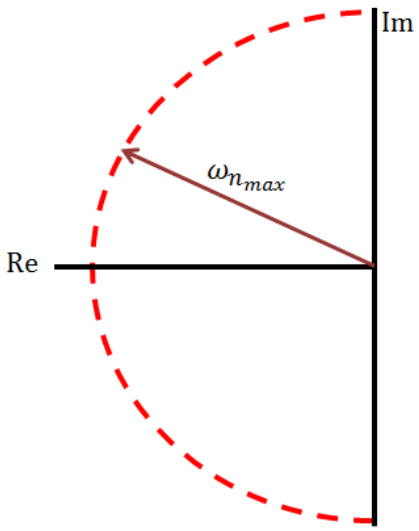

Figure 4.4: Illustration of the altered definition of stability by enforcement of a maximum natural frequency constraint

natural frequency bound, like that shown in Figure 4.4, would require a system to have all

of its poles within the limit to be considered stable. An open-loop LTI system satisfies this altered stability definition if it satisfies the LMI

$$\begin{bmatrix} -rQ & AQ \\ QA^T & -rQ \end{bmatrix} < 0, \tag{4.126}$$

where the matrices A and Q correspond to those in the Lyapunov inequality in Eq. (4.102), and the scalar $r = \omega_{n_{\max}}$. This is easily extended to the closed-loop system, $A + BK$, by making use of the substitution $K = YQ^{-1}$ such that

$$\begin{bmatrix} -rQ & AQ + BY \\ QA^T + Y^T B^T & -rQ \end{bmatrix} < 0. \tag{4.127}$$

It is important to note that Eq. (4.127) modifies the mathematical definition of stability for every mode in $A + BK$, and thus does not provide the independent control of specific state behavior that is achievable with bounds on the state variances. This can be problematic when additional states are included with the rigid-body motions. For example, if it is desired to observe the actuator rate dynamics, then each actuator will require the addition of state equations to the system. Eigenvalues associated with actuators are orders of magnitude faster than those of the rigid body modes, and a global maximum natural frequency constraint would be highly undesirable. Nonetheless, by choosing the bounding radius, r, to be $\omega_{n_{\max}}$, the constraint can help mitigate undesirably fast closed-loop poles.

4.5.6 Combined LMI Statement

The preceding sections have introduced closed-loop LMI constraints available to a designer, all of which could be implemented into the design of a feedback control system. Methods are available to enforce stability, to place performance constraints on the states through the state

variances, to bound the maximum allowable deflection of single and multiple actuators, to bound the maximum allowable deflection rate for single and multiple actuators, and to place global constraints on the fastest allowable natural frequency. Each constraint is formulated as an LMI, and it is therefore easily concatenated with any other constraint to assemble the desired feasibility problem for the MDO framework.

An example combination of LMI constraints is the one used later in Chapter 6 during the horizontal tail design of a transport aircraft. In this design problem, the flying qualities requirements provide state variance upper bounds, and the elevator has a saturation limit and an actuation rate limit that the control system design must observe. The result is the combined LMI system

$$QA^T + AQ + Y^T B^T + BY + X_0 < 0, \quad \begin{bmatrix} Q & Y^T \\ Y & u_{\max}^2 \mathbb{I} \end{bmatrix} \geq 0, \quad \begin{bmatrix} 1 & x(0)^T \\ x(0) & Q \end{bmatrix} \geq 0,$$

$$Q > 0, \qquad Q_{kk} \leq \sigma_{k_{\max}}, \qquad \begin{bmatrix} Q & a[Y - [\mathbf{0} \quad 1]Q]^T \\ a[Y - [\mathbf{0} \quad 1]Q] & \dot{u}_{\max}^2 \end{bmatrix} \geq 0, \tag{4.128}$$

where $\sigma_{k_{\max}}$ is the variance bound computed from the flying qualities guidelines, $u_{\max}$ is the maximum allowable elevator deflection, and $\dot{u}_{\max}$ is the maximum allowable elevator deflection rate. Finding a set of matrices $Q > 0$ and Y that satisfy Eq. (4.128) for a given initial condition $x(0)$, provides a feedback control law $K = YQ^{-1}$ that stabilizes the system and satisfies the state variance approximation of the flying qualities requirements without exceeding the actuator constraints.

4.6 VCFQ Process Summary

The VCFQ approach represents only a portion of the S&C module developed for the MDO framework, though it certainly is the most theoretically complicated portion. Before a dynamic analysis using the VCFQ approach can even be run, a number of upstream analyses are conducted to compute all the necessary preliminary data. Once these analyses have been executed, a trim and static stability analysis follows. A dynamic analysis is unnecessary if the available control effectors are incapable of trimming or fulfilling static constraints on the vehicle. Finally, the VCFQ approach is utilized to assess the closed-loop dynamic performance of the aircraft. A summary of this process follows in Table 4.3.

Table 4.3: Summary of Variance Constrained Flying Qualities Process

1. Linearize equations of motion about equilibrium conditions of interest
2. At each equilibrium, determine disturbance cases of interest either from gust requirements or from engineering judgment
3. Compute maximum state variances that occur within the flying qualities acceptable modal domain using the methods of Section 4.4 and the chosen disturbance cases
4. Use results of static analyses and trim solution to determine available actuator travel limits
5. Construct combined LMI feasibility problem which applies the desired constraints
6. Use convex optimization tools to search for a control system which will satisfy all of the constraints

Chapter 5

Implementation of the Stability and Control Module

The subject of the previous chapters was predominately the theoretical approach to the S&C module development. This chapter presents the details of its computational implementation into the VT High-Speed Aircraft MDO and a review of the influential upstream disciplines in the N^2 diagram of Figure 1.5. The first topic addressed is the data architecture which supports the S&C module and the VCFQ approach—the Matlab Object Oriented Stability & Control Framework (MOOSCF). Immediately following that, the generation of the geometry and its affiliated structural preprocessor are discussed, since they represent some of the most significant disciplines of the entire VT High-Speed Aircraft MDO framework. The aerodynamic and structural analyses, which are essential preliminary data sources for the S&C module, are then reviewed. These disciplines have multiple programs of varying fidelity levels. The chapter concludes with a discussion of the assembly of each discipline into ModelCenter^{TM} and the particulars of its execution.

5.1 Matlab Object Oriented Stability and Control Framework

A tremendous amount of aerodynamic and mass property data is required by a dynamic S&C analysis, and an object oriented data-handling framework, called the Matlab Object Oriented Stability and Control Framework (MOOSCF), was developed expressly for its storage and manipulation. This framework, depicted by a block diagram in Figure 5.1, creates a plane object with all the properties necessary for S&C analysis stored as private attributes. A plane object contains a bank of aircraft level attributes, which includes properties such as geometric parameters and actuator information (maximum deflection, maximum rate), and a bank of flight condition attributes. Flight conditions are themselves objects, and they have all of the pertinent flight condition dependent properties stored as attributes. This includes aerodynamic and inertial properties, as well as flags for indicating active or inactive static and dynamic performance constraints. Within the flight condition attributes, the linearized models of the equations of motion are also stored as LTI systems using the Matlab Control System Toolbox state space system construct [90]. Data for the MOOSCF are supplied by aerodynamic and structural models that are upstream in the N^2 diagram.

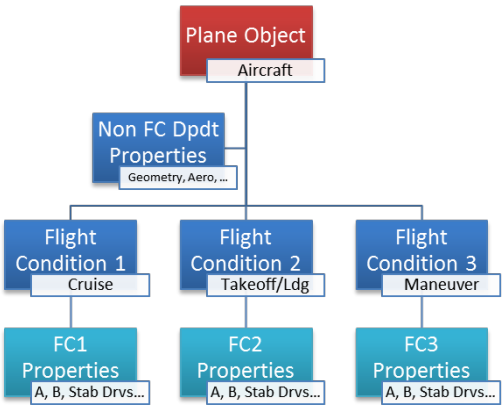

Figure 5.1: Matlab Object Oriented Stability and Control Framework

A framework of this type is beneficial in that it standardizes the format of the input and output data, necessitating only one set of tools to be developed to analyze the S&C characteristics of the aircraft. Matlab's object oriented capabilities include several particularly desirable traits, including dependent properties and dynamic arrays. Dependent properties allow for the calculation of a piece of data at the time of function call, and they are capable of calling other functions as needed. This allows for the automatic calculation of data so that the user isn't required to explicitly compute it. For example, once the span b and the wing area S are declared, a call to the variable Aspect Ratio AR, will automatically compute the value according to the dependent property relationship $AR = b^2/S$. This simple example may illustrate the utility of dependent properties, but it cannot singularly convey the convenience dependent properties provide when parsing data and establishing default values for parameters.

Dynamic arrays and dynamic memory allocation are also important benefits of using Matlab's object oriented programming. These capabilities allow for the automatic expansion or contraction of a variable's dimension in memory without having to call a destructor and then a constructor. This can be a significant computational time savings when the MDO framework is run hundreds or thousands of times. Should additional flight conditions be desired, for example, no rebuilding of the aircraft or its existing flight conditions is necessary, as new flight conditions can be dynamically added and analyzed without disturbing existing data.

The data structure inside of MOOSCF is general in that it makes no requirement on the upstream source of the data. Geometric and flight condition properties can be computed using any software upstream of the S&C module, and then parsed to populate the MOOSCF. Several application specific functions have been developed, however, and the MOOSCF works particularly well with the NASTRAN Aeroelastic Solver, Digital DATCOM, and Tornado

Vortex Lattice Method (VLM) aerodynamic codes. Data from the MOOSCF can then be accessed by both the static and dynamic analysis routines, with the results passed back into the MOOSCF to be stored as aircraft attributes and used by the MDO framework optimizer.

5.2 Geometry Generation

Aircraft conceptual design is the subject of generating a geometry which fulfills a set of analysis objectives and constraints. More than 90% of the design variables in the VT High-Speed Aircraft MDO framework pertain to the geometry, with the remainder belonging to the mission performance and propulsion disciplines. The design of the outer mold line (OML) geometry and the internal structural layout are the fundamental objectives of, and the motive for creating, an MDO framework. As such, considerable effort was expended in developing the geometry model, the Virginia Tech Class Shape Transformation (VT-CST), for the MDO framework. This code, which is fully detailed in Ref. [25], was the foundation of the design optimization studies conducted using the VT High-Speed Aircraft MDO framework by Allison et al. [23, 24]. VT-CST was designed for the generation of supersonic configurations, but the mathematical methods on which it operates are not limited to these configurations. An example of some of the capabilities of VT-CST are shown in Figure 5.2. VT-CST does not directly pass data to the MOOSCF, but its significant influence on upstream disciplines demands its recognition herein.

The internal structural layout of a configuration can be just as influential as the OML. Until very recently, the VT High-Speed Aircraft MDO framework has lacked any internal geometry capabilities and has been exercised using empirical models of existing aircraft configurations to predict the weight and structural behavior of the airframe. One of the MDO

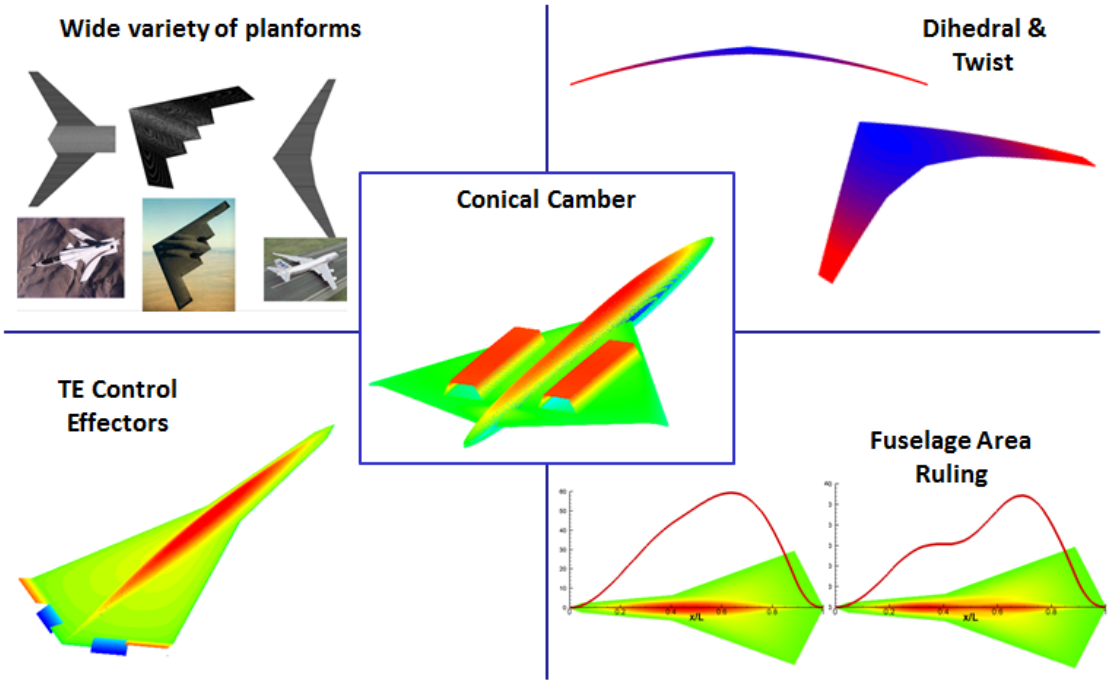

Figure 5.2: Example capabilities of the VT-CST geometry generation module

framework collaborators, Dr. Edward Alyanak, has helped to remedy this shortcoming with the development of MSTCGEOM, a geometry and aero-structural preprocessing engine.

5.2.1 MSTCGEOM

MSTCGEOM is a conceptual design preprocessing tool which takes high-level aircraft design parameters and structural information, and translates this information into a large number of input decks for a suite of aircraft design related software [91]. A summary of the available software interfaces can be seen in Figure 5.3. As stated in the reference guide written by the authors of the code, "MSTCGEOM has been developed to aid the air vehicle design engineer in generating physics based models for assessing the performance of a given concept. ...[MSTCGEOM] enables the production of information that is typically thought of as preliminary design information." [92]

Figure 5.3: Illustration of the available software interfaces within MSTCGEOM. *Note: many applications are still in the development stage

MSTCGEOM is a research code, and as such, the interfaces with different software packages are at different stages in the development process. The NASTRAN Aeroelastic Solver is one of the most developed, for example, and a number of the more detailed capabilities of NASTRAN are accessible through MSTCGEOM, including sizing optimization, composite materials analysis, static aeroelastic trim analysis, and flutter analysis. MSTCGEOM even includes an aerodynamic and structural mesh generator, requiring only the most fundamental of geometric inputs from the designer.

The MSTCGEOM code can be run as a standalone MATLAB executable, or executed within a MATLAB environment. Input is provided through a single text file that uses a 'card' style input deck. At the lowest level, a designer constructs components such as cross

sections and wing sections by defining the number of ribs, spars, bulkheads, etc., their sizes, and the material properties. Assembly cards are then used to make wings and fuselages from the individual components. In this manner a configuration can be 'prototyped' quite rapidly, and the designer still has excellent local control should it be desired. After defining a few flight condition and global property cards, the designers input file of a few hundred lines (often less) is translated into tens of thousands of lines of input file code for the desired programs. This is a powerful utility whose importance can't be overstated for MDO. An ongoing effort at Virginia Tech seeks to combine the OML abilities of VT-CST with the internal structural generation abilities of MSTCGEOM.

5.3 Aerodynamic Analyses

The S&C module and the associated MOOSCF are both data source independent. A large number of aerodynamic tools are capable of providing the required S&C data at varying levels of fidelity. Only those for which significant interface development efforts have been completed are reviewed herein. Each aerodynamic tool possesses certain benefits and limitations, and the review that follows is primarily intended to accentuate these characteristics.

5.3.1 NASTRAN Aeroelastic Solver

The most well developed of all MOOSCF interfaces is that for the NASTRAN Aeroelastic Solver. This is due to several factors, but chief among them is the thoroughly developed interface between MSTCGEOM and NASTRAN, which allowed for rapid implementation. The solver is capable of solutions for subsonic and supersonic flight, and is coupled with the structural solvers for which NASTRAN is known [93]. Subsonic solutions are obtained

through a Doublet Lattice Method (DLM), which comes with the implicit assumption of steady or harmonically oscillating flow over lifting surfaces which are nearly aligned with the flow direction. Solutions for subsonic flow also include modifications to the standard DLM to account for wing-body interference effects when a slender body is modeled. Supersonic solutions rely upon the ZONA51 solver, a linearized aerodynamic small disturbance solver produced by ZONA Technology, Inc. Much like the subsonic theory, this code also assumes lifting surfaces are nearly aligned with the flow. Neither solver is capable of capturing the effects of thickness of the lifting surface, but both are capable of computing S&C derivatives.

In addition to MSTCGEOM's ability to generate the required meshes, the NASTRAN Aeroelastic Solver's native coupling with the structural solver is a significant benefit to the user. Traditionally, aerodynamic codes require splining of loads between an aerodynamic solution and a structural mesh—a programmatic nightmare when developing code for design automation. NASTRAN and MSTCGEOM handle all splining of loads internally, and automatically compute trimmed solutions for the statically deflected aircraft shape. Stability and control analyses can then be conducted using either the rigid or the flexible stability derivatives, and the flexible-to-rigid ratios that are often sought by designers can be easily computed.

Despite the many benefits, the NASTRAN Aeroelastic Solver also has several drawbacks. For one, the input and output of the program are large and complex. Input complication is handled largely by MSTCGEOM, but the output files are tens of thousands of lines long and can vary drastically depending on run options. A file parsing utility has been developed within the MOOSCF to handle this, and it has proven to be quite robust. The most significant shortcomings of the NASTRAN Aeroelastic Solver are in the aerodynamic fidelity. NASTRAN's aerodynamic solvers cannot resolve thickness effects, predict aerodynamic fric-

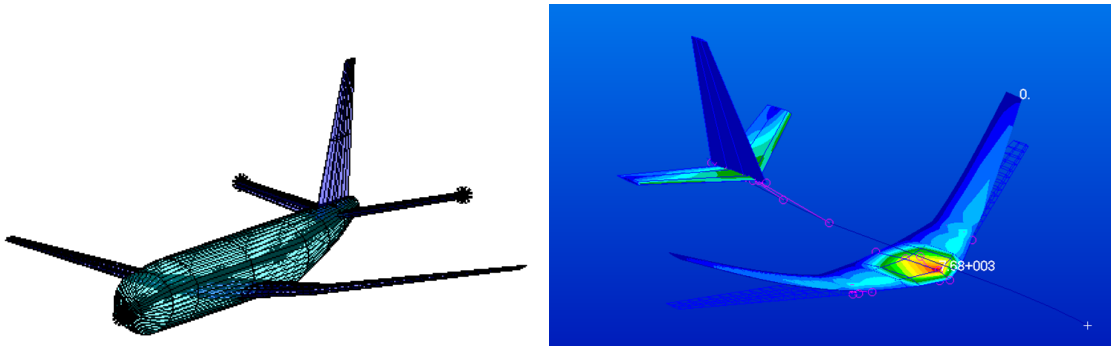

(a) Three Dimensional Transport Model

(b) NASTRAN results showing deflected structure and interal force contours

Figure 5.4: Comparison of a fully three dimensional transport configuration with the beam-fuselage and flat plate wing approximation of NASTRAN

tion or heating, and most detrimentally, it cannot predict drag of any kind. NASTRAN results must be supplemented with drag results from other sources. An example transport configuration created in MSTCGEOM is shown in Figure 5.4. Figure 5.4a illustrates the three dimensional model which was input, and Figure 5.4b shows the flat plate aerodynamic model about which NASTRAN solves the fluid equations.

5.3.2 ZONAIR

Advancing the fidelity of the aerodynamics can be accomplished through the ZONA Technology, Inc. software suite. These aerodynamic programs, which include ZAERO, ZONAIR, and ZEUS, all have great commonality in their input formats with varying intended uses and fidelity levels. ZONAIR, a subsonic/supersonic/hypersonic high-order panel method, currently serves as the primary aerodynamic analysis tool for the full MDO framework [94]. It features many of the same output capabilities of NASTRAN's Aeroelastic Solver, including the generation of S&C derivatives and the capability to model static aeroelastic effects

when coupled with a structural solver (though it requires load splining).

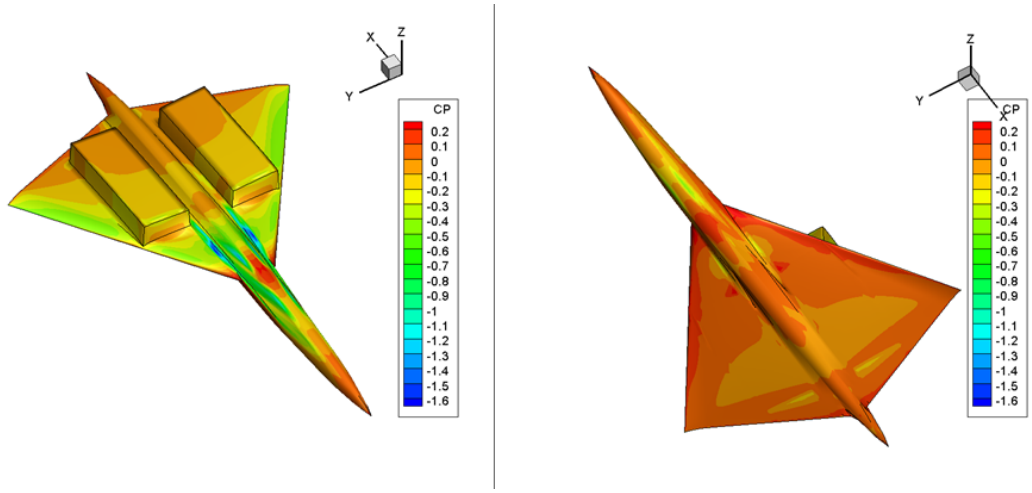

Figure 5.5: Example ZONAIR aerodynamic solution illustrating the ability to capture geometric thickness and conical camber effects

Additional features which make this program desirable are the resolution of lifting surface thickness, high angle of attack nonlinearity corrections, aerodynamic heating predictions, and drag predictions for induced, wave, and friction drag components. ZONAIR was even successful in predicting the aerodynamic performance of a wing with conical camber, a three dimensional wing shaping technique that other aerodynamic programs were found to be incapable of resolving [24]. An example of results computed by ZONAIR on a configuration with conical camber can be seen in Figure 5.5. VT-CST is already capable of producing the ZONAIR input files, but the output file parsing interface with MOOSCF is a task for future development. Fortunately, the output of ZONAIR and the other ZONA software products are very similar to that from NASTRAN, and a great deal of the NASTRAN file parsing utility will be able to be repurposed.

5.3.3 Digital DATCOM

Digital DATCOM, which is the digitized version of the USAF Stability and Control Data Compendium (DATCOM) [95, 96, 97], is a computer program which semiempircally computes S&C related parameters. The program leverages results from existing aircraft and physics-based relationships with empirical corrections to predict aerodynamic and S&C behavior. A text file input must be provided by the user which contains the geometric and flight condition information. Outputs from Digital DATCOM include trim data, static and dynamic stability derivatives, control derivatives, and estimates of aerodynamic performance (force and moment coefficients). Due to the sources of data available for the development of DATCOM, uncertainties in the results increase dramatically as the configuration being analyzed deviates from conventional tube-and-wing or fighter configurations. Digital DATCOM is also incapable of providing local values such as pressure distributions. Nonetheless, Digital DATCOM still exists as one of the most computationally efficient and accurate means by which to produce S&C derivatives. It has been well integrated with the MOOSCF, where the MATLAB Stability and Control Toolbox Digital DATCOM file parser is used to quickly extract data in a structured matrix format from the output text files [98].

5.3.4 Tornado Vortex Lattice Method

Tornado Vortex Lattice Method is a linear aerodynamic model which has been developed for conceptual aircraft design and educational purposes [99]. The code was constructed in Matlab, and features a command line input and many graphical techniques for convenient display of the output. All of the functions within Tornado are available to download as source files, and with the assistance of Dr. Alyanak, these functions are called directly by the MOOSCF to generate the desired data without the need for command line input or

Graphical User Interfaces (GUI). Many stability derivatives and aerodynamic properties are produced by Tornado, and there is significant overlap with the capabilities of the previously discussed aerodynamic analyses. Tornado is typically used to provide supplemental data to other analyses packages when required by the MOOSCF. The input files for Tornado are automatically generated by MSTCGEOM, which shortcut any interface development time that would have otherwise been required.

5.3.5 Low Fidelity Aerodynamic Suite

Three aerodynamic analysis codes known as WINGDES [100], AWAVE [101], and FRICTION [102], are collectively identified as the Low Fidelity Suite. These codes are of considerable value in the MDO framework due to their long history of validation and their split second execution times. They do not function well for unconventional configurations [24], but reasonable estimates of aerodynamic performance are easily obtained when the aircraft is more traditional. WINGDES is a panel method which computes global wing characteristics such as lift and induced drag. AWAVE is a modified version of the Harris wave drag code that can predict the volumetric wave drag for supersonic configurations. FRICTION, a code developed at Virginia Tech by Dr. William Mason, estimates the laminar and turbulent skin friction and form drag using equivalent flat plate skin friction methods. This suite of codes can be used to develop the drag polar under a superposition assumption—the total drag coefficient is the sum of the induced, friction, form, and wave drag components. Both VT-CST and MSTCGEOM are capable of producing input files to all three of these codes.

The low-fidelity suite is not without limits. Drag is a particularly difficult aerodynamic result to predict due to its intimate connection to viscous behavior, and these codes have been found to have large uncertainties under certain conditions [24]. Additionally, no means

of computing stability derivatives is available through their use, and they are incapable of modeling high lift devices. Despite these limitations, the low-fidelity suite of codes is an acceptable supplement to NASTRAN, for example, when drag prediction must be accomplished by another program.

5.4 Propulsion Analysis

The equations of motion developed in Chapter 3 explicitly included the thrust parameters in the derivation. It is common upon linearization about an equilibrium to model the thrust as an actuator with an appropriate dynamic model of the propulsion system to account for the inherently slow response of thrust actuation [61]. Alternatively, the thrust itself may be modeled as 'static' while its line of action is actuated to achieve thrust vectoring. Either way, it has become common in high-performance aircraft for thrust to be manipulated by a control system in some manner. While thrust control has yet to be implemented in the current S&C module, there are no technical assumptions which prevent its implementation. So, it is worth mentioning the propulsion models available in the VT High-Speed Aircraft MDO framework, though they are not exercised in the results of Chapter 6.

Two propulsion models have been implemented into the VT High-Speed Aircraft MDO framework [23]. The lower-fidelity model is based on the FLOPS Engine Cycle Analysis Module. FLOPS, or Flight Optimization System, is a lower fidelity aircraft design code composed of many different disciplinary models [53]. The engine cycle analysis module is designed specifically for early design generation of an engine deck—a structured table which details the thrust, fuel flow, and other performance data as a function of Mach number and altitude. The higher fidelity propulsion module uses NPSS, or the Numerical Propulsion Simulation System. NPSS is a state-of-the-art semiempirical model developed jointly by

government and industry. This program is quite complex, and its implementation into the VT High-Speed Aircraft MDO framework by Allison [23] is a noteworthy accomplishment. The output of FLOPs or NPSS could be used to develop a dynamic model of an engine to be used in the control system design.

5.5 Stability and Control Module Implementation

With all of the supporting disciplines outlined, the remaining details of the S&C module deal with its implementation into an MDO environment. The VT High-Speed Aircraft MDO framework is constructed and executed in Phoenix Integration's ModelCenter™ software. Modelcenter™ is a graphical environment which supports automation, integration, and design optimization [103]. The use of ModelCenter™ will be illustrated in Chapter 6 during the assembly of the transport aircraft empennage design problem. For now, it suffices to identify ModelCenter™ as a means by which data can be passed between functions either in volatile memory or via file format.

The simplest block diagram of the inputs and outputs of the S&C module is provided in Figure 5.6. Specific programs from those previously discussed are shown in the diagram, though the choice is not unique. Other analyses packages could replace those in the diagram, or they could be added to provide additional data. The process begins with geometry generation, either by VT-CST or another source, which requires a text file input from the user. Output from the geometry codes is written to a MSTCGEOM compatible format. In addition to the geometry data, MSTCGEOM also requires information regarding the flight conditions and desired input files it should generate. These must also be provided by the user, and are combined with the geometry data via ModelCenter™ file wrapper utilities to create a MSTCGEOM input deck. MSTCGEOM is executed and produces a host of output files.

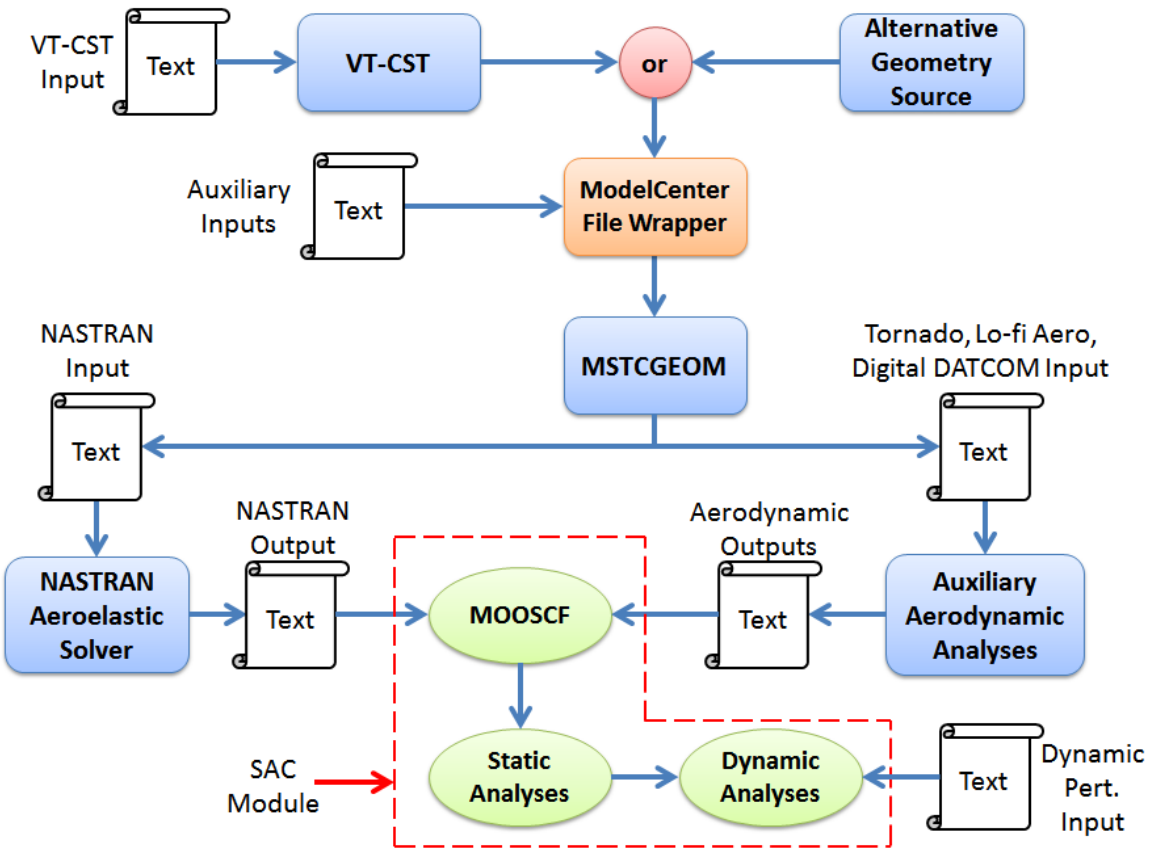

Figure 5.6: Block diagram of the data structure required upstream of the S&C module

Those shown in the block diagram include the NASTRAN, Tornado, and the low-fidelity aerodynamic suite input files. Note that Digital DATCOM is not currently supported by MSTCGEOM, and when utilized in the S&C module, the input file must be produced by a ModelCenter^{TM} file wrapper (or a similar external wrapper). The executables of these codes are then called, and their respective outputs made available to the MOOSCF, which parses them into volatile memory within the Matlab environment. Execution of the S&C module then takes place, which includes the static and dynamic analyses scripts. Static analyses check the applicable static stability constraints from Chapter 3, or in many cases, simply check flags passed in from the trim analysis of the preceding aerodynamic analysis. For each flight condition for which a dynamic analysis is desired, the static constraints are checked

first. If they are found to be satisfactory, the linearized models are constructed about the trim condition and the VCFQ method of Chapter 4 is initiated. Additional user input is required

```
# numCon = number of perturbation conditions for this FC
# nonDim = nondimensional units flag to indicate inputs are nondim, if false, units converted internally
# alpha  = vector (double) angle of attack disturbance (degrees, radians if nonDim=1);
# qhat   = vector (double) pitch rate disturbance (degrees/sec, nondim qhat if nonDim=1, qhat = q*cbar/(2*Uo))
# uhat   = vector (double) forward velocity disturbance (ft/sec, nondim uhat if nonDim=1, uhat = du/U)
# theta  = vector (double) pitch angle disturbance (degrees, radians if nonDim=1);
# beta   = vector (double) angle of sideslip distubance (degrees, radians if nonDim=1);
# phat   = vector (double) roll rate disturbance (degrees/sec, nondim phat if nonDim =1, phat = p*b/(2*Uo))
# rhat   = vector (double) yaw rate disturbance (degrees/sec, nondim rhat if nonDim =1, rhat = r*b/(2*Uo))
# phi    = vector (double) roll angle disturbance (degrees, radians if nonDim =1);
#
#   ~    = an empty spot, a 0.0 is NOT the same as empty!!

&Trim1
    numCon = 3
    nonDim = 0
    alpha =  [7,10,~]
    qhat = [~,~,~]
    uhat = [30,~,~]
    theta = [~,~,~]
    beta = [~,~,8]
    phat = [~,~,0.2]
    rhat = [~,~,~]
    phi = [~,~,~]
/

&Trim2
    numCon = 2
    nonDim = 0
    alpha =  [7,5]
    qhat = [~,0.1]
    uhat = [30,~]
```

Figure 5.7: Example dynamic perturbation condition input file

by the VCFQ approach in order to analyze the desired disturbance conditions. The input file, called the dynamic perturbation condition input file (`dyn_pert_con.inp`), is structured to allow for multiple gust cases for each flight condition constructed in MOOSCF. For example, a user could analyze a single gust case at climb and ten gust cases during cruise. An excerpt of an example dynamic perturbation condition input file can be seen in Figure 5.7.

Following the static analyses, the construction of the LTI systems about the trim conditions and the parsing of the dynamic perturbation condition input file, the LMI constraints of Chapter 4 are ready to be assembled. Each gust case for each flight condition for which a dynamic S&C analysis is desired will have its own LMI system, and each will require its own search for a feasible control system. In this manner, a designer is assessing the feasibility that

feedback control could make the aircraft perform satisfactorily at different flight conditions under a range of stimuli. Once the LMI's have been constructed, any of a number of convex optimization techniques and software packages can be used to find feasible solutions [46]. Since the remainder of the S&C module is executed within Matlab, it is convenient to use the Robust Controls Toolbox and the associated LMI Toolbox built into Matlab [104]. The LMI toolbox has many powerful functions for solving a breadth of control and system identification problems, but it is also capable of solving generic LMI systems established by the user. A special feasibility function, `feasp`, searches for solutions $x \in \mathbb{R}^n$, which constitute the elements of matrix variables $X_1, \ldots, X_k$ (with prescribed structure), that satisfy the LMI system

$$A(x) < B(x), \tag{5.1}$$

where $A(x)$ and $B(x)$ are any generic LMI. Solutions to the decision variables, x, are sought using an interior-point algorithm called the Projective Algorithm [105]. This algorithm is known to be of polynomial-time complexity [104], therefore the number of flops $F(\epsilon)$ needed to compute an ϵ-accurate solution is bounded by

$$F(\epsilon) \leq MN^3 \log(V/\epsilon), \tag{5.2}$$

where M is the row size of the LMI system, N is the total number of scalar decision variables, and V is a data-dependent scaling factor. The existence of this upper bound is important, since numerical search without any guarantee of convergence could be cost prohibitive for use inside of an MDO environment.

Chapter 6

Transport Aircraft Empennage Design Example

As the VCFQ approach matured, and the S&C module began to develop into a software utility capable of fulfilling the demands of the MDO framework, the need for a practical development problem became apparent. The ideal example problem would be of genuine engineering interest, but contain fewer complications than the high-performance aircraft with nontraditional control effectors for which the VT High-Speed Aircraft MDO framework is designed. Fortunately, Virginia Tech plays host to other multidisciplinary aircraft design projects, and among these are efforts in the design of advanced transport aircraft like the Truss-Braced Wing (TBW). TBW aircraft, like that in Figure 6.1, seek to leverage the added structural support of a truss to reduce the thickness of wings, reduce the wing sweep, and increase the span to achieve an overall structural weight savings. Design projects involving the TBW have been at Virginia Tech for more than ten years, and the result is a mature MDO framework, called the VT Transport Aircraft MDO, which continues to see regular development [39, 21, 22]. In addition to truss-braced configurations, the VT Transport

Aircraft MDO is capable of design optimizations for strut-braced and traditional cantilever configurations.

Figure 6.1: An example Truss-Braced Wing configuration

The VT Transport Aircraft MDO framework is not unlike the VT High-Speed Aircraft MDO for which the new S&C module is being primarily developed. Both use an N^2 diagram approach and are implemented in a ModelCenter^{TM} environment, both use FLOPS for a portion of the weights calculation and for mission performance analysis, and both use a similar low fidelity suite of aerodynamic codes (appropriately modified to account for the truss-related aerodynamics in the VT Transport Aircraft MDO). What is absent from both, until now, is any kind of S&C analysis. The VT Transport Aircraft MDO framework has a particular emphasis on the structural design of the wing and truss members, and static or dynamic S&C considerations have not yet been taken into account. In fact, the empennage of the aircraft is simply developed from a baseline configuration and left unchanged, despite reconfiguration of the wing and truss—an assumption with potentially serious consequences as the *CG* and the wing aerodynamic center move with the unsweeping of the wing. A stated future objective of the TBW researchers has long been to include empennage sizing to provide for longitudinal and lateral-directional stability [22]. An example of a typical transport aircraft empennage can be seen in Figure 6.2.

Figure 6.2: Photograph of an empennage, or tail assembly, from a typical modern transport aircraft

The empennage design effort that follows was constructed to exercise the new S&C module for development purposes, and to establish the means by which it could be used for empennage sizing in the VT Transport Aircraft MDO. Transport aircraft are less complicated from an S&C point of view than high-performance configurations, since the aerodynamics are largely decoupled and the control effectors exhibit fewer cross-axis moments. Even though the S&C module was designed to handle complicated high- and low-speed configurations with many cross-coupled actuators, it should work equally well with conventional configurations. The TBW does contain a certain degree of atypical aerodynamic behavior due to the presence of trusses and struts, which will likely interact with the empennage through vortex shedding and wake interactions. This phenomena must be captured by the aerodynamics discipline for its influence on S&C to be fully realized. The TBW group did a thorough study of the drag penalties associated with wing-strut intersections through computational fluid dynamics (CFD) analysis and response surface modeling [106], but these efforts did not focus on downwash and performance penalties which would result on the tail. So, the empennage sizing example was conducted on a typical cantilever-wing configuration to avoid the complications of truss-empennage interactions.

6.1 Relaxed Static Stability Design Problem

The goal of this design study was to redesign the empennage of a typical transport aircraft subject to dynamic and relaxed static stability constraints using the tools developed for the S&C module. A model which is similar to the Boeing 737-800, shown in Figure 6.3, was used as the baseline configuration. This medium-range configuration is derived from the same baseline as the TBW study conducted in [107]. The baseline is sized for a mid-range mission of 3,115 nautical miles, a cruise Mach number of 0.78, and to seat 189 passengers. A complete set of the major model parameters are included in Table 6.1 of Section 6.1.1.

Figure 6.3: A Boeing 737-800 shortly after takeoff

Design optimization of the empennage was conducted in two parts. First, the horizontal tail was sized using a scissor plot technique combined with a dynamic analysis using the VCFQ approach. Second, the vertical tail was designed using static constraints and a dynamic analysis using the VCFQ approach. Several assumptions were used in the design optimization to simplify other technical disciplines and yet fully exercise the S&C module's capabilities. Chief among these is that the only dimensions to be altered during optimization were those of the tail itself. This is consistent with the two-tiered optimization approach that would likely be taken by in the VT Transport Aircraft MDO framework, wherein a fixed

configuration would be analyzed and fitted with the best possible tail—leaving modification of other aircraft parameters to a higher tier of the optimization process. The tails will also only be scaled in area, since the selection of sweep, thickness to chord ($^t/_c$), and aspect ratio are typically made based on transonic aerodynamic performance and not S&C considerations [59]. Thus, the design problem is like a hypothetical exercise to retrofit an existing aircraft with smaller tails if Federal Regulators decided that the static stability demands of the FAR's could be relaxed.

6.1.1 Baseline Model Details

Before design optimization of an RSS aircraft can begin, the baseline model must be constructed. Only minimal changes in the geometry are required during the redesign, so the geometry is driven by a simple Python script. Table 6.1 contains the details of the geometry of the baseline configuration. Many of the dimensions were estimated from figures in resources published by Boeing [108] for the purposes of airport management, and airfoils for the tail were selected based on initial sizing principals in Refs. [4] and [5]. Wing airfoil coordinates for the 737 were found in the well known airfoil database in Ref. [109]. Control surface sizes and maximum deflections were extracted from figures and data available from Ref. [110] for similar aircraft.

In addition to the OML parameters in the table, significant effort was expended in the modeling of the internal structure of the configuration. This process was greatly aided by MSTCGEOM, and was carried out using an approximate structural layout ascertained from cutaway figures available in the public domain [111]. The Python script which drives the tail area is wrapped, via ModelCenter^{TM}, with MSTCGEOM to generate and manipulate the baseline configuration seen in Figure 6.4. The aerodynamic model is presented in Figure 6.4a

Table 6.1: Baseline Configuration Model Parameters

Characteristic	Value
TOGW, lb	173,930
Total Span, ft	113
Wing $^1/_4$ Chord Sweep, deg	25.08
Wing Area, ft^2	1413
Wing Root Chord, ft	24.5
Wing Root t/c	0.14
Wing t/c at Engine	0.13
Wing Tip Chord, ft	5.0
Wing Tip t/c	0.115
H-Tail $^1/_4$ Chord Sweep, deg	28.8
H-Tail Area, ft^2	516.2
H-Tail Root Chord, ft	13.07
H-Tail Root t/c	0.08
H-Tail Tip Chord, ft	8.0
H-Tail Tip t/c	0.08
V-Tail $^1/_4$ Chord Sweep, deg	28.8
V-Tail Area, ft^2	356.5
V-Tail Root Chord, ft	18.0
V-Tail Root t/c	0.08
V-Tail Tip Chord, ft	5.0
V-Tail Tip t/c	0.08
Max Elevator Def., deg	25.0
Max Elevator Def. Rate, deg/s	50.0
Elevator bandwidth, rad/s	30.0
Max Rudder Def., deg	25.0
Max Rudder Def. Rate, deg/s	50.0
Rudder bandwidth, rad/s	30.0
Max Aileron Def., deg	20.0
Max Aileron Def. Rate, deg	50.0
Aileron bandwidth, rad/s	30.0
Maximum Thrust, lb	27,300
Design Cruise Altitude, ft	35,000
Fuel Weight, lbs	46,000

and 6.4c, where the modeled OML is translucent to allow viewing of the internal structure. Figures 6.4b and 6.4d show the structural model as input into NASTRAN. The fuselage is modeled as a beam and represented by the bold black line. Red markers near the leading

edges of the wing indicate the point-masses which are placed to account for the weight of the engines.

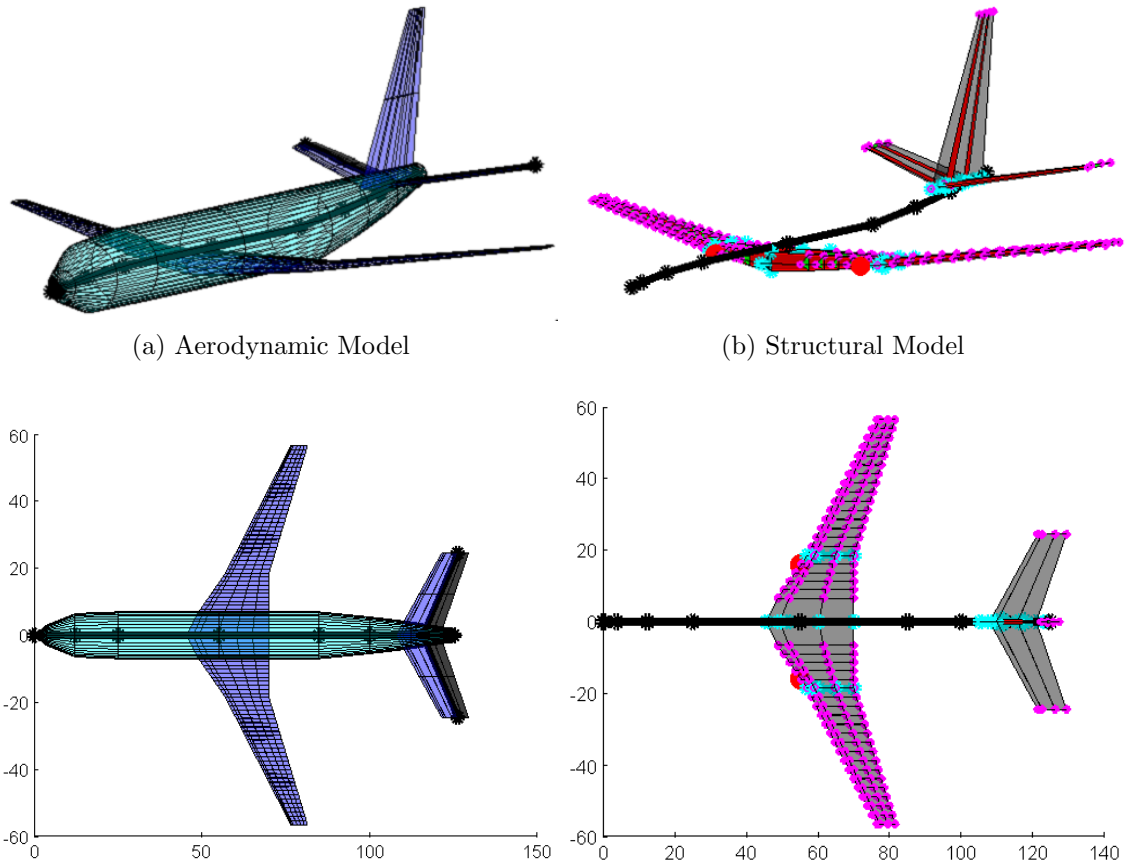

(a) Aerodynamic Model

(b) Structural Model

(c) Aerodynamic Model Top View

(d) Structural Model Top View

Figure 6.4: Baseline configuration based on the 737-800 and generated by MSTCGEOM

The wings were broken into multiple material property 'groups', along with fuselage, horizontal tail, and vertical tail material groups. These component groups could be independently assigned a density and an elastic modulus, which facilitated the matching of scaled aircraft mass and inertial properties which were provided by the TBW research group for a similar configuration. First, holding the elastic moduli fixed, the density of each material group was varied by an optimizer in order to minimize the error between the desired mass

and moments of inertia of the model with those of the reference configuration. Then, holding the material densities fixed, the elastic moduli of the wing groups were optimized to match the wing deflection at several points along the wing. The final baseline configuration is then one which matches the global parameters of mass and inertia well, and simultaneously captures the static-aeroelastically deflected shape of the wing. The elastic moduli of the fuselage and tails were set to be arbitrarily high, effectively making these components rigid. It is important to note that despite the matching of the inertial properties and the static aeroelastic shape, the distribution of mass and stiffness within the structure may still not be precise. Analyses which are sensitive to the distribution of material properties, such as a flutter analysis and its subsequent modal analysis, would likely require further consideration.

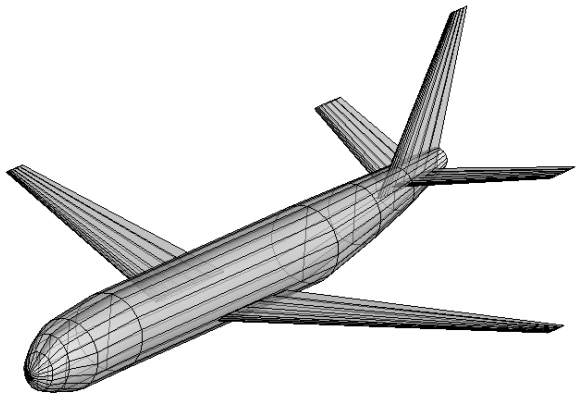

Figure 6.5: The baseline configuration as modeled in Digital DATCOM

A Digital DATCOM model of the baseline configuration was also constructed. This model, shown in Figure 6.5, is geometrically identical to the NASTRAN model with the exception of the break in the wing trailing edge (due to modeling limitations of Digital DATCOM). The mass properties and trimmed conditions computed in NASTRAN are passed to Digital DATCOM via ModelCenter^{TM} for analysis. Digital DATCOM is capable of generating certain stability derivatives that NASTRAN cannot produce. In particular, the dynamic

derivatives which deal with $\dot{\alpha}$, and drag coefficients are not computed by NASTRAN.

6.2 Horizontal Tail Sizing

It is common in the literature to use the redesign of the horizontal tail of an otherwise fixed configuration to demonstrate a new integrated control design technique [41, 45, 112]. Not surprisingly, this same task is useful in demonstrating the utility of the VCFQ approach. The sections that follow detail the process by which the RSS aircraft's horizontal tail was sized. A rigorous demonstration of the process is given on the initial baseline configuration, and then the final results of the design optimization are presented.

6.2.1 Scissor Plots

When designing the empennage of an aircraft during the preliminary design phase, it is useful to utilize a diagrammatic tool known as a scissor plot. Details of scissor plot construction can be found in many aircraft design texts, but one of the more thorough studies is found in Ref. [59]. The axes of a scissor plot are the horizontal tail area S_{HT} on the ordinate, and the nondimensional CG location $\bar{x}_{cg}$ on the abscissa. Often the horizontal tail area will be reported as a nondimensional tail area ratio given by

$$S_{r_{\mathrm{HT}}} = \frac{S_{\mathrm{HT}}}{S_{\mathrm{ref}}}. \tag{6.1}$$

The purpose of the scissor plot is to graphically depict the static stability and static control boundaries of the aircraft as a function of the CG location. When constructed, a scissor plot helps identify the smallest tail capable of generating the necessary moments for a given range of CG locations. Every aircraft requires a range of trimmable CG locations to ac-

commodate changes in mass distribution from fuel burn, payload changes, and passenger movement. An example of a simplified scissor plot is shown in Figure 6.6. The forward *CG* boundary is a static control boundary, indicating the aircraft is incapable of trimming when the *CG* is forward of that line. Forward *CG* boundaries are typically derived from low-speed control requirements where the dynamic pressure over the tail is at a minimum, and yet the moments demanded of the tail are at a maximum. Static control constraints were discussed in Section 3.3, and include cases such as takeoff rotation and high-lift trim requirements. The aft boundary is a stability boundary dictated by a prescribed degree of

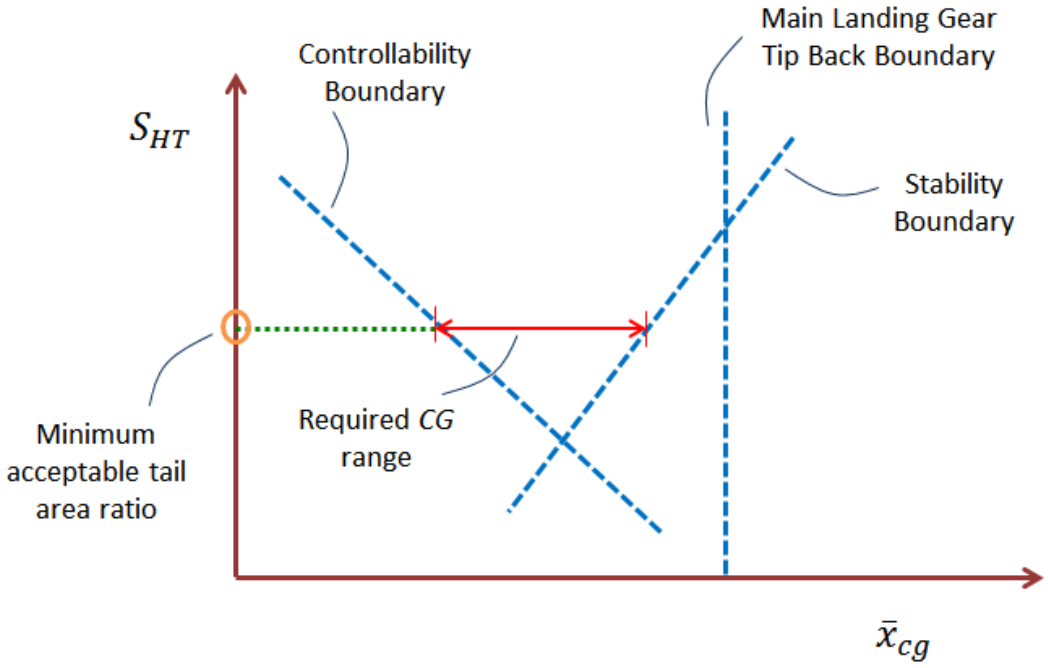

Figure 6.6: Simplified scissor plot showing forward and aft *CG* boundaries for a given tail area

static stability and the main landing gear location (to prevent tip back when on the taxiway). Typical static margins for transport aircraft range from 5-20%, and can be zero or negative for higher performance aircraft [4]. When designing an RSS aircraft, it is precisely these aft stability boundaries which we seek to relax. Rather than a hard constraint on the static

margin, a dynamic constraint is instead applied which requires the configuration closed-loop performance to satisfy dynamic requirements.

6.2.2 Longitudinal Test Cases

Linearized, time invariant systems were constructed at each flight condition using the results and assumptions of Section 3.2.4 and Appendix A. The resulting longitudinal state vector is

$$x_{\text{long}} = \begin{bmatrix} V & \alpha & \hat{q} & \theta \end{bmatrix}^T. \tag{6.2}$$

Six flight conditions were chosen to construct the scissor plots based on engineering judgment of where the most critical conditions are likely to exist. The six flight conditions are: takeoff at sea level, heavy configuration at climb, heavy configuration at cruise, light configuration at cruise, light configuration at descent, and light configuration at landing. Heavy configurations are assumed to have burned 5% of the total fuel weight and have a baseline Gross Weight (GW) of 171,630 lbs., and light configurations are assumed to have burned 75% of the total fuel weight with a baseline GW of 139,430 lbs. Here, baseline refers to the weight of the baseline configuration, since with each tail size perturbation the aircraft weight will necessarily change. The thrust at each trimmed condition is modeled as being constant. Each of the six flight conditions is subjected to a combination of static control and/or dynamic performance constraints which must be achieved. Table 6.2 provides the test matrix of longitudinal flight conditions and their associated static constraints and dynamic perturbation conditions.

For each Flight Condition, a trim card was created in the NASTRAN input file via MSTCGEOM to compute the trimmed aeroelastic solution. Static trim constraints can be explicitly executed by NASTRAN, and failure to trim the configuration prevents the data

Table 6.2: Longitudinal Flight Condition Test Matrix

Flight Condition (FC)	Description	Static Analyses	Dynamic Analyses
FC-I	Heavy @ Takeoff Mach = 0.2 Alt. = 0.0 ft n = 1.0 GW = 171,630 lbs	• Takeoff rotation • Trim at max lift	• No dynamic cases
FC-II	Heavy @ Climb Mach = 0.5 Alt. = 10,000 ft n = 1.0, 2.5 GW = 171,630 lbs	• Trim • Trim at high load factor	• Vertical gust • Horizontal gust • Mixed gust
FC-III	Heavy @ Cruise Mach = 0.7 Alt. = 35,000 ft n = 1.0 GW = 171,630 lbs	• Trim	• Vertical gust • Horizontal gust • Mixed gust
FC-IV	Light @ Cruise Mach = 0.7 Alt. = 35,000 ft n = 1.0 GW = 139,430 lbs	• Trim	• Vertical gust • Horizontal gust • Mixed gust
FC-V	Light @ Descent Mach = 0.5 Alt. = 10,000 ft n = 1.0, 2.5 GW = 139,430 lbs	• Trim • Trim at high load factor	• Vertical gust • Horizontal gust • Mixed gust
FC-VI	Light @ Landing Mach = 0.2 Alt. = 0.0 ft n = 1.0 GW = 139,430 lbs	• Trim at max lift	• No dynamic cases

for dynamic analysis from being generated. As the tail area changes, the airframe structure is regenerated and the mass and aerodynamic properties recomputed. The *CG* location was

then forcibly moved fore and aft to find the boundaries of acceptable performance. Center of gravity repositioning was accomplished through the reallocation of material density within the fuselage while maintaining a fixed total vehicle mass. The elevator, which is modeled as being the last 30% of the horizontal tail chord and spanning the full width of the tail, is scaled along with the tail area.

Dynamic perturbation conditions were generated from the derived equivalent gusts discussed in Section 4.4.4. Vertical and horizontal gusts were applied to the α and V state, respectively, where the α perturbation was computed using Eq. (3.5), and the V perturbation was directly obtained from the gust magnitude. Mixed gusts, that is a gust applied about both the vertical and horizontal conditions, were applied such that the magnitude of the gust velocity was equal parts vertical and horizontal.

6.2.3 Baseline Longitudinal Characteristics

Perhaps the best way to illustrate the horizontal tail sizing process is to perform the search for the most forward and aft CG locations on the baseline configuration. By holding the tail size fixed and only moving the CG location, the bounds for this single tail area can be computed.

Before beginning the optimization of an RSS transport aircraft, it is helpful to examine the open-loop characteristics of the baseline configuration. The open-loop eigenvalues of the baseline configuration during the heavy cruise condition are shown in Figure 6.7a, with those during the climb condition in Figure 6.7b. Similar plots for the lightweight configuration cruise and descent conditions can be seen in Figures 6.8a and 6.8b, respectively. Plotted along with the eigenvalues are the short-period modal boundaries, computed for each flight condition, as given by the MIL-STD-1797. These pole plots clearly indicate that the open-

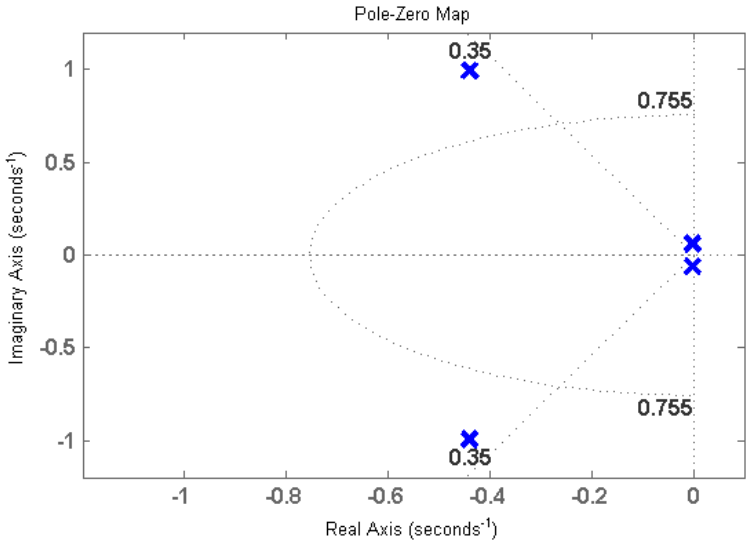

(a) Heavy Cruise Condition

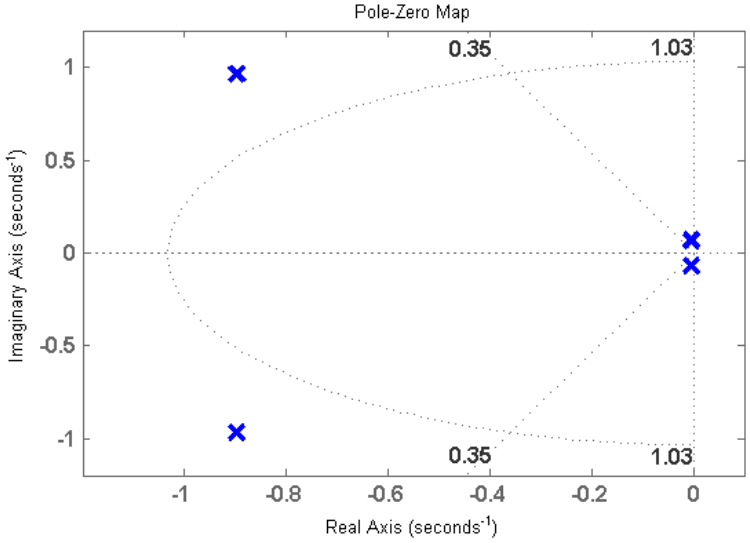

(b) Heavy Climb Condition

Figure 6.7: Open-loop eigenvalues of the longitudinal equations of motion for the heavy baseline configuration. Dotted lines represent the computed MIL-STD-1797 short period modal boundaries

loop baseline configuration satisfies the flying qualities requirements at each flight condition and loading. The static margin, SM, of the baseline configuration for each flight condition and loading is given in Table 6.3. These values are typical of transport aircraft [4, 5], and

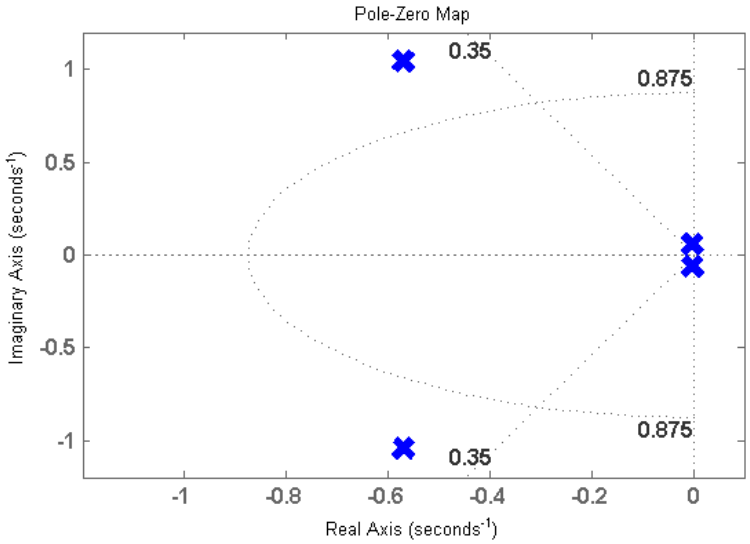

(a) Light Cruise Condition

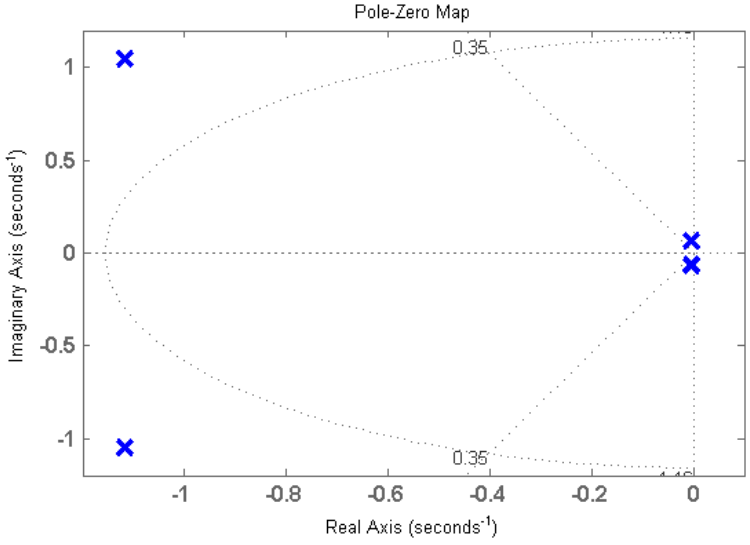

(b) Light Descent Condition

Figure 6.8: Open-loop eigenvalues of the longitudinal equations of motion for the light baseline configuration. Dotted lines represent the computed MIL-STD-1797 short period modal boundaries

the fact that they are all positive reflects the FAR requirement of static stability during all phases of flight.

Table 6.3: Baseline Configuration Static Margin

Flight Condition	Lightweight	Heavyweight
Sea Level	0.095	0.087
Climb	0.127	0.131
Cruise	0.186	0.222

To find the range of acceptable *CG* locations subject to the constraints of Table 6.2, a design optimization was constructed in the ModelCenter™ environment. The model includes a pair of high-level scripts to control the size of the horizontal and vertical tails, as well as the *CG* location. These models were wrapped into MSTCGEOM, where the aero-structural model was produced and then analyzed by the subsequent analysis, NASTRAN. Outputs from NASTRAN are passed through a preprocessor, written in Matlab, to extract geometric and trim condition information so that Digital DATCOM can be executed at the identical flight conditions. A wrapper passes all the pertinent information to Digital DATCOM, which is then executed. All of the results from the upstream disciplines are then passed into the S&C module. The S&C module is written in Matlab, and all of the static and dynamic constraints placed on each flight condition are evaluated within this module. A wrapper returns all of the data from the S&C module back to the ModelCenter™ environment, where optimizers and post-processing routines can operate on the results. The empennage design framework can be seen in Figure 6.9.

Search for the aft *CG* Limit

The first case to be examined was the aft *CG* search for both the light and heavy loading conditions. A gradient based optimizer was given control of the *CG* location, and the value was maximized (moved aft) until one of the static or dynamic constraints was violated. As predicted, the dynamic constraints were the first to be encumbered as the configuration

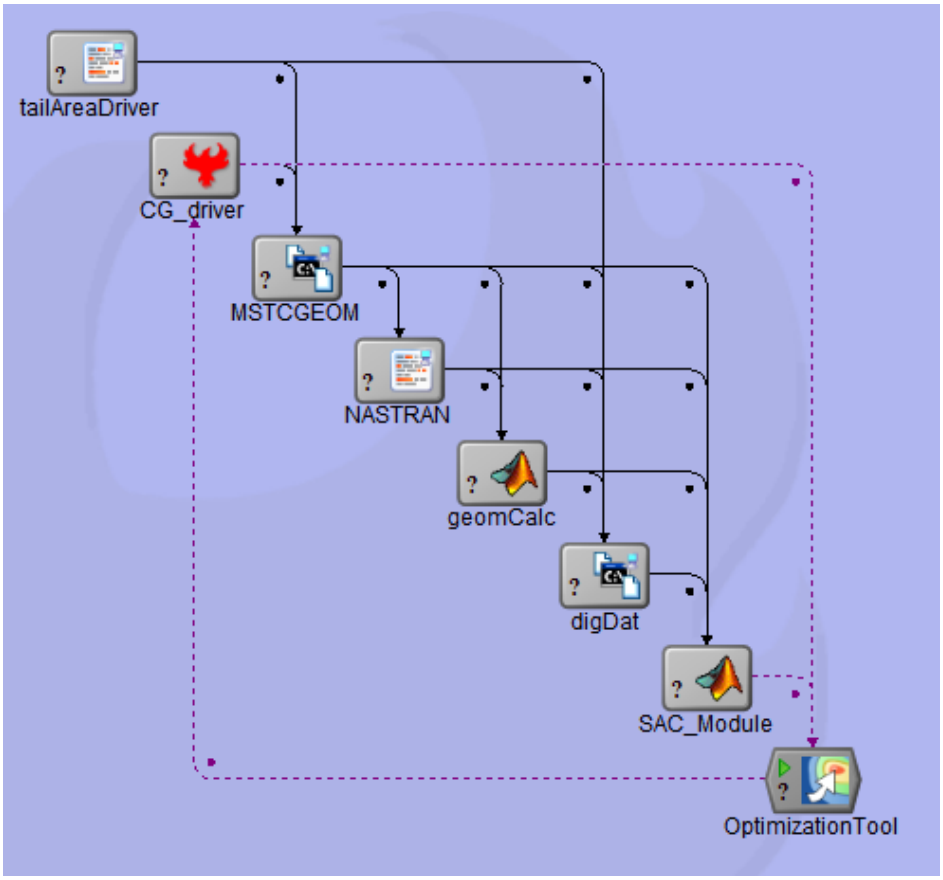

Figure 6.9: Screenshot of the empennage design framework within the ModelCenter™ environment

grew less stable, and the required augmentation of the dynamics became greater. Figure 6.10 shows the variation of the static margin at each flight condition and loading, clearly indicating the static instability which results from an aft CG location. Samples in Figure 6.10 may appear to have been taken sporadically along the x-axis, but this is simply a consequence of the optimizer's search for the aft-most CG. In fact, the cluster of points around $\bar{x}_{cg} = 0.9$ is indicative of the optimizer refining the local search to find the aft-most CG near this region. From the figure, it is easily discerned that the baseline configuration becomes statically unstable at approximately $\bar{x}_{cg} = 0.6$ in each flight and loading condition. It is also interesting to observe the shift in the open-loop eigenvalues of the configuration as the CG is moved

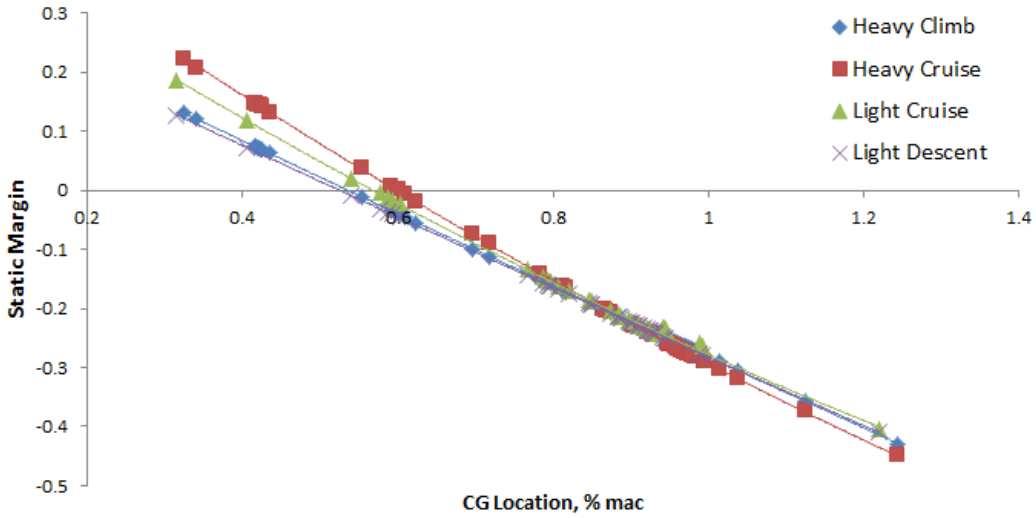

Figure 6.10: Baseline configuration: static margin vs. $\bar{x}_{cg}$

aft. The behavior in both heavy and light configurations in climb/descent and cruise is qualitatively identical, so only the open-loop eigenvalues of the heavy climb condition are shown in Figure 6.11. The results are representative of the classical behavior of an aircraft as it becomes less stable [60]. Short-period eigenvalues, which are typically oscillatory in nature, degenerate into overdamped real roots which rapidly diverge from each other along the real axis. Eventually, one of these short-period roots blends with the phugoid eigenvalues near the origin before crossing into the right-half plane and becoming unstable. The fact that the baseline configuration exhibits the predicted behavior with the aft movement of the *CG* is a good indicator that the model is capturing the correct dynamic effects in response to a reduction in static stability.

Before constructing dynamic models at each flight condition and performing the closed-loop analysis, a static trim analysis was executed in NASTRAN. Figure 6.12 illustrates the resulting elevator deflection to trim for each of the flight conditions where dynamic cases were considered. Results of the trim analysis are intuitive in that the elevator deflection to trim decreases as the aircraft becomes unstable, and ultimately changes direction. The magnitude

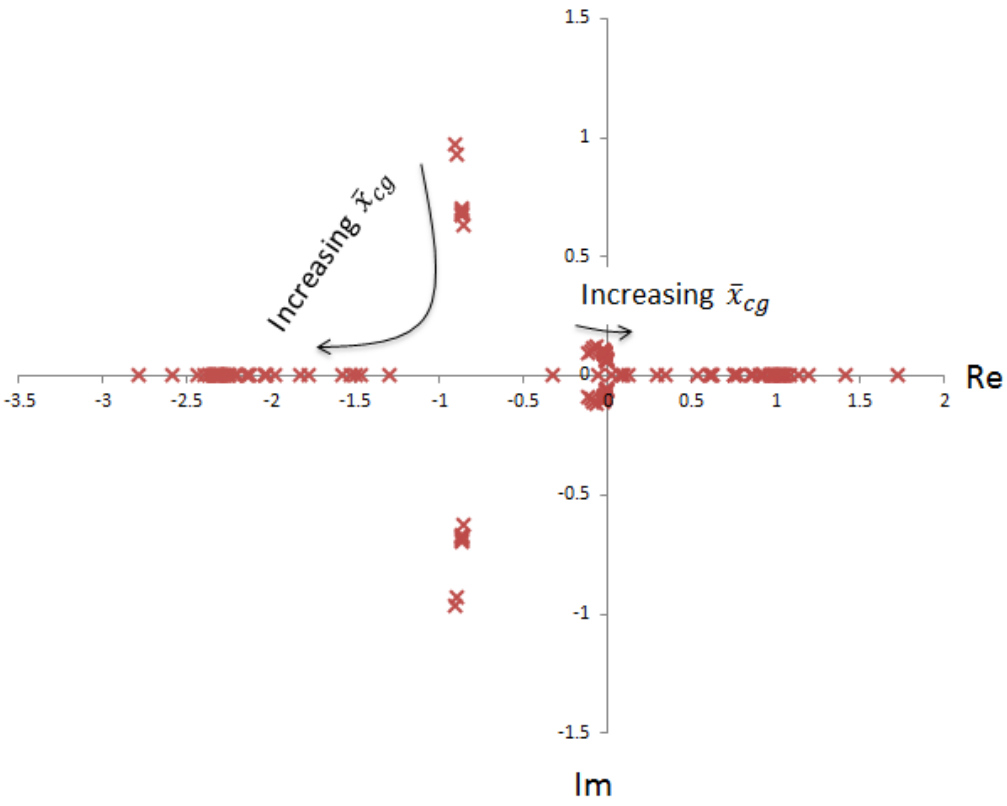

Figure 6.11: Open-loop eigenvalues of the longitudinal model of the baseline configuration in the heavy climb flight condition, computed for each $\bar{x}_{cg}$

of the trimmed deflections must be accounted for in the dynamic analyses, since the maximum allowable elevator travel must account for the total contributions of the static trim inputs, dynamic disturbance rejection inputs, and maneuver margin. For this reason, the maximum elevator travel available in the dynamic analysis is also flight condition dependent, and is governed by the relationship

$$\delta_{\text{dyn}} = \delta_{\text{max}} - |\delta_{\text{trim}}| - \delta_{\text{mmar}}, \tag{6.3}$$

where δ_{max} is the total maximum elevator deflection given in Table 6.1, δ_{trim} is the trimmed elevator deflection, and δ_{mmar} is the maneuver margin. The absolute value sign is indicative

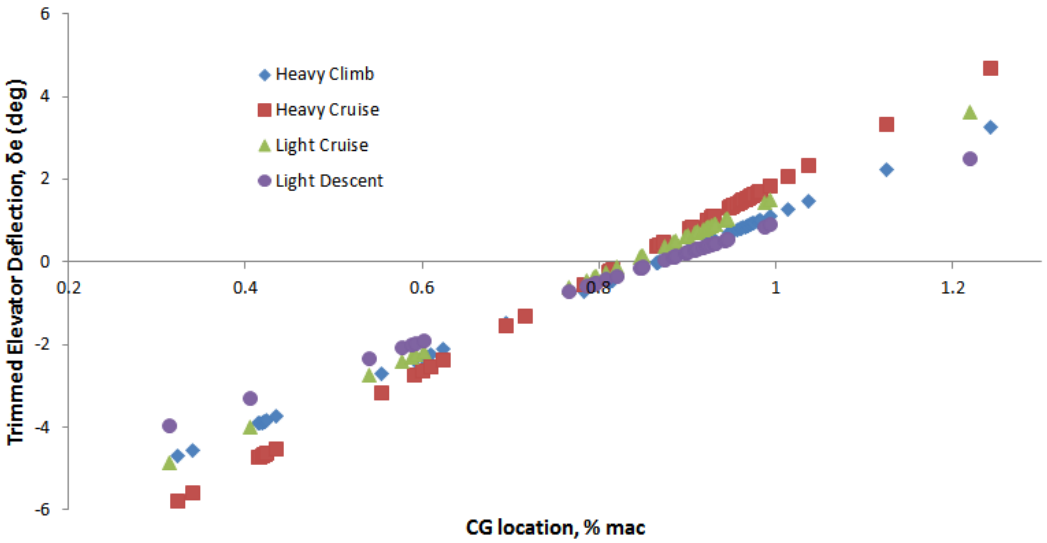

Figure 6.12: Trimmed elevator deflection, δ_e, computed for each flight condition, plotted versus $\bar{x}_{cg}$

of the fact that the net reduction in available input due to static trim is assumed to be symmetrical about the elevator zero deflection state. For example, if the trimmed deflection is elevator-up at five degrees, then there is technically $\delta_{\max}+5°$ of available downward elevator travel and $\delta_{\max} - 5°$ of available upward elevator travel—an asymmetry which cannot be modeled using the LMI's of Chapter 4. Thus, the conservative choice of a symmetrical reduction in both upward and downward elevator travel was made. When the trimmed elevator deflection is small, as is typical of RSS aircraft, the error associated with this approximation is small. In compliance with the FAR's, δ_{mmar} is assumed to be 25% of the maximum effector travel [13, 14].

An interesting observation regarding the trimmed elevator deflection of Figure 6.12 is the slight nonlinearity present in the curves. The aeroelastic effects resolved by NASTRAN during the trim solution are the source of this nonlinearity. Figures 6.13 and 6.14 show the aerodynamic forces applied to the configuration at the baseline forward *CG* location of $\bar{x}_{cg} = 0.32$, and an aft *CG* location of $\bar{x}_{cg} = 1.0$ at the heavy cruise condition. When

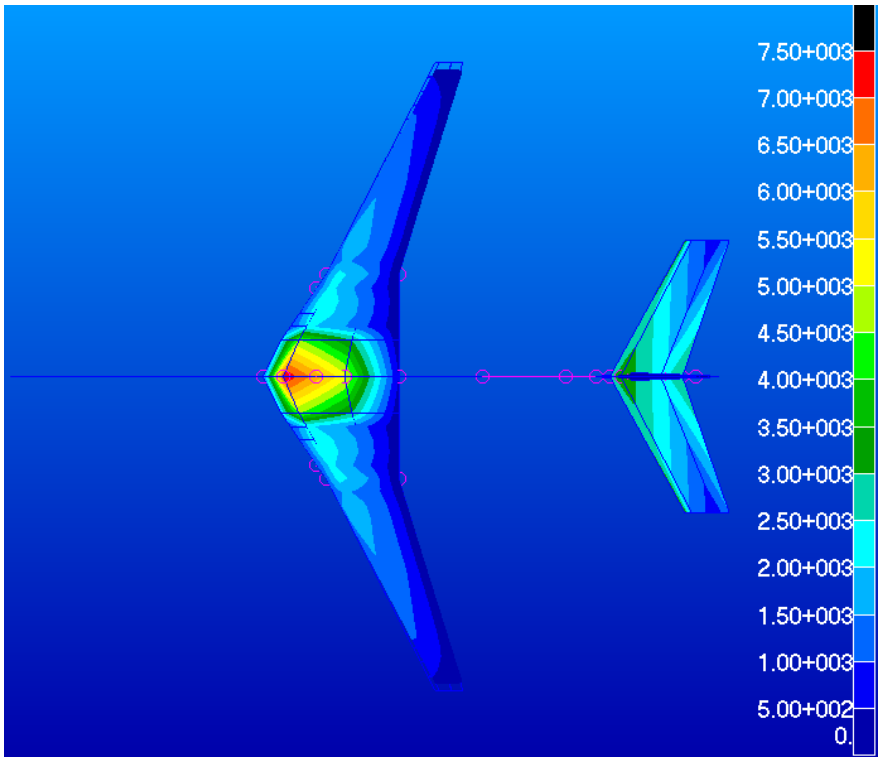

Figure 6.13: Aerodynamic force contours overlayed on the baseline configuration during heavy cruise, $\bar{x}_{cg} = 0.32$

the *CG* shifts aft, the wing is gradually unloaded while the horizontal tail is loaded in order to maintain the lift equal to the weight. This effect can be easily seen by comparing the magnitudes of the forces resolved on the tail in Figure 6.14 as compared to those in Figure 6.13. The change in wing loading also causes a change in the wing displacement, which in turn alters the aerodynamic performance of the wing. Nonlinearity in the trim results, therefore, are a direct result of the wing aeroelastic response to a redistribution of lift on the configuration.

Not surprisingly, the elevator deflection to trim also has strong implications on the trimmed drag increment, $\Delta C_{D_{\text{trim}}}$. Figure 6.15 shows the trimmed drag increment versus the *CG* location for the four up-and-away flight conditions as predicted by Digital DATCOM. The results are in agreement with those of Refs. [5] and [113], and they illustrate

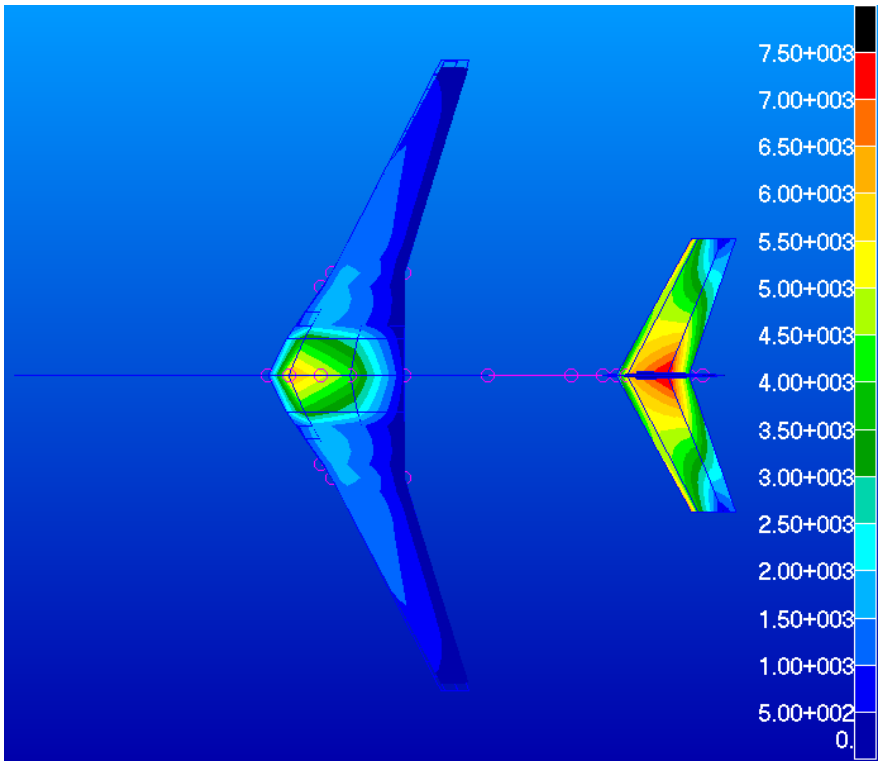

Figure 6.14: Aerodynamic force contours overlayed on the baseline configuration during heavy cruise, $\bar{x}_{cg} = 1.0$

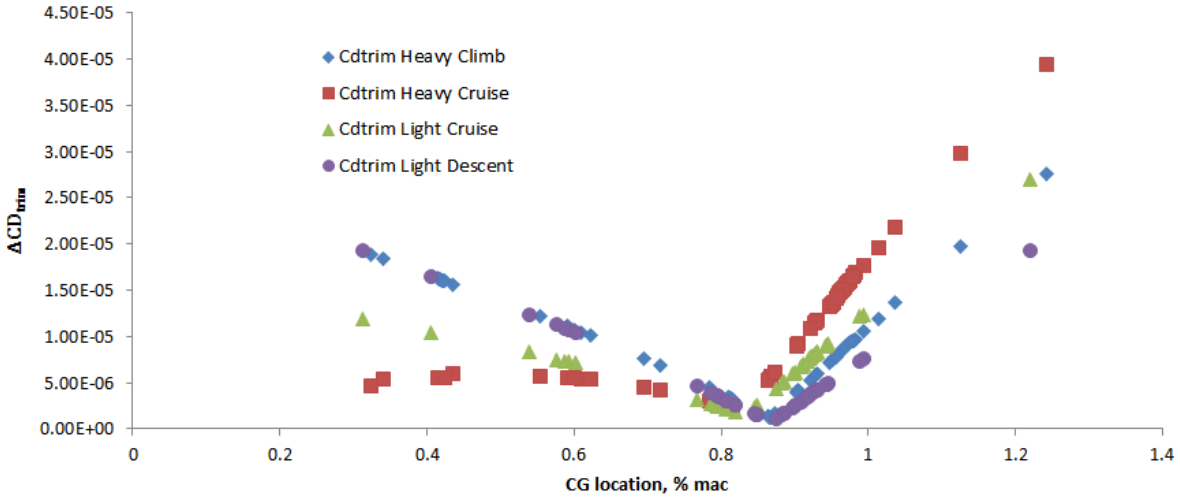

Figure 6.15: Trimmed drag increment $\Delta C_{D_{\text{trim}}}$ due to elevator deflection versus $\bar{x}_{cg}$ for the baseline configuration

the relationship between static stability and the trimmed drag increment. For most aircraft configurations, a static margin of between 5-15% unstable will yield the minimum trimmed drag coefficient—a result of the almost negligible amount of elevator deflection required to trim. In Figure 6.15, the minimum drag in each flight condition occurs at approximately $\bar{x}_{cg} = 0.85$, which corresponds to static margin values of approximately 12-15% unstable in Figure 6.10.

The last observations to be made regarding the baseline configuration will be the closed-loop behavior as the *CG* moves aft. Results from the dynamic analyses must be presented by cases representative of typical results due to the large quantity of the data produced. For example, the closed-loop LTI systems achieved during iteration are computed at each flight condition and each disturbance—there are 12 closed-loop LTI systems created at each of the 100 iterations over the *CG* location, resulting in more than 1,000 pole-zero plots. Similarly, the achieved state variances can be computed and compared to the enforced upper bounds for each state, flight condition, disturbance case, and *CG* location, resulting in very large quantities of data.

At each *CG* location, the upperbound on the state variances was recomputed by searching the MIL-STD-1797 domain as in Chapter 4. As expected, since the desired eigenvector structure is held constant as the *CG* moves, the computed $\sigma_{\max}$ varies only a very small amount in response to the slight change in the shape of the modal domain. The phugoid domain is invariant for all configurations of the same aircraft classification, but the short-period domain is a function of the CAP from Eq. (3.110). As the *CG* moves and the trim condition changes, the magnitude of the CAP changes slightly, and the bounds on the short-period mode change accordingly. Figure 6.16 shows the maximum allowable state variances as computed from the MIL-STD-1797 modal boundaries for each of the longitudinal states of the baseline configuration in the heavy cruise flight condition, subject to the mixed gust

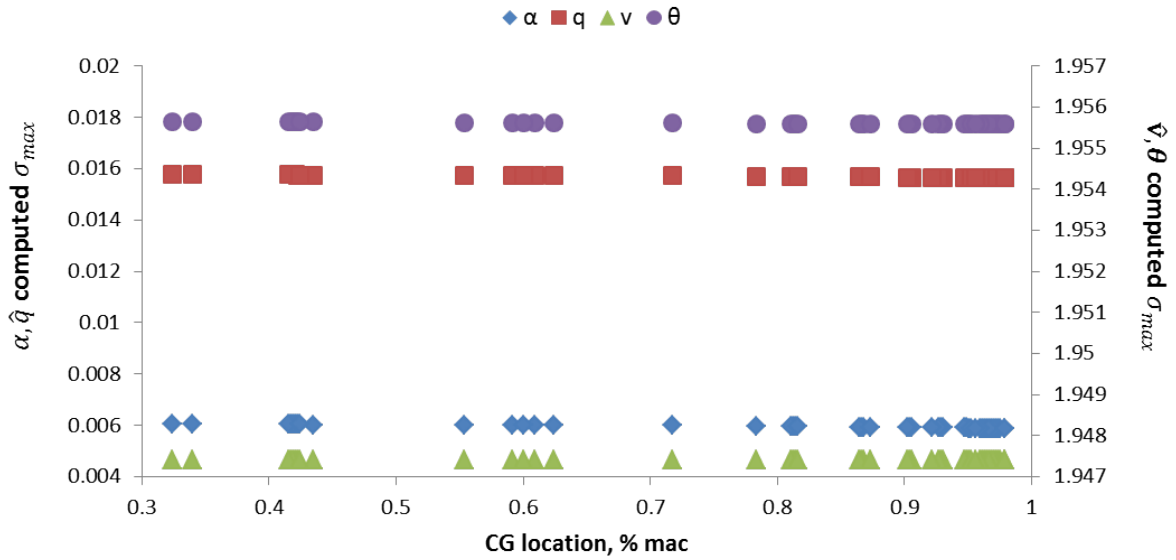

Figure 6.16: Computed maximum allowable state variances for the baseline aircraft in the heavy cruise condition under a mixed gust disturbance, plotted versus $\bar{x}_{cg}$

disturbance, and plotted as a function of the *CG* location. Note that the plotted maximum allowable state variances correspond to the nondimensional states, including the velocity V, which is plotted as $\hat{v} = \Delta V/V$. Plots of this type for the other flight conditions and disturbance cases are qualitatively identical. It is physically intuitive that the maximum allowable state variances which a pilot would deem satisfactory should be invariant with the *CG* location since the rest of the aircraft remains unchanged. Indeed, Figure 6.16 confirms this.

To illustrate the closed-loop results achieved during the search for the maximum aft *CG* location, Figure 6.17 shows a pole-zero plot of all of the closed-loop longitudinal eigenvalues computed during the optimization for the heavy cruise flight condition when subjected to the vertical gust scenario. Also shown on the figure are the short-period minimum damping ratio and the approximate minimum natural frequency boundaries (approximate because it varies with the computation of the CAP, but only by a very small amount). Absent from the plot

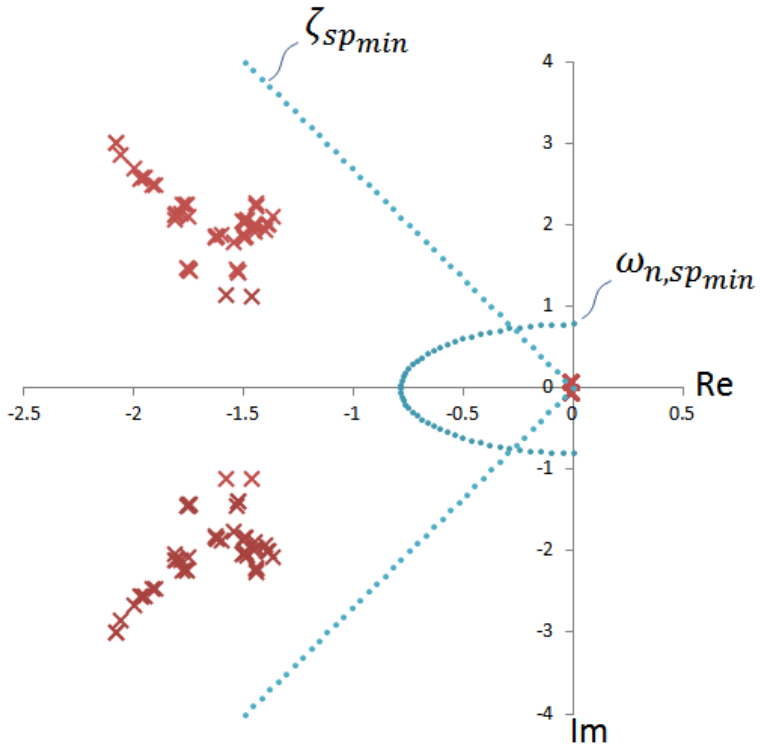

Figure 6.17: Closed-loop eigenvalues of the longitudinal model of the baseline configuration in the heavy cruise flight condition with a vertical gust, plotted for each value of $\bar{x}_{cg}$. Dotted lines represent the (approximate) minimum natural frequency and minimum damping ratio constraints of the short-period mode.

is the elevator actuator eigenvalue, which is a real eigenvalue that is an order of magnitude faster than the rigid body modes and tends to distort the limits of the plot. Unlike the open-loop results, there is no discernible order to the closed-loop eigenvalues as the *CG* is moved aft. This is a result of the feasibility problem accomplished via the LMI's, wherein the first valid solution stops the search for feedback control laws. Though the numerics behind LMI's are convex and trivial to solve numerically, the relationship between a smoothly varying convex matrix variable and the closed-loop eigenvalues is highly nonlinear. It is clear from Figure 6.17 that the achieved short-period eigenvalues are well within the minimum damping ratio and natural frequency boundaries prescribed by the MIL-STD-1797.

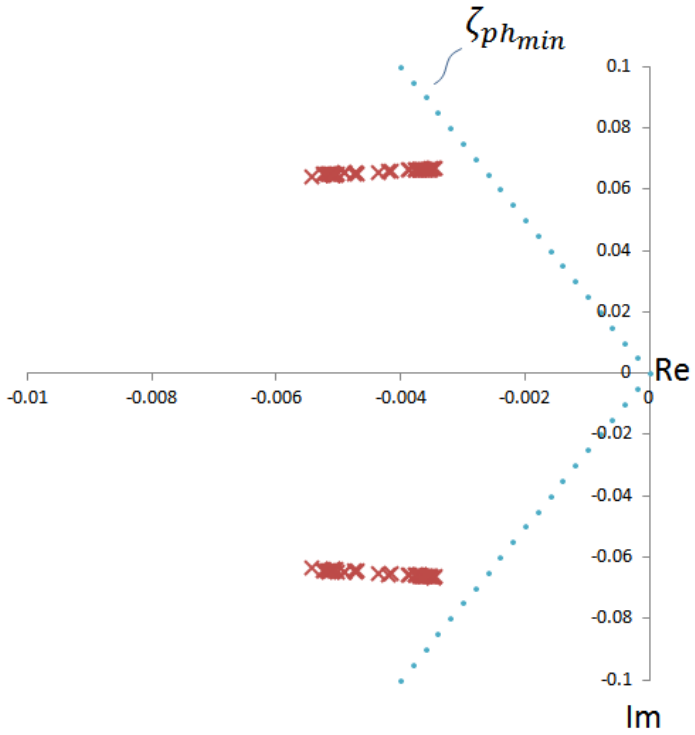

Figure 6.18: Closed-loop phugoid mode eigenvalues of the longitudinal model of the baseline configuration in the heavy cruise flight condition with a vertical gust, plotted for each value of $\bar{x}_{cg}$. Dotted lines represent the minimum damping ratio constraints of the phugoid mode.

It is not easy to discern the behavior of the phugoid closed-loop eigenvalues in Figure 6.17, which appear to have collapsed to a single point. Figure 6.18 was constructed from the same data set as Figure 6.17, but with the axes limits adjusted to only reflect a very small region around the origin. The minimum phugoid damping ratio is also plotted in the figure for reference. Again, it is apparent that at each *CG* location, the static state feedback controller developed is capable of stabilizing the configuration and satisfying the flying qualities requirements (via the variance constraints). Many of the closed-loop systems in Figures 6.17 and 6.18 correspond to systems which were open-loop unstable. As mentioned, closed-loop pole-zero plots of this type could be reproduced for each *CG* location, flight condition, and

dynamic perturbation condition, but the results of Figures 6.17 and 6.18 are characteristic of the behavior seen under these other conditions.

An unfortunate consequence of using an LMI feasibility problem is the inability of the LMI solver to directly identify the active constraint when a feasible solution can't be found. During the aft *CG* search, the ModelCenter™ optimizer continues to push the *CG* aft until an error flag is thrown by the LMI solver which identifies the flight condition and dynamic perturbation condition which failed to meet the dynamic constraints. It is up to the user to then analyze the aft *CG* optimization history and draw conclusions as to the likely reason the LMI's were found infeasible—that is, whether it was a state variance constraint, actuator amplitude constraint, or actuator rate constraint which was the likely active constraint. Often, it is not clear which constraint was activated, as many of them may approach their boundary early in the optimization and remain there, while others may oscillate. Nonetheless, it can be useful to make plots of certain parameters during the optimization to construct a 'history' as the *CG* is moved aft.

During the aft *CG* search for the baseline configuration, the first flight condition to fail was the light descent condition subject to the vertical gust at a *CG* location of $\bar{x}_{cg} = 0.93$. This particular case was used to develop optimization history plots for the elevator input, the elevator rate, and the achieved closed-loop state variances. Figure 6.19 shows the component contributions and the cumulative elevator deflection utilized by the aircraft as a function of *CG* location during the light descent stage when subjected to the vertical gust. The three lowest curves represent the elevator response to the dynamic perturbation condition, the trimmed deflection, and the 25% margin required to be maintained for maneuver capabilities. These curves were summed to produce the total deflection curve, which clearly indicates that the elevator's actual deflected state is less than the maximum allowable of 20°. Peak values of total elevator deflection occur at the aft most *CG* locations, and never exceed 15°. The

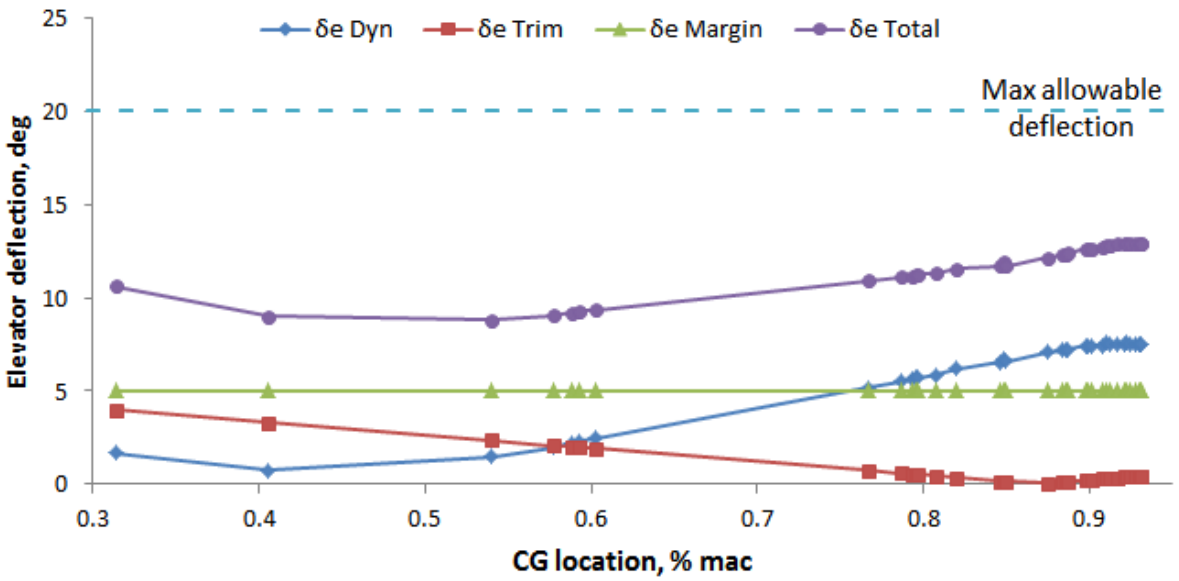

Figure 6.19: Component contributions and total elevator response to a vertical gust in the light descent flight condition, plotted versus $\bar{x}_{cg}$

results shown in Figure 6.19 were obtained via post-processing to illustrate the behavior of the LMI solution process.

The elevator deflection rate versus CG location is similarly plotted in Figure 6.20. As expected, the maximum elevator deflection rates occur at the aft-most CG locations, though they are always well below the maximum allowable of 50 deg/s. Clearly, the solutions found by the LMI feasibility problem are capable of satisfying both the actuator deflection and the deflection rate constraint.

Perhaps the most interesting result is that obtained from comparing the achieved closed-loop state variances to their respective upper bounds obtained from the flying qualities modal domain search. As in Chapter 4, the actual state variances (σ_k) of the system can be computed via post processing by solving the Lyapunov equality

$$(A + BK)X + X(A + BK)^T + X_0 = 0, \tag{6.4}$$

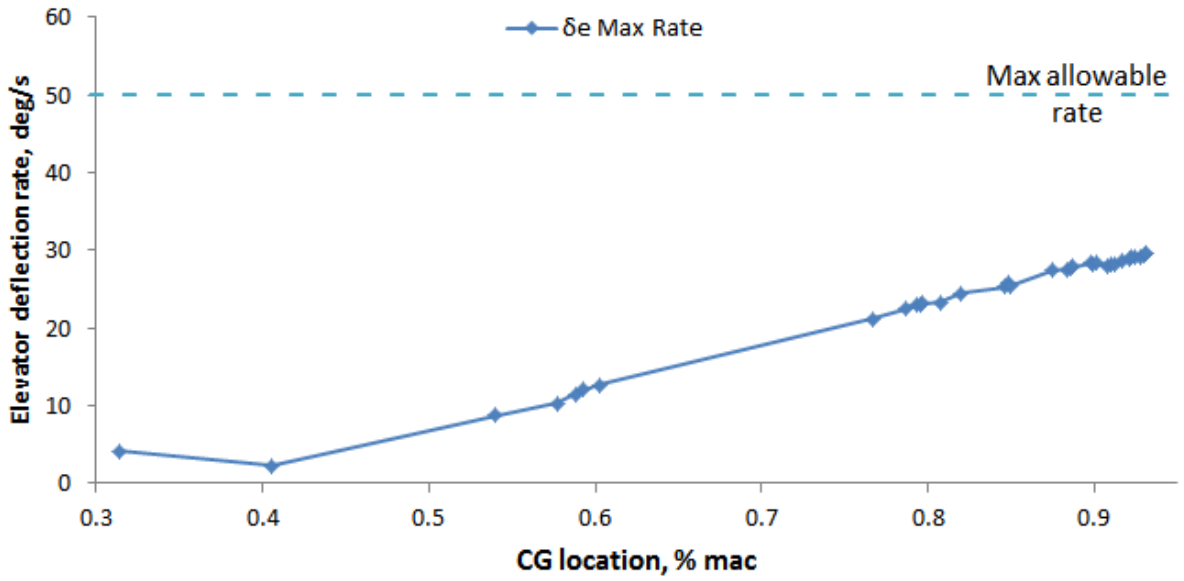

Figure 6.20: Elevator deflection rate to a vertical gust in the light descent flight condition, plotted versus $\bar{x}_{cg}$

where $\sigma_k = X_{kk}$, and where K is the state feedback gain matrix produced by the LMI feasibility solution. Figure 6.21 contains plots of each of the achieved state variances and the upper bounds computed for the longitudinal states, plotted versus the CG location. The two states classically associated with the short-period response, $\hat{q}$ and α, are clearly much closer to their respective upper bounds than the phugoid states, $\hat{v}$ and θ. It is likely that the asymptotic behavior of the short-period states near the aft CG limit is the reason the optimizer was unable to further maximize the CG location, since even a small aft perturbation would result in a large increase in the short-period variances. The flight condition plotted in Figure 6.21 is also a vertical gust condition, so it is not surprising that the stimulated state (α) appears to be the limiting state.

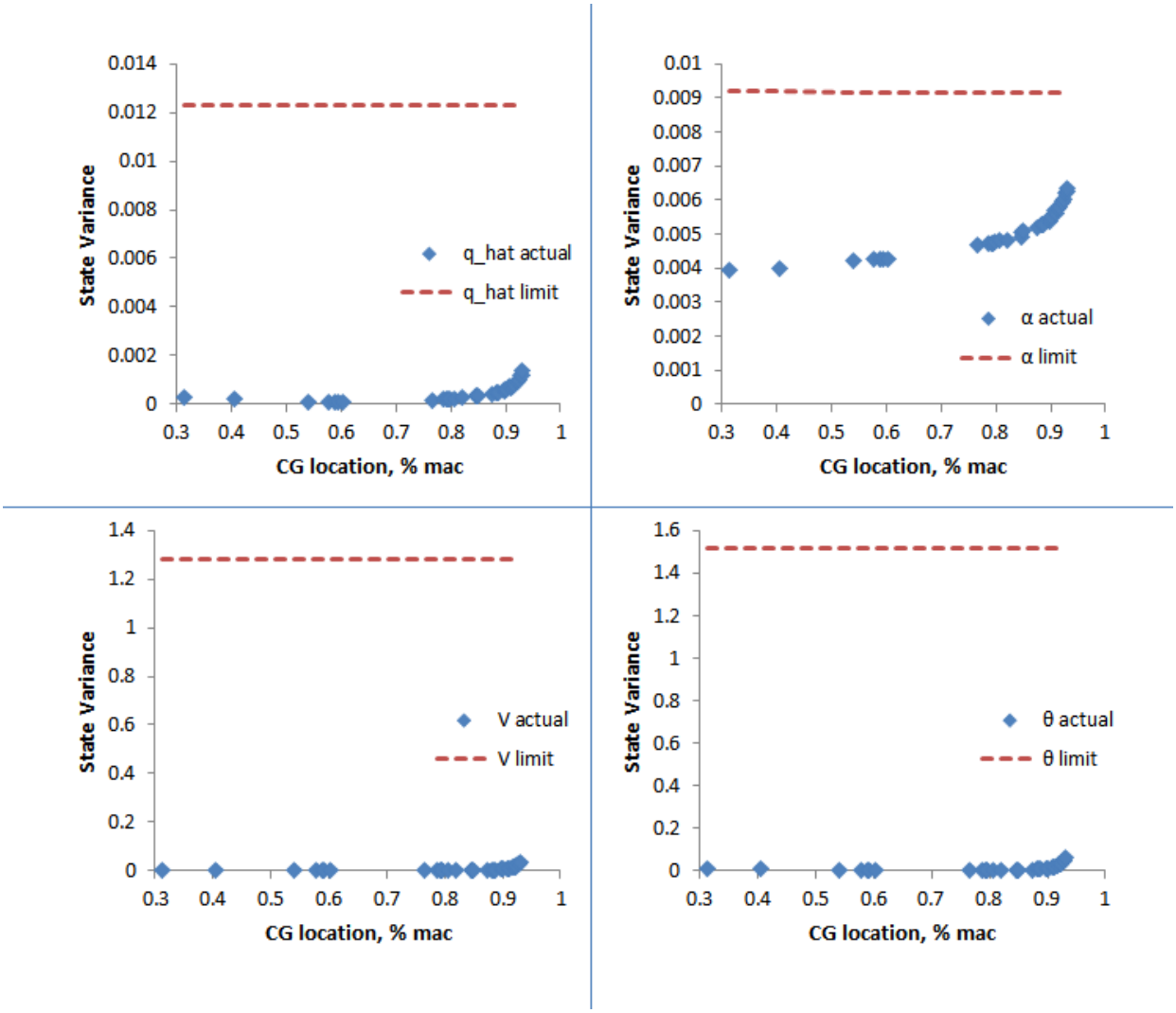

Figure 6.21: Upper bounds and actual state variances of each longitudinal state for the light descent flight condition subject to a vertical gust, plotted versus *CG* location. All variables are nondimensional

Search for the forward *CG* Limit

The search for the forward *CG* boundary is made far simpler by the fact that it only deals with static analyses. In Chapter 3, several critical static sizing scenarios were identified, including high load factor trim, low speed, high lift trim, and takeoff rotation. The first of these two are easily handled by the trim analysis within NASTRAN and are included in

the test matrix of Table 6.2. Just as with the aft *CG* search, the *CG* location was moved forward by a redistribution of material density within the fuselage (keeping the total vehicle weight constant) until NASTRAN indicates that it can no longer trim the vehicle. Allowing NASTRAN to handle the trim analysis also captures the static aeroelastic influence on the trimmed condition. High lift trim at low speeds is accomplished with flaps deployed for both the takeoff and approach conditions. During takeoff, a half-flap deployment (15°) is used, with full flaps (30°) used during approach.

Computing the forward *CG* for the takeoff rotation constraint requires additional consideration. In Eq. (3.81), the horizontal tail size is given as an explicit function of aerodynamic and geometric parameters, as well as the *CG* location. What this analysis fails to capture is the dependence of the *CG* location on the horizontal tail size, which actually makes the equation an implicit function of the tail area, S_{HT}. An alternative strategy is to rearrange Eq. (3.81) to solve explicitly for the rotation rate, $\dot{\theta}_r$. Then, by using the mass properties as computed by NASTRAN, an optimizer can iterate over $\bar{x}_{cg}$ to find the forward-most *CG* location which can still provide a sufficient rotation rate. The rotation rate constraint was set to be $\dot{\theta}_r \geq 4$ deg/s, a value taken directly from a publication by Boeing [114]. This analysis proved to be one of the most challenging to model due to the complexity of the flight conditions at takeoff. Ground effect is not modeled by NASTRAN, and the prediction of $C_{L_{\max}}$ is also likely to be in error since NASTRAN cannot capture viscous effects. Installed engine performance and the direction of the net thrust vector are also important parameters which influence the calculation. For these reasons, a large portion of the required data was generated by Digital DATCOM or estimated from handbook methods in Ref. [59]. Results from these analyses did prove to be sensitive to several parameters which were necessarily estimated, in particular $C_{L_{\max}}$ and the horizontal tail lift coefficient during rotation. Nonetheless, the takeoff rotation constraint did not prove to be the limiting forward *CG*

location—a result that is in agreement with a previous study on a similar configuration [78].

Results from the forward *CG* search for the baseline configuration are collected in Table 6.4. It turns out that the high-C_L trim in the heavy configuration is the limiting forward *CG* at $\bar{x}_{cg} = 0.475$. This, combined with the results of the previous section, means the allowable *CG* travel computed for the baseline configuration is $0.475 \leq \bar{x}_{cg} \leq 0.93$. Within these limits, the static trim constraints can all be satisfied, and the aircraft can satisfy the Level 1 flying qualities requirements established by the MIL-STD-1797.

Table 6.4: Baseline Configuration Most Forward *CG* Results

Flight Condition	Description	Minimum $\bar{x}_{cg}$
FC-I	Takeoff Rotation, heavy	0.358
FC-I	High-C_L trim, heavy	0.475
FC-II	High-g trim, heavy	0.177
FC-V	High-g trim, light	0.028
FC-VI	High-C_L trim, light	0.368

6.2.4 Relaxed Static Stability Horizontal Tail Sizing Results

The process which was executed to find the forward and aft *CG* limits for the baseline configuration was repeated for a range of horizontal tail sizes from 30% to 100% of the baseline horizontal tail area. A parametric study was constructed in ModelCenter™ to carry out the exercise. Results of the forward *CG* study, which can be seen in Figure 6.22, were somewhat unexpected, though physically justifiable. The conventional scissor plot has forward *CG* boundaries that have negative slopes like that shown in Figure 6.6. With the exception of the high load factor trim in the light configuration, every one of the forward *CG* boundaries computed for the transport aircraft has a positive slope. This unexpected characteristic was cause for many hours of modeling verification work before the results were well understood. Results from both Digital DATCOM and NASTRAN static analyses gave

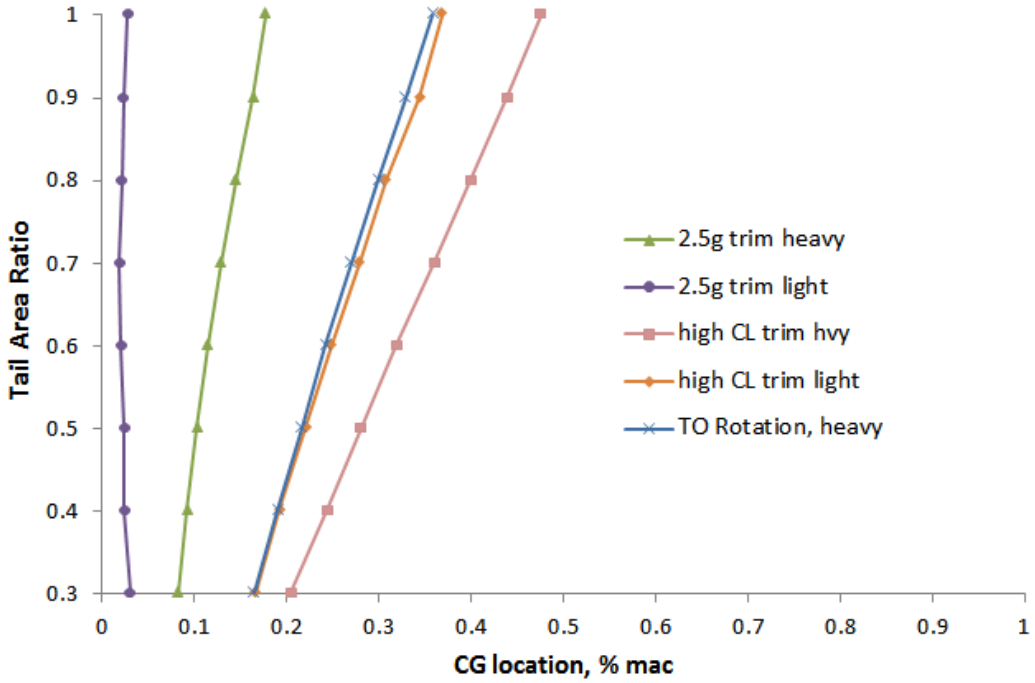

Figure 6.22: Forward *CG* boundaries for each horizontal tail area ratio $S_{r_{\mathrm{HT}}}$ versus the nondimensional *CG* location

similar trends, indicating it was not simply an error in the code. The source of the error was ultimately identified as horizontal tail mass effects. Typical scissor plots constructed using techniques like those in Ref. [59] operate under the assumption that the horizontal tail mass contribution to the total mass is very small. Changes in horizontal tail area are then made under the assumption of constant total mass—a numerical convenience that facilitates rapid sizing analyses during early design studies. By traditional conceptual design standards, the model used in the creation of Figure 6.22 is very advanced, and is therefore able to capture the horizontal tail influence on the total mass that would have otherwise been ignored.

The influence of the horizontal tail mass on the forward *CG* limits was further exaggerated by mass estimation errors in the vehicle structural model. Figure 6.23 illustrates the influence of the horizontal tail size on the vehicle gross weight when all other parameters are held fixed. A difference of approximately 6,100 lbs exists between the vehicle gross weight

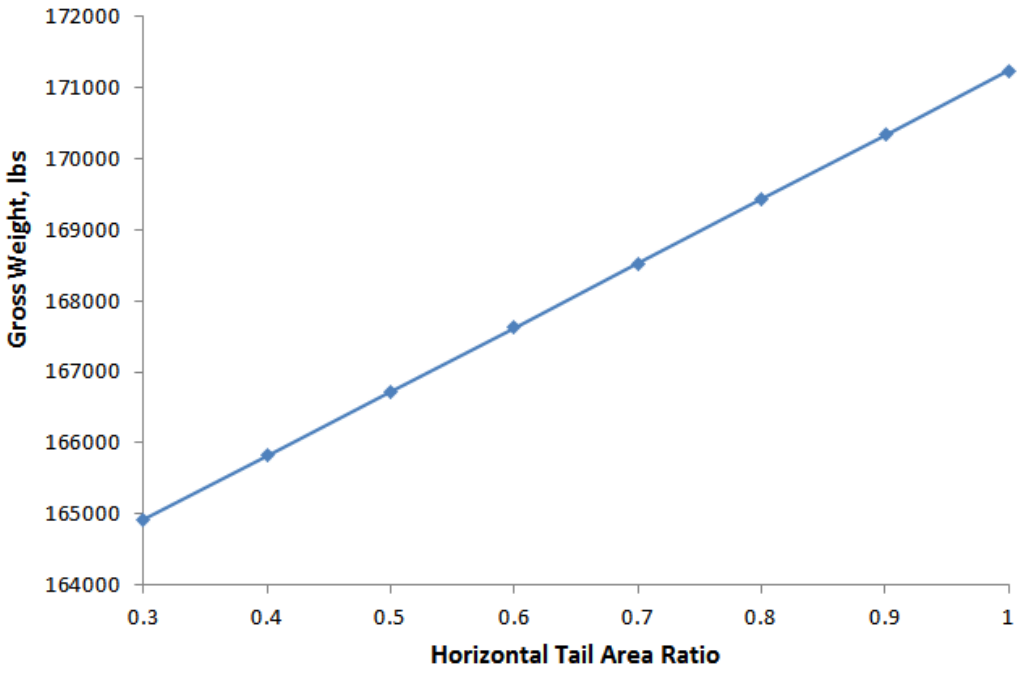

Figure 6.23: Vehicle gross weight versus horizontal tail area ratio $S_{r_{\mathbf{HT}}}$

when the horizontal tail is scaled down to just 30% of its original area, numbers which indicate a total horizontal tail weight of approximately 8,700 lbs. Recall from Section 6.1.1 that the baseline configuration was developed to match the global mass properties of a model provided by the Truss Braced Wing team. The mass, moments of inertia, and products of inertia were all matched by allowing an optimizer to vary material densities in the model to minimize the error in these values, producing a model which had less than 1% error in each global mass parameter. The fuselage and the tails were then made rigid by assigning an arbitrarily high elastic modulus, and the elastic moduli of each wing section was optimized to match the static aeroelastic deflection at several stations along the wing of the reference TBW model. It was also identified that this approach neglects the local distribution of mass—a seemingly inconsequential result when structural dynamics analyses are not being performed. A typical aircraft of this size would have a combined horizontal and vertical tail

weight of approximately 7,000-10,000 lbs. (exact data for the 737-800 was unavailable) [5], which suggests that the structural matching procedure overestimated the mass placed in the horizontal tail in order to achieve the correct global mass properties. It is likely that fixed and secondary masses in the empennage region of the baseline aircraft exacerbated this error. For example, auxiliary power units (APU) for aircraft of this size have typical installed masses of 1,000 lbs. or more [4], and are installed in the empennage. The mass of hydraulic systems, actuators, sealants, and other devices installed in the empennage are also appreciable. These masses were not independently modeled during the inertia matching procedure, and were aggregated into the tail masses. Since the fuselage and tails were made rigid, the influence of the heavy horizontal tail was not captured during the study of the baseline configuration due to the fact that the inertias and total mass behaved as expected. Despite this apparent error in the structural model, the results were repeatedly verified and are correct for the given model.

Results from the dynamic analysis, conducted using the VCFQ approach, create similar curves for the aft-CG limit which are shown in Figure 6.24. These curves represent the furthest the CG is allowed to travel aft before one of the dynamic constraints is violated. There are only two curves plotted since the results are aggregated by the vehicle loading condition. This is a consequence of NASTRAN's ability to simultaneously analyze many trim conditions for a vehicle with constant mass properties. During the aft CG search, a flag was thrown by the optimizer as soon as any one of the dynamic perturbation conditions failed under the light or heavy loading conditions. The results display the expected trend in that the aft CG boundary typically exhibits a positive slope. Influence of the tail mass overestimation is likely to have increased the slope of the curves in the same manner it affected the static analyses, though this hypothesis requires further investigation. As with the static analyses, repeated code verification efforts were conducted to ensure the analyses

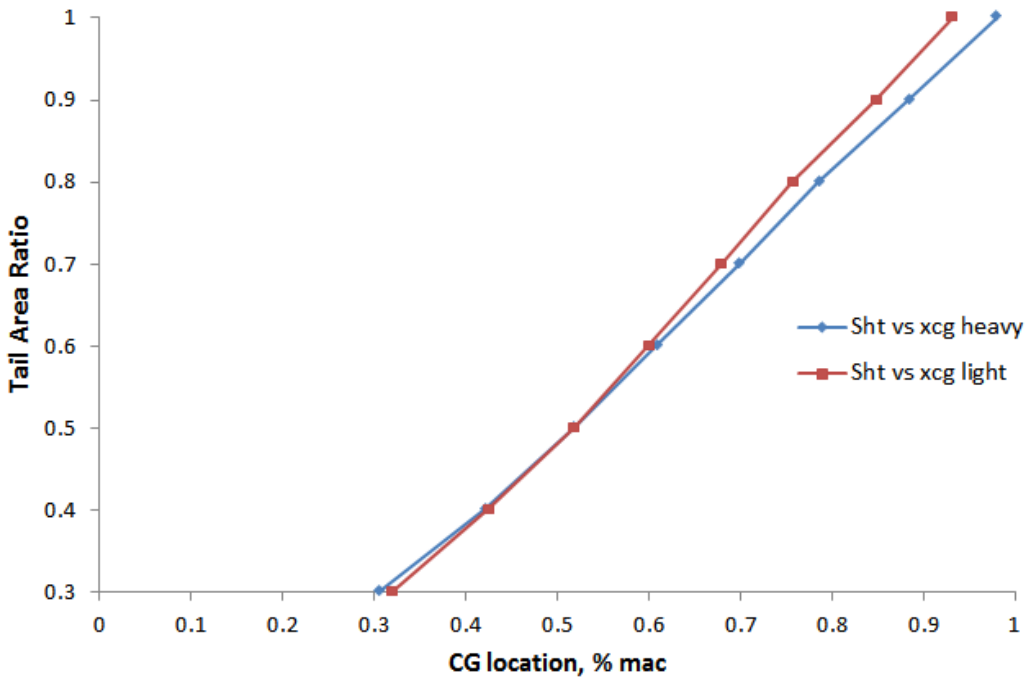

Figure 6.24: Aft *CG* boundaries for each horizontal tail area ratio $S_{r_{\mathbf{HT}}}$ versus the nondimensional *CG* location under a relaxed static stability assumption

were correct for the given model.

With forward and aft boundaries established, the results can be combined to extract the minimum allowable horizontal tail size for the required *CG* range of travel. The actual *CG* limits for the 737-800 are available in Ref. [115]. Operational aircraft have very complex *CG* limits which are functions of the flight condition, loading, and thrust setting, making it difficult to extract a single number for a required *CG* range of travel. Allowable *CG* travel varies from as little as 17.3% to as much as 31% of the mean aerodynamic chord for the operational 737-800, but throughout much of the in-flight envelope, the *CG* range is approximately 30%. In conceptual design, it is common to adopt a single value for the required *CG* range to avoid the intricacies of operational aircraft *CG* envelopes [59]—a strategy which also imparts conservatism into the results. Therefore, the approximate value

of 30%, a typical value for transport aircraft [5], was used in the selection of the minimum horizontal tail size in the relaxed static stability study.

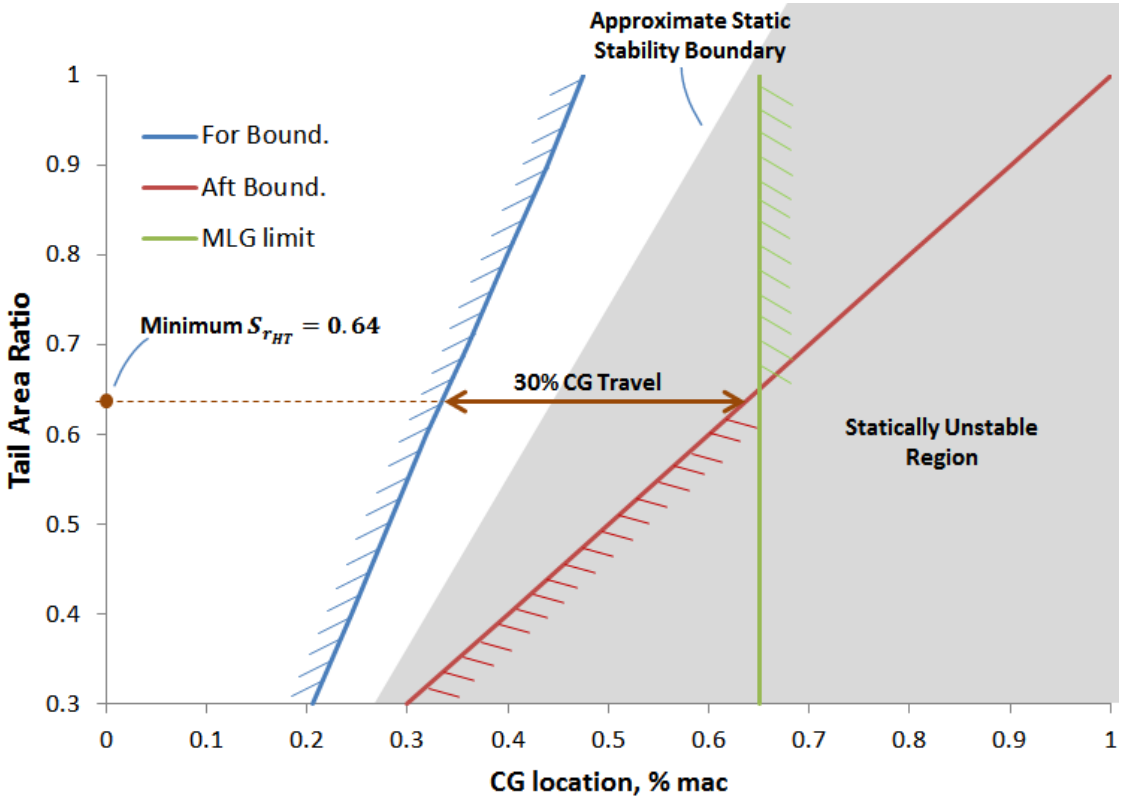

Figure 6.25: Minimum horizontal tail area ratio $S_{r_{\mathrm{HT}}}$ selection from the results of the forward and aft *CG* limit studies under a relaxed static stability assumption. Shaded region represents region of static instability

The results of the scissor plot horizontal tail sizing exercise are shown in Figure 6.25. The limiting forward *CG* constraint was the high lift trim condition immediately following takeoff, while the limiting aft *CG* constraint was set by either the light or heavy loading condition results depending on the tail area ratio. An additional curve which represents the aft *CG* limit demanded by the location of the main landing gear (to prevent tip back on the ground) is plotted in Figure 6.25 as well, though this constraint is often ignored since *CG* constraints on the ground can be relaxed once airborne. The shaded region in the figure is the

approximate region of static instability. The region is approximate since the static margin is a function of the flight condition and instability may arise in one flight condition before another. Examination of the results for the baseline configuration, $S_{r_{\mathrm{HT}}} = 1.0$, indicate an allowable *CG* travel of approximately 16% between the forward *CG* boundary and the static instability limit. This is markedly smaller than the estimated 30% *CG* travel previously identified, but is a reasonable approximation of the operational 737-800 heavy condition takeoff *CG* requirements of a 19% allowable *CG* travel. Returning to the forward *CG* results for the baseline configuration in Table 6.4, the next most-limiting forward *CG* location is established by the high lift trim condition on approach at $\bar{x}_{cg} = 0.368$. Using this value as the forward limit gives a *CG* range of approximately 27%, which is quite close to the operational light landing condition value of 26.3%. These results indicate good consistency with available data on the baseline configuration, but also illustrate the conservatism inherent to scissor plots. By simplifying a required *CG* envelope down to a constant number, the potential benefits achieved though *CG* range scheduling and fuel transfer management are ignored.

Ultimately, the smallest horizontal tail which still provided the required 30% *CG* travel has a tail area of just 64% of the baseline configuration, $S_{r_{\mathrm{HT}}} = 0.64$. This results in an absolute horizontal tail area of S_{HT} =330.4 ft^2, a weight savings of 3,132 lbs, and a *CG* range of $0.33 \leq \bar{x}_{cg} \leq 0.63$. There is also significant drag reduction, according to the Digital DATCOM analysis (recall NASTRAN cannot predict drag coefficients). At a *CG* location of $\bar{x}_{cg} = 0.5$, the trim drag of the RSS configuration in the heavy cruise flight condition was just 36% of the baseline configuration, and the total drag coefficient was reduced from 0.050 to 0.046, an 8% savings over the baseline configuration. This drag savings is achieved through a reduction in the profile and friction drag, but also the induced drag, since the aircraft is flying closer to neutral stability. At $\bar{x}_{cg} = 0.5$, the cruise static margin is approximately -5%. In fact, the *CG* range of the optimized horizontal tail configuration is statically unstable in

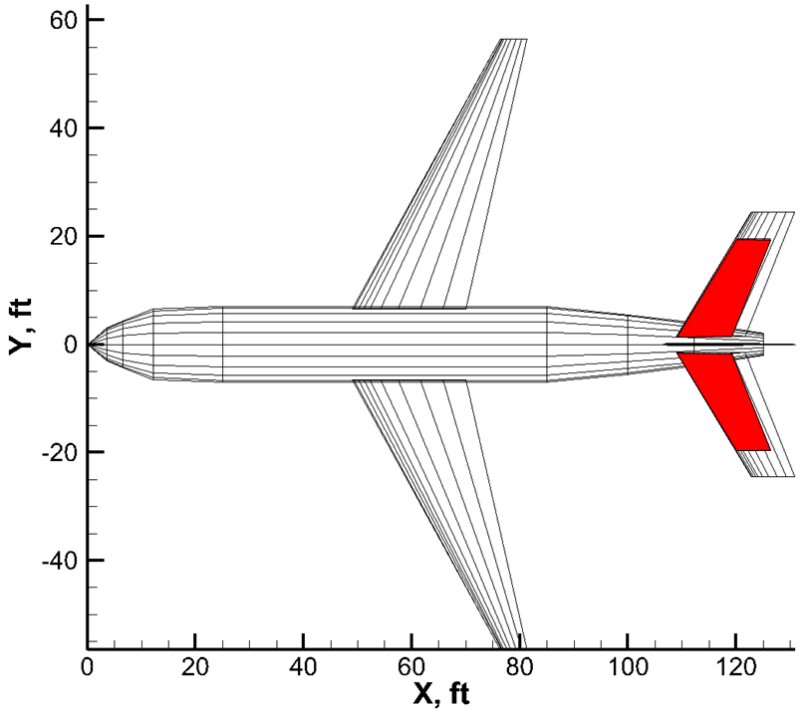

Figure 6.26: Comparison of the baseline horizontal tail (black, wireframe) and the optimized RSS horizontal tail (red, shaded)

cruise aft of $\bar{x}_{cg} \approx 0.40$—approximately two thirds of the allowable CG travel for the optimized configuration is statically unstable and requires stability augmentation. At the aft CG limit of $\bar{x}_{cg} = 0.63$, the cruise static margin is approximately -13%. Clearly, the relaxation of the static stability requirements is a critical assumption in this design study. Figure 6.26 shows a comparison of the baseline configuration and the optimized RSS horizontal tail.

6.3 Vertical Tail Sizing

Design of the horizontal and vertical tails of a transport aircraft are not strictly decoupled. In fact, there are mutual structural and aerodynamic influences between the two which may not be inconsequential. However, throughout the conceptual and early preliminary design phases, the standard approach to tail sizing is to assume they can be designed under a

decoupled assumption [4, 5, 59]. This decoupled design approach will be utilized herein due to its utility in separately demonstrating the longitudinal and lateral-directional application of the VCFQ approach. It should be recognized that ultimately the S&C module will serve as an analysis capability within a larger MDO process, and a fixed configuration with fixed mass properties will be analyzed by the S&C module. Therefore, any design optimization assumptions made during the RSS transport empennage design are not inherent limitations of the S&C module.

In some ways, the lateral-directional analysis is simpler than the longitudinal analysis since the *CG* range has already been determined, but in other ways it is more difficult. The greatest challenge to the lateral-directional analysis is the modeling aspect. NASTRAN does not aerodynamically model the fuselage, which is problematic, since it exerts a nontrivial influence on the lateral-directional S&C derivatives. Digital DATCOM can be used to predict many of these derivatives, but it has its own shortcomings. For example, Digital DATCOM, and the more elaborate 'paper' DATCOM upon which the code is based, are incapable of predicting rudder control derivatives, and they are only capable of predicting aileron behavior under certain restrictive modeling assumptions [95, 96, 97]. The two programs were executed in tandem, and their results were combined to construct a lateral-directional model from the equations of motion in Chapter 3.

The lateral-directional analysis also requires the use of multiple control effectors. Roll and yaw motions are typically too coupled to be treated separately, so the ailerons and the rudder must necessarily be analyzed at the same time. The VCFQ approach is quite capable of handling multiple effectors, and this lateral-directional study is an excellent means of demonstrating that capability. As with the elevator, first-order models for the ailerons and rudder were used to capture the actuator dynamics and to limit the allowable deflection rates. It was also assumed that the left and right aileron are rigidly linked by a uniform one-

to-one ratio such that a right aileron down command results in a left aileron up command of equivalent magnitude. On operational aircraft with fly-by-wire capabilities, this ratio can be nonlinear and flight condition dependent.

6.3.1 Lateral-Directional Test Cases

With the appropriate *CG* range identified and the horizontal tail area minimized, the vertical tail can be sized according to the static and dynamic constraints discussed in Chapter 3. Static cases considered include engine-out trim during takeoff and crosswind landing trim. Dynamic cases considered were crosswind gusts at the heavy climb and cruise conditions, and the light cruise and descent conditions. Both the static and the dynamic cases are detailed in Table 6.5. Each case was tested at the aft *CG* limit which resulted from the horizontal tail sizing study ($\bar{x}_{cg} = 0.63$). Only the aft *CG* limit was used, since the vertical tail lever arm is the shortest under that condition, requiring the largest aerodynamic forces to be generated [4].

As before, an LTI system was constructed for each flight condition using the equations of motion derived in Chapter 3 with the lateral-directional state vector

$$x_{\text{latdir}} = \begin{bmatrix} \beta & \hat{r} & \hat{p} & \phi \end{bmatrix}^T. \tag{6.5}$$

NASTRAN trim cards and a Digital DATCOM input deck were generated for each test condition in the table in order to provide the necessary aerodynamic and structural properties to create each system. Static lateral-directional cases were not directly handled by NASTRAN as they were in the longitudinal study, a consequence of the required augmentation of the NASTRAN S&C derivative predictions with results from Digital DATCOM. Engine-out rudder deflection was computed using Eq. 3.87, where the engine drag of the inoperative engine

Table 6.5: Lateral-Directional Flight Condition Test Matrix

Flight Condition (FC)	Description	Static Analyses	Dynamic Analyses
FC-I	Heavy @ Takeoff Mach = 0.2 Alt. = 0.0 ft n = 1.0	• Engine-out trim	• No dynamic cases
FC-II	Heavy @ Climb Mach = 0.5 Alt. = 10,000 ft n = 1.0	• Crosswind trim	• Directional gust
FC-III	Heavy @ Cruise Mach = 0.7 Alt. = 35,000 ft n = 1.0	• Crosswind trim	• Directional gust
FC-IV	Light @ Cruise Mach = 0.7 Alt. = 35,000 ft n = 1.0	• Crosswind trim	• Directional gust
FC-V	Light @ Descent Mach = 0.5 Alt. = 10,000 ft n = 1.0	• Crosswind trim	• Directional gust
FC-VI	Light @ Approach Mach = 0.3 Alt. = 0.0 ft n = 1.0	• Crosswind trim	• No dynamic cases

was estimated using handbook methods found in Ref. [59]. Similarly, the rudder deflection required to trim during a crosswind scenario was computed using Eq. (3.86). Static trim at the climb and cruise conditions was enforced under a steady 25 knot crosswind as prescribed by the FAR's, and the resulting rudder deflection was subtracted from the allowable rudder travel (in addition to the required 25% maneuver margin) made available to the VCFQ approach during the dynamic analyses.

Vertical tail mass effects were captured just as the horizontal tail mass effects were. At each iteration, the airframe structure was regenerated, and the mass and aerodynamic properties were recomputed. In reality, an iteration would be required between the horizontal tail and the vertical tail sizing processes, since changes in the vertical tail will alter the mass distribution as well as their mutual aerodynamic influences. However, for configurations that are well approximated by a decoupling assumption (such as transport aircraft), aerodynamic interactions and the vertical tail influence on the CG are quite small. The rudder, which was modeled as being the last 30% of the vertical tail chord and spanning the full width of the tail, was scaled along with the tail area. Similar to the longitudinal study, dynamic perturbation conditions were generated from the derived equivalent gusts discussed in Section 4.4.4. Lateral gusts were applied to the sideslip angle β, where the β perturbation was computed using Eq. (3.6).

6.3.2 Baseline Lateral-Directional Characteristics

The open-loop eigenvalues for the lateral-directional models for both the climb/descent and cruise flight conditions under heavy and light loadings for the baseline aircraft are shown in Figure 6.27 and 6.28. Also shown in the figures are the natural frequency, damping ratio, and damped natural frequency boundaries for the Dutch roll mode, as well as the time constant boundary for the roll mode. These constraints are taken directly from Tables 3.12 and 3.14 for a Class II aircraft in flight category B.

The baseline configuration satisfies the lateral-directional flying qualities requirements, though it does approach unsatisfactory Dutch roll characteristics in the heavy cruise condition. Nonetheless, these dynamics have been identified by pilots as being satisfactory, therefore the eigenvector structure for each flight condition and loading was adopted as an

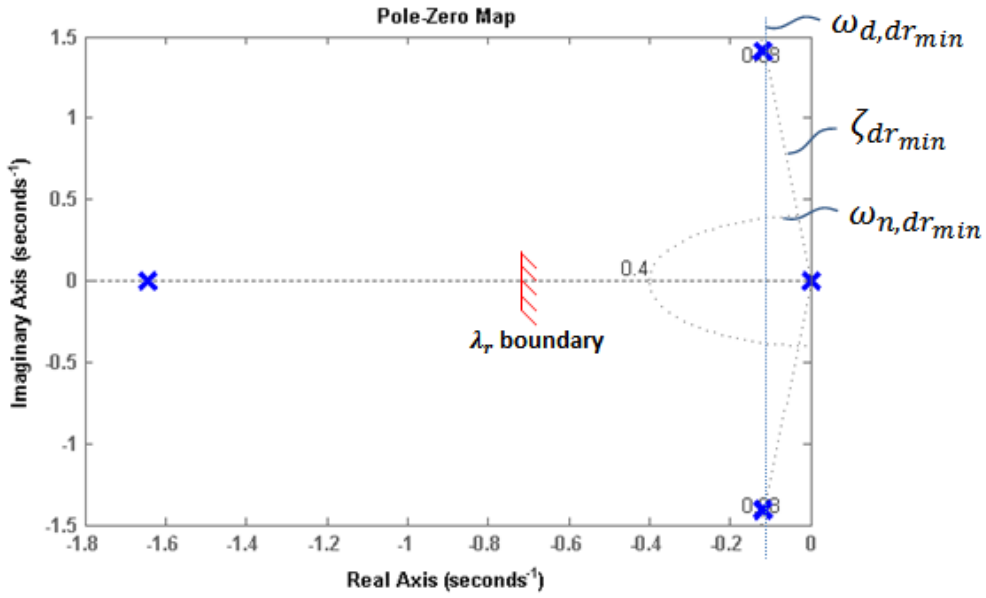

(a) Heavy Cruise Condition

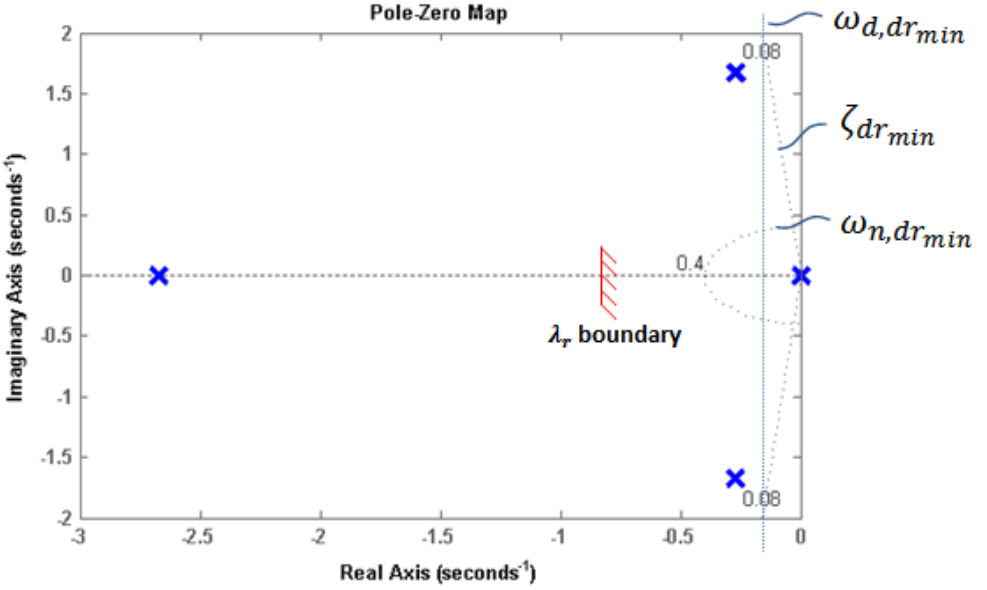

(b) Heavy Climb Condition

Figure 6.27: Open-loop eigenvalues of the lateral-directional equations of motion for the heavyweight baseline configuration

appropriate reference structure for the VCFQ approach. Several other observations regarding the baseline lateral-directional behavior can be made by perturbing one parameter and

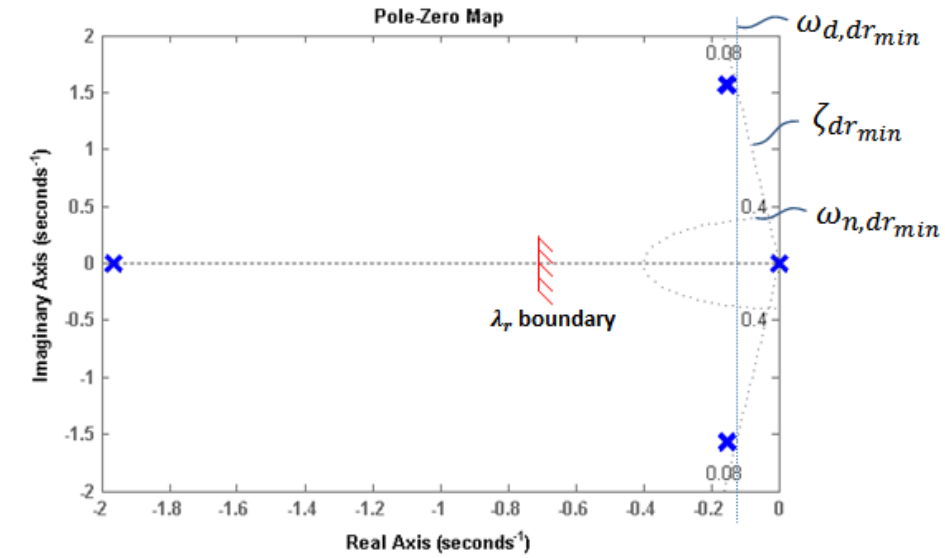

(a) Light Cruise Condition

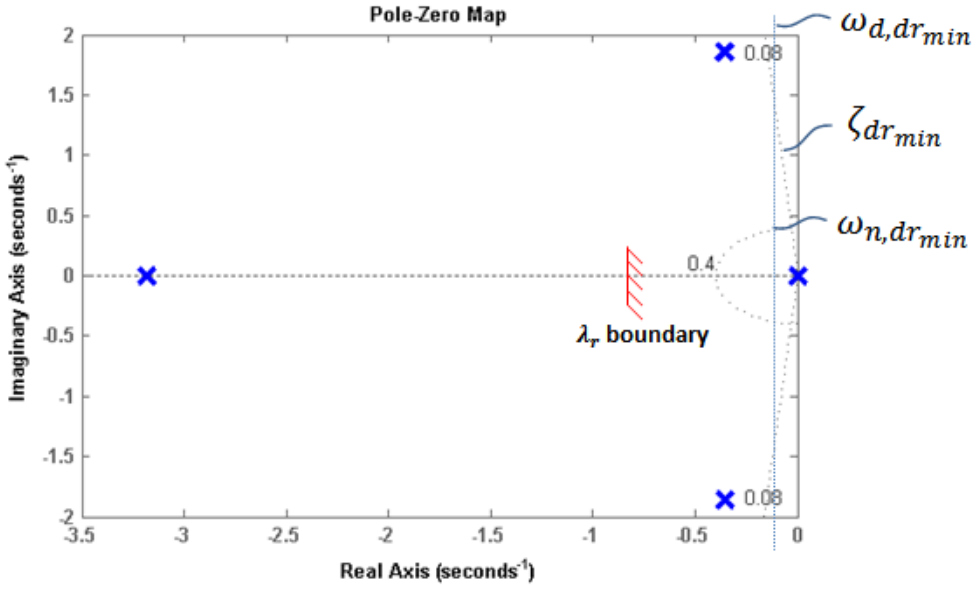

(b) Light Descent Condition

Figure 6.28: Open-loop eigenvalues of the lateral-directional equations of motion for the lightweight baseline configuration

examining the change in the open-loop eigenvalues of the system. All of the results which follow utilize the heavy climb condition to illustrate the open-loop eigenvalue behavior, though the results are characteristic of the responses observed for the heavy cruise and light con-

ditions as well. The first case to be examined is the behavior of the open-loop system as the *CG* location is varied over $0.0 \leq \bar{x}_{cg} \leq 1.0$, the results of which can be seen in Figure 6.29. Over a broad range of *CG* locations, there is very little variation in the open-loop

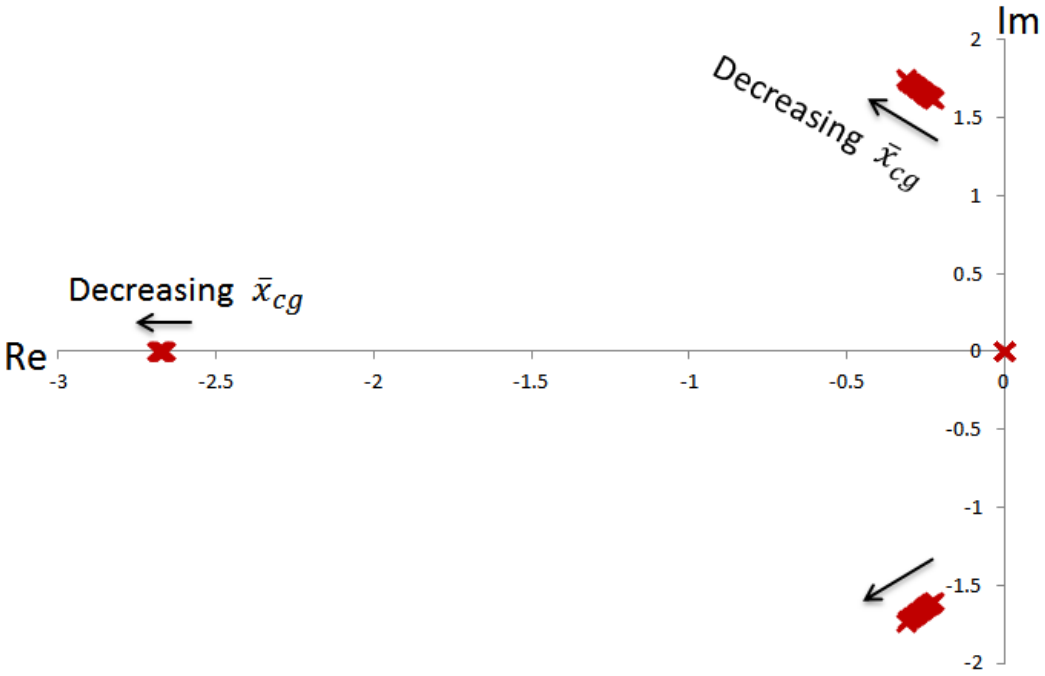

Figure 6.29: Lateral-directional open-loop eigenvalues in the heavy climb condition as the *CG* is varied between $0.0 \leq \bar{x}_{cg} \leq 1.0$

pole locations. The Dutch roll mode and the roll mode do become slightly more stable as $\bar{x}_{cg}$ is decreased, which is a result of the increased lever-arm distance between the vertical tail aerodynamic center and the *CG* location. The neutrally stable spiral mode is unaffected by perturbations in *CG* location and remains at the origin. It is a generally known result that lateral-directional flying qualities are not particularly sensitive to the *CG* location [61], which is confirmed by the results of Figure 6.29.

Another similar result is that obtained by observing the variation in the open-loop eigenvalues with a change in the horizontal tail area, S_{HT}. In Figure 6.30, the horizontal tail area ratio is reduced from 1.0 to 0.3 while the *CG* location is held constant at $\bar{x}_{cg} = 0.5$.

The results show that as with the *CG* location, the lateral-directional eigenvalues are largely

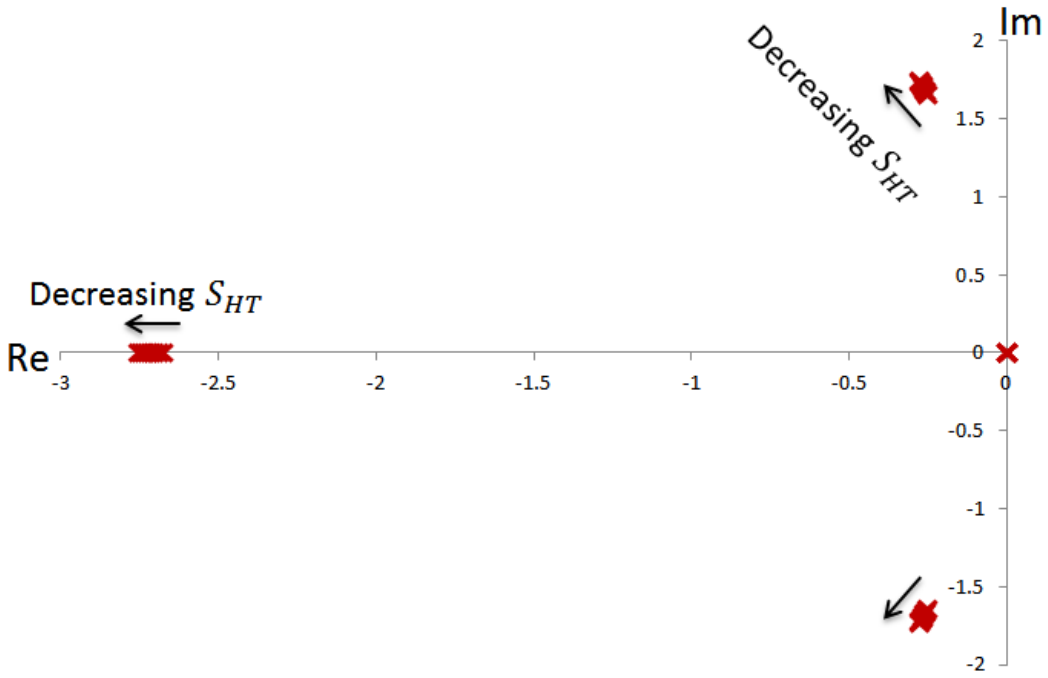

Figure 6.30: Lateral-directional open-loop eigenvalues in the heavy climb condition as the horizontal tail area ratio is varied over $0.3 \leq S_{r_{\mathbf{HT}}} \leq 1.0$ with fixed $\bar{x}_{cg} = 0.5$

invariant with changes in $S_{r_{\mathrm{HT}}}$. This result is not surprising since the longitudinal and lateral-directional dynamics were assumed to be decoupled, and it is unlikely that the fidelity of the aerodynamic analysis is sufficient to resolve significant aerodynamic coupling. The small change in the open-loop eigenvalues is likely a result of the decreasing mass of the vehicle as the horizontal tail is made smaller, which creates slight variations in the trimmed condition. Results from Figure 6.30 also indicate that the lateral-directional characteristics of the configuration with the optimized horizontal tail are quite similar to those of the baseline configuration.

A more interesting open-loop result is captured by varying the size of the vertical tail. Figure 6.31 shows the open-loop lateral-directional eigenvalues for the heavy climb condition

as the vertical tail area ratio is reduced from 1.0 to 0.3. As to be expected, the results

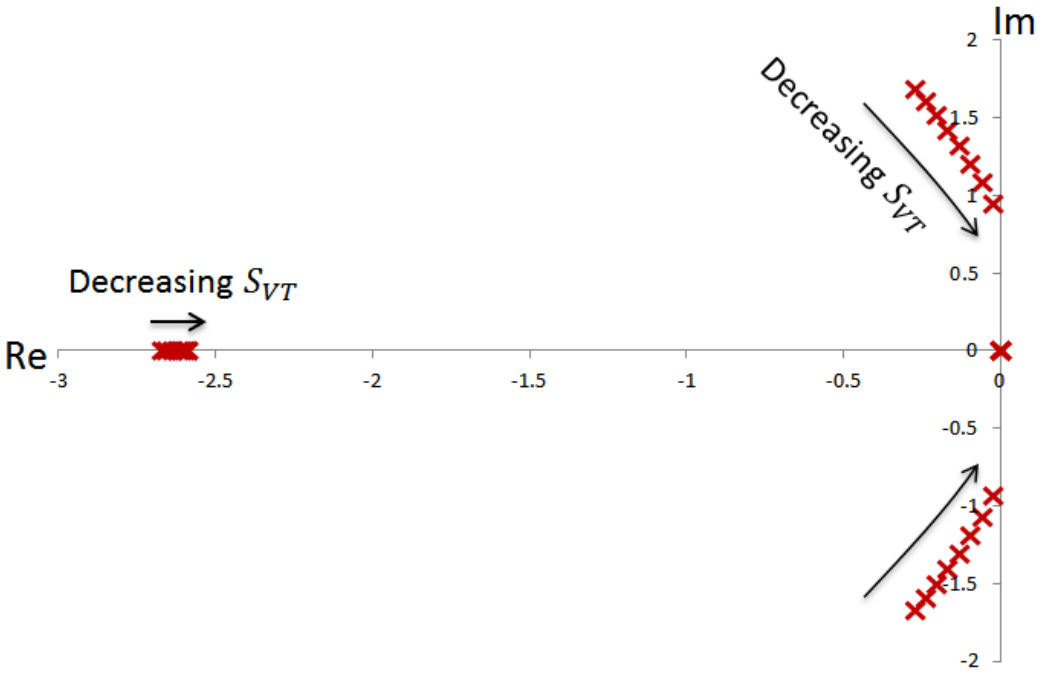

Figure 6.31: Lateral-directional open-loop eigenvalues in the heavy climb condition as the vertical tail area ratio is varied over $0.3 \leq S_{r_{\mathbf{VT}}} \leq 1.0$

show significant variation in the lateral-directional modal response as the vertical tail area is reduced. Dutch roll mode eigenvalues are most significantly affected, approaching the imaginary axis and moving towards instability. C_{n_β} is the most influential S&C derivative on the Dutch roll natural frequency, and the largest contributor to C_{n_β} is the vertical tail. Thus, the reduction in natural frequency indicates that the model is capturing the reduction in C_{n_β} that is to be expected when the tail is reduced. The roll mode eigenvalue varies less, though there is a marginal increase in the time constant as $S_{r_{\mathrm{VT}}}$ is reduced. Aerodynamically, the largest contributor to the roll mode behavior is the wing via the aerodynamic coefficient C_{l_p} [60]. Since the wing remains unchanged in this study, it is not surprising that the roll mode also remains largely unchanged. The spiral mode eigenvalue remains neutrally stable at the origin.

6.3.3 Relaxed Static Stability Vertical Tail Sizing Results

Unlike the horizontal tail minimization, where there were effectively two parameters to optimize over, $S_{r_{\mathrm{HT}}}$ and $\bar{x}_{cg}$, the vertical tail only requires study of $S_{r_{\mathrm{VT}}}$. The CG location is held fixed at the aft-most value allowed by the horizontal tail optimization results—a process accomplished by using the fuselage mass distribution to compensate for any CG shift due to a reduction in vertical tail mass. During the optimization, for each value of $S_{r_{\mathrm{VT}}}$, an inner-iteration redistributes the fuselage mass to maintain a constant $\bar{x}_{cg}$ at the aft limit of $\bar{x}_{cg} = 0.63$. The static and dynamic test cases of Table 6.5 were checked for feasibility using the static analyses discussed in Chapter 3 and the VCFQ approach.

State variance upper bounds were extracted from the lateral-directional flying qualities domain prescribed by the MIL-STD-1797 using the approach detailed in Chapter 4 and the reference eigenvector structure of the baseline configuration. In contrast to the longitudinal flying qualities requirements, which varied as a function of the Control Anticipation Parameter, the lateral-directional requirements do not vary with the flight condition. State variance upper bounds, therefore, do not need to be recomputed with each change in the configuration geometry since they are fixed for a given flight condition and dynamic perturbation condition. The appropriate discrete gust from Table 4.2 was used for the dynamic perturbation condition and was applied to the sideslip state, β. Results from the maximum allowable lateral-directional state variance search are tabulated in Table 6.6.

The system of LMI's of Section 4.5.6 was then constructed using these state variance upper bounds and the actuator rate and saturation constraints detailed in Table 6.1. An optimizer within ModelCenter$^{\mathrm{TM}}$ was used to minimize the tail subject to the existence of a solution to the LMI system. Following the optimization, a post processing study was conducted to simulate the closed-loop response of each synthesized aircraft and extract the

Table 6.6: Lateral-directional state variance upper bounds for each flight condition at $\bar{x}_{cg} = 0.63$

State	Heavy Climb	Heavy Cruise	Light Cruise	Light Descent
β	0.0177	0.0097	0.0096	0.0181
ϕ	0.0422	0.0242	0.0273	0.0442
$\hat{p}$	0.0709	0.0348	0.0527	0.0938
$\hat{r}$	0.0375	0.0169	0.0208	0.0475

maximum control effector deflections, deflection rates, and the achieved state variances when subjected to the gust case. The limiting dynamic perturbation case was the light descent condition, which bounded the vertical tail area ratio to be $S_{r_{\text{VT}}} \geq 0.551$. Interestingly, the lower limit for the heavy climb condition had a very similar result with $S_{r_{\text{VT}}} \geq 0.550$.

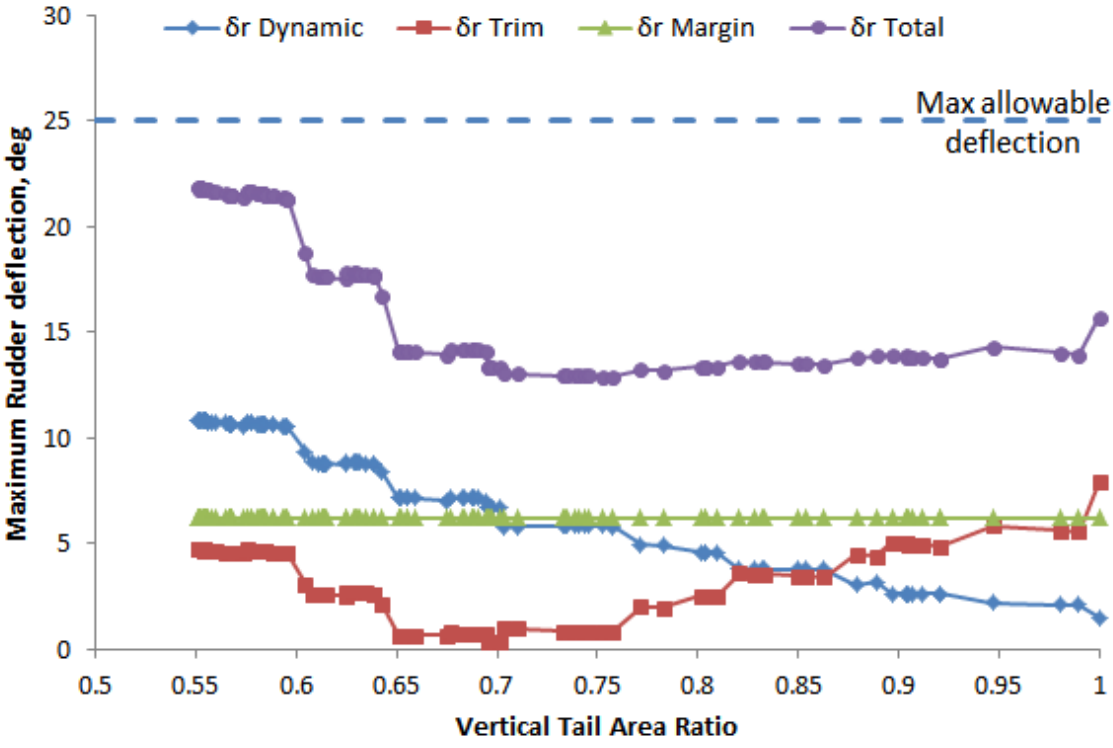

Figure 6.32: Component contributions and maximum total rudder response to a lateral gust in the light descent flight condition versus $S_{r_{\text{VT}}}$

Figure 6.32 shows the closed-loop rudder response versus the vertical tail area ratio, $S_{r_{\mathrm{VT}}}$. Each component of the total rudder deflection is plotted, along with their summed total deflection and the maximum deflection limit. As $S_{r_{\mathrm{VT}}}$ is decreased, the required rudder deflection to trim first decreases as the configuration becomes less stable and then increases as additional rudder (in the opposite direction) is required to trim the unstable configuration. Just like the elevator response, the absolute value of the trimmed response is plotted in the figure. The maximum rudder deflection in response to the gust increases as $S_{r_{\mathrm{VT}}}$ decreases. This result is expected since the configuration is growing less stable, and the rudder is made smaller with each decrease in $S_{r_{\mathrm{VT}}}$. A 25% maneuver margin is also required in the event that a pilot would need to maneuver while trimmed in a crosswind under gust disturbances. By summing the trim, dynamic, and maneuver margin components together, the total elevator response as a function of $S_{r_{\mathrm{VT}}}$ can also be plotted. It is interesting to note that the total required rudder deflection is essentially constant near 14 degrees over a broad range of $S_{r_{\mathrm{VT}}}$, a consequence of the cancellation effect from the decreasing demands for the crosswind trim and increasing demands for gust response suppression. Below $S_{r_{\mathrm{VT}}} \approx 0.7$, the required total elevator deflection begins to rise rapidly, since the slopes of the trimmed and dynamic deflection curves have the same sign, eliminating the cancellation behavior. The apparent noise in the data is likely attributed to the nature of a feasibility problem, wherein the first feasible solution to the LMI constraints triggers an exit from the convex optimization. It is likely that this problem is more apparent in the lateral-directional results than the longitudinal results due to the presence of multiple actuators. For controllable linear systems with multiple inputs, there can be many control system solutions which satisfy the same closed-loop objective. Thus, the same feasibility problem run with two different initial solutions may result in different answers which are equally satisfactory for a given objective.

The aileron response to the lateral gust in the light descent flight condition is shown in

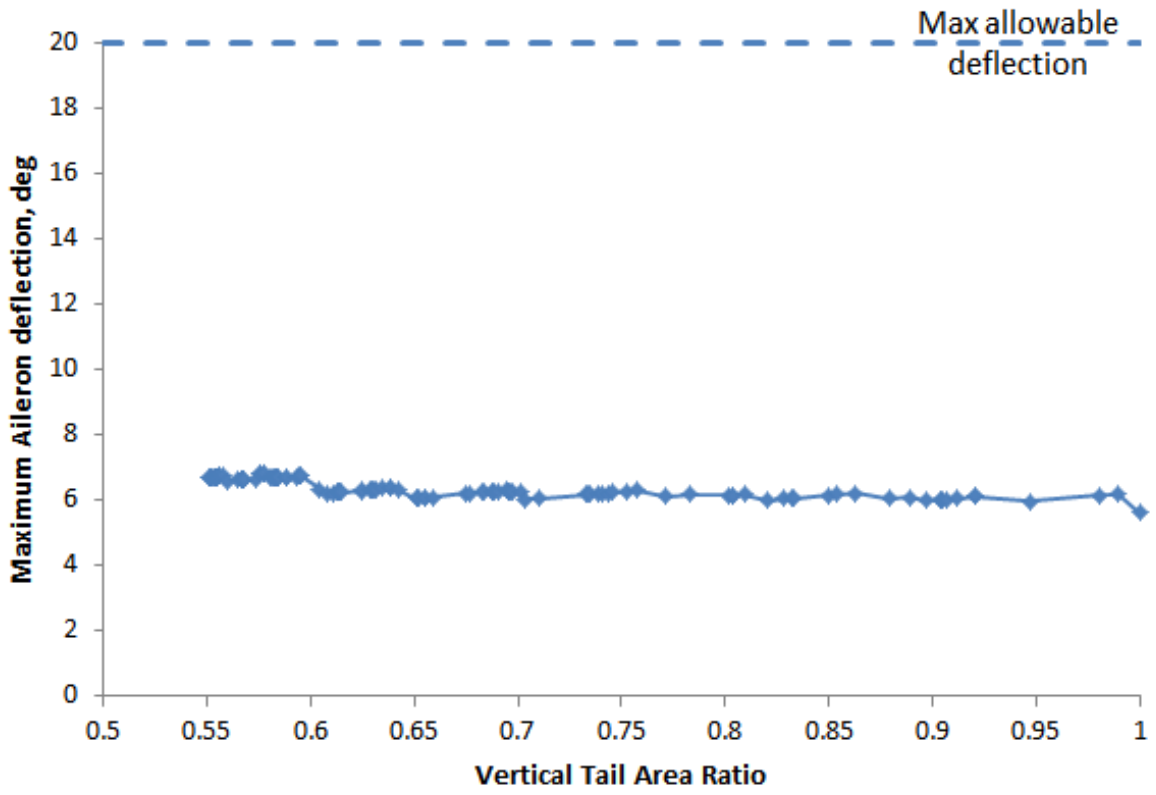

Figure 6.33: Maximum aileron response to a lateral gust in the light descent flight condition versus $S_{r_{\mathbf{VT}}}$

Figure 6.33, where the maximum deflection of the ailerons is plotted versus the $S_{r_{\mathrm{VT}}}$. Aileron size was not a design variable in this study, so the response to a gust is largely invariant with respect to $S_{r_{\mathrm{VT}}}$. A small increase is noticeable from a maximum deflection of approximately 5 degrees for the baseline configuration to approximately 7 degrees at $S_{r_{\mathrm{VT}}} = 0.55$. While the aileron response is not likely to be limiting for the vertical tail design, Figure 6.33 clearly shows the capability of the VCFQ approach to identify solutions for multiple input systems that can accommodate multiple actuator constraints.

Actuator rates were also constrained during the solution of the LMI's, with both the ailerons and the rudder limited to a maximum deflection rate of 50.0 deg/s. Post-simulation of the closed-loop results provides the maximum aileron and rudder rate responses as shown

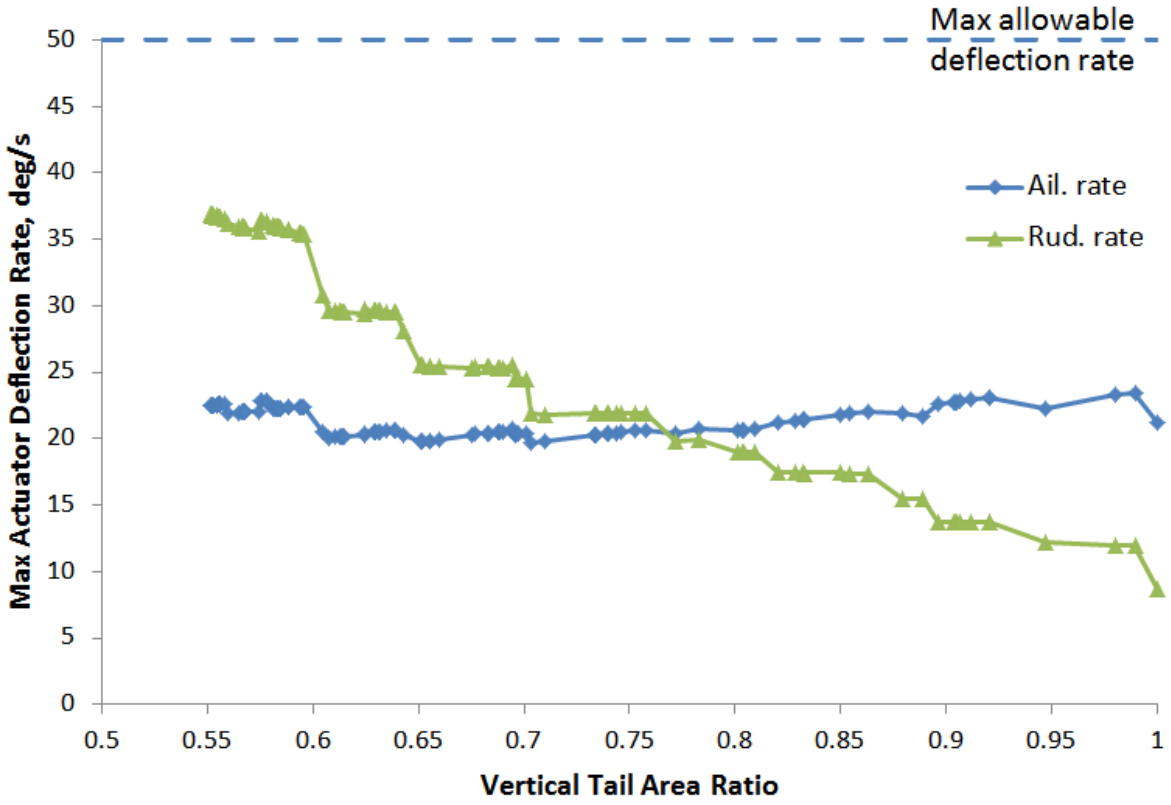

Figure 6.34: Maximum aileron response to a lateral gust in the light descent flight condition versus $S_{r_{\mathrm{VT}}}$

in Figure 6.34. As expected, the aileron deflection rate is largely invariant with respect to $S_{r_{\mathrm{VT}}}$, and the rudder deflection rate increases monotonically as $S_{r_{\mathrm{VT}}}$ is decreased. At the minimum value of $S_{r_{\mathrm{VT}}} = 0.551$, the peak elevator deflection rate is approximately 37 deg/s. As before, the apparent noise in the response is likely due to the nature of the LMI feasibility problem already discussed. Figure 6.34 demonstrates that the VCFQ approach is also capable of constraining the actuation rate of multiple input systems.

Post-simulation can also reveal the state variances actually achieved by the closed-loop system as the vertical tail area is reduced. Figure 6.35 illustrates the change in the achieved state variances in the light descent flight condition when subjected to a lateral gust. Each closed-loop system generated by the VCFQ approach clearly satisfies the state variance upper

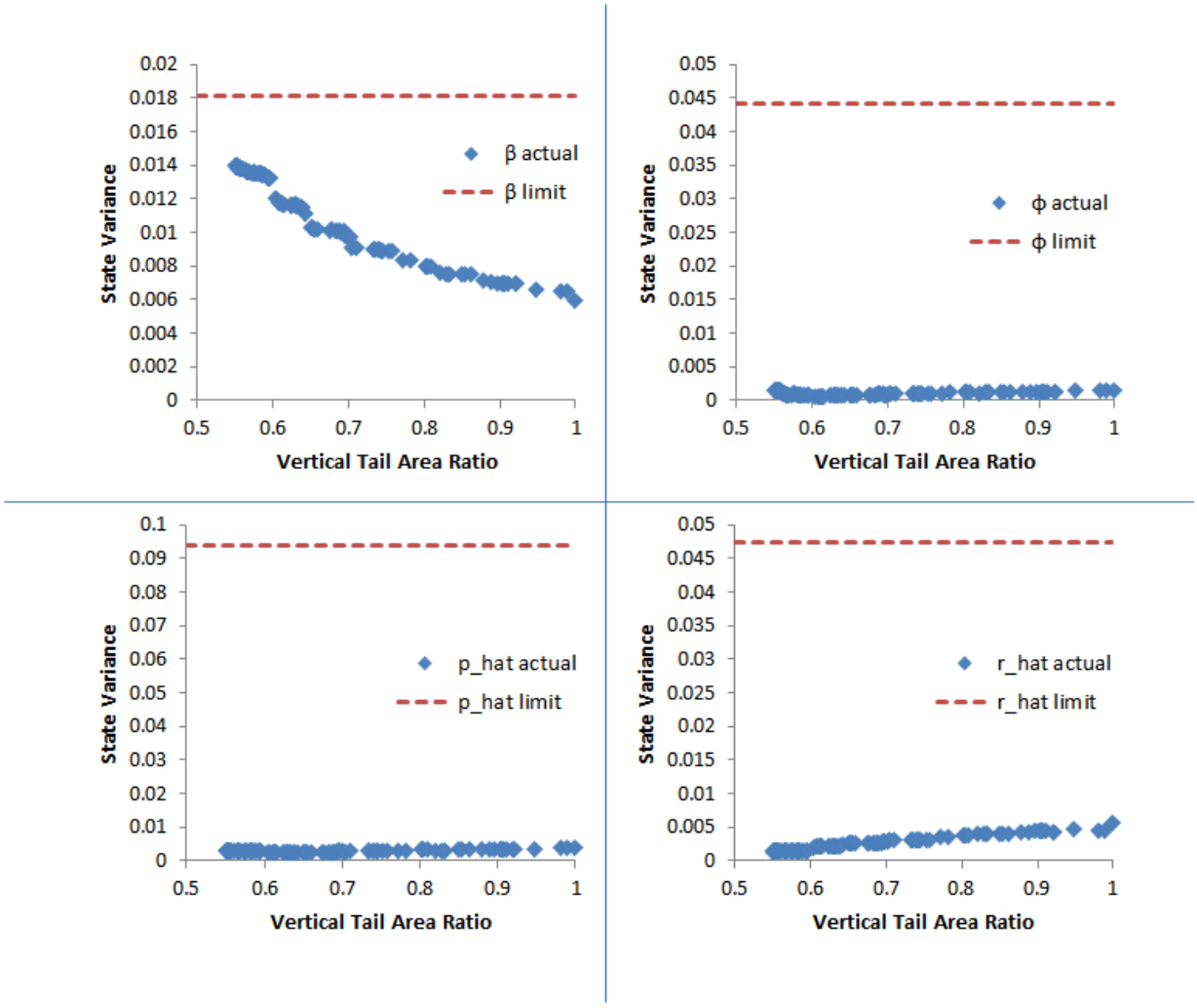

Figure 6.35: Upper bounds and actual state variances of each lateral-directional state for the light descent flight condition subject to a lateral gust, plotted versus $S_{r_{VT}}$. All variables are nondimensional

bounds computed from the MIL-STD-1797. One of the four lateral-directional states, the sideslip angle β, stands out as the state variance which is closest to its upper bound. As already identified during the discussion of the longitudinal results, it can be challenging to identify the active constraint when a feasible solution to the LMI's can't be found. Trends in the results can often identify the limiting constraint, but in this case, they are not obvious.

Both the rudder deflection and the state variance of the sideslip angle approach their upper bounds, but neither appears to demonstrate the asymptotic behavior of the longitudinal states in Section 6.2.4. Similar trends are also evident in the light cruise and heavy flight conditions.

A final result of the dynamic analysis is to examine the achieved closed-loop poles. Recall that one of the objectives of the VCFQ approach is to replace the modal constraints with a more functional constraint on the state variances. Nonetheless, it is helpful to plot the closed-loop eigenvalues in the complex plane to examine the accuracy of the approximation obtained via the VCFQ approach. With the addition of two first-order actuator models, the dimension of the lateral-directional system matrices has grown to six. Two of the closed-loop eigenvalues are an order of magnitude larger than the others—indicative of the much faster response of the first-order actuator models than the rigid-body airframe dynamics. These faster eigenvalues tend to distort the scale of the complex plane plot, so they were omitted for convenience.

The closed-loop lateral-directional eigenvalues for the light descent flight condition are shown in Figure 6.36. Also drawn on the figure are the Dutch roll mode damping ratio, natural frequency, and damped natural frequency boundaries as given in Section 3.4.2. The roll mode maximum time constant boundary is also shown as a limit on the roll mode eigenvalue. The spiral mode, which is not required to be stable to satisfy Level I flying qualities requirements, does not have any boundaries drawn on the figure. It is evident that the closed-loop system easily satisfies each of the modal constraints given by the MIL-STD-1797. The feedback control laws developed not only stabilize the spiral mode, but also significantly increase the damping of the Dutch roll mode. It is not uncommon for aircraft to require additional yaw damping via stability augmentation [60], and it is interesting that the results of the LMI feasibility problem appear to naturally provide for this (it was not

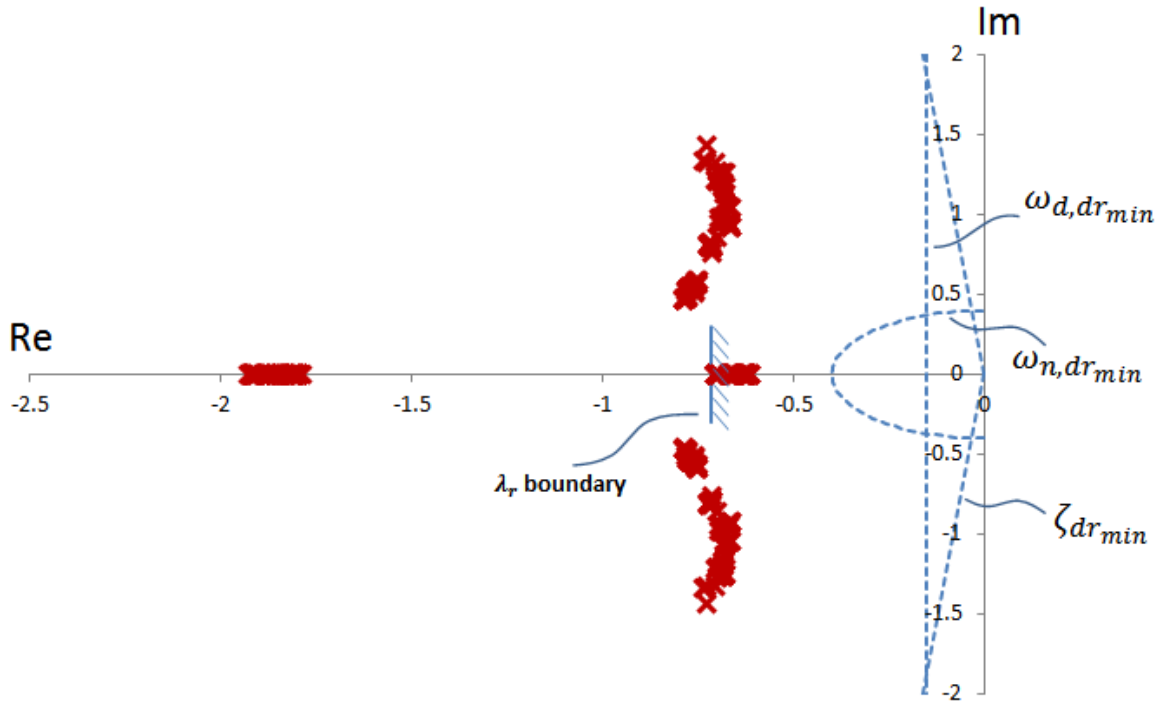

Figure 6.36: Closed-loop lateral-directional eigenvalues for each configuration synthesized during the minimization of the vertical tail area in the light descent flight condition

an explicitly prescribed objective). Roll mode eigenvalues, which are the real eigenvalues furtherest to the left along the real axis in Figure 6.36, satisfy the maximum time constant constraint with ease. Again, this is likely a result of the roll modes close affiliation with the wing aerodynamics, which remained unchanged in this study.

Of potentially equal importance to the minimization of the vertical tail area are the static analyses. The static scenarios of interest in this study are the engine-out at takeoff and the crosswind landing at approach described in Table 6.5. Figure 6.37 shows the required elevator deflection to trim the vehicle under each of the static scenarios. Federal regulations dictate that the aircraft be able to trim during an engine-out at takeoff or in heavy crosswind during landing without exceeding 75% of the available rudder travel. Examining the results

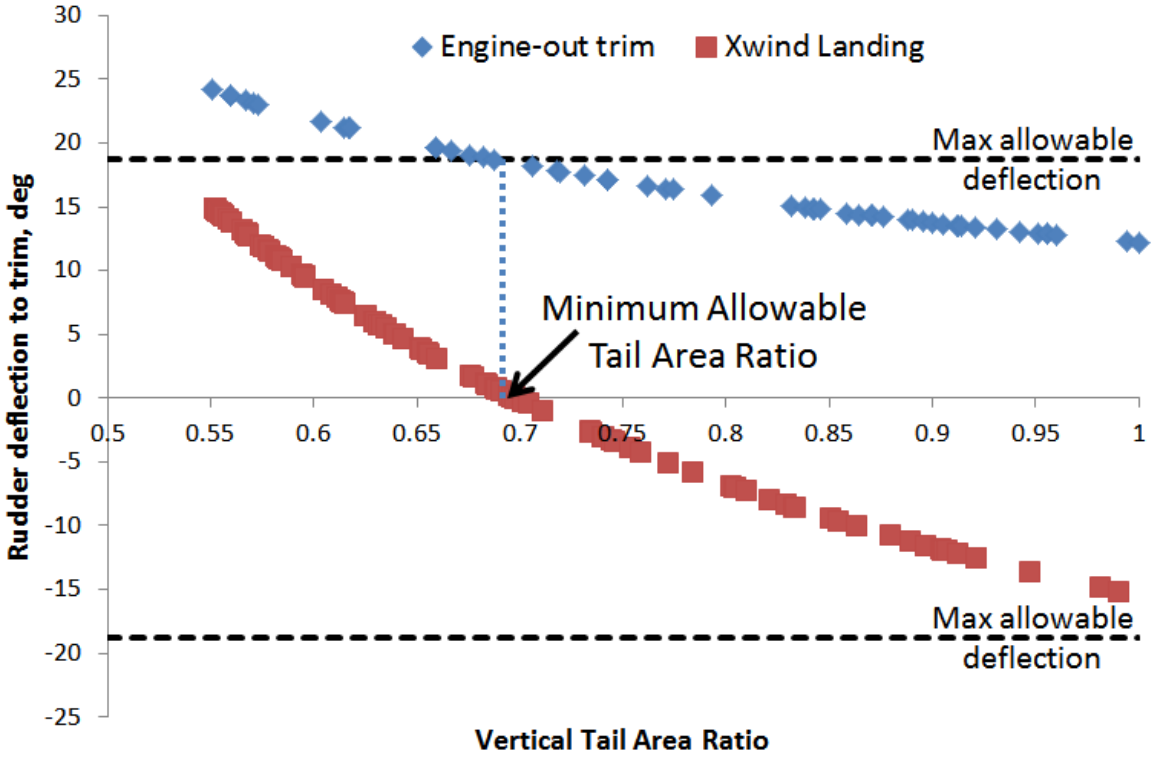

Figure 6.37: Engine-out and crosswind landing trimmed rudder deflection requirements versus $S_{r_{\mathrm{VT}}}$

in Figure 6.37 reveals that the minimum value of $S_{r_{\mathrm{VT}}}$ which doesn't violate the 75% rudder travel constraint is $S_{r_{\mathrm{VT}}} = 0.68$. That is, when the vertical tail area is reduced by 32% from the baseline configuration, the required rudder deflection to trim during takeoff with one engine inoperative is at the limit of 75% of the available rudder travel. The crosswind constraint was not the limiting condition for tail minimization, primarily due to the higher dynamic pressure during the landing condition. Results of the static stability analysis were very sensitive to the flight condition velocity since it appears as a squared term in the dynamic pressure. At higher elevations or when the ambient pressure is lower, the takeoff velocity would have to be increased in order to maintain the same dynamic pressure and level of static control authority. The fact that the engine-out scenario proved to be the most limiting constraint is an important result, since it highlights the necessity of conducting

static stability analyses in tandem with studies of the flight dynamics.

At first it may seem curious that the results of a static analysis would indicate that the vertical tail could be made smaller. If that is the case, why did the manufacturer not capitalize on the available performance gains? The answer to this question is two fold. First, federal regulations demand that a configuration be statically stable about each axis (see Chapter 3). For static directional stability, this implies that $C_{n_\beta} > 0$. At a value of $S_{r_{\mathrm{VT}}} = 0.68$ and at the aft CG limit, the static stability of the RSS configuration is unstable in climb and neutrally stable in cruise. Therefore, without relaxation of the static stability requirements, the optimized configuration would not satisfy regulatory constraints. A likely second reason the operational 737-800 tail is so large is robustness to uncertainties. Other than variations in loading, atmospheric conditions, and pilot capabilities, the vertical tail performance can also be plagued by viscous interactions with the wing and fuselage. At higher angles of attack, particularly near stall, the downwash and separation of the flow on the wing and fuselage impart severely turbulent flow on the empennage. This turbulence has a strong negative impact on the effectiveness of the tail surfaces, and may be a cause for an increase in tail surface area. Among the modeling shortcomings identified in this study was the inability to characterize the viscous interactions which dominate wake effects with the available tools—a shortcoming which is discussed further in the suggestions for future work in the next chapter.

With the vertical tail area reduced to 68% of that of the baseline configuration, an additional weight and drag savings is realized. Results from NASTRAN indicate that a weight reduction of 2,142 lbs can be had, however, this value is likely to be overestimated like the horizontal tail. Digital DATCOM predicts an additional drag reduction over the optimized horizontal tail configuration of 4.4%, resulting in a cruise drag coefficient of 0.044. This is a total drag savings of 12.0% over the baseline configuration. Figure 6.38 shows a

comparison of the optimized vertical tail and the baseline configuration vertical tail.

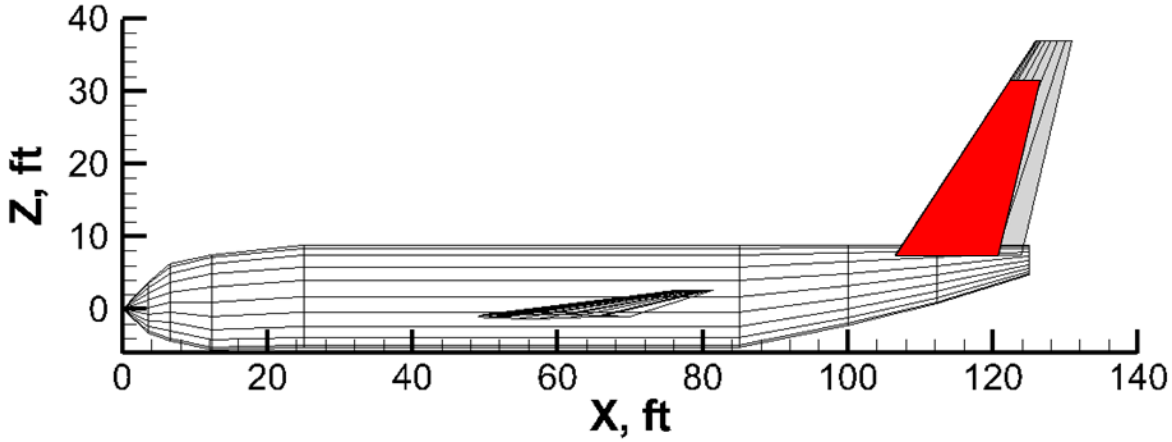

Figure 6.38: Comparison of the baseline vertical tail (black, wireframe) and the optimized RSS vertical tail (red, shaded)

6.4 Recoupling the Equations of Motion

The previous sections worked with models of the decoupled longitudinal and lateral-directional equations of motion. Throughout this thesis, the need to recouple the equations of motion to perform an analysis of the linearized, coupled equations of motion was repeatedly addressed. The state variance upper bounds computed from the MIL-STD-1797 using the VCFQ approach can be easily applied to the coupled equations, and the LMI constraints presented in Chapter 4 are extensible to very large systems. What is lacking, however, is an aerodynamic model which is capable of producing the necessary S&C derivatives. Digital DATCOM, for one, does not predict a single stability or control coupling derivative between the longitudinal and lateral-directional states. The NASTRAN aeroelastic solver is capable of predicting some (but not all) of the coupling stability derivatives like C_{M_r}—the pitching moment due to yaw rate. Further investigation into the validity of these coupling stability derivatives is required, since many of these terms are near machine-precision zero. This may be caused

by the fact that NASTRAN does not capture any aerodynamic influences of the fuselage. Control derivatives can be produced by NASTRAN, the magnitudes of which appear to be much more realistic. However, for a given control device, the coupling control derivatives are quite small relative to that devices primary axis, which is likely a result of the natural decoupling present in most transport aircraft. Recoupling the equations of motion using the current aerostructural models results in a system of the form

$$\begin{bmatrix} \dot{x}_{\text{long}} \\ \cdots \\ \dot{x}_{\text{latdir}} \end{bmatrix} = \left(\begin{bmatrix} & A_{\text{long}} & \\ & & \\ & & \end{bmatrix} \begin{bmatrix} * & \cdots & * \\ \vdots & \ddots & \vdots \\ * & \cdots & * \end{bmatrix} \begin{bmatrix} * & \cdots & * \\ \vdots & \ddots & \vdots \\ * & \cdots & * \end{bmatrix} \begin{bmatrix} & & \\ & A_{\text{latdir}} & \\ & & \end{bmatrix} \right) \begin{bmatrix} x_{\text{long}} \\ \cdots \\ x_{\text{latdir}} \end{bmatrix} + \left(\begin{bmatrix} & B_{\text{long}} & \\ & & \end{bmatrix} \begin{bmatrix} * \\ \vdots \\ * \end{bmatrix} \begin{bmatrix} * & * \\ \vdots & \vdots \\ * & * \end{bmatrix} \begin{bmatrix} & B_{\text{latdir}} & \\ & & \end{bmatrix} \right) \begin{bmatrix} \delta_{\text{elev}} \\ \delta_{\text{ail}} \\ \delta_{\text{rud}} \end{bmatrix} \quad (6.6)$$

where A_{long} and B_{long} are the decoupled longitudinal system matrices, A_{latdir} and B_{latdir} are the decoupled lateral-directional system matrices, and the $*$ is indicative of terms which are very small relative to the neighboring values ($\approx$ two orders of magnitude less or smaller). Many of the starred terms which couple the A matrices are not available at all. Clearly, recoupling the equations while using the current aerostructural model would result in a larger system of equations that are still approximately decoupled (particularly if zeros are used to fill in terms which are not computed). Until these modeling shortcomings are addressed, or until an aircraft configuration is analyzed which exhibits a greater degree of control cross-coupling, there is no advantage or additional insight to be gained by recoupling the equations.

Modeling has proven to be one of the most difficult aspects of the S&C module implementation. In the literature, absence of S&C data is traditionally remedied on a case-by-case basis via semi-empirical relations, CFD analysis, or experimental investigations. When operating within an MDO environment, the models must be general in nature and fully

automated. The need to address these shortcomings in the modeling process is discussed further in Chapter 7.

6.5 Summary of Relaxed Static Stability Empennage Design Results

The benefits of the simultaneous design of the control system and the configuration are well illustrated by the results achieved in the relaxed static stability aircraft design study. A detailed static and dynamic S&C study indicates that the baseline configuration could perform sufficiently well with smaller tails and a stability augmentation system, while at the same time reducing the vehicle gross weight and the trimmed drag if the static stability requirements of Federal regulations could be relaxed. The horizontal tail size was reduced to just 64% of the baseline horizontal tail area, and the vertical tail was reduced to 68% of the baseline vertical tail area. A total weight savings of 5,274 lbs. was achieved, though this number may be too large due to the overestimation of the empennage mass properties in the baseline model. The trimmed drag reduction at cruise was also significant, with Digital DATCOM predicting a 12.0% reduction of the RSS configuration drag at cruise as compared to the baseline configuration.

A preliminary estimate of the added range the RSS transport configuration could achieve can be obtained from the Breguet range equation

$$R = \frac{V}{g}\frac{1}{SFC}\frac{C_L}{C_D}\ln\left(\frac{W_{\text{initial}}}{W_{\text{final}}}\right), \tag{6.7}$$

where SFC is the specific fuel consumption of the engines, and W_{initial} and W_{final} are the total vehicle weights at the beginning and the end of a flight. If the weight fraction is assumed

to be approximately constant, and the baseline and RSS configurations are compared at the same loading condition such that the lift coefficients are approximately the same, an estimate of the RSS aircraft range can be obtained from the relation

$$R_{\text{RSS}} = R_{\text{base}} \frac{C_{D_{\text{base}}}}{C_{D_{\text{RSS}}}}, \tag{6.8}$$

where R_{base} is the range of the baseline configuration and R_{RSS} is the range of the RSS configuration. From the results of Sections 6.2 and 6.3, the RSS aircraft had a total reduction in the cruise trimmed drag coefficient of 12.0%. Thus, from Eq. (6.8), the RSS configuration would have an additional range capability of approximately 13.6% over the baseline aircraft. If the range of the baseline configuration is taken as that of the production Boeing 737-800 aircraft at 3,115 nautical miles [116], this translates to approximately 425 nautical miles of additional range.

During the horizontal tail minimization, it was found that the limiting static control case which established the forward CG boundary was the high C_L trim under the heavy loading condition. This result is not surprising, since deployed high lift devices tend to increase the nose down pitching moment and require greater elevator control power to trim the vehicle. The aft CG boundary, determined from the results of the dynamic stability analysis, was limited by the dynamics of the light loading condition. Results from both light and heavy loadings followed very similar trends (see Figure 6.24), though in general, the light condition was slightly more restrictive. The vertical tail minimization yielded similar results, with the light and heavy configurations both failing to meet their dynamic performance metrics at approximately $S_{r_{\text{VT}}} = 0.55$ at the aft-most CG location. Static results of the vertical tail sizing study actually proved to be more limiting than the dynamic constraints. As the vertical tail was reduced in size and the inherent yaw stability of the configuration was similarly reduced, the required rudder deflection to trim during an engine-out necessarily

increased. The dynamic pressures associated with takeoff and landing are low, causing the required rudder deflection to be quite large. This study did not allow for the rudder size relative to the vertical tail to change, though it is possible that investigations of larger rudder fractions may allow for the generation of larger aerodynamic forces and a further reduction in vertical tail area. However, larger rudder fractions lead to larger hinge moments, so considerations of actuator sizing and aerodynamic balancing would become important.

Chapter 7

Conclusions

Despite the successes in aeronautical engineering in just over a century of flight, the limitations of conventional design processes are evident throughout history. Typically, these limitations manifest themselves as performance shortcomings that require costly redesigns of the aircraft. Multidisciplinary Design Optimization is a computational tool which holds great potential to revolutionize aircraft conceptual design by introducing higher-fidelity physics earlier into the aircraft design cycle. The assembly and automation of analysis codes into a structured N^2 diagram provides an aircraft designer with a rapid analysis and design optimization capability that could capture synergistic phenomena that traditional design processes would have overlooked.

For all the praise given to MDO and its potential, current trends in MDO have a clear shortcoming in the field of Stability & Control. With few exceptions, the literature is devoid of full aircraft MDO frameworks which attempt to capture S&C performance characteristics beyond the most simple of static stability analyses. There is a strong need for dynamic S&C considerations in conceptual aircraft MDO. Futhermore, for advanced aircraft with relaxed stability characteristics, the control system and control effectors are so paramount that the

aircraft would be incapable of achieving flight without them. However, existing techniques to introduce dynamic S&C into an integrated design environment suffer from limitations that prevent their implementation into a multiple-input-multiple-output, highly coupled, full-scale aircraft MDO.

In this work, a Stability & Control module was constructed for integration into a collaboratively developed MDO framework for advanced aircraft conceptual design. The new S&C module contains both static and dynamic analyses, with the latter being facilitated by the Variance Constrained Flying Qualities approach and an automated, LMI-based control system design strategy. The VCFQ approach was introduced as a means to approximate the modal-based flying qualities criteria of the MIL-STD-1797 as deterministic state variance upper bounds computed from a given initial condition. State variance based control system design strategies can use these upper bounds as guarantees on the closed-loop system performance, enforcing dynamic stability and facilitating state-by-state performance constraints. This is in contrast to pole placement and other classical control design techniques which focus on modal parameters and only enforce performance constraints on the state vector as a whole. When the problem dimension becomes large, it is difficult, or impossible, to distinguish the modes and design for satisfactory flying qualities using these techniques. The state-by-state performance constraints enforced through the VCFQ approach allows for the conventionally decoupled longitudinal and lateral-directional equations of motion to be recoupled. Recoupling of the equations is important to capture coupling in the dynamics, but also the aerodynamic coupling which arises from the use of nontraditional control effectors. Using a state variance based approach also allows for additional models to be appended to the system to capture other dynamics of interest, including actuator dynamics, structural deflections, or unsteady aerodynamic terms, for example. Control system design is accomplished using an LMI feasibility problem, which is a convex problem formulation that

facilitates rapid numerical solutions and is scalable to very large systems. Extensibility of the LMI solution techniques allows for the inclusion of many states and actuators within the model to simultaneously guarantee state performance and control effector performance as constraints during the design of the controller.

An example design study was conducted on a typical transonic transport aircraft to demonstrate the capabilities and the benefits of the new S&C module. The goal of the design study was to resize the horizontal and vertical tails to reduce the aircraft gross weight and the trimmed drag coefficient under an assumed relaxation of the static stability requirements imparted by Federal regulations. The baseline configuration was developed from the dimensions and mass properties of the Boeing 737-800, and aerodynamic and structural models were constructed in NASTRAN and Digital DATCOM. Minimization of the tail areas was accomplished with all other aircraft configuration parameters held fixed. At each iteration, the relaxed static stability aircraft being synthesized was checked for satisfactory static and dynamic S&C characteristics. Using the VCFQ approach, it was successfully demonstrated that when the Federal Aviation Regulation static stability constraints are relaxed, tremendous savings can be made in both weight and drag of the vehicle. The final result of the design study was a horizontal tail area reduction of 36%, a vertical tail area reduction of 32%, a weight reduction of 5,274 lbs., and a total drag reduction of approximately 12.0% when compared to the baseline configuration. The static margin of the relaxed static stability configuration was marginally stable or unstable throughout the flight envelope, with the aft-most CG location corresponding to a static margin of approximately -13% in the cruise condition.

The dynamic S&C analysis also guaranteed that the closed-loop performance of the RSS transport always met the state variance based approximation of the Level 1 flying qualities requirements without saturating any control effectors or the effector rate limits. The VCFQ

approach completely avoided the total pole placement limitations of previous methods, and established a clear avenue for the introduction of control system design constraints which consider higher-order objectives. In an MDO framework with a more mature aero-structural model, more coupling S&C derivatives can be estimated and the VCFQ approach will facilitate the recoupling of the rigid-body equations of motion to analyze the full, linearized equations of motion. High performance configurations exhibit far more aerodynamic and kinematic coupling than transport aircraft, and the ability to include dynamic S&C constraints which consider the full set of rigid-body equations is critical.

Empennage design optimization of the transport aircraft was successful in demonstrating the capabilities of the VCFQ approach and the S&C module. In addition, it emphasized the importance and potential of S&C analyses in the conceptual design of high performance aircraft. Another conclusion which this work helped to expose is the importance and difficulty of modeling for stability and control. Unlike mission performance calculations or empirically based S&C sizing techniques, static and dynamic S&C analyses require information regarding the local physics, not just the global properties. For example, with little more than lift and drag estimates over a range of Mach numbers and altitudes, the range and endurance of an aircraft can be estimated. In contrast, predicting the static stability of the configuration requires a sound estimate of the aerodynamic moments, which are functions of the local distribution of pressure on each surface. In addition to that, dynamic analyses require estimates of the inertia tensor, which is a function of the local distribution of mass. This demand for locally accurate behavior is not inconsequential, and modeling for the RSS transport design problem proved to be a significant challenge. The extra data required to execute a thorough stability and control analysis begins to push the boundaries of the traditional conceptual design process, and may even begin to encroach upon preliminary design. One of the most critical topics of future study is to address the challenges of modeling

for S&C of high performance aircraft.

7.1 Topics for Future Study

The most pressing demand for future work on this topic is that of accurate and complete modeling for stability and control. In addition to the challenges of producing locally accurate data already discussed, several other challenges inherent to S&C make the task difficult. For one, control effector performance is known to be closely related to viscous phenomena, and the linear results obtained from many aerodynamic solvers may be incapable of properly characterizing the relevant physics. The performance of many advanced and nontraditional control effectors is dominated by separation or manipulation of the boundary layer—both of which are completely unobserved through linear methods. It may be necessary to develop surrogate models based on CFD or experimental results to accurately capture effector performance. Another S&C modeling challenge is that the achieved performance of an effector can be drastically reduced by aeroelastic phenomena. Fuselage and wing flexibility can reduce (or reverse, in extreme cases) the effectiveness of control devices, thus the structural model must sufficiently capture this behavior for realistic predictions of vehicle performance to be made. It is essential that a user of an MDO framework exercise sound judgment when selecting and implementing an aero-structural model for the purposes of S&C analysis.

The VCFQ approach established many opportunities for future study other than advancements in modeling. Some of the more intuitive extensions to the VCFQ approach may include flutter suppression, ride qualities analysis, or hinge moment constraints. Each of these objectives could be obtained by developing linear(ized) models of their behavior, appending them to the rigid body states, and including the variances of these new states as performance objectives in the control system design. In this manner, many higher order ob-

jectives could simultaneously constrain the control system design. Future studies should also examine the closely related output variance constrained techniques to handle scenarios when all of the states may not be measurable and available for feedback control design. Output (rather than state) variance techniques would also allow for the study of sensor dynamics and placement, should the level of fidelity where sensor design becomes important ever be reached.

Another area of recommended study is the selection of the eigenvector structure in the VCFQ approach. For new aircraft, no existing baseline eigenstructure exists from which to extract the desired eigenvector structure. Fortunately, results from the eigenstructure control literature have sought to address the estimation of an ideal eigenstructure for aircraft flying qualities, and these results can be leveraged to construct an idealized eigenvector structure for the VCFQ approach. The use of an ideal eigenvector structure was explored, though never implemented due to the fact that most eigenstructure assignment literature deals with high performance fighter and attack aircraft—additional study would be required to extend these results to transport configurations.

The final recommendations for future study deal with the estimation of the maximum allowable state variances and the choice of gust models. While the VCFQ approach leverages the countless man-hours that went into the development of the MIL-STD-1797 and its associated modal domain flying qualities requirements, there may be better means of obtaining state variance performance constraints. It is possible to reduce flight test data during measured gust conditions to compute maximum allowable state variances directly. However, this task would be very difficult, since real world gusts are nondeterministic and nearly impossible to fully characterize in flight. An alternative strategy may be to use control surface perturbations while flying through clean air to simulate a deterministic disturbances. Simulation may also yield useful results, provided that the pilot is subjected to accelerations

during simulation.

Modeling of the gusts used to compute the state variances also deserves further investigation. The discrete gusts used in this work were originally developed as preliminary gust cases for use in structural design. While these gust cases are likely to define the corners of the performance envelope for the airframe structure, engineering judgment must be exercised in using these cases for S&C analysis. For familiar aircraft with familiar flight envelopes, like a transonic transport, it is often a simple task to identify the likely critical conditions. With more advanced, unconventional configurations, it may be more difficult to select the critical flight conditions. Extensions to variance constrained control strategies which bound the output performance for a given class of input disturbances may prove to be a more robust solution. For example, output performance guarantees could be made for any disturbance which satisfies an upper bound on its energy norm. Investigations into energy based disturbances may also lead to the ability to include more advanced stochastic gust models in the search for the maximum allowable state variances.

Bibliography

[1] G. Cayley, "On Aerial Navigation, Part I," *Nicholson's Journal of Natural Philosophy*, Sept. 1809.

[2] G. Cayley, "On Aerial Navigation, Part II," *Nicholson's Journal of Natural Philosophy*, Feb. 1810.

[3] G. Cayley, "On Aerial Navigation, Part III," *Nicholson's Journal of Natural Philosophy*, March 1810.

[4] D. P. Raymer, *Aircraft Design: A Conceptual Approach*. American Institute of Aeronautics and Astronautics, Inc., Third ed., 1999.

[5] L. M. Nicolai and G. E. Carichner, *Fundamentals of Aircraft and Airship Design, Volume 1 - Aircraft Design*. AIAA Education Series, American Institute of Aeronautics and Astronautics, 2010.

[6] F. R. Swortzel and A. F. Barfield, "The fighter CCV program-Demonstrating new control methods for tactical aircraft," in *Aircraft Systems and Technology Meeting*, Sept. 1976.

[7] M. R. Anderson and W. H. Mason, "An MDO approach to Control-Configured-Vehicle Design," in *NASA, and ISSMO, Symposium on Multidisciplinary Analysis and Optimization*, Sept. 1996.

[8] AIAA Technical Committee, "Multidisciplinary Design Optimization (MDO), White Paper on Current State-of-the-Art," Tech. Rep. AIAA, Jan. 1991.

[9] L. T. Nguyen, M. E. Ogburn, W. P. Gilbert, K. S. Kibler, P. W. Brown, and P. L. Deal, "Simulator Study of Stall/Post-Stall Characteristics of a Fighter Airplane with Relaxed Longitudinal Static Stability," Tech. Rep. NASA Scientific and Technical Information Branch, 1979.

[10] M. J. Abzug, *Airplane Stability and Control: A History of the Technologies that made Aviation Possible*. Cambridge Aeropsace Series, 1997.

[11] I. T. Waaland, "Technology in the Lives of an Aircraft Designer," in *AIAA Wright Brothers Lecture*, Sept. 1991.

[12] T. A. Talay, "Introduction to the Aerodynamics of Flight," Tech. Rep. NASA SP-367, NASA History Division, NASA Langley Research Center, 1975.

[13] Unknown, "Far part 23—airworthiness standards: Normal, utility, acrobatic, and commuter category airplanes." US Government Printing Office Website, 2013. http://www.ecfr.gov/cgi-bin/text-idx?c=ecfr&rgn=div5&view=text&node=14:1.0.1.3.10&idno=14#14:1.0.1.3.10.2, Accessed 4 Sept 2013.

[14] Unknown, "Far part 25—airworthiness standards: Transport category airplanes." US Government Printing Office Website, 2013. http://www.ecfr.gov/cgi-bin/text-idx?c=ecfr&rgn=div5&view=text&node=14:1.0.1.3.11&idno=14, Accessed 4 Sept 2013.

[15] Department of Defense, *Department of Defense Interface Standard, Flying Qualities of Piloted Aircraft*, Feb. 2006. MIL-STD-1797B.

[16] M. L. Spearman, "Historical Development of World Wide Supersonic Aircraft," AIAA-79-1815, 1979.

[17] R. T. Whitcomb, "A Study of the Zero-Lift Drag-Rise Characteristics of Wing-Body Combinations Near the Speed of Sound," NACA report 1273, 1956.

[18] P. W. Merlin, *From Archangel to Senior Crown: Design and Development of the Blackbird*. AIAA Library of Flight, 2008.

[19] Unknown, "Douglas dc-3 commercial transport history." Boeing History Website, 2013. http://www.boeing.com/boeing/history/mdc/dc-3.page, Accessed 5 Sept 2013.

[20] J. E. Barnes, "Pentagon toils to build a bomber on a budget." Wall Street Journal Website, Nov. 2013. http://online.wsj.com/news/articles/SB10001424052702304384104579141982099354454, Accessed: 4 Dec. 2013.

[21] O. Gur, M. Bhatia, J. A. Schetz, W. H. Mason, R. K. Kapania, and D. Mavris, "Multidisciplinary Optimization of a Truss-Braced Wing Aircraft," *AIAA Journal of Aircraft*, vol. 47, pp. 1907–1917, Nov-Dec 2010.

[22] O. Gur, M. Bhatia, W. H. Mason, J. A. Schetz, R. K. Kapania, and T. Nam, "Development of a Framework for Trussed-Braced Wing Conceptual MDO," *Structural and Multidisciplinary Optimization*, vol. 44, pp. 277–298, August 2011.

[23] D. L. Allison, C. C. Morris, J. A. Schetz, R. K. Kapania, C. Sultan, L. T. Watson, J. D. Deaton, and R. V. Grandhi, "A Multidisciplinary Design Optimization Framework for Design Studies of an Efficient Supersonic Air Vehicle," in *AIAA Multidisciplinary Analysis and Optimization Conference*, Sept. 2012. AIAA-2012-5492.

[24] D. Allison, *Multidisciplinary Design Optimization and Design Space Exploration of an Efficient Supersonic Air Vehicle*. PhD thesis, Virginia tech, 2013. Publication pending.

[25] C. C. Morris, D. L. Allison, J. A. Schetz, and R. K. Kapania, "Parametric Geometry Model for Multidisciplinary Design Optimization of Tailless Supersonic Aircraft," in *AIAA Modeling and Simulation Technologies Conference*, Aug. 2012. AIAA-2012-4580.

[26] J. D. Deaton and R. V. Grandhi, "Thermal-Structural Design and Optimization of Engine Exhaust-Washed Structures," in *52nd AIAA/ASME/ASCE/AHS/ASC Structures, Structural Dynamics, and Materials Conference*, April 2011. AIAA-2011-1903.

[27] K. M. Dorsett and D. R. Mehl, "Innovative Control Effectors (ICE) Phase I," Tech. Rep. WL-TR-96-3043, Lockheed Martin Tactical Aircraft Systems, Jan. 1996.

[28] E. L. Roetman, S. A. Northcraft, and J. R. Dawdy, "Innovative Control Effectors (ICE) Phase Ib," Tech. Rep. WL-TR-96-3074, Boeing Defense and Space Group, March 1996.

[29] K. M. Dorsett and S. P. Fears, "Innovative Control Effectors (ICE) Phase II," Tech. Rep. WL-TR-97-3059, Lockheed Martin Tactical Aircraft Systems, Aug. 1997.

[30] G. E. Cooper and R. P. Harper, "The Use of Pilot Rating in the Evaluation of Aircraft Handling Qualities," Tech. Rep. TN D-5153, NASA, April 1969.

[31] D. G. Mitchell, D. B. Doman, D. L. Key, D. H. Klyde, D. B. Leggett, D. J. Moorhouse, D. H. Mason, D. L. Raney, and D. K. Schmidt, "The Evolution, Revolution, and Challenges of Handling Quailties," in *AIAA Atmospheric Flight Mechanics Conference and Exhibit*, Aug. 2003. AIAA-2003-5465.

[32] R. R. Gilruth, "Requirements for Satisfactory Flying Qualities of Airplanes," Tech. Rep. 755, NACA, 1943.

[33] United States Air Force, *Military Specification Flying Qualities of Piloted Airplanes*, Nov. 1968. MIL-F-8785A.

[34] Department of Defense, *Military Specification Flying Qualities of Piloted Airplanes*, Nov. 1969. MIL-F-8785B.

[35] Department of Defense, *Military Specification Flying Qualities of Piloted Airplanes*, Nov. 1980. MIL-F-8785C.

[36] Department of Defense, *Department of Defense Interface Standard, Flying Qualities of Piloted Aircraft*, Feb. 1990. MIL-STD-1797A.

[37] Department of Defense, *Department of Defense Handbook, Flying Qualities of Piloted Aircraft*, Dec. 1997. MIL-HDBK-1797.

[38] L. P. Ozoroski, E. W. Shields, J. J. Berton, J. S. Gray, S. M. Jones, C. G. Naiman, J. A. Seidel, K. T. Moore, B. A. Naylor, and S. Townsend, *Initial Multidisciplinary Design and Analysis Framework*. NASA Langley Research Center, June 2010. TM-2010-216711.

[39] J. M. Grasmeyer, "Multidisciplinary Design Optimization of a Strut-Braced Wing Aircraft," Master's thesis, Virginia Tech, April 1998.

[40] A. A. Giunta, *Aircraft Multidisciplinary Design Optimization Using Design of Experiments Theory and Response Surface Modeling Methods*. PhD thesis, Virginia Tech, 1997.

[41] S. J. Morris and I. Kroo, "Aircraft Design Optimization with Dynamic Performance Constraints," *Journal of Aircraft*, vol. 27, pp. 1060–1067, Oct. 1989.

[42] L. G. Cresp and S. P. Kenny, *Matlab Stability and Control Toolbox: Trim and Static Stability Module*. NASA Langley Research Center, Nov. 2006.

[43] P. E. MacMillan, "Trim, Control, and Performance Effects in Variable-Complexity High-Speed Civil Transport Design," Master's thesis, Virginia Polytechnic Institute and State University, 1996.

[44] E. G. Rynaski and N. C. Weingarten, "Flight Control Principles for Control Configured Vehicles," Tech. Rep. AFFDL-TR-71-154, Cornell Aeronautical Laboratory, 1972.

[45] I. I. Kaminer, R. M. Howard, and C. S. Buttrill, "Development of Closed-Loop Tail-Sizing Criteria for a High Speed Civil Transport," *Journal of Aircraft*, vol. 34, 1997.

[46] S. Boyd, L. E. Ghaoui, E. Feron, and V. Balakrishan, *Linear Matrix Inequalities in Systems and Control Theory*. SIAM, 1994.

[47] C. Scherer and S. Weiland, *Linear Matrix Inequalities in Control*. Delft University, 2005.

[48] J. G. VanAntwerp and R. D. Braatz, "A Tutorial on Linear and Bilinear Matrix Inequalities," *Journal of Process Control*, vol. 10, pp. 363–385, 2000.

[49] D. L. Knill, *Implementing Aerodynamic Predictions from Computational Fluid Dynamics in Multidisciplinary Design Optimization of a High-Speed Civil Transport*. PhD thesis, Virginia Tech, 1997.

[50] R. E. Perez, H. H. T. Liu, and K. Behdinan, "Multidisciplinary Optimization Framework for Control-Configuration Integration in Aircraft Conceptual Design," *Journal of Aircraft*, vol. 43, no. 6, 2006.

[51] R. Braun, P. Gage, I. Kroo, and I. Sobieski, "Implementation and Performance Issues in Collaborative Optimization," in *6th AIAA, NASA, and ISSMO, Symposium on Multidisciplinary Analysis and Optimization*, Sept. AIAA-1996-4017.

[52] L. P. Ozoroski, "Correspondence detailing MaSCoT implementation." Email Correspondence, Oct. 2011.

[53] L. A. McCullers, *Flight Optimization System User's Guide*. NASA Langley Research Center, Release 8.20 ed., Feb. 2011.

[54] AVID LLC., *AVID ACS-ACSYNT Capabilities Sheet*, 2010.

[55] G. Coleman and B. Chudoba, "A Generic Stability and Conrol Tool for Conceptual Design: Prototype System Overview," in *45th AIAA Aerospace Sciences Meeting and Exhibit*, Jan. 2007. AIAA-2007-659.

[56] A. Omoragbon, "An Integration of a Modern Flight Control System Design Technique into a Conceptual Design Stabilty and Controls Tool, *AEROMECH*," Master's thesis, The University of Texas at Arlington, Aug. 2010.

[57] "CEASIOM Scientific Publications." Ceasiom Website. `http://www.ceasiom.com/`, Accessed: 19 Feb. 2013.

[58] unknown, "Pacelab APD product data sheet." PACE Website, Nov. 2012. `http://www.pace.de/fileadmin/user_upload/dokumente/Resources/PacelabAPD_2p_web.pdf`, Accessed: 4 Dec. 2013.

[59] E. Torenbeek, *Synthesis of Subsonic Airplane Design*. Delft University Press, 1981.

[60] B. N. Pamadi, *Performance, Stability, Dynamics, and Control of Airplanes*. AIAA Education Series, 2nd ed., 2004.

[61] B. Etikin, *Dynamics of Atmospheric Flight*. John Wiley, 1st ed., 1972.

[62] E. L. Duke, R. F. Antoniewicz, and K. D. Krambeer, "Derivation and Definition of a Linear Aircraft Model," Tech. Rep. NASA Ref. Pub. 1207, NASA Dryden Flight Research Facility, 1988.

[63] G. H. Bryan, *Stability in Aviation*. McMillan, 1911.

[64] V. Klein and K. D. Noderer, "Modeling of Aircraft Unsteady Aerodyanmic Characteristics," Tech. Rep. TM-109120, NASA Langley Research Center, 1994.

[65] J. Boiffier, *The Dynamics of Flight: The Equations*. Wiley, 1998.

[66] J. Rech and C. S. Leyman, "A Case Study by Aerospatiale and British Aerospace on the Concorde," Tech. Rep. AIAA Professional Study Series, 1980.

[67] A. M. Lyapunov, *The General Problem of the Stability of Motion*. PhD thesis, Univ. Kharkov, 1892. Published in Russian.

[68] R. E. Skelton, *Dynamic Systems Control, Linear Systems Analysis and Synthesis*. Wiley, 1988.

[69] H. Khalil, *Nonlinear Systems*. Prentice Hall, 2002.

[70] G. L. Teper, "Aircraft Stability and Control Data," Tech. Rep. CR-96008, NASA, April 1969.

[71] R. E. Skelton, T. Iwasaki, and K. M. Grigoriadis, *A Unified Algebraic Approach to Linear Control Design*. Taylor & Francis, 1998.

[72] R. L. Williams and D. A. Lawrence, *Linear State-Space Control Systems*. John Wiley & Sons, 2007.

[73] L. S. Shieh, H. M. Dib, and B. C. McInnis, "Linear Quadratic Regulators with Eigenvalue Placement in a Vertical Strip," *IEEE Trans. Automat. Contr.*, vol. AC-31, pp. 236–239, 1986.

[74] N. Kawasaki and E. Shimemura, "Determining Quadratic Weighting Matrices to Locate Poles in a Specified Region," *Automatica*, vol. 19, no. 5, pp. 557 – 560, 1983.

[75] K. Furuta and S. Kim, "Pole Assignment in a Specified Disk," *Automatic Control, IEEE Transactions on*, vol. 32, pp. 423 – 427, May 1987.

[76] P. Misra, "LQR Design with Prescribed Damping and Degree of Stability," in *Computer-Aided Control System Design, Proceedings of the 1996 IEEE International Symposium on*, pp. 68 –70, Sept. 1996.

[77] M. Chilali and P. Gahinet, "H_∞ Design with Pole Placement Constraints: An LMI Approach," *IEEE Transactions on Automatic Control*, vol. 41, pp. 358–367, March 1996.

[78] C. C. Morris, C. Sultan, D. L. Allison, J. A. Schetz, and R. K. Kapania, "Flying Quality Constraints in a Multidisciplinary Design Optimization of a Supersonic Tailless Aircraft," in *14th AIAA/ISSMO Multidisciplinary Analysis and Optimization Conference*, no. AIAA-2012-5517, Sept. 2012.

[79] E. Collins and R. E. Skelton, "A Theory of State Covariance Assignment for Discrete Systems," *IEEE Transactions on Automatic Control*, vol. 32, Jan. 1987.

[80] A. Hotz and R. E. Skelton, "Covariance Control Theory," *International Journal of Control*, 1987.

[81] V. Sreeram, W. Q. Liu, and M. Diab, "Theory of State Covariance Assignment for Linear Single-input Systems," *IEEE Proc.-Control Theory Appl.*, vol. 143, May 1996.

[82] H. Khaloozadeh and S. Baromand, "State Covariance Assignment Problem," *IET Control Theory and Applications*, 2010.

[83] D. G. Goddard and D. Gleason, "Eigenstructure Selection for Longitudinal Flying Qualities Considerations," in *Aerospace and Electronics, Proceedings of the IEEE 1988 Conference, 1988*, vol. 2, pp. 470–478, 1988.

[84] A. N. S., K. K. Rao, and K. M. Lizy, "Eigenstructure Assignment Applied to the Longitudinal Control of Aircraft," in *10th National Conference on Technological Trends*, Trivandrum College of Engineering, Nov 2009.

[85] J. B. Davidson and D. A. II, "Lateral-Directional Eigenvector Flying Qualities Guidelines for High Performance Aircraft," Tech. Rep. NASA Langley Research Center, 1996.

[86] S. Srinathkumar, *Eigenstructure Control Algorithms: Application to aircraft/rotorcraft handling qualities design*. The Institution of Engineering and Technology, 2011.

[87] C. Nieto-Wire and K. Sobel, "Flight Control Design for a Tailless Aircraft Using Eigenstructure Assignment," *International Journal of Aerospace Engineering*, vol. 2011, Jan. 2011.

[88] F. M. Hoblit, *Gust Loads on Aircraft: Concepts and Applications*. AIAA Education Series, 1988.

[89] T. Oktay, *Constrained Control of Complex Helicopter Models*. PhD thesis, Virginia Tech, March 2012.

[90] "Matlab Control System Toolbox State space model documentation." Matlab Documentation Center. `http://www.mathworks.com/help/control/ref/ss.html`, Accessed: 22 Sept. 2013.

[91] E. J. Alyanak and R. Kolonay, "Efficient Supersonic Air Vehicle Structural Modeling for Conceptual Design," in *12th AIAA Aviation Technology, Integration, and Operations Conference and 14th AIAA/ISSM*. AIAA-2012-5519.

[92] *MSTCGEOM Reference Guide*.

[93] MSC Nastran, *Aeroelastic Analysis User's Guide*, 2004. Version 68.

[94] ZONA Technology, Inc., *ZONAIR User's Manual*, 2010. Version 4.2.

[95] J. E. Williams and S. R. Vukelich, *USAF Stability and Control Digital DATCOM Volume 1, Users Manual*.

[96] J. E. Williams and S. R. Vukelich, *USAF Stability and Control Digital DATCOM Volume 2, Implementation of Datcom Methods*.

[97] J. E. Williams and S. R. Vukelich, *USAF Stability and Control Digital DATCOM Volume 3, Plot Module*.

[98] "Matlab Aerospace System Toolbox DATCOM Import documentation." Matlab Documentation Center. `http://www.mathworks.com/help/aerotbx/ug/datcomimport.html`, Accessed: 22 Sept. 2013.

[99] T. Melin, *User's Guide, Tornado 1.0*, Jan 2001. Release 2.3.

[100] L. A. McCullers, *Program WINGDES - Release 2001.1 User's Manual*. University of Virginia Mechanical and Aerospace Engineering Department, Feb 2008.

[101] *AWAVE User's Guide for the Revised Wave Drag Analysis Program*.

[102] W. H. Mason, *FRICTION User's Guide*. Virginia Tech Department of Aerospace and Ocean Engineering, Blacksburg, VA, 2006.

[103] "Phoenix Integration ModelCenter." website. `http://www.phoenix-int.com/software/phx-modelcenter.php`, Accessed: 22 Sept 2013.

[104] P. Gahinet, A. Nemirovski, A. J. Laub, and M. Chilali, *MATLAB LMI Control Toolbox*. The Mathworks, 1995.

[105] A. Nemirovski and P. Gahinet, "The Projective Method for Solving Linear Matrix Inequalities," in *Proc. Amer. Contr. Conf.*

[106] P. Tétrault, J. A. Schetz, and B. Grossman, "Numerical Prediction of Interference Drag of Strut-Surface Intersection in Transonic Flow," *AIAA Journal*, vol. 39, May 2001.

[107] N. A. Meadows, J. A. Schetz, R. K. Kapania, M. Bhatia, and G. Seber, "Multidisciplinary Design Optimization of Medium Range Transonic Truss-Braced Wing Transport Aircraft," *Journal of Aircraft*, 2012.

[108] B. A. Company, "Detailed technical characteristics for airport planning: 737 scale drawings." Available on `http://www.boeing.com/boeing/commercial/airports/737.page`, Accessed: 24 Sept 2013, May 2011. D6-58325-6.

[109] "UIUC Airfoil Coordinates Database." website. `http://aerospace.illinois.edu/m-selig/ads/coord_database.html`, Accessed: 24 Sept. 2013.

[110] *Aircraft Design: A Systems Engineering Approach*. Wiley, 2012.

[111] "Flight Global General Aviation Cutaways – Boeing 737-700." website. http://www.flightglobal.com/airspace/media/generalaviationcutaways/boeing-737-700-cutaway-drawing-83030.aspx, Accessed: 24 Sept. 2013.

[112] D. J. Moorhouse and M. W. M. Jenkins, "Use of Short Period Frequency Requirements in Horizontal Tail Sizing," *Journal of Aircraft*, vol. 12, pp. 560–561, Oct 1974. AIAA-44474-494.

[113] F. H. Lutze, "Trimmed Drag Considerations," *AIAA Journal of Aircraft*, vol. 14, no. 6, pp. 544–546, 1976.

[114] T. B. Company, "Exceeding tire speed rating during takeoff." Boeing Magazine, 2009.

[115] Uknown, *Boeing 737-600/-700/-800/-900 Airplane Flight Manual*. The Boeing Company, July 2013.

[116] Unknown, "Boeing 737-800 technical characteristics." Boeing Website, 2013. http://www.boeing.com/boeing/commercial/737family/pf/pf_800tech.page, Accessed: 6 Nov. 2013.

Appendix A

Equations of Motion: Wind Axes Forces

This appendix details the complete scalar equations of motion as they are implemented within the S&C module. The angular rates are resolved in the body axes, the velocities and aerodynamic angles in the wind axes, the Euler angles are the relationship between the body and inertial axes, and the navigational states are described in the inertial axes. All of these equations are fully derived in the work of Duke, et al.[62], and are repeated here for completeness.

Define the inertia tensor as in Eq. (3.12) as

$$I = \begin{bmatrix} I_{xx} & -I_{xy} & -I_{xz} \\ -I_{xy} & I_{yy} & -I_{yz} \\ -I_{xz} & -I_{yz} & I_{zz} \end{bmatrix} \tag{A.1}$$

Define the inverse of the inertia tensor, I^{-1} as

$$I^{-1} = \frac{1}{\det I} \begin{bmatrix} I_1 & I_2 & I_3 \\ I_2 & I_4 & I_5 \\ I_3 & I_5 & I_6 \end{bmatrix} \tag{A.2}$$

where

$$\det I = I_{xx}I_{yy}I_{zz} - I_{xx}I_{yz}^2 - I_{zz}I_{xy}^2 - I_{yy}I_{xz}^2 - 2I_{yz}I_{xz}I_{xy} \tag{A.3}$$
$$I_1 = I_{yy}I_{zz} - I_{yz}^2 \tag{A.4}$$
$$I_2 = I_{xy}I_{zz} + I_{yz}I_{xz} \tag{A.5}$$
$$I_3 = I_{xy}I_{yz} + I_{yy}I_{xz} \tag{A.6}$$
$$I_4 = I_{xx}I_{zz} - I_{xz}^2 \tag{A.7}$$
$$I_5 = I_{xx}I_{yz} + I_{xy}I_{xz} \tag{A.8}$$
$$I_6 = I_{xx}I_{yy} - I_{xy}^2. \tag{A.9}$$

Also, define

$$D_x = I_{zz} - I_{yy} \tag{A.10}$$
$$D_y = I_{xx} - I_{zz} \tag{A.11}$$
$$D_z = I_{yy} - I_{xx} \tag{A.12}$$

Body Axis Rotational Accelerations

Using the definition of the body axis angular velocity as

$$\omega = \begin{bmatrix} p & q & r \end{bmatrix}^T, \tag{A.13}$$

the rotational acceleration equations of motion can be expressed as

$$\begin{aligned}\dot{p} = \frac{1}{\det I}\big[&LI_1 + MI_2 + NI_3 - p^2\left(I_{xz}I_2 - I_{xy}I_3\right) + pq\left(I_{xz}I_1 - I_{yz}I_2 - D_zI_3\right) \\ &- pr\left(I_{xy}I_1 + D_yI_2 - I_{yz}I_3\right) + q^2\left(I_{yz}I_1 - I_{xy}I_3\right) - qr\left(D_xI_1 - I_{xy}I_2 + I_{xz}I_3\right) \\ &-r^2\left(I_{yz}I_1 - I_{xz}I_2\right)\big]\end{aligned} \tag{A.14}$$

$$\begin{aligned}\dot{q} = \frac{1}{\det I}\big[&LI_2 + MI_4 + NI_5 - p^2\left(I_{xz}I_4 - I_{xy}I_5\right) + pq\left(I_{xz}I_2 - I_{yz}I_4 - D_zI_5\right) \\ &- pr\left(I_{xy}I_2 + D_yI_4 - I_{yz}I_5\right) + q^2\left(I_{yz}I_2 - I_{xy}I_5\right) - qr\left(D_xI_2 - I_{xy}I_4 + I_{xz}I_5\right) \\ &-r^2\left(I_{yz}I_2 - I_{xz}I_4\right)\big]\end{aligned} \tag{A.15}$$

$$\begin{aligned}\dot{r} = \frac{1}{\det I}\big[&LI_3 + MI_5 + NI_6 - p^2\left(I_{xz}I_5 - I_{xy}I_6\right) + pq\left(I_{xz}I_3 - I_{yz}I_5 - D_zI_6\right) \\ &- pr\left(I_{xy}I_3 + D_yI_5 - I_{yz}I_6\right) + q^2\left(I_{yz}I_3 - I_{xy}I_6\right) - qr\left(D_xI_3 - I_{xy}I_5 + I_{xz}I_6\right) \\ &-r^2\left(I_{yz}I_3 - I_{xz}I_5\right)\big]\end{aligned} \tag{A.16}$$

Wind Axis Translational Accelerations

Derivation of the force equations led to expressions in terms of the body axis velocities and accelerations. Using the definitions of the wind axis terms of total velocity V, angle of attack α, and angle of sideslip β as

$$V = |V_B| = \left(u^2 + v^2 + w^2\right)^{1/2} \tag{A.17}$$

$$\alpha = \tan^{-1}\left(\frac{w}{u}\right) \tag{A.18}$$

$$\beta = \sin^{-1}\left(\frac{v}{V}\right), \tag{A.19}$$

the translational acceleration equations of motion can be rewritten in the wind axes as

$$\begin{aligned}\dot{V} =& \frac{1}{m}\left[-D\cos\beta + Y\sin\beta + X_T\cos\alpha\cos\beta + Y_T\sin\beta + Z_T\sin\alpha\cos\beta\right.\\ &\left.-mg\left(\cos\alpha\cos\beta\sin\theta - \sin\beta\sin\phi\cos\theta - \sin\alpha\cos\beta\cos\phi\cos\theta\right)\right] \qquad \text{(A.20)}\\ \dot{\alpha} =& \frac{1}{Vm\cos\beta}\left[-L + Z_T\cos\alpha - X_T\sin\alpha + mg\left(\cos\alpha\cos\phi\cos\theta + \sin\alpha\sin\theta\right)\right]\\ &q - \tan\beta\left(p\cos\alpha + r\sin\alpha\right) \qquad \text{(A.21)}\\ \dot{\beta} =& \frac{1}{mV}\left[D\sin\beta + Y\cos\beta - X_T\cos\alpha\sin\beta + Y_T\cos\beta - Z_T\sin\alpha\sin\beta + mg\left(\cos\alpha\sin\beta\sin\theta\right.\right.\\ &\left.\left.+\cos\beta\sin\phi\cos\theta - \sin\alpha\sin\beta\cos\phi\cos\theta\right)\right] + p\sin\alpha - r\cos\alpha, \qquad \text{(A.22)}\end{aligned}$$

where L, D, and Y are the aerodynamic lift, drag, and side forces, and X_T, Y_T, and Z_T are the components of thrust about the body x, y, and z axes.

Attitude Rates

The Euler angle rates which described the relationship between the body axes and the inertial axes are unchanged from before as

$$\dot{\phi} = p + q\tan\theta\sin\phi + r\tan\theta\cos\phi \tag{A.23}$$

$$\dot{\theta} = q\cos\phi - r\sin\phi \tag{A.24}$$

$$\dot{\psi} = q\sec\theta\sin\phi + r\sec\theta\cos\phi. \tag{A.25}$$

Navigation Equations in the Wind Axes

Converting Eq. (3.23) to be congruent with the wind axes variables gives

$$\dot{h} = V\left(\cos\alpha\cos\beta\sin\theta - \sin\beta\sin\phi\cos\theta - \sin\alpha\cos\beta\cos\phi\cos\theta\right) \tag{A.26}$$

$$\begin{aligned}\dot{x} =& V\left[\cos\alpha\cos\beta\cos\theta\cos\psi + \sin\beta\left(\sin\phi\sin\theta\cos\psi - \cos\phi\sin\psi\right)\right.\\ &\left. + \sin\alpha\cos\beta\left(\cos\phi\sin\theta\cos\psi + \sin\phi\sin\psi\right)\right]\end{aligned} \tag{A.27}$$

$$\begin{aligned}\dot{y} =& V\left[\cos\alpha\cos\beta\cos\theta\sin\psi + \sin\beta\left(\cos\phi\cos\psi + \sin\phi\sin\theta\sin\psi\right)\right.\\ &\left. + \sin\alpha\cos\beta\left(\cos\phi\sin\theta\sin\psi - \sin\phi\cos\psi\right)\right]\end{aligned} \tag{A.28}$$